THERMOMECHANICAL PROCESSING OF SPARK PLASMA SINTERED ALUMINUM POWDER METALLURGY ALLOYS VIA ASYMMETRIC ROLLING AND UPSET FORGING

by

Mark Yao Amegadzie

Submitted in partial fulfilment of the requirements
for the degree of Doctor of Philosophy

at

Dalhousie University
Halifax, Nova Scotia
December 2019

I dedicate this thesis to my parents (Fidelis and Celestine) who have instilled discipline, thought me values, encouraged and guided me throughout my life.

TABLE OF CONTENTS

LIST OF TABLES

LIST OF FIGURES

ABSTRACT

The research in this study was completed to investigate the effects of thermal-mechanical working on spark plasma sintered (SPS) powder metallurgy (PM) preforms. Two alloys (PA2219 and an Al-Sc-Zr ternary) were considered as were two means of working – asymmetric rolling (ASR) and upset forging. To gain a firm understanding of the fundamental elements of ASR and ultimately deduce the best rolling parameters for the SPS PM alloys, research in this area commenced with studies on the well-known wrought aluminum alloy 6061. Results indicated that the utilization of a higher velocity ratio as well as a small initial thickness of the sample imparted gains in mechanical properties to the finished product. Meanwhile, changes to roller velocities and rolling direction were found to be insignificant. EBSD analysis revealed that the microstructure became more homogenized with a reduction in the number of passes. The findings from preliminary studies on AA6061 were then used to process the SPS PM alloys. The rolling schedules resulted in full densification of the sintered Al-Sc-Zr billets while $Al_3(Sc,Zr)$ precipitates observed via transmission electron microscopy (TEM) in the sintered preforms were seemingly unaffected by the rolling process. Generally, decreases in the rolling temperature yielded marginal gains in mechanical properties. The Al-Sc-Zr alloy sintered at 500ºC and rolled at 200ºC exhibited the highest concentration of low angle grain boundaries (LAGBs) and the most desirable combination of hardness and tensile properties. In forging trials, all strains and strain rates were found to impart full densification of the Al-Sc-Zr preforms. Interestingly, the lowest forging strain considered (0.4 mm/mm) imparted sizable improvements in tensile properties. In particular, tensile ductility was ~40x greater than that measured in the as-sintered counterpart. However, excessive plastic strain (1.6) fostered dynamic recrystallization and possibly the formation of adiabatic shear bands that invoked declines in tensile properties. Strain rate was also found to be influential as lower rates enhanced recrystallization prompting reductions in yield strength and minor gains in ductility.

For the PA2219 PM alloy, forging achieved full densification of sintered preforms. In addition, the forging process imparted gains in the tensile properties. Further improvements in tensile strength were realized in the heat treated (T87) specimens. For instance, the yield strength of the forged-T87 products were some 40-60% higher than counterpart specimens tested in the as-forged (T1) state. The optimum tensile properties were obtained for the specimen SPS processed 550ºC and Forged (T87) at 500ºC (YS=354MPa, UTS = 466MPa, Elongation =13%). One of the critical observations made was that a continuous oxide film was present in the microstructure of the spark plasma sintered billet. Fortunately, this tenacious layer was disrupted through upset forging. The discretization of this oxide network would have contributed towards the improved tensile properties in the forged products especially the ductility.

LIST OF ABBREVIATIONS AND SYMBOLS USED

AA	Aluminum Alloy
Ag	Silver
Al	Aluminum
ASTM	American Society for Testing and Materials
ASR	Asymmetric Rolling
BCC	Body Centered Cubic
BF	Bright Field
cos	Cosine
Cu	Copper
Cr	Chromium
Cd	Cadmium
EBSD	Electron Backscatter Diffraction
EDS	Energy Dispersive Spectroscopy
FCC	Face Centered Cubic
Fe	Iron
Ga	Gallium
Ge	Germanium
h	Thickness
HAADF	High Angle Annular Dark Field
HAGB	High Angle Grain Boundary
HRB	Rockwell Hardness B-Scale
HV	Vickers Hardness
ICPS	Inductively Coupled Plasma Spectroscopy
kN	Kilo Newton
LAGB	Low Angle Grain Boundary
Li	Lithium
Mg	Magnesium
MPa	Mega Pascal
mm	millimeters
Mn	Manganese

n	Strain Hardening Exponent
NA	Normal Axis
Ni	Nickel
NSERC	Natural Sciences and Engineering Research Council of Canada
OM	Optical Microscope
PA	Prealloyed
Pb	Lead
PM	Powder Metallurgy
RA	Rolling Axis
R	Radius
rpm	revolutions per minute
SAD	Selected Area Diffraction
Sc	Scandium
SEM	Scanning Electron Microscope
SPS	Spark Plasma Sintering
Si	Silicon
Sn	Tin
TA	Transverse Axis
TEM	Transmission Electron Microscope
Ti	Titanium
UD	Unidirectional
UTS	Ultimate Tensile Strength
VR	Velocity Ratio
YS	Yield Strength
Zn	Zinc
Zr	Zirconium
γ	Shear Strain
v	Velocity
σ	Stress
ε	Strain
{hkl}	Family of Crystallographic Planes

<uvw>	Crystallographic Direction

ACKNOWLEDGEMENTS

I will first and foremost like to thank my supervisor Professor Paul Bishop for his guidance, advice, financial support and particularly his patience throughout my program. His indomitable support throughout my entire PhD program is highly appreciated.

I am very grateful to our industrial partners Mr. Ian Donaldson, Mr. Richard Hexemer and Mr. Alan Taylor all of GKN Sinter Metals whose inputs were valuable to this research. I wish to express my gratitude to Dr. Bruce Williams of CanMET Materials who aided our ability to use their forging infrastructure and TEM. Also, my sincere appreciation to Dr. Caley who facilitated the completion of additional TEM studies at the University of Manitoba.

My appreciation goes to my friends and colleagues who have contributed in diverse ways to my project. I will like to express my gratitude to our research engineer, Randy Cooke as well as Dean Grijm, Angus MacPherson, Peter Jones and Mark Macdonald for their technical help in the laboratory throughout my program.

Many thanks to my loving and adorable wife, Abigail Dufie Addo who has supported me in a very special way throughout my years as a student.

Finally, I will like to thank The Almighty Faithful Jehovah Jireh God for granting me wisdom, knowledge, good health in body and mind to undertake this program.

CHAPTER 1 INTRODUCTION

Powder metallurgy (PM) is a net-shape metal fabrication technology used to produce components with close dimensional tolerances. This technology has become very attractive because of the cost-effectiveness in high volume production of net or near net shape products. This advantage is largely underpinned by the fact that secondary operations such as machining, which are energy-intensive and can increase the cost of manufacturing parts significantly, are greatly reduced or even eliminated in PM products. PM also offers advantages in producing parts that are homogeneous in properties and composition.

Modern day PM parts find applications in a variety of industries but remain dominated by those in the automotive sector where ferrous products have historically represented ~80% of the total market sales [1]. However, as the automobile industry has gradually become increasingly concerned with greenhouse gas reductions, vehicle manufacturers are, in turn, becoming more interested in lightweight PM materials that offer a means to reduce net vehicular weight. Fortunately, aluminum PM technology has proven to be a cost-effective option due to the high strength to weight ratio of aluminum alloys. Indeed, it has been demonstrated that PM parts when produced to achieve full densification could exhibit strengths that surpass those of their wrought counterparts [2].

The conventional process for producing aluminum PM parts employs the proverbial "press and sinter" approach. Here, the starting powder mixture is die compacted into the required shape and then sintered in a controlled nitrogen atmosphere with each procedure

carried out in separate pieces of equipment. Relative to ferrous systems, the sintering stage for aluminum is somewhat more complex, as the inherent oxide found on the particles cannot be reduced by gases such as H_2 and CO. Hence, practitioners must include magnesium within all "press and sinter" alloys as this will react to form MgO and/or $MgAl_2O_4$. These reactions perforate the Al_2O_3 shell and thereby allow liquid phase sintering to transpire. However, a largely continuous network of oxides is still retained in the sintered product which is known to be detrimental to tensile ductility and fatigue properties.

An emerging technology known as spark plasma sintering (SPS) combines compaction and sintering into a single step event and avoids the requirement for magnesium additions. SPS consolidates particles by the concurrent application of a pulsed DC current and a uniaxial force. Orru et al theorized that, particle bonding during SPS is enhanced due to the plasma cleaning of particles and spark impact pressure. As a result, surface conditions are improved leading to the elimination of contaminants [3]. The processing atmosphere offered by SPS is usually a vacuum. While this helps to minimize oxidation, it does not overcome the fact that all powder particles are inevitably oxidized prior to SPS. For instance, a microstructural investigation by Phung et al has revealed that crystalline aluminum particles are encased in an amorphous oxide shell that is ~2.2nm thick [4]. Although this tenacious layer impedes conventional sintering, it is certainly less impactful in SPS. Here, more and more studies demonstrate that full densification is readily achieved as are excellent tensile properties; including that of ductility. However,

these same studies also attest to the fact that a residual oxide network prevails in an SPS aluminum product.

It would be logical to assume that the aforementioned network prevents aluminum-based SPS products from realizing their full mechanical property potential and that a disruption of it would have the capacity to manifest gains in these attributes. Accordingly, it is envisaged that manufacturing processes which could be leveraged to invoke shear deformation in SPS aluminum materials may be advantageous. One rather obvious option is hot forging as it is known to impart significant benefits to conventionally sintered aluminum alloys [5][6][7]. Another is hot asymmetric rolling (ASR). ASR is a less common technology yet is of considerable interest since it is known to induce exceptionally high levels of shear deformation gains that improve the mechanical properties of conventional wrought materials [8][9][10]. Therefore, the objective of this research was to investigate the effects of ASR and upset forging on sintered aluminum preforms initially consolidated through SPS. Such studies were applied to two aluminum alloy systems. One was a prealloyed powder prepared through the gas atomization of the aluminum alloy 2219. The second was produced in the same manner but had a nominal chemistry of Al-0.3Sc-0.2Zr. In order to accomplish this objective, samples were processed through an array of SPS+forge and SPS+ASR sequences and characterized in detail.

The over-arching objective was divided into the following sub-tasks:

1. Determine the optimal processing parameters for ASR of PM products. This study was conducted by using wrought AA6061 as a precursory material. The goal here was to study how the primary features of ASR (i.e. roller velocity, velocity ratio, rolling direction, number of rolling passes, starting thickness of the specimen) influenced the microstructure and mechanical properties of the finished product.

2. Utilize the best ASR parameters developed for AA6061 to process SPS preforms. The PM alloy of interest was a ternary Al-Sc-Zr composition. The target here was to assess the impact of ASR on the mechanical properties and microstructure of this material.

3. Investigate hot upset forging as an alternate means to process SPS samples of the Al-Sc-Zr and PA2219 PM alloys. In doing so, assess the impact of forging on the mechanical properties and microstructures of these materials and then compare the results to SPS+ASR counterparts.

4. Characterize the evolution of the tenacious aluminum oxide phase present in one of the PM alloys (PA2219) processed via hot upset forging.

CHAPTER 2 : BACKGROUND

2.1 INTRODUCTION

Aluminum ranks as the third most abundant element found in the earth's crust. By far, it is also the most widely used non-ferrous metal. It finds applications in the automotive industry mainly due to its favourable strength to weight ratio. Compared to steel, aluminum is ~2.5 times lighter and can be alloyed to attain strengths comparable to certain grades of plain carbon steel. The main methods utilized to increase the strength of aluminum include [11]:

- Dispersion of alloying elements in solid solution and cold working the alloy (work hardening alloys)
- Dissolution of alloying elements into solid solution and then aging to produce precipitates (precipitation-hardening alloys).

The solid solubility of select elements in aluminum is given in Table 2-1. Interestingly, only nine of these meet the requirements typically sought for precipitation hardening - a maximum solid solubility greater than 1wt%, substantially lower solubilities at lower temperatures, and the ability to form an aluminide phase. Among this sub-group, silver (Ag), gallium (Ga), and germanium (Ge) are expensive whereas lithium (Li) is difficult to process and is often limited to use in special alloys. The remainders (zinc (Zn), magnesium (Mg), copper (Cu), manganese (Mn) and silicon (Si)) form the basis of the principal alloying elements added to the bulk of commercial aluminum alloys.

In and of themselves, aluminum alloys are principally classified as cast or wrought systems [12]. Table 2-2 shows the alloy designations of wrought aluminum alloys. This coding system contains 4 numerical digits. The first represents the major alloy class and in turn, the principal alloying addition(s) present. The second defines the general level of impurity tolerance ranging from 0 to 6, with these boundaries correlating to the highest and lowest levels of acceptable impurities respectively. The last two digits simply identify the specific chemistry of the alloy.

Beyond identification of the actual alloy itself, it is also imperative that the way it has been processed be identified as well. This is typically referred to as the temper designation. A listing of the different options and their respective meaning is shown in Table 2-3. For example, “F” is used to denote the alloy in the as fabricated condition, “O” equates to annealed, “H” strain hardened, “W” solution heat treated, and “T” heat treated (i.e. solutionized, quenched, and aged). Typically, the temper designation is presented a hyphenated addition shown after the alloy chemistry code, for example 2219-T6. For the purpose of this work, discussions will be limited to the 2xxx series and Al-Sc aluminum alloys.

Table 2-1 Element solubility limits in binary aluminum alloys [11].

Element	Temperature(a) °C	°F	Liquid solubility wt%	at.%	Solid solubility wt%	at.%
Ag	570	1060	72.0	60.9	55.6	23.8
Au	640	1180	5	0.7	0.36	0.049
B	660	1220	0.022	0.054	<0.001	<0.002
Be	645	1190	0.87	2.56	0.063	0.188
Bi	660(b)	1220(b)	3.4	0.45	<0.1	<0.01
Ca	620	1150	7.6	5.25	<0.1	<0.05
Cd	650(b)	1200(b)	6.7	1.69	0.47	0.11
Co	660	1220	1.0	0.46	<0.02	<0.01
Cr	660(c)	1220(c)	0.41	0.21	0.77	0.40
Cu	550	1020	33.15	17.39	5.67	2.48
Fe	655	1210	1.87	0.91	0.052	0.025
Ga	30	80	98.9	97.2	20.0	8.82
Gd	640	1180	11.5	2.18	<0.1	<0.01
Ge	425	800	53.0	29.5	6.0	2.30
Hf	660(c)	1220(c)	0.49	0.074	1.22	0.186
In	640	1180	17.5	4.65	0.17	0.04
Li	600	1110	9.9	30.0	4.0	13.9
Mg	450	840	35.0	37.34	14.9	16.26
Mn	660	1220	1.95	0.97	1.82	0.90
Mo	660(c)	1220(c)	0.1	0.03	0.25	0.056
Na	660(b)	1220(b)	0.18	0.21	<0.003	<0.003
Nb	660(c)	1220(c)	0.01	0.003	0.22	0.064
Ni	640	1180	6.12	2.91	0.05	0.023
Pb	660	1220	1.52	0.20	0.15	0.02
Pd	615	1140	24.2	7.5	<0.1	<0.02
Rh	660	1220	1.09	0.29	<0.1	<0.02
Ru	660	1220	0.69	0.185	<0.1	<0.02
Sb	660	1220	1.1	0.25	<0.1	<0.02
Sc	660	1220	0.52	0.31	0.38	0.23
Si	580	1080	12.6	12.16	1.65	1.59
Sn	230	450	99.5	97.83	<0.01	<0.002
Sr	655	1210	...	...	...	...
Th	635	1180	25.0	3.73	<0.1	<0.01
Ti	665(c)	1230(c)	0.15	0.084	1.00	0.57
Tm	645	1190	10.0	1.74	<0.1	<0.01
U	640	1180	13.0	1.67	<0.1	<0.01
V	665(c)	1230(c)	0.25	0.133	0.6	0.32
Y	645	1190	7.7	2.47	<0.1	<0.03
Zn	380	720	95.0	88.7	82.8	66.4
Zr	660(c)	1220(c)	0.11	0.033	0.28	0.085

(a) Eutectic reactions unless designated otherwise. (b) Monotectic reaction. (c) Peritectic reaction.

Table 2-2 Wrought aluminum alloy groups.

Aluminum, 99.00 percent minimum and greater	1xxx
Aluminum alloys grouped by major alloying elements	
Copper	2xxx
Manganese	3xxx
Silicon	4xxx
Magnesium	5xxx
Magnesium and Silicon	6xxx
Zinc	7xxx
Other element	8xxx
Unused series	9xxx

Table 2-3 Temper designations used for aluminum alloys [12].

Temper Designation	**Definition**
H1	Strain hardened only.
H2	Strain hardened and partially annealed.
H3	Strain hardened and stabilized.
T1	Cooled from the fabrication temperature and naturally aged.
T2	Cooled from the fabrication temperature, cold worked, and naturally aged.
T3	Solution treated, cold worked and naturally aged.
T4	Solution treated and naturally aged.
T5	Cooled from the fabrication temperature and artificially aged.
T6	Solution treated and artificially aged.
T7	Solution treated and stabilized by overaging.
T8	Solution treated, cold worked and artificially aged.
T9	Solution treated, artificially aged and cold worked.
T10	Cooled from the fabrication temperature, cold worked, and artificially aged.

2.2 2XXX SERIES ALUMINUM

2xxx series of aluminum alloys contain copper as the principal alloying element. Generally, members of this category exhibit relatively high strengths at ambient, and in some cases, elevated temperatures, in combination with moderate resistance to stress corrosion cracking, and weldability. Over the years, numerous modifications and developments pertinent to 2xxx alloys have transpired. The series now includes 35 chemically discrete alloys. Examples of some of the more popular systems are listed in Table 2-4. Normally, all members of this series are alloyed with appreciable amounts of Cu or Cu and Mg in combination. Copper produces considerable solid-solution strengthening and with proper heat treatment provides greatly increased strength by precipitate formation. Copper has a maximum solid solubility of about 5.65% at the eutectic temperature (548°C) as shown in Figure 2-2. The solubility of copper in aluminum decreases rapidly with decreasing temperature from 5.65% to less than 0.1% at room temperature. In order to attain the maximum effect of precipitation strengthening, aluminum-copper alloys are solution heat treated in the single phase α-solid-solution phase field, quenched rapidly to room temperature, and artificially aged to produce $CuAl_2$ precipitates (Figure 2-1). During the solution heat treatment stage, the copper and aluminum atoms diffuse randomly to produce a uniform solid solution. After solutionizing, the alloy is quenched to produce a super saturated solid solution of copper in aluminum at room temperature. When this happens, the driving force for the precipitation of metastable phases is dictated by the high-energy state of the unstable supersaturated solid solution [12].

Table 2-4 Compositions of some 2xxx series aluminum alloys [12].

Alloy Designation	Composition (Wt%)						
	Cu	**Mg**	**Mn**	**Si**	**Ni**	**Other**	**Al**
2011	5.5	-	-	-	-	0.4 Bi, 0.4 Pb	Balanced
2025	4.5	-	0.8			0.8 Si	Balanced
2219	6.3	-	0.3	-	-	0.06 Ti, 0.10 V, 0.18 Zr	Balanced
2014	4.4	0.5	0.8	0.8	-	-	Balanced
2017	4	0.6	0.7	0.8	-	-	Balanced
2018	4	0.7	-	-	2	-	Balanced
2218	4	1.5	-	-	2	-	Balanced
2024	4.4	1.5	0.6	-	-	-	Balanced
2618	2.3	1.6	-	-	-	0.18 Si, 1.0 Ni, 1.1 Fe, 0.07 Ti	Balanced

In some instances, alloys contain a concentration of copper that is at or exceeds the solid solubility maximum. For example, in 1926, aluminum alloy 2025 containing 5.5wt% copper was first discovered in the United States. This alloy was then replaced by a system with a higher content of 6.3 wt% in 1954, now known as alloy 2219 [13]. Here, the microstructure cannot evolve into a single-phase solid solution and thereby consists of α-aluminum and undissolved $CuAl_2$ at all temperatures below the solidus.

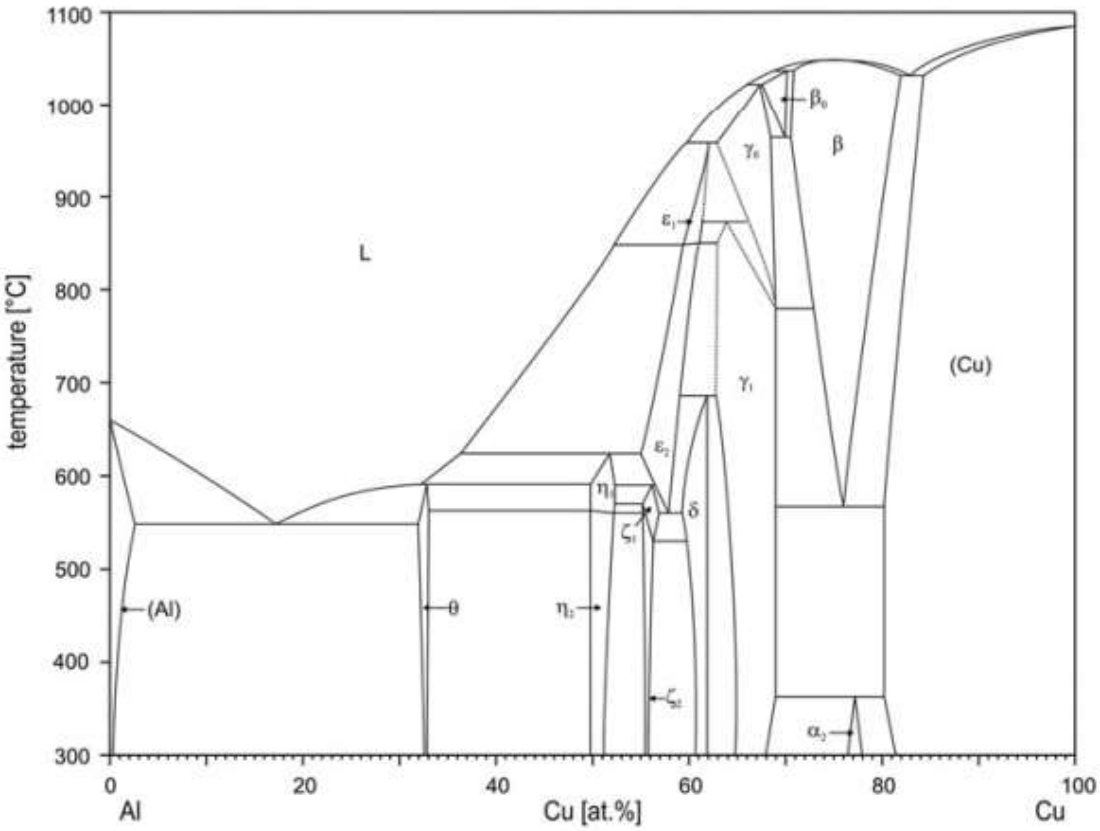

Figure 2-1 Phase diagram of the Al-Cu binary system [14].

Typically, decomposition of the super saturated solid solution is then executed in a somewhat controlled manner by isothermally holding the freshly quenched alloy at a moderate temperature to invoke age hardening. This temperature can be ambient in the case of natural age hardening, or one within the range of 130°C to 190°C for what is termed artificial age hardening. When naturally aging, the progressive strength increase with ageing time has been attributed to an increase in the number of GP zones in some systems and an increased size of the GP zones in others [12]. The presence of impurities in small amounts can interact with vacancies, stifle zone formation and consequently reduce the extent of natural age hardening that transpires. For example, cadmium (Cd) and tin (Sn) present in concentrations of only 0.1% in aluminum-copper base alloys may

lead to the suppression of ageing at room temperature [11]. Cadmium (Cd) lowers the free energy of aluminum alloys by tying vacancies to their local positions. Therefore, aluminum alloys containing Cd will not age at room temperature. The full effect of Cd in Al can be minimized in the presence of Mg since Cd reacts with Mg to form precipitates [11].

Over the years, extensive research has been done in order to understand the crystallographic structures that form progressively during the ageing heat treatment of Al-Cu alloys. The ageing sequence is generally accepted to follow:

Supersaturated $\alpha \longrightarrow$ GP1 Zones $\longrightarrow$ GP2 Zones $\longrightarrow \theta' \longrightarrow \theta$ ($CuAl_2$) [12].

GP1 zones are created by copper atoms segregating within the supersaturated solid solution. These consist of two-dimensional copper rich regions of a disk like shape oriented parallel to the {100} planes of the matrix. Moreover, the cubic lattice parameter of the zone is less than that of the matrix and is strained tetragonally. This is because a copper atom has a diameter that is some 11 percent less than an aluminum atom. The diameter of the zone is estimated to be 8 to 10 nm and does not change with ageing at room temperature. The zones are known to impede dislocation movement which results in an increase in hardness and a decrease in ductility.

At temperatures above 100°C, GP1 zones disappear and are replaced by GP2 zones which also have a tetragonal structure and are coherent with {100} matrix planes. Their size ranges from 10 to 100 nm in diameter [12]. Increasing the ageing time may lead to the transformation or replacement of these zones by a crystal structure referred to as transition precipitates. Essentially, the transition precipitates possess specific crystallographic orientation relationships with the solid solution, such that the two phases remain coherent on specific planes by adaptation of the matrix through localized elastic strain. There is continual increase in strength as the size of the precipitates increases provided the dislocations continue to cut through the precipitate particles. As the precipitation reaction progresses, the precipitates grow and are accompanied by an increase in the coherency strains until the strength of the interfacial bond collapses and coherency disappears. When this occurs, strengthening effects are now a function of the stress required to cause a dislocation to loop around the precipitate instead of shearing through it. With continued ageing, the θ' phase is formed within the alloy. Its presence is generally felt to be characteristic with the onset of over ageing and it is usually incoherent with the matrix. θ' nucleates heterogeneously, particularly on dislocations [12]. Deformation prior to ageing can accelerate the formation of θ' by producing dislocations that can serve as preferred nucleation sites. Its size is dependent on the temperature and time of ageing, and commonly ranges between 10 and 60 nm in diameter. Eventually, strength decreases in a more definitive manner with the emergence/growth of the equilibrium phase θ and the concomitant increase in the inter-particle spacing. This phase is fully incoherent with the matrix and forms at the expense of the θ' phase in a highly overaged condition.

The 2xxx series of aluminum alloys typically find applications in the aerospace and automotive industries. Some applications in the latter include bolted and riveted construction. Notably, AA2219 lends itself exceptionally well to welding by gas tungsten are welding or gas metal arc welding. Hence, this specific alloy is useful in applications where this method of joining is desired [15]. Table 2-5 shows the typical applications and mechanical properties of select member of the 2xxx series.

Table 2-5 Typical applications and mechanical properties of wrought aluminum alloys.

Alloy	Temper	Yield Strength (MPa)	Tensile Strength (MPa)	Elongation (%)	Applications
2014	T6	414	483	13	Aircraft structures and truck frames [12].
2017	T4	276	427	22	Fasteners and screw-machine stock [12].
2024	T86	489	516	6	Aircraft structures, truck wheels and screw machine stock [12].
2219	T87	393	476	10	Propellant tanks and storage tanks for liquid oxygen and nitrogen [16] [17].

2.3 ALUMINUM SCANDIUM ALLOYS

As an alloying addition, scandium (Sc) became remarkably important in the aluminum industry in 1971 after the publication of a patent by L. A. Willey [18]. His work demonstrated that minor additions of Sc could improve the strength of aluminum and its alloys. For example, it was reported that adding 0.3wt% Sc to Al-Mg 1wt% and Al-Mg

5.3wt% alloys increased their yield strengths from 43MPa to 288MPa and from 147MPa to 366MPa respectively [18]. The same publication reported significant improvements in strength upon the addition of Sc to 1xxx and 3xxx series aluminum alloys.

Unfortunately, as Sc is prohibitively expensive, its scope of commercial applications has been largely restricted to the aerospace and sports industries to date. For example, Sc-containing 7xxx aluminum alloys have been used to produce bats for softball and baseball by Arhurst Technology and Kaiser Aluminum. Alcoa later developed a competitive brand of sport bats that also utilized a scandium containing alloy [19]. These developments led to the introduction of high rated bats into the sports market. In producing these, Sc was added to purposefully enhance the yield strength of the alloy which in effect gave a stronger "spring effect" to the bat upon impact with the ball. Other products which have been manufactured with Sc containing aluminum alloys include frames of handguns, tent poles and tubing for bicycle frames [19]. The strength improvement offered by the addition of Sc is partly attributable to the formation uniformly distributed Al_3Sc precipitates. This phase possesses an $L1_2$ structure and is coherent with the Al matrix to a size of ~30nm [20].

The Al-Sc phase diagram was first proposed in 1964 [21]. However, there were some differences noted in later studies [22][23]. One was that Al had a very high solid solubility in solid Sc and a eutectoid reaction (β-Sc = $AlSc_2$ + α-Sc) occurred at 970°C. These differences were accounted for in the binary phase diagram provided in Figure 2-2. It has also been reported that the line depicting the AlSc phase was stoichiometrically

inaccurate. Instead, it has a composition within the range of about 52-54 atomic % Sc [23]. It can be observed from the binary phase diagram, that Al and Sc form several intermetallic phases including AlSc, Al_2Sc, $AlSc_2$ and Al_3Sc; the latter happening to be in equilibrium with Al. There has also been some contention over the exact nature of the solvus curve on the Al-rich end. A version commonly accepted is shown in Figure 2-3. Here, the maximum solubility of Sc is estimated to be 0.38 wt% [24]. It has been shown that the eutectic reaction ($L = Al + Al_3Sc$) occurs at some point between 655°C - 659°C with a Sc concentration of 0.5-0.6 wt% [25][26].

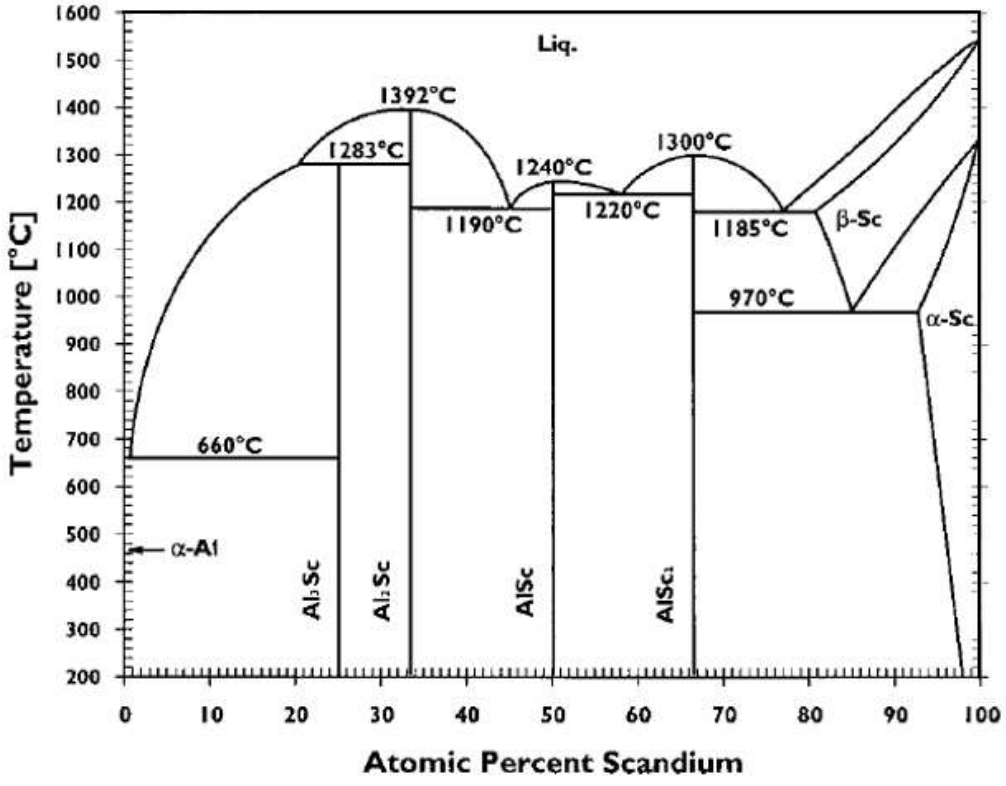

Figure 2-2 Al -Sc phase diagram [23][27].

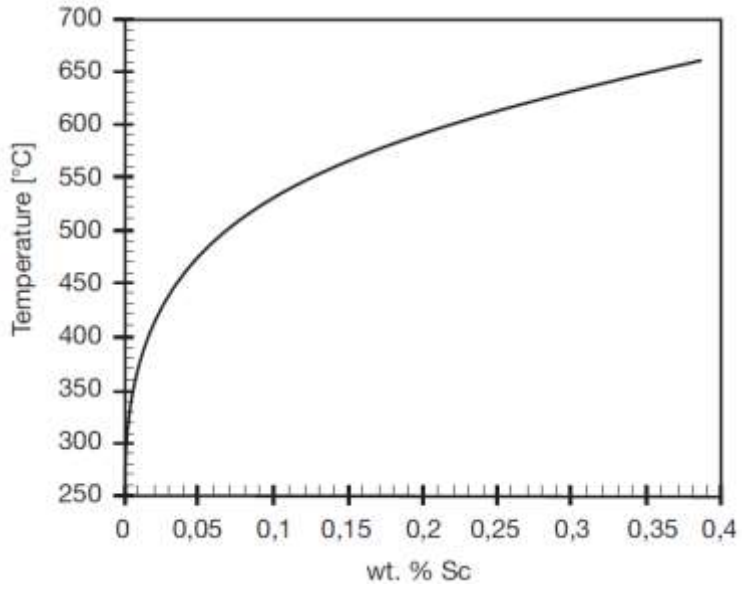

Figure 2-3 The solvus line of Sc in Al [24].

There are various modes by which Al_3Sc can form in Al-Sc alloys. For one, it can occur through the decomposition of supersaturated solid solution into Al and Al_3Sc at a moving grain boundary [19]. Here, grain boundary migration is controlled by the volume free energy released during precipitation. Therefore, as the grain boundary migrates, it leaves behind an array of precipitates. This process of forming Al_3Sc is termed discontinuous precipitation and is driven by the excessive supersaturation of Sc in the Al matrix. A study by Røyset et al revealed that Al_3Sc particles formed in an Al-0.2 wt% Sc alloy through discontinuous precipitation by annealing at 450˚C (Figure 2-4(a)) [24]. Secondly, Al_3Sc precipitates can form through continuous precipitation. Here, the aluminide precipitates form through a nominally homogeneous nucleation and subsequent growth/coarsening of the Al_3Sc phase within α-Al grains (Figure 2-4(b)) [28][29]. This process is associated with a concomitant reduction of Sc within the solid solution. The morphology of the precipitate formed is dictated by aging temperature,

aging time, and Sc concentration. It is notable that heterogenous nucleation can also transpire whereby Al_3Sc precipitates form on dislocations and grain boundaries.

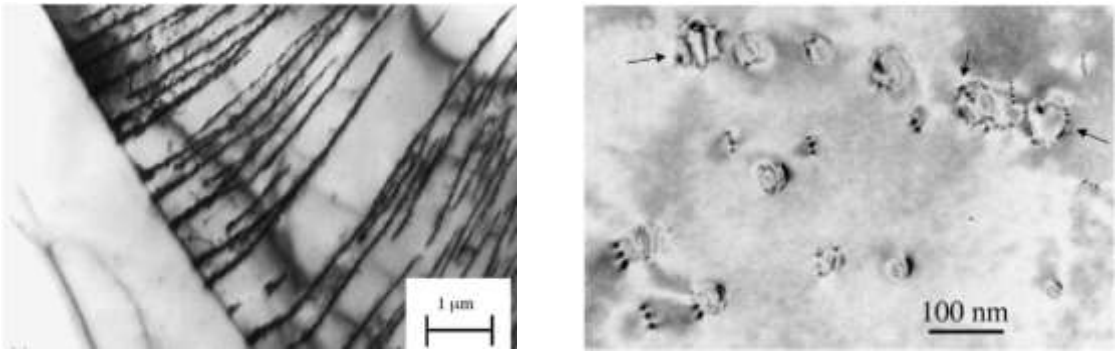

(a) (b)

Figure 2-4 Bright-field TEM images showing Al_3Sc precipitates formed through (a) discontinuous precipitation in Al-0.2wt%Sc annealed at 450°C for 10 minutes [24] and (b) continuous precipitation in a Al-0.3wt%Sc aged at 400°C for 120 hours [28].

Al_3Sc precipitates are noted for their sustained strength and sluggish growth at temperatures upwards of 300°C. Beyond this threshold, the precipitates tend to coarsen rapidly and lose their potency to impart substantive gains in strength. Other elements can be added to Al-Sc alloys to help mitigate this effect. For example, small additions of Zirconium (Zr) improve elevated temperature strength by forming $Al_3(Sc,Zr)$ precipitates [30][31][32]. Figure 2-5 shows such precipitates in an extruded Al-Sc-Zr alloy as observed using transmission electron microscopy (TEM). The mechanism by which Zr helps to improve the thermal stability of the alloy can be explained through the phenomena of coherency loss and dislocation-precipitate interaction. A key factor is that Zr has a much lower diffusivity in Al than Sc which leads to the formation of a core-shell precipitate structure. In this sense, the rapidly diffusing Sc initially forms small Al_3Sc precipitates. With continued ageing time, the slowly migrating Zr atoms diffuse into the

Al_3Sc structure to form a shell of Al_3Zr around it. It has been shown that the coarsening rate of this core-shell precipitate ($Al_3(Sc,Zr)$) is much slower than that of its Al_3Sc precursor [33]. Essentially, the Zr rich shell serves as a diffusion barrier that impedes the growth kinetics of the Sc rich core.

Other elements added to Al-Sc alloys do not necessarily form a Sc-rich precipitate as is the case of Zr. For example, elements including Cu, Li, and Zn do not affect the precipitation kinetics of Al_3Sc. Interestingly, it has been found that Zn promotes the discontinuous precipitation of Al_3Sc while Cu suppresses it. Zakhrov has done extensive work on the precipitation kinetics of Al_3Sc in the presence of ternary alloying additions [39]. His research revealed that Mg and Zn were not influential on the precipitation of Al_3Sc. It was contended that this was observed as both elements exhibit appreciable solubilities in Al [34]. However, others have reported different results in the case of Mg. For example, it has been shown that this element actually reduces the age hardening effect of Al-Sc alloys since some amount of Sc dissolves in the Al_3Mg_2 phase[35]. On the contrary, it has also been reported that more acute gains in hardness were realized in an Al-Mg-Sc alloy than in an exclusive Al-Sc binary counterpart [35]. Such ambiguities imply that precipitation in the Al-Sc system is complex and that more work would likely have to be done in this field to fully understand the effects of alloying elements on the properties of Sc containing Al alloys.

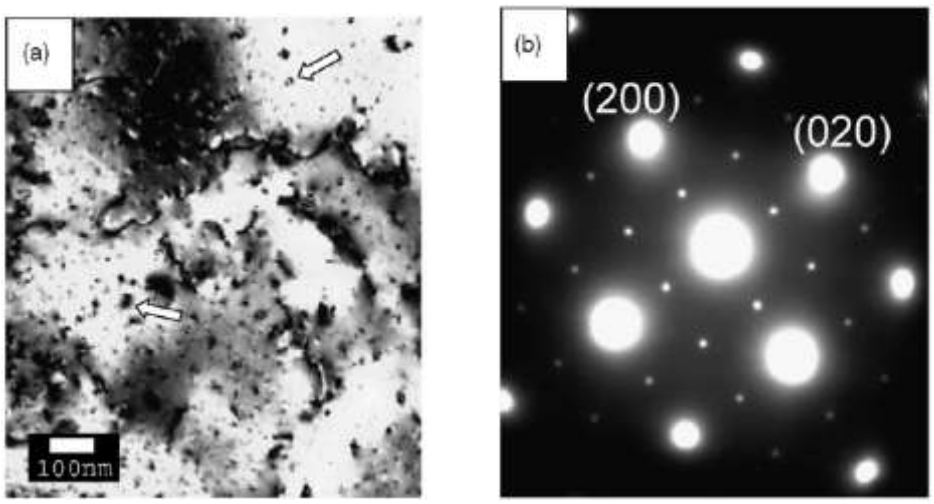

(a) (b)

Figure 2-5 TEM analysis of $Al_3(Sc,Zr)$ precipitates in an extruded Al-Sc-Zr alloy. (a) Bright field image and (b) corresponding diffraction pattern taken with the beam closely parallel to the <001> zone axis [30].

2.4 POWDER FABRICATION

In general terms, PM is concerned with the consolidation of powder particles through elevated temperature with or without external pressure to produce near net shape components with mechanical properties similar to products fabricated via ingot metallurgy. The metallurgical benefits derived from PM can be linked to powder attributes such as compositional flexibility, development of fine microstructures and reduced segregation of alloying elements [2]. The approach used to produce a powder is dependent on the material, costs, and the desired purity. Commercially, metal powders are commonly produced by atomization as well as chemical, mechanical and electrolytic means. Atomization has become the most attractive process as it is relatively inexpensive and the output rate is higher compared to other technologies. For example, water atomization is attractive for producing iron powder mainly due to high production rates that are known to reach 400 kg/minute [36]. Atomization also lends itself to the production of powders with

a controlled chemistry whereby each powder particle is prealloyed to achieve the desired composition. Apart from this, atomization also affords some control over the size, size distribution, morphology, and purity of the powder particles produced [37].

Atomization can be described as a process used to transform bulk liquid metal into a spray of fine droplets that solidify in a gaseous atmosphere [2]. Two of the more popular approaches utilized to produce powders for the PM sector are water and gas atomization. Water atomization finds applications in the fabrication of non-reactive metal powders such as those based on iron and copper. However, it is not recommended for aluminum powder production due to the propensity of molten aluminum to react violently when in contact with water. Hence, other techniques including close-coupled gas atomization [37], ultrasonic capillary wave atomization [38], and rotating disk atomization [39] are used instead.

An exemplary water atomization process utilized in the production of iron powder is shown in Figure 2-6. Here, high pressure water jets impact the melt stream, causing it to disintegrate and rapidly solidify. This is a relatively inexpensive technique given that the atomizing media (water) is cheap and readily available. However, the resultant powder particles are typically irregular in shape and can exhibit a relatively high oxygen content. The average size of metal powders produced via water atomization is dependent on the water pressure utilized. Typically, higher pressures produce higher velocities and yield smaller particle sizes. The empirical relation between the mean particle size (D) and the operating parameters can be represented by [2]:

$$D = -\frac{\beta \ln(P/Po)}{V \sin \alpha} \qquad (1)$$

where β is a material constant, P is the water pressure at the outlet, Po is a reference water pressure, V is the water velocity, and α is the angle between the melt stream and the water jets.

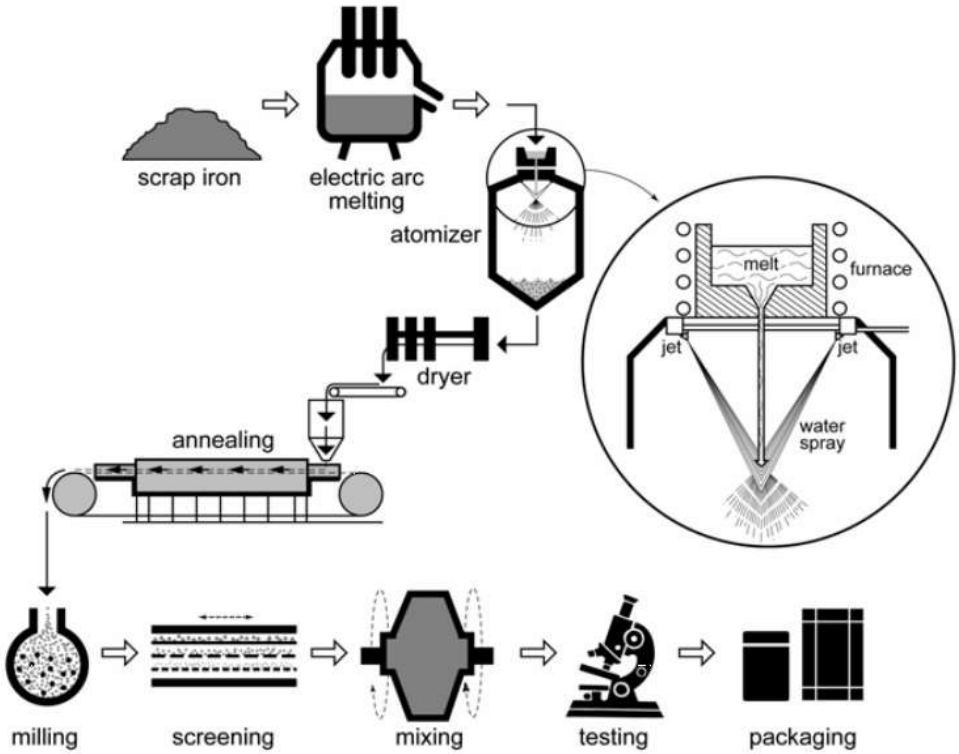

Figure 2-6 Schematic of a typical water atomization process utilized in the production of iron powder [2].

In gas atomization the molten stream is disintegrated with the aid of a high pressure gas, typically, within a controlled atmosphere. Several gases can be used for this purpose including air and inert gases (nitrogen, helium, argon) although the latter are preferred when there is a need to produce powder with a reduced level of oxygen contamination (i.e

titanium). The set up for a gas atomizer is either vertical or horizontal. Materials such as tin (Sn) and lead (Pb) with low melting temperatures are normally atomized using a horizontal approach [2] as shown in Figure 2-7. These systems operate on the basis of suction created by a high velocity gas passing through a nozzle and pulling the melt into a gas expansion chamber. As the droplets move through the collection chamber, they lose heat and solidify.

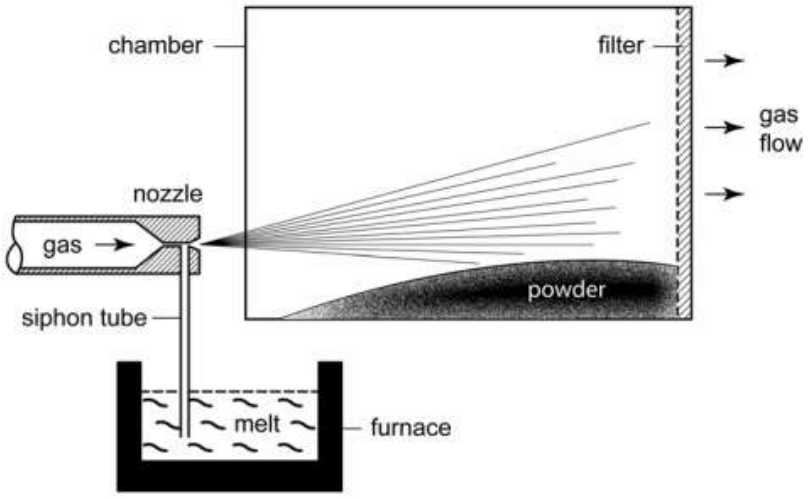

Figure 2-7 Schematic diagram of a horizontal gas atomizer [2].

In a vertical atomizer, the required metal/alloy is typically melted in an induction furnace and then poured through a nozzle before entering the atomization die (Figure 2-8). Here, the atomizing gas rapidly de-pressurizes, and in doing so, physically disintegrates the melt stream. Gas expansion leads to the development of a melt cone that is sheared into sheets. These then evolve through a sequence of morphologies with a progressively lower surface area to volume ratio, concluding with the formation of spherical particles if solidification does not transpire before this stage is reached. A cyclone is usually attached to the vertical

gas atomizer to separate the very fine powders and prevent them from re-entering the atomization zone. This reduces the tendency to form satellites adhered to the larger particles. Satellites act to roughen the powder particle surfaces to an extent that can have adverse effects on key bulk properties such as flow and apparent density.

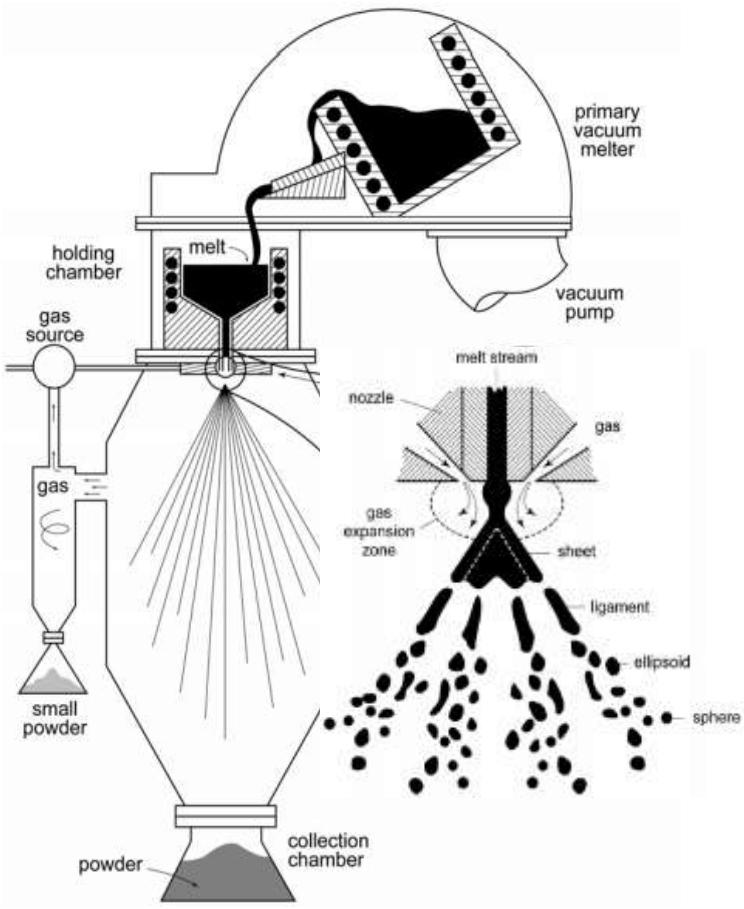

Figure 2-8 Schematic of a vertical gas atomization process [2].

In gas atomization, the average particle size (D_{50}) depends on the mass flow ratio as [2]:

$$D_{50} = Kd\left[1 + \frac{M_m}{M_g}\right]\left(\frac{\eta_m}{W_e \eta_g}\right) \qquad (2)$$

where K is an empirical constant, M_g and M_m are the gas and liquid flowrates, η_g and η_m are the gas and liquid viscosities, d is the diameter of the liquid nozzle, while We is the dimensionless Weber number defined as the measure of the relative importance for the melt inertia in comparison to its surface tension. It is defined as:

$$W_e = \frac{\rho_G V^2 d}{2\gamma_{LV}} \qquad (3)$$

where, ρ_G is the gas density, V is the gas velocity, d is the melt ligament diameter, γ_{LV} is the liquid-vapour surface energy for the melt.

Rapid solidification is inherent to all atomization processes and invokes the formation of non-equilibrium microstructures. A comparison between those of a conventional cast material and that of a rapidly solidified powder is shown in Figure 2-9. As can be seen, the former displays a coarse dendritic structure while the latter exhibits a fine and uniform microstructure indicative of significantly reduced segregation during solidification. The cast material would have experienced relatively slow cooling. Conversely, the refined structure of the powder particle is attributable to a very fast cooling rate. This is largely driven by the facts that a molten droplet exhibits a steep core to surface temperature gradient as well as a small thermal mass. Combined, these factors promote accelerated

heat removal manifested as rapid solidification. Solidification of an atomized molten droplet can also be initiated through a heterogenous nucleation mechanism. Figure 2-10 shows an example of this wherein this process was instigated by contact with a small previously solidified particle. The microstructure of this powder thereby exhibited a radial dendrite structure originating from the nucleation site [2].

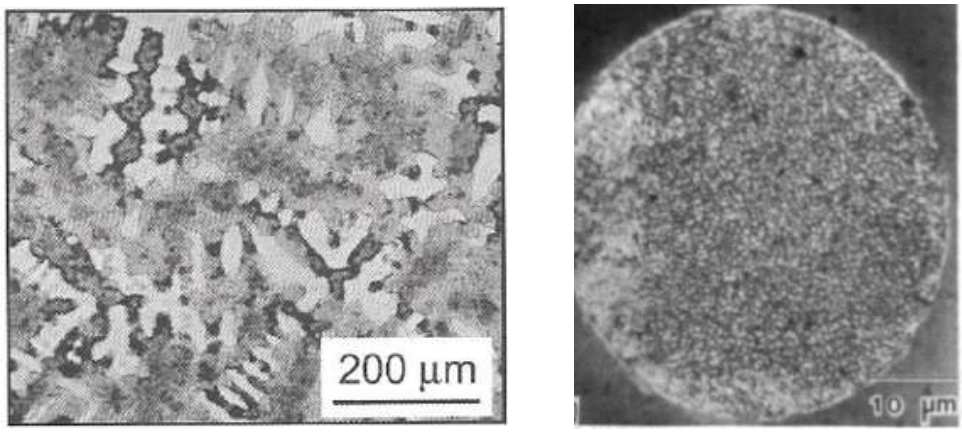

(a) (b)

Figure 2-9 Comparison of the microstructures of (a) a typical conventional casting [2] and (b) a rapidly solidified atomized powder [40]. Note the differences in scale.

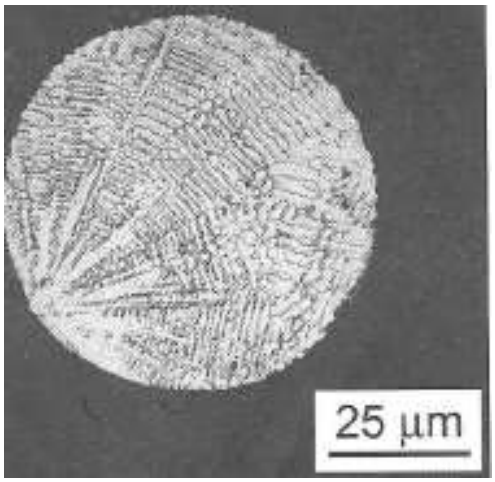

Figure 2-10 Optical micrograph of a gas atomized powder showing a radial dendrite structure originating from a surface nucleation site [2].

As stated earlier, contamination can be an issue for powders produced through atomization. Typically, this comes in the form of non-metallic secondary phases. This can yield inclusions in the powder that are then translated into the finished component produced from it. These are undesirable features as they act as stress concentrators, and in turn, sites for the preferential initiation of fatigue cracks. One source of inclusions emerges when the molten metal/alloy reacts with the crucible and/or the pouring nozzle utilized in the atomizer. A second source is the oxide surface film present on the particles when they passivate after/during atomization. This source is particularly acute for metals such as aluminum. Here, the resultant oxide exhibits a high thermodynamic stability that ensures it cannot be eliminated via gaseous reduction and/or dissolution during sintering.

In one study, the surface film on a commercially pure aluminum powder was found to be a complex structure of alumina (Al_2O_3) and alumina trihydrate ($Al_2O_3 \cdot 3H_2O$) coupled with physiosorbed water on the exterior surface [41]. The alumina component itself has been estimated to be ~3nm thick and can exhibit an amorphous structure (Figure 2-11) [42]. Degassing is commonly employed to remove adsorbates and decompose the $Al_2O_3 \cdot 3H_2O$. It has been shown that outgassing of H_2O and H_2 occur during this process through a variety of reactions [43][44][45]:

$$Al_2O_3 \cdot 3H_2O = Al_2O_3 \cdot H_2O + 2H_2O \quad (4)$$

$$Al_2O_3 \cdot 3H_2O = Al_2O_3 + 3H_2O \quad (5)$$

$$Al_2O_3 \cdot H_2O = \gamma - Al_2O_3 + H_2O \quad (6)$$

$$2Al + 3H_2O(g) = Al_2O_3 + 3H_2 \quad (7)$$

$$2Al + 6H_2O(g) = Al_2O_3 \cdot 3H_2O + 3H_2 \quad (8)$$

$$Mg + H_2O(g) = MgO + H_2 \quad (9)$$

According to studies conducted by Estrada et al, vacuum degassing at room temperature releases partially the physiosorbed water whereas no indication of the release of hydrogen occurs regardless of the evacuation time [45]. When the temperature is raised, the physiosorbed H_2O is outgassed at about 150°C. Hydrated alumina is decomposed at temperatures up to 350°C according to equations (5) and (6) [43]. At temperatures above 200°C, hydrogen is probably evolved due to equations (7) or (8) [43]. The reaction in equation (9) occurs when the particle is alloyed with Mg.

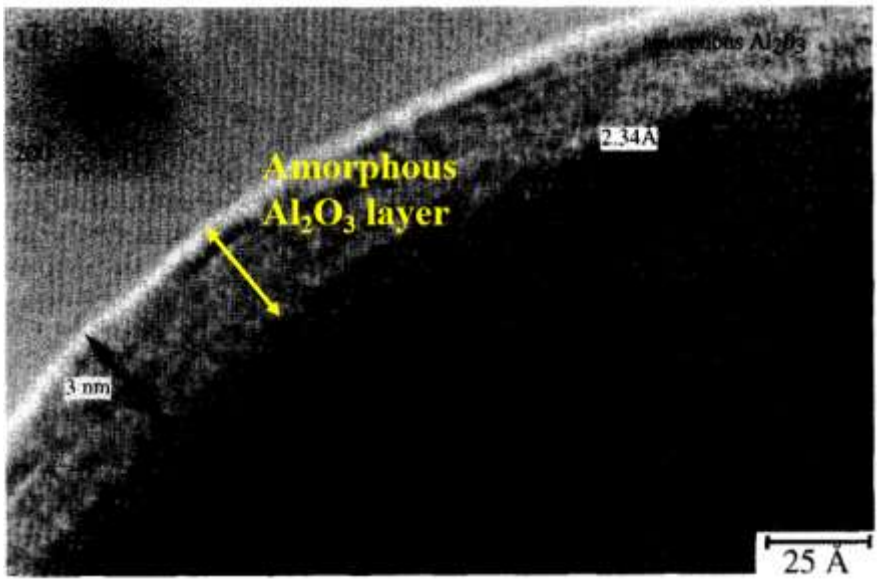

Figure 2-11 High resolution electron microscope (HREM) image showing the amorphous alumina layer on an atomized aluminum particle. Sample oriented with the [011] direction parallel to the electron beam [42].

2.5 SPARK PLASMA SINTERING

Conventional approaches to sintering emphasize liquid phase sintering (LPS) and solid-state sintering which both transpire at relatively high temperatures [2]. Solid state sintering, as the name suggests, occurs below the solidus and exclusively through solid-state mechanisms. In contrast, LPS involves the presence of a liquid phase that facilitates enhanced rates of diffusion and densification, albeit at the expense of an increased propensity for distortion. An alternative, non-conventional, sintering technique that has received considerable attention as of late is spark plasma sintering (SPS). Here, powder is consolidated by the simultaneous application of a pulsed DC current and a uniaxial pressure [46]. This affords unique advantages including the ability to achieve exceptionally high heating rates (i.e. 1000K/min), an abbreviated sintering time, limited microstructural coarsening, and fully dense products.

In operation, pulsed DC low voltage/high current is transmitted from the power source to one of the system rams (Figure 2-12). This then permits the flow of a high electric current through the conductive tooling that contains the powder of interest. Graphite tooling is typically preferred although other materials such as cemented tungsten carbide and silicon carbide have also been utilized. Graphite is desirable as it is relatively inexpensive, easily machined, retains strength at temperatures upwards of 2400°C, and exhibits exceptional thermal and electric conductivities [47]. The DC pulse profile is readily adjustable and creates a high concentration of electric current at the points of contact between adjacent particles. Intense heat is thereby generated at these locations, reportedly leading to localized vaporization and/or cleansing of the particle surfaces. This

forms the basic heating mechanism in SPS for metallic powders known as Joule heating [3][48][49][50]. The entire process is typically carried out in a vacuum atmosphere with the aim of reducing the extent of oxidation that transpires.

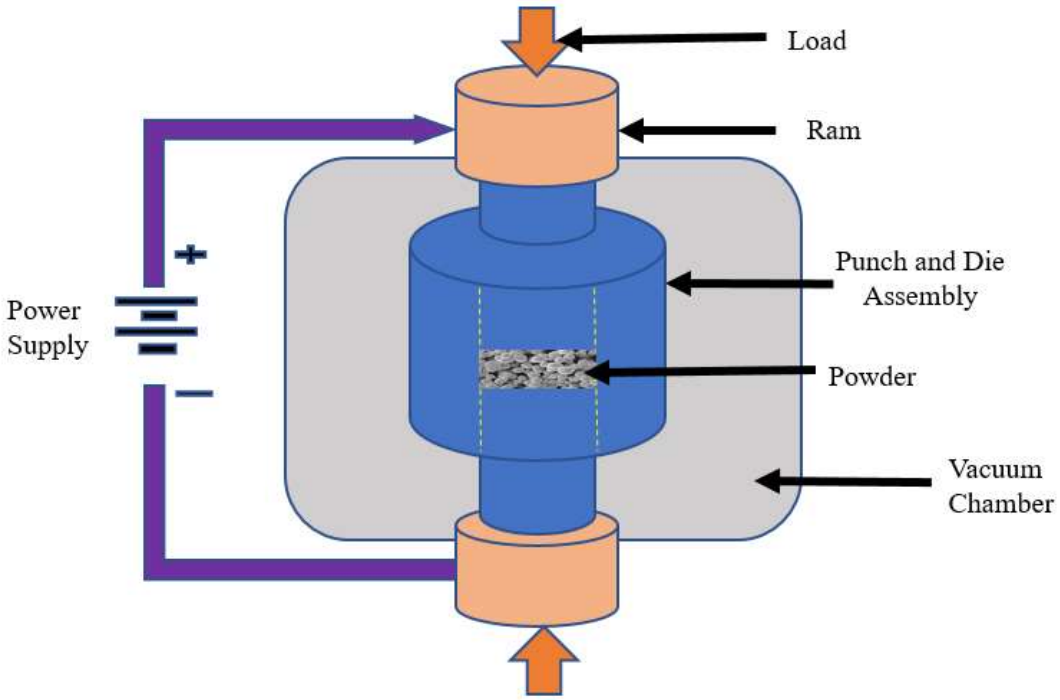

Figure 2-12 Schematic of a SPS system.

It has been reported that the electric current in SPS instills a number of thermal effects [51]. These include high heating rates, high local temperature gradients, and non-uniform temperature distributions on a microscopic and macroscopic level. Collectively, these work to enhance/expedite densification and create thermal stresses that intensify dislocation creep. The values attainable are quite unique and can readily approach figures upwards of 1000K/min [3]. The issue of microstructural coarsening which can occur during conventional heating is reduced during SPS. It has been demonstrated

through modelling that surface diffusion does not occur at low temperatures in SPS unlike in conventional sintering [52]. Surface diffusion essentially promotes neck development between particles and does not contribute to densification [53]. At higher temperatures, the small radius of curvature of pore tips is retained since neck development is retarded. This allows grain boundary diffusion to transpire at temperatures that favor this mechanism thereby increasing the diffusion kinetics and rates. When sintering is conducted in a vacuum, the pore present between particles exist in the form of vacancies. This means a small pore possesses an inherently high concentration of vacancies which then diffuse to grain boundaries or interfaces where they are annihilated when the temperature is increased [54]. Advantageously, these can facilitate full densification of even relatively large powder particles while limiting grain growth and microstructural coarsening due to the reduced level of thermal exposure [51]. Munir et al have affirmed this finding by reporting that, the grain growth of a compact was inversely proportional to the heating rate [53]. SPS can also instill athermal effects. Electromigration and intensified diffusion in ionic conductors, electroplasticity mechanisms, ponderomotive forces, electromagnetic ‘‘pinch’’ effects, dielectric breakdown of oxide films (cleansing effect), and secondary phase nucleation and growth are exemplary phenomena [51], [53].

As noted earlier, an inherent oxide layer exists on atomized aluminum powder particles. The following chemical reactions represent the potential mechanisms of its breakdown due to the addition of Mg.

$$3Mg + 4Al_2O_3 = 3MgAl_2O_4 + 2Al \qquad (10)$$

$$3Mg + Al_2O_3 = 3MgO + 2Al \quad (11)$$

Interestingly, it has been postulated that oxide breakdown is more effective in SPS than conventional sintering [55][56]. This is reportedly underpinned by the concentrated flow of current coupled with the fact that the resistivity of Al_2O_3 is significantly higher than that of metallic Al. Accordingly, resistive heating is invoked such that the interfacial temperature between particles during SPS is significantly higher than that of a corresponding bulk sample measurement [57][58]. Hence, Mg-rich oxide phases such as MgO and $MgAl_2O_4$ are formed at relatively low bulk temperatures. When coupled with enhanced densification via the application of an external pressure, significant gains in the mechanical properties of products derived from aluminum-based powders can transpire. For example, as shown in Figure 2-13, SPS manifests significant improvements in mechanical properties in both pure Al and an Al-Mg alloy compared to conventional sintering [56].

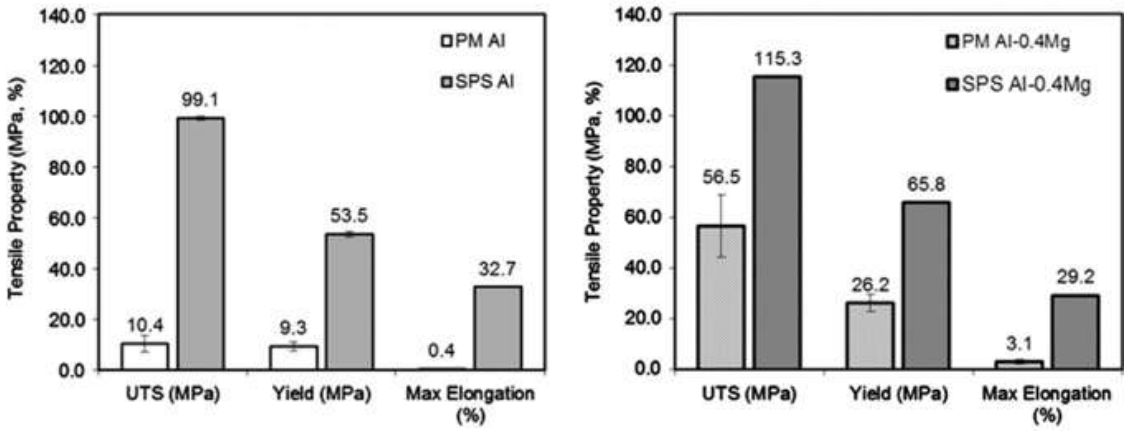

Figure 2-13 Comparison of the tensile properties measured for materials prepared through conventional PM and SPS processing. (a) Al and (b) Al–0.4Mg powders [56].

2.6 ASYMMETRIC ROLLING

Rolling of metallic materials is a common means of producing sheet and plate products. In conventional approaches, the starting billet is passed between two rollers that are rotated in the same direction and at the same speed. In this balanced, "symmetric" approach, the material is thereby subjected to high compressive stresses from the squeezing action of the rollers and to the surface shear stresses present between the rollers and the material to instill plastic deformation.

An alternate, non-conventional approach is asymmetric rolling (ASR). Here, a deliberate imbalance between the rollers is established by [59]:

- Geometric asymmetry: using rollers with different diameters
- Kinematic asymmetry: using rollers with the same diameter but different velocities
- Tribological asymmetry: produced by different frictional coefficients stemming from the use of different roller materials.

The imbalance created through ASR produces an additional shear stress field to the compression strain typically found in conventional rolling. This implies that the workpiece processed through ASR is subjected to a net plastic deformation comprised of plane strain deformation and an additional shear component.

Before a workpiece is inserted in-between two rollers operating in either a conventional or asymmetric manner, the velocity of the rollers initially is higher than the velocity of the workpiece at the inlet side of the roll gap. When the workpiece is in-between the rollers

and about to exit the roll gap, it moves at a faster velocity than the rollers. However, there is a point called the neutral point within the roll gap where the velocity of the rollers equals the velocity of the workpiece; at this point, no slip occurs [60]. In symmetric rolling, the neutral points associated with both rollers reside at the same position within the roll gap as shown in Figure 2-14a. In the case of ASR, the neutral points are positioned at different locations within the roll gap (Figure 2-14b). This is becasue the neutral point associated with the slower roller is shifted towards the entrance whereas the neutral point associated with the faster roller is shifted towards the exit within the roll gap. This positional misalignment of the neutral points thereby produces an additional cross shear zone within the roll gap. This phenomenon was also confirmed by Yu et al, where they too showed that an additional shear zone transpired during ASR with rollers of different velocities (Figure 2-15) [61]. Furthermore, their researh also concluded that the physical size of this shear zone increased with increasing roller velocity ratio [61].

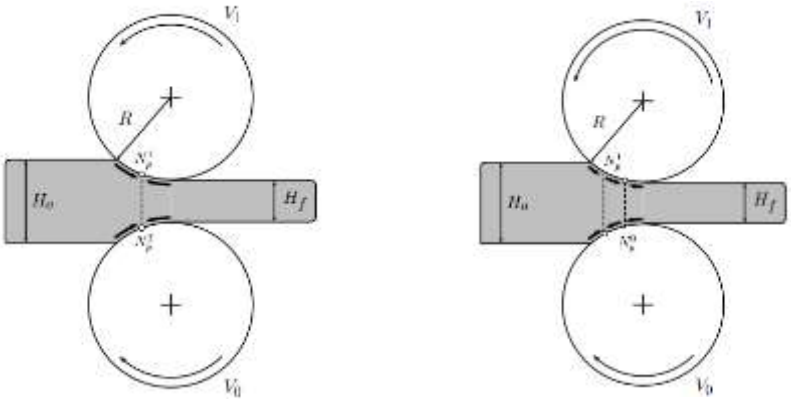

Figure 2-14 A schematic diagram showing (a) symmetric and (b) asymmetric rolling [62].

Genrally, ASR yields products with mechanical properties that are superior to counterpart products rolled in a conventional (symmetric) manner [63][64][65][66]. Such improvements have been attributed mainly to grain refinement and the resultant shear textures. Typically, the applied rolling force during ASR is smaller than the force applied in symmetric rolling [67][67]. This enviably makes ASR technologically feasible for rolling thin sheets in industry. ASR is also beneficial in that it can eliminate some of the defects peculiar to conventional rolling. For instance, Kalutskii et al have shown through experimental investigations that drawbacks such as camber and destruction of the rolled material caused by non-uniform distribution of contact stresses could be eliminated through ASR [68]. Also, numerical simulations have shown that the curvature associated with warping is reduced significantly with increasing velocity ratio [69]. It is interesting to note that the genesis of most problems encountered in conventional rolling procedures are attributable to bending of the rollers. Typically, roller bending produces sheets with non-uniform thickness. To alleviate this problem, rollers are normally cambered to compensate for this. However, if the rollers are not cambered sufficiently, the center region of the rolled material is left in tension whiles the edges are subjected to compression [70]. This usually causes the center of the material to crack, warp, and develop edge wrinkling as shown in Figure 2-16. On the other hand, when the rollers are over cambered, the center of the workpiece is left in compression whiles the edges are subjected to tension. This potentially results in a wavy center, centerline and edge cracking (Figure 2-17(d)) [70].

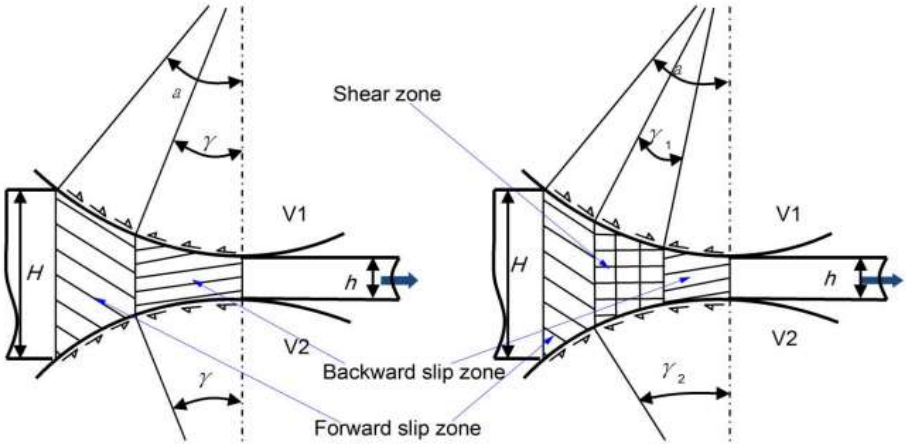

(a) (b)

Figure 2-15 Schematic diagram showing the friction force distribution in (a) symmetric rolling and (b) ASR [71].

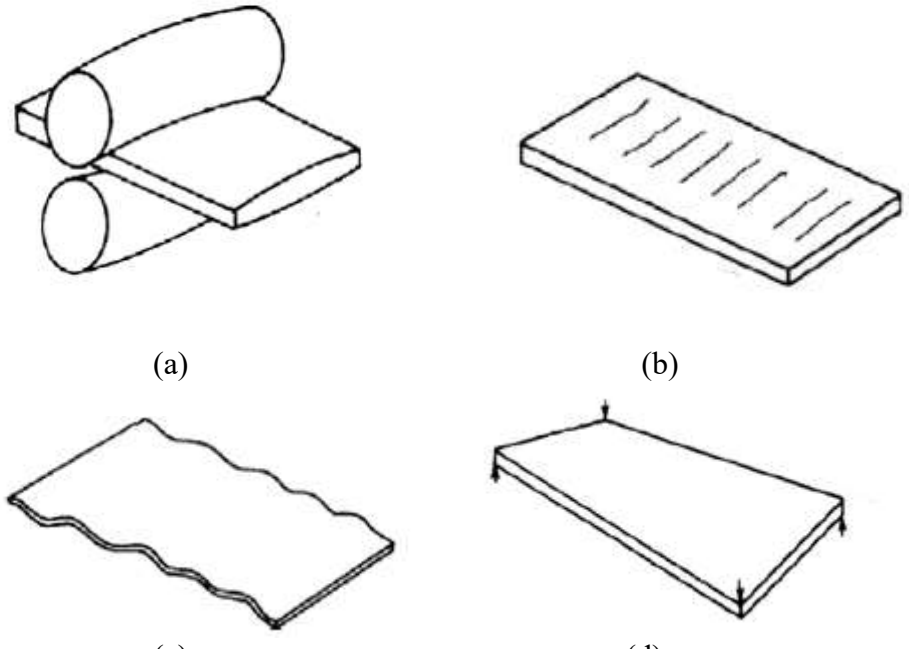

(a) (b)

(c) (d)

Figure 2-16 Schematic illustrations of (a) insufficient camber and the ensuing outcomes of (b) center cracking (c) warping, and (d) edge wrinkling [70].

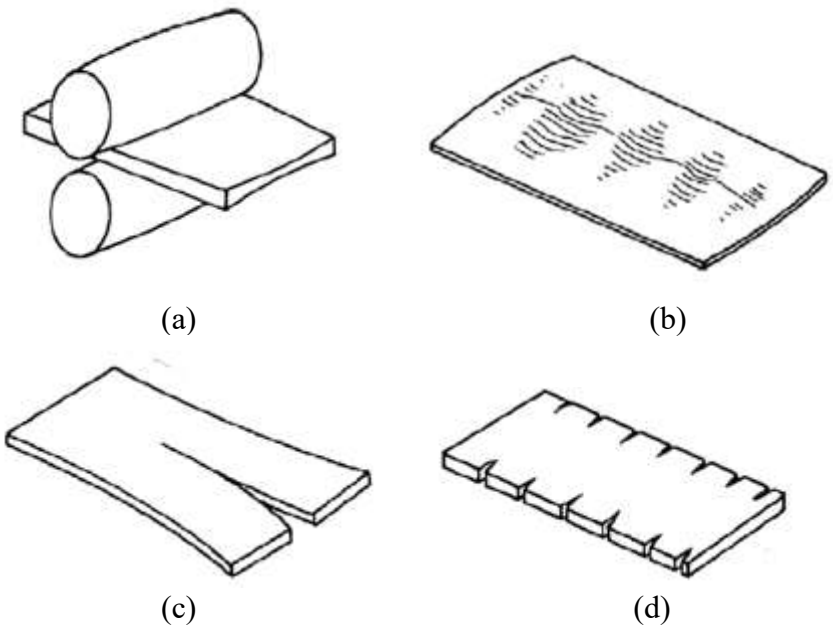

Figure 2-17 Schematic illustrations of (a) over-cambering and the ensuing outcomes of (b) wavy center (c) centerline splitting, and (d) edge cracking [70].

2.7 POWDER FORGING

Another form of metal shaping of considerable interest to this research is powder forging. Like ASR, this process also has the capability to instill shear deformation and produce PM parts with improved physical and mechanical properties. Forging refers to the working of a metal into a useful shape by hammering or pressing [60]. It is regarded as the oldest of the metal working arts. The inception of this art can be traced to the primitive blacksmiths of Biblical times. Types of forging include swaging, punching, piercing, edging, etc. [60]. Powder forging (PF) basically is a uniaxial technique that uses a sintered preform as the starting material. It is typically forged to achieve full densification and reshape it into the prescribed geometry [2]. This is commonly completed as upsetting or hot pressing. In the former, the starting billet is appreciably smaller than the forging die itself which ensures that a significant degree of lateral

material flow occurs. This typically affords maximized mechanical properties at the expense of a reduction in geometric precision. In the latter, the sintered preform is much closer in size/shape to the intended product. This limits the net gains in mechanical properties, but improves the dimensional accuracy of the forged product [72]. Figure 2-18 shows a comparison between these approaches to PF. In both instances the process is typically completed at an elevated temperature. Here, the tooling and/or preform are heated to soften the material and improve its capacity to flow without fracture.

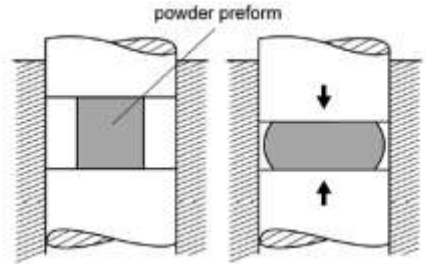

(a)

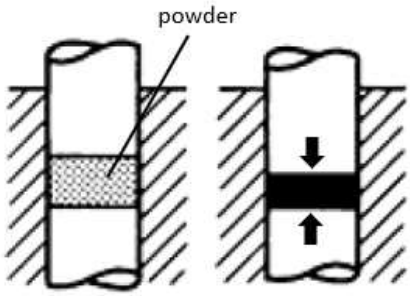

(b)

Figure 2-18 Schematic diagrams showing forging modes for (a) upsetting [2] and (b) hot pressing [72].

PF can be carried out in an open or closed die. In open die forging, there is either no or minimal constraint. Hence, lateral flow is controlled by the applied load, heat transfer effects between the workpiece and the die/platens, total reduction in the workpiece height, and frictional boundary conditions [73]. Open die forgings can produce a wide

range of shapes yet it is important to note that in the absence of lateral constraint, the preform could eventually crack at the outer barreled region where the tensile stresses are large [2]. In closed die forging, shaping of the metal is accomplished within the walls or cavities of two dies that come together to enclose the workpiece on all sides [74]. Here, the impression for the forging is either split between the top and bottom dies or confined to entirely one of the dies. A provision for a flash is sometimes made with the die to allow excess metal to flow from the die and in turn modulate the pressure within safe limits while the die is being filled. It is important to note that in certain instances, a closed die design may exclude a flash. This is commonly termed flashless forging. Figure 2-19 illustrates the differences between open and closed-die forgings.

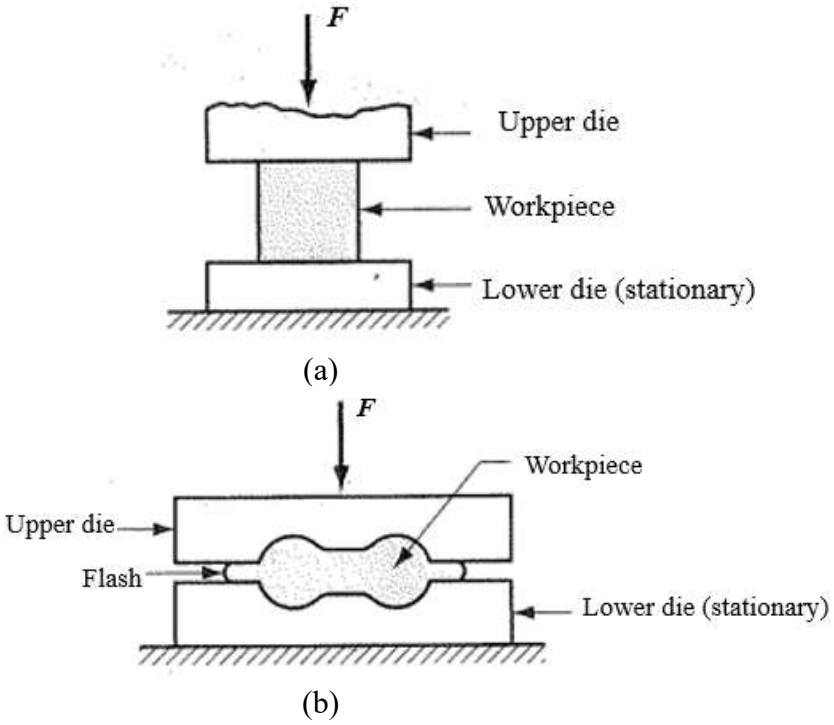

Figure 2-19 Schematic diagrams showing (a) open die and (b) closed die forging [75].

During PF, the mass of the material remains constant but is accompanied by a decrease in volume due to pore collapse. The behavior of a representative material containing a pore

subjected to upsetting and hot pressing is compared in Figure 2-20 [72]. In hot pressing, the pore simply collapses under axial deformation. However, in upsetting, the intensified lateral flow results in significant shear stress. This is a more effective means of pore collapse and includes the additional benefit of a more intense disruption of any residual oxide phase(s) that persevered through sintering [72].

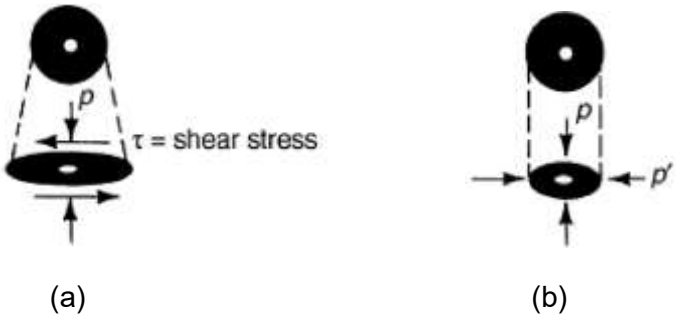

Figure 2-20 General effects of (a) upsetting and (b) hot pressing on residual pores within sintered preforms [72].

A plot depicting the relative forgeability of various aluminum alloys is shown in Figure 2-21 [74]. These data were developed by taking into consideration the tendency of the alloy to crack and the difficulty in achieving specific degrees of severity in deformation. The prevailing trend for all alloys is that forgeability increases with increasing forging temperature. 6061 demonstrates the highest forgeability while those of the other alloys shown are less favourable and are typically viable over narrower temperature ranges. The differences become particularly acute for 2xxx, 5xxx, and 7xxx systems. The explanation for this is that these alloys, as compared to 6061, do not easily lend themselves to deformation since the stresses required to plastically deform them are significantly higher. Another factor that affects the forgeability of aluminum alloys is

their strain rate sensitivity given that flow stress generally increases with increasing strain rate [76][74].

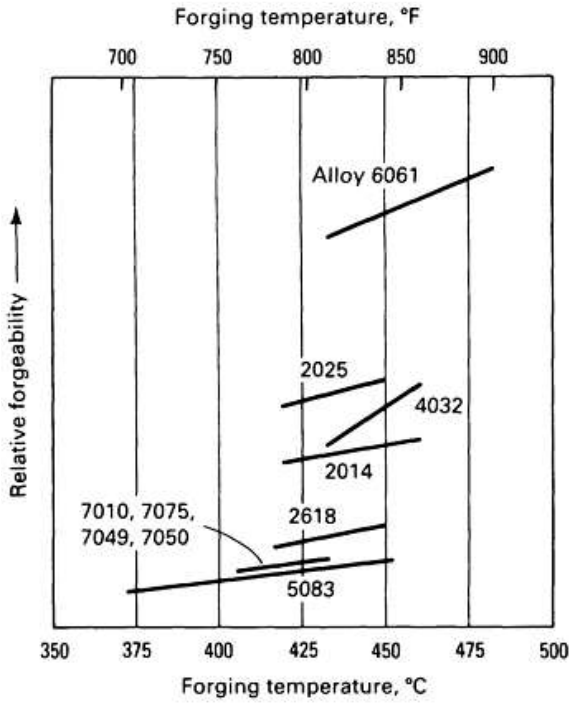

Figure 2-21 Relative forgeability and ideal forging temperature range for various aluminum alloys [74].

Elevated temperatures are typically imperative to forging and ASR as noted earlier. Under such conditions, the metal is subjected to "hot working" – a generic term that refers to deformation of a metal above a homologous temperature of 0.5Tm, with typical hot working temperatures being 70 to 80% of the absolute melting temperature [73]. When metals are deformed under these conditions, dislocations and stacking faults are generated within the metal. Regarding the latter, it is important to note that the stacking fault energy is related to the dislocation structure of a crystal [72]. Aluminum for instance has a high stacking fault energy which implies that it has a narrow stacking fault. This

means that the movement of dislocations by climb and cross slip are favored which is known to limit the extent of work hardening observed. On the contrary, other FCC metals such as brass and austenitic stainless steel, with low stacking fault energies, exhibit greater resistance to dislocation movement and a high rate of work hardening.

The hot working of metals activates slip and *in-situ* (a.k.a. "dynamic) microstructural transitions that can include dynamic recovery [77][78], dynamic recrystallization [77] [79][80][81], and dynamic precipitation [82][83]. Dynamic recovery involves the rearrangement and annihilation of dislocations. Although it transpires *in-situ*, the underlying mechanism remains similar to that involved in static recovery; a process activated through post-deformation heat treatment of a cold worked metal. A schematic representation of a plastically deformed metal undergoing static recovery is shown in Figure 2-22 [84]. Here, the dislocations formed through deformation are initially tangled (Figure 2-22(a)) but eventually begin to form cells (Figure 2-22(b)). As this progresses, many of the dislocations within the cells are annihilated (Figure 2-22(c)). This is followed by the formation of sub-grains that eventually grow but remain characterized by low misorientation angles. The same sequence is replicated during dynamic recovery except that the associated series of events overlap and do not transpire as separate and sequential transitions. However, the extent to which the stages of dynamic recovery transpire depends on the strain, strain rate and temperature.

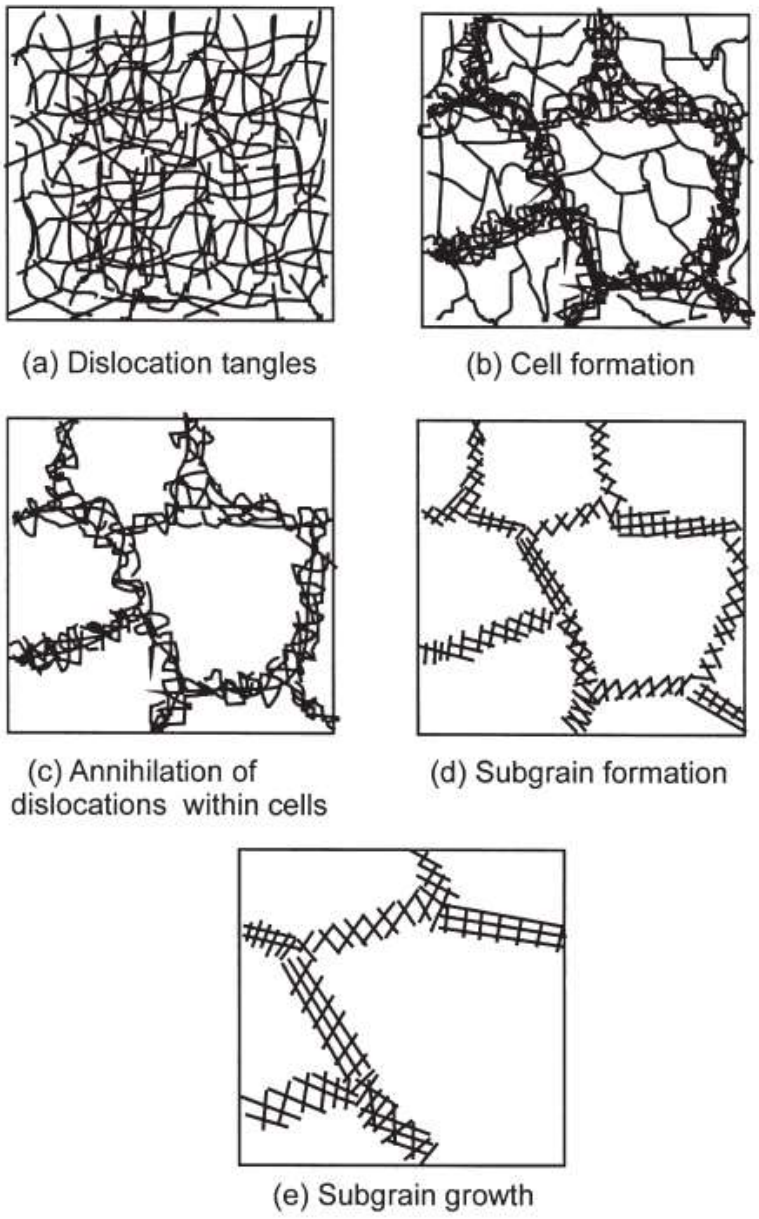

Figure 2-22 Stages involved in the static recovery of a plastically deformed metal [84].

Whereas dynamic recovery concludes with the formation of small sub-grains that have low angle grain boundaries, the microstructure evolves to a greater extent in dynamic recrystallization. Here, grains in the product are now larger and exhibit high angle grain boundaries. The mechanism of dynamic recrystallization can transpire in several modes

including discontinuous, continuous, and geometric. The former is illustrated in Figure 2-23 [84]. Here, new grains begin to nucleate at existing or old grain boundaries as shown in Figure 2-23 (a) and (b) during high temperature deformation. This continues until a thickened band of recrystallized grains is formed (Figure 2-23(c)). Assuming that the difference in the size of the initial and recrystallized grains was very large then a necklace type of grain structure will be formed (Figure 2-23(d)). This continues until the microstructure becomes fully recrystallized depending on the process conditions. Conversely, the process of continuous dynamic recrystallization occurs by the transformation of sub-grains into high angle grain boundaries. During hot deformation, sub-grains are normally produced and begin to move by virtue of dislocation arrays localized within them. However, if their movement is obstructed due to particle or precipitate pinning, sub-grain boundary migration and annihilation become retarded [85]. This eventually results in the accumulation of sub-grain boundaries and their subsequent transformation into high angle grain boundaries.

Geometric dynamic recrystallization is the third variant [86][87]. When a material is subjected to a large reduction in cross section, for example by hot compression or hot rolling, the original grains become flattened as shown schematically in Figure 2-24 [84]. As the hot deformation advances, high angle grain boundaries become closer as shown in Figure 2-24b. With increasing strain, the size of the high angle boundary serrations become comparable with the thickness of the sub-grains. Eventually, there is interpenetration of the scalloped boundaries to produce a microstructure of small equiaxed grains [84] (Figure 2-24(c)).

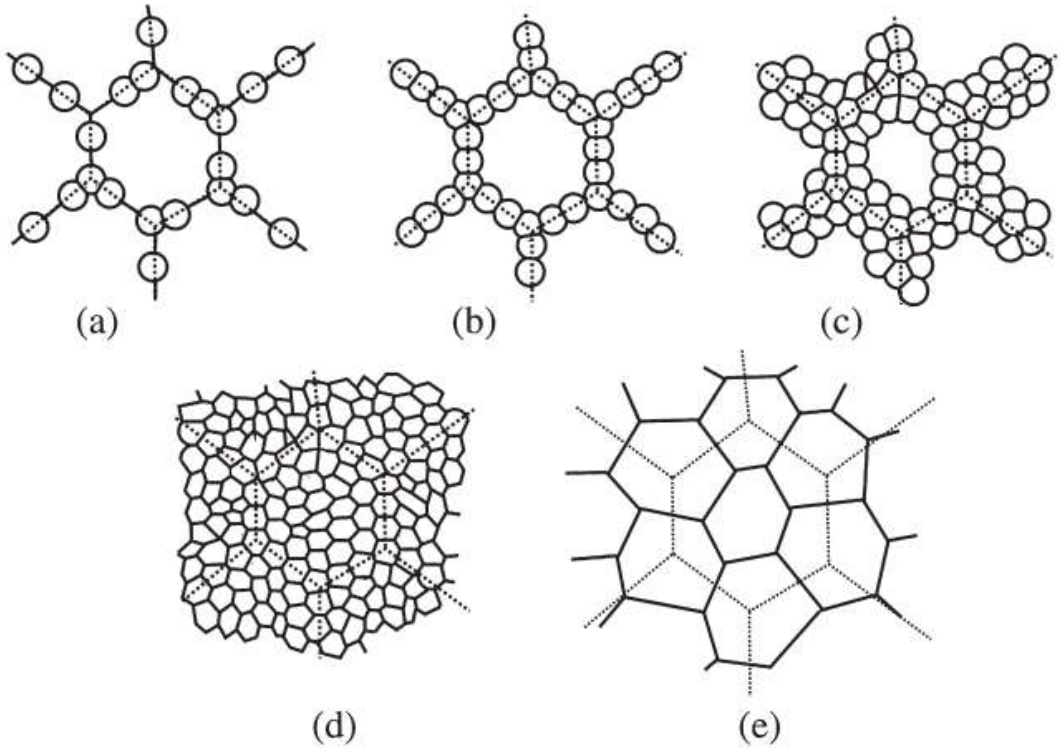

Figure 2-23 The microstructure development during discontinuous dynamic recrystallization. Dotted lines denote prior grain boundaries [84].

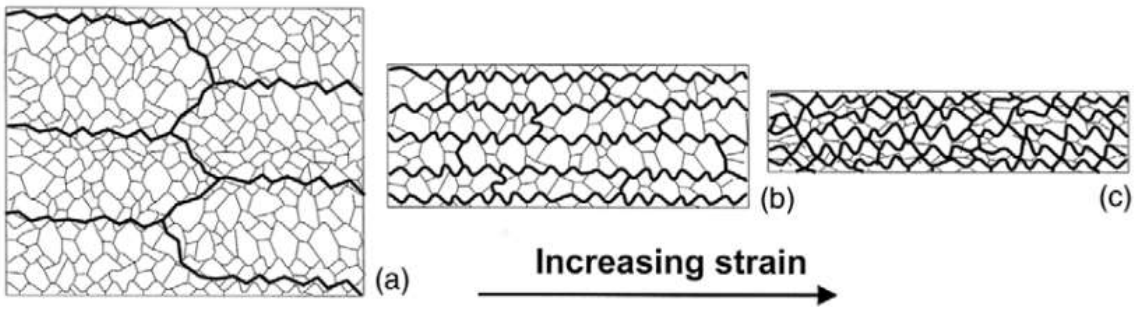

Figure 2-24 Schematic diagram illustrating the evolution of grains due to geometric dynamic recrystallization. Thicker lines represent high angle grain boundaries whereas thin lines denote subgrains [84].

2.8 ELECTRON BACKSCATTER DIFFRACTION (EBSD)

The distinguishing features of the aforementioned recovery/recrystallization mechanisms are not easily analyzed with optical and standard scanning electron microscopes. However, a powerful technique that combines SEM and orientation imaging known as electron backscatter diffraction (EBSD) has proven to be a very useful tool in imaging and analyzing the evolution of grain boundaries in materials. In and of itself, EBSD is an orientation imaging microscopy technique that is used to determine the texture, crystallographic orientation, phase identity, and phase distribution within a small volume of a polycrystalline material. This technique was first investigated by Nishikawa and Kikuchi in 1928 [88] and was later explored and developed in conjunction with a SEM in the 1970s [89][90]. Since then, EBSD has become a useful tool in the acquisition of advanced data for microstructural studies. A typical automated EBSD system consists of the SEM, a Kikuchi pattern detector, and proprietary software. The set-up is configured such that the surface of a highly polished specimen is tilted at an angle of 70º to the incident beam (Figure 2-25) to increase the quantity of electrons diffracted from it towards the EBSD detector. The detector itself is typically a phosphorous screen attached to a camera that images the cone of 'Bragg' diffracted electrons as Kikuchi patterns with each corresponding to diffraction from a distinct family of crystal lattice planes.

Essentially, Kikuchi patterns include numerous pairs of band-like parallel lines that frequently intersect each other (Figure 2-26). Each pair of parallel lines within the pattern represents a lattice plane whereas the width between them is inversely proportional to the respective interplanar spacing [91]. In addition, the intersections between Kikuchi bands

correspond to the projected locations of zone axes ([uvw]) in a crystal. In practice, the Kikuchi patterns are captured on a phosphor screen and relayed to the EBSD software for indexing. The software performs this task by quantifying the attributes defined in Figure 2-26. The crystallographic orientation data from EBSD is then converted into a graphical format so as to produce pole or inverse pole figures that represent the texture within the sample of interest.

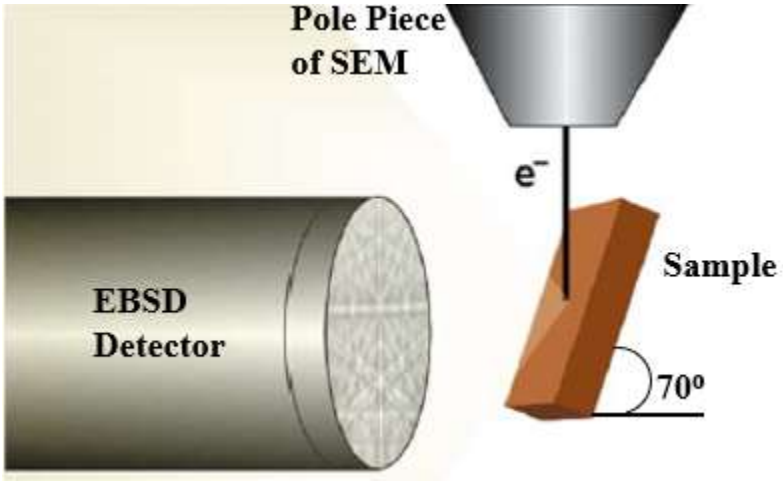

Figure 2-25 Schematic diagram showing a typical EBSD configuration [92].

Specifically, a pole figure is a gnomonic stereographic projection that is used to represent the orientation distribution of crystallographic directions in a material. Essentially, the crystallographic directions are projected into the sample frame of reference whereas for an inverse pole figure, they are projected into a crystallographic frame of reference [91][93][94]. A cubic unit cell residing within a sample with axes Xs, Ys and Zs is used to illustrate the construction of a pole figure (Figure 2-27). It should be noted that the terms poles and hemisphere are terminologies that relate to “earth” and are used in the metallurgical sense in this context. In stereographic projections, the normal of any

crystallographic plane termed a ‘pole’ intersects the reference sphere in the upper (northern) half [91]. Note that the reference sphere is the starting point for the well-known stereographic projection [91]. Here it is imagined as a 3-dimensional spherical space in which for example the unit cell of a cubic crystal resides at the center as labeled in Figure 2-27a [91]. This point is then projected to meet the southern pole of the sphere and in doing so, intersects the equatorial projection plane. In this case, the unit cell of the crystal is thought of as if it resided at the center of the sphere (Figure 2-27a). After this, the equatorial projection plane is extracted and shown as the 2-dimensional pole figure (Figure 2-27b). The clustering of poles (i.e. intersection points) in a certain area of the projection plane is indicative of preferred orientation of grains in a material whereas a more uniform distribution of poles translates into the absence of this effect.

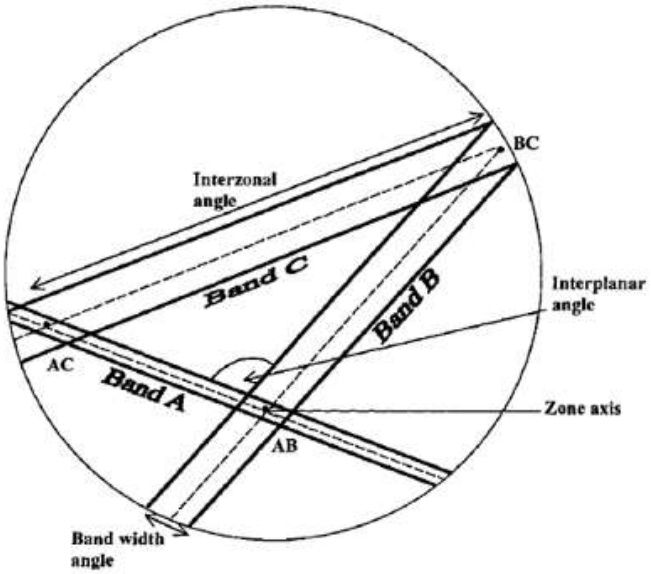

Figure 2-26 Schematic illustration of the features of a Kikuchi pattern. Image adapted from the Kikuchi pattern of iron showing an example of an interplanar angle, interzonal angle, zone axes (AB, BC and AC) and band width angle [91].

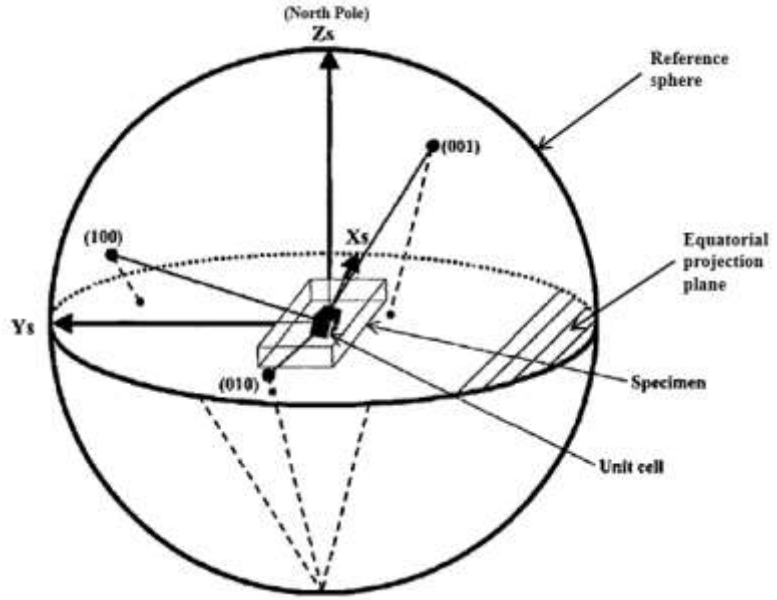

(a)

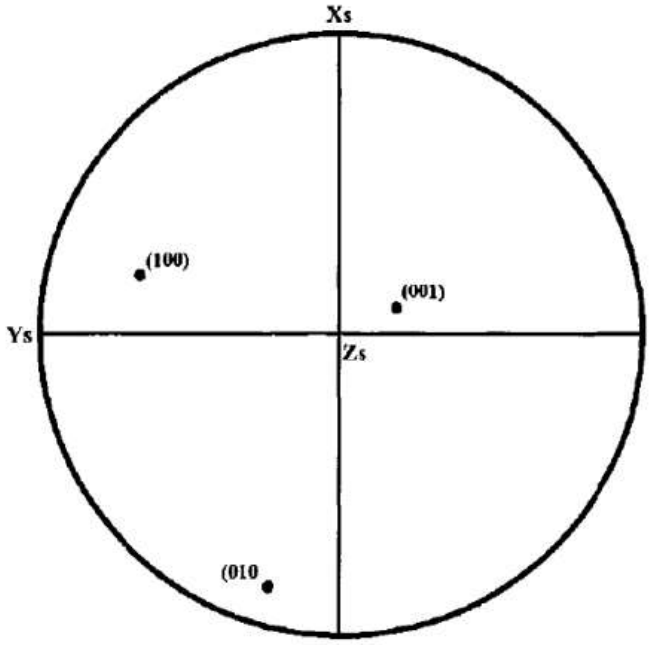

(b)

Figure 2-27 Illustrations of depicting pole figure construction. (a) Reference sphere showing projection of select crystal axes and (b) equatorial projection plane extracted from (a) [91].

An inverse pole figure, on the other hand, is a very useful means to visually display the micro-texture from axially symmetric specimens particularly where only one direction of the specimen is of importance or interest. When constructing an inverse pole figure, the vector pointing along a given specimen direction is projected onto planes determined by the local crystallographic orientation [92]. Note that in the pole figure shown in Figure 2-27(b), the orientation data were plotted with reference to the specimen axes Xs, Ys and Zs. So therefore, the inverse pole figure is always plotted for a specific specimen direction which must be chosen carefully for it to be meaningful. For instance, in rolled sheet, the longitudinal direction parallel to the rolling direction is commonly utilized.

Since the frame of reference for an inverse pole figure is always defined by the local crystal orientation, the symmetry of the crystals is reflected in it [92]. For example, the normal direction inverse pole figure for a specimen with a cube texture is shown in Figure 2-28. The fine lines in Figure 2-28(a) indicates how the cubic crystal symmetry of the specimen with the cube texture divides the projections into twenty four stereographic triangles. Note that each triangle contains identical orientation information. The triangle highlighted in Figure 2-28(a) is extracted and plotted in Figure 2-28(b).

Since crystals are three-dimensional entities, pole and inverse pole figures are considered as semi-quantitative methods of examining texture. A better representation of texture can be achieved by using orientation distribution functions (ODFs) which utilize three-dimensional Euler space with Euler angles to represent texture. For the purpose of the work completed in this thesis, the discussion will not be extended to ODFs.

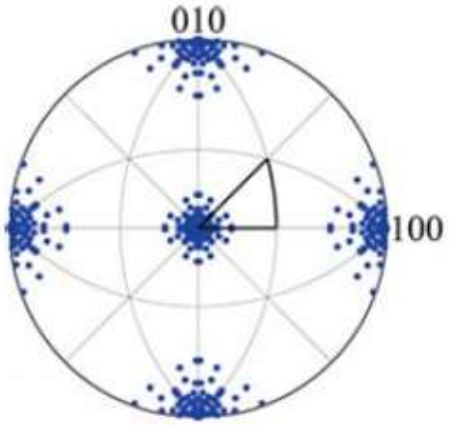

(a)

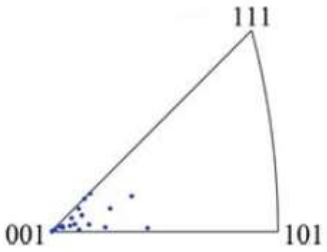

(b)

Figure 2-28 (a) A normal direction inverse pole figure of a cube texture (b) a unit stereographic triangle seperated out from figure (a) [92].

2.8.1 INTERPRETATION OF POLE AND INVERSE POLE FIGURES

Due to the scope of this work, the discussion here is limited to only cubic crystal materials. Since most materials are not grown as single crystals, they possess small crytallites where each crystal exhibits its own crystallographic orientation. Collectively, these orientations could be random, or they may have a preferred orientation about a particular direction. The orientation pattern exhibited by the crystallites is what determines the texture [95]. Generally, the texture in a material can be described as random, fiber or biaxial. When the crystallites in material do not exhibit any preferrred orientation the texture is described as random whereas for a fiber texture, the

crystallographic directions of most grains are parallel to one preferred direction of the sample. A biaxial texture on the other hand as the name suggests has two preferred directions. For example, in a rolled sheet the texture is represented by texture components written as $\{hkl\} < uvw >$ [95]. This essentially means that most of the grains in the sheet material are such that their {hkl} planes are nearly parallel to the rolling plane and the (uvw) directions of the grains are nearly parallel to the rolling direction[95]. Practically, the grains in a rolled material could exhibit several combination of textures where the net texture is represented as $\{h_1k_1l_1\}\langle u_1v_1w_1\rangle$, $\{h_2k_2l_2\}\langle u_2v_2w_2\rangle$....., etc. Hence, such a complex texture can be represented as shown below [94]:

$$\text{Overall texture} = \sum w_i.\ \{hkl\}_i\ .\ \langle uvw\rangle_i \qquad (12)$$

where w_i is a weighting factor that is introduced to allow for relative intensities of the different components. To understand and interpret texture from pole figures, standard stereographic projections are required to assist in deciphering it.

A stereographic projection is defined as a 2-dimensional projection of a 3-dimensional crystal (or unit cell) in which the angular relationships between different planes, different directions and between planes, and directions in a crystal or unit cell is deduced [94]. In other words, this is a projection in which the positions and intensities of specific cyrtallographic orientations are plotted in relation to the specimen geometry. The construction of a standard stereographic projection is synonymous to how a pole figure is constructed. Figure 2-29 illustrates how a stereographic projection is constructed. It is

assumed that a small unit cell resides at the center of a large sphere, known as the reference sphere. Perpendicular lines to the six cube faces of the unit cell are drawn and extended to intersect the reference sphere. Note that the resultant poles are the normals to the planes (100), $(\bar{1}00)$, (010), $(0\bar{1}0)$, (001) and $(00\bar{1})$ as shown in Figure 2-29a. Assuming a source of light was situated at the 001 pole position and shone to allow the light rays pass through the 100, $\bar{1}00$, 010 and $0\bar{1}0$ to fall on a cardboard aligned perpendicular to the 001-$00\bar{1}$ axis, then the lower half of the reference sphere will projected as a circle which in actual fact is the projection plane parallel to the (001) plane of the unit cell. Because the plane of projection is parallel to the (001) plane, the projectioin plane here is referred to as the (001) projection plane of the cubic unit cell [94]. It can be seen that in Figure 2-29b, the poles of only the {100}-type planes were plotted. However, the poles of more than one type of crytallographic plane could be plotted on the same stereographic projection. Such a projection which contains poles of different crystallographic plane types is known as a standard stereographic projection[94]. Therefore, for a cubic unit cell, the poles of the {100}, {110} and {111} planes are plotted with (001), (110) and (111) as the planes of projection consituting their respective standard stereographic projections as shown in Figure 2-30. Now that the standard stereographic projections have been established, an example illustrating how they are used to identify texture in a pole figure is discussed next.

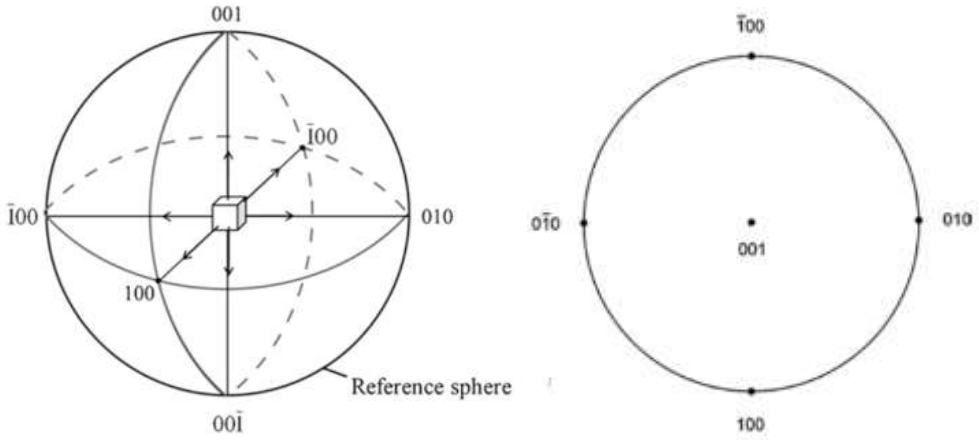

(a) (b)

Figure 2-29 Schamatic representation of a stereographic projection. (a) Plane normals of the cube present at the center of the reference sphere intersect with the surface of the sphere and provide poles (100), $(\bar{1}00)$, (010), $(0\bar{1}0)$, (001) and $(00\bar{1})$. (b) The basic circle from (a) depicting the (001) stereographic projection [94].

For instance, the pole densities of {111}-type planes in a rolled and recrystallized sheet of Ni, plotted in the form of a pole figure with reference to the sample geometric parameters RD (rolling direction), TD (transverse direction) and ND (normal direction) is shown in Figure 2-31[94]. Indeed, the clustering of poles at distinct locations indicates that the material is textured. To identify this texture, the standard (001) stereographic projection of a cubic material is superimposed on the pole figure in question. It would be noticed that the regions with the highest pole densities coincide specifically with {111} positions of the stereographic projection. Assuming most of the grains in the Ni sample had their {111} planes lying parallel to the sheet plane, then their plane normals would have pointed towards the ND which implies the highest pole densities would have accrued in and around ND. Since this was not the case, it means these are not {111} planes but some other {hkl} planes where majority of the grains must be lying parallel to the rolling (sheet) plane. Hence, when we superimpose the standard (001) stereographic

projection on {111} pole figure of Ni, it implies that that the projection plane of the stereogram (001) is the same as the projection plane of the pole figure thus the rolling (sheet) plane. Therefore, under this condition, the densely populated pole regions match perfectly with the {111} locations of the the standard (001) stereographic projection. Hence, the densely populated pole regions of the pole figure can be accounted for if only the sheet plane is (001). When this condition is satisfied, the RD of the pole figure lies exactly at the $[\bar{1}00]$ location of the standard stereographic projection. Hence, the texture of the Ni sample can be described as (001)[$\bar{1}00$].

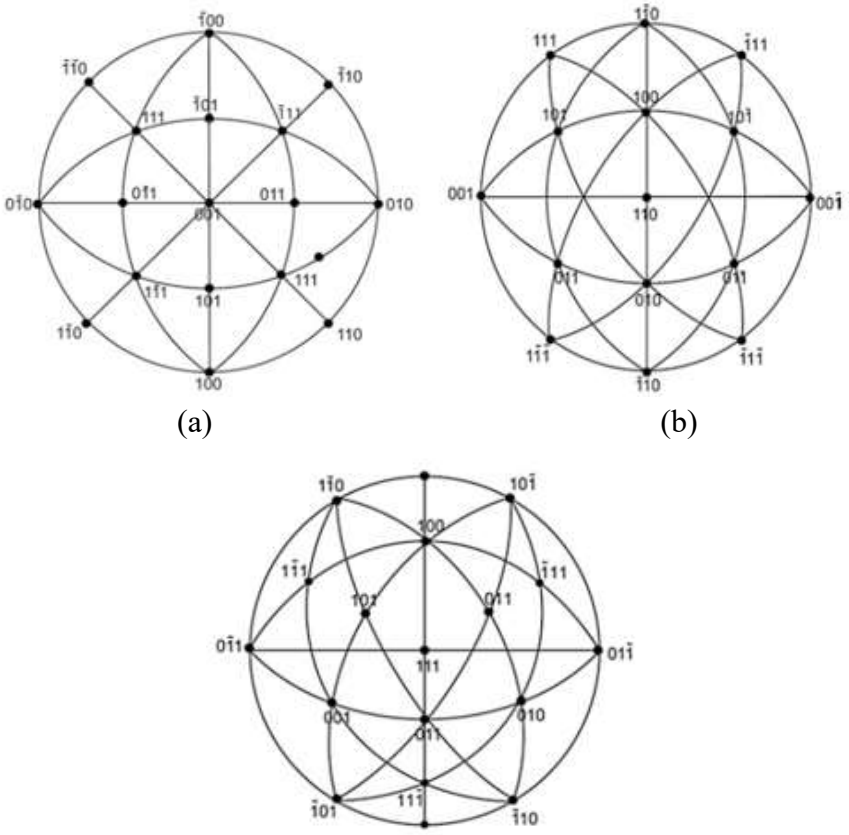

Figure 2-30 (a) (001), (b) (110) and (c) (111) stereograms for cubic materisls [94]

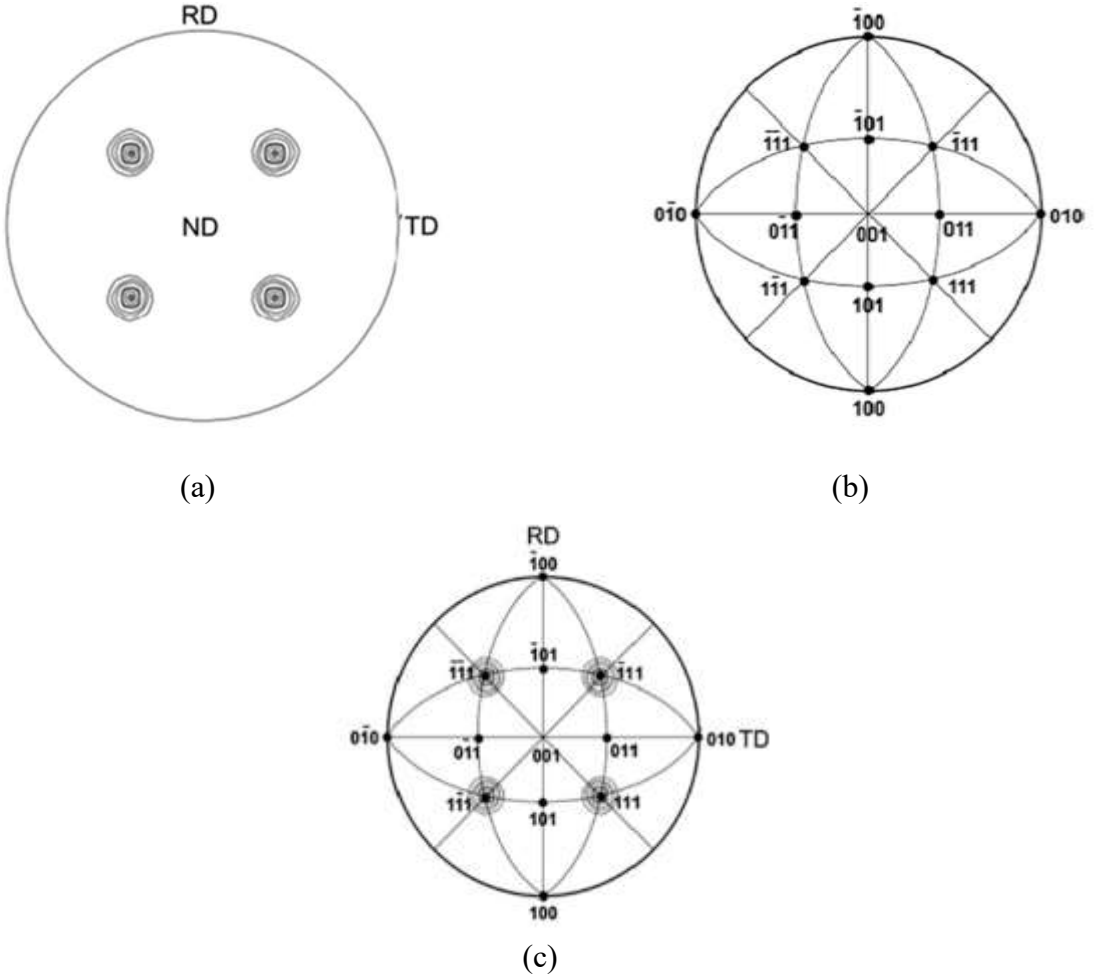

Figure 2-31 (a) {111} pole figure for a rolled sheet. (b) (001) stereographic projection and (c) pole figure and stereographic projection superimposed on each other [94].

It should be noted that the aforementioned scenario was a very simple case of identifying texture. It would have been more complicated if the {111} pole densities did not coincide with the {111} locations on the standard stereogram. For example, assume that the {110} poles in a given pole figure (Figure 2-32) did not at the first instance coincide with {110} locations of a standard stereogram [94]. Here, the pole figure has to be rotated around ND relatively with respect to the relevant stereogram to make the poles coincide as shown in Figure 2-32b. This implies that the texture here can be interpreted as (110) [001]. It should be noted that for the interpreation of pole figures, it is imperative or necessary to

have the locations of some important ideal orientations in pole figure form [94]. For example, ideal texture components are extremely useful in identifying texture component(s) present in experimental pole figures [94]. The ideal positions of a few important texture compenents encountered in FCC materials are presented in Figure 2-33. The texture components typically encountered in deformed FCC materials include brass $\{110\}\langle 112\rangle$, copper $\{112\}\langle 111\rangle$ and S $\{123\}\langle 634\rangle$ [94][96]. These textures would most likely evolve into cube texture upon recrystallization [96]. It is typical of recrystallized or annealed FCC materials to predominantly exhibit the cube texture $\{100\}\langle 001\rangle$. Other texture components that are manifested due to shear deformation in FCC materials include $\{001\}\langle 110\rangle$, $\{111\}\langle 110\rangle$ and $\{111\}\langle 112\rangle$ [63].

There are other instances where the texture in a material exhibits rotational symmetry due to an axially symmetric deformation. As such, they are described by specifying the crytallographic direcion $\langle uvw\rangle$, which is parallel or nearly parallel to the axis of deformation [94]. This type of texture is referred to as fiber texture whilst the axis is called the fiber axis [94]. The variables or components belonging to a particular texture are obtained by rotation about the fiber axis, and this type of texture is represented in the pole figure by continuous bands of orientations (Figure 2-34). A perfect fiber is obtained when the bands are populated uniformly; when sparcely populated, this is said to constitute a partial fiber texture [94]. Notably, inverse pole figures are useful for representing texture in an axisymmetric deformed material where only one axis needs to be specified [94].

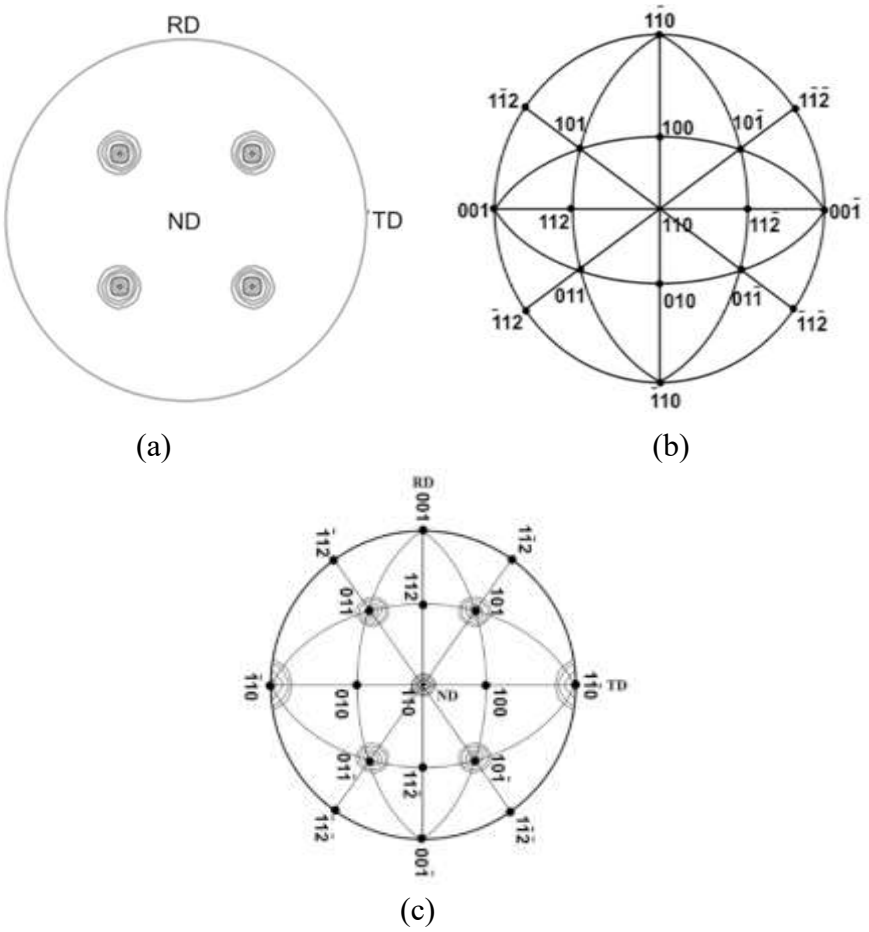

Figure 2-32 (a) {110} pole figure for a rolled sheet. (b) (110) standard stereographic projection and (c) superimposition of (a) and (b) [94].

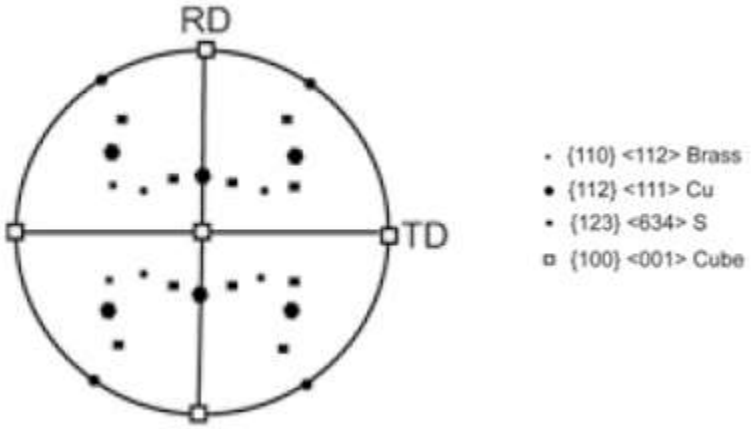

Figure 2-33 Standard (200) pole figures showing ideal texture components encountered in deformed and recrystallize FCC materials [94].

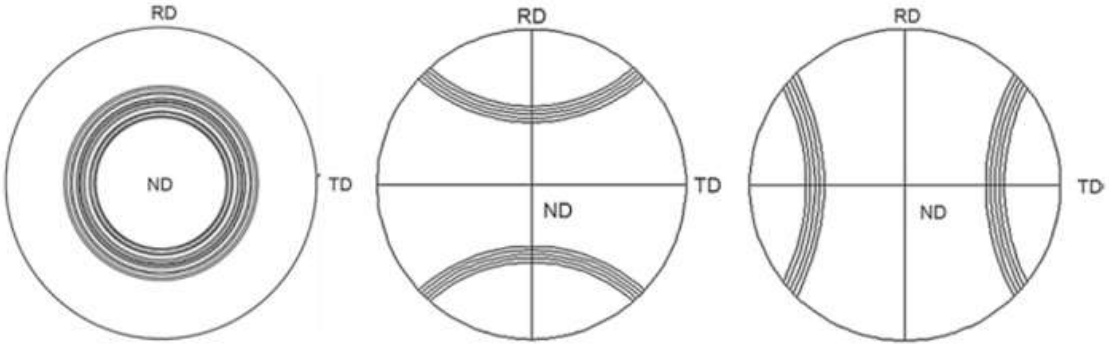

(a) (b) (c)

Figure 2-34 Pole figure showing (110) fiber along (a) ND (b) RD and (c) TD.

It is normal to find that discrete points or colours are used to represent poles. For example, the inverse pole figure shown in Figure 2-28(b) represents a cube texture in a material. Contour lines are preferred when there is ambiguity in the data. The numbers assigned to the contour lines or 'isopleths' indicate the pole densities relative to that which would be expected for a specimen that is textureless or random [94]. Therefore, contour lines greater than 1 times random signify a concentration of poles whereas contour lines less than 1 times random imply a depletion of poles [94]. It is important to note that pole and inverse pole figures are often viewed together to aid data interpretation.

CHAPTER 3 EFFECT OF ASYMMETRIC ROLLING ON THE MICROSTRUCTURE AND MECHANICAL PROPERTIES OF WROUGHT 6061 ALUMINUM

Mark Y. Amagadzie[1] and D. Paul Bishop[2]

1 – Graduate Student, Dalhousie University, Halifax, Nova Scotia, Canada
2 – Professor, Materials Engineering, Dalhousie University, Halifax, Nova Scotia, Canada

Status: Paper submitted to the journal "Materials Characterization".

Author contribution: The experimental procedure was conceptualized by Mark Y. Amegadzie and D. Paul Bishop. All experimental work was completed by Mark Y. Amegadzie as well as the first draft of the paper. Supervision and editing of the final manuscript were performed by D. Paul Bishop.

3.1 ABSTRACT

In the open literature, researchers have investigated the effects of asymmetric rolling (ASR) on various metals such as iron and magnesium-based alloys in many studies. However, comparative information dedicated to the influence of ASR on the microstructure and mechanical properties of aluminum alloys is limited. Hence, the objective of this research was to investigate the effect of the core processing parameters of interest (roller velocities, velocity ratio, rolling direction, starting thickness of specimen and extent of reduction) on an aluminum alloy utilized in many commercial applications - AA6061 (Al-0.6Si-1.0Mg). Experimental findings indicated that ASRed specimens exhibited superior tensile properties to symmetrically rolled counterparts provided that the net reduction was achieved in a minimum number of passes. Conversely, no significant gains were recorded in the

mechanical properties due to increases in roller velocities or altering the rolling direction. Comparisons of the resultant microstructures within asymmetrical and conventionally rolled counterparts as assessed through electron back scatter diffraction (EBSD) are also presented. The undeformed base metal revealed the presence of a cubic texture {100} <001>. This texture however evolved into shear {111}<110> and brass {110}<112> texture components in specimens subjected to asymmetric (VR=2.2) and symmetric rolling respectively.

3.2 INTRODUCTION

Asymmetric rolling (ASR) is a metal forming technology that yields a metal sheet or foil product through the application of exceptionally high levels of plastic deformation. Asymmetry is key to this concept and is typically achieved by driving equivalent sized rollers at different velocities or different diameter rollers at the same velocity. Both approaches act to create an imbalance between the rollers such that the material is subjected to a unique combination of acute shear and compressive deformation which can thereby influence the mechanical properties and microstructure of the rolled product. The shear strain induced through the thickness of a material via conventional rolling is normally symmetric and localized to the surface of the material [63]. Conversely, in ASR, this feature is far more intense and changes continually through the thickness of the material [8][9].

The strain induced in the rolled material can lead to ultrafine grain refinement and high dislocation densities needed for increased strength [10]. For example, rolled products

with average grain sizes of 1-2μm, 1.4-2μm and ~0.2μm were obtained for pure aluminum [66][65][97][98], magnesium [99] and iron [100] respectively when processed by ASR. Some researchers have shown that the shear strain produced during ASR facilitates grain subdivision and rotation which forms the basis of this grain refinement as well as crystallographic texture evolution [101][64]. Mostly, annealed and recrystallized aluminium alloys are typically characterized by a cube texture {100} <001>. ASR unlike symmetric rolling produces shear strains that in turn instill shear textures that can positively impact the formability and strength of aluminium alloys. The typical rolling textures produced in aluminium alloys include Goss{110}<100>, S {123}<634>, Brass {110}<112> and Cu {112}<11$\bar{1}$>. Also, shear texture {111}<011> and {111}<112> components are known for impacting strength in aluminium alloys. Interestingly, one of the proposed mechanisms responsible for the ultra-fine grain formation during ASR is in-situ dynamic recrystallization. According to this phenomenon, when a material is subjected to the conditions of plastic deformation within the high strain regime, the subdivision of grains due to increased boundary mis-orientation ultimately leads to the formation of high angle grain boundaries [102]. Such features are of considerable practical interest as the presence of a large fraction of high angle grain boundaries is essential to achieving unique and superior properties [103]. Furthermore, Kawalek et al have shown that the rolling force required during ASR is smaller compared to that required in conventional symmetric rolling [67]; an advantageous trait that further bolsters the technological interest of applying ASR on an industrial scale. The use of ASR in processing aluminum alloys has become particularly important since the process results in the modification of microstructural features and mechanical properties alike

[63][65][97][64][104][105][106]. Indeed, numerous alloy systems have been studied including AA1050, AA6111, AA5754 and AA7075. In addition, information regarding the effect of rolling route have been reported for pure aluminum [101] and an aluminum alloy [105] through finite element analysis and experimental studies respectively. AA6061 is a general purpose structural alloy used extensively in many industries [12]. This is because AA6061 possesses exceptional attributes such as corrosion resistance, good formability, weldability and lower cost compared to other aluminium alloys. In addition, AA6061 is an age-hardenable alloy that can be strengthened through heat treatment [12]. Hence, the purpose of this work was to study the physical response of AA6061 to the core parameters inherent to ASR. In particular, the effects of the rolling direction, starting thickness, number of passes, roller velocity and roller velocity ratio have been investigated.

3.2 MATERIALS AND EXPERIMENTAL PROCEDURES

The chemical assay of the extruded AA6061 bar stock utilized in this research was measured via inductively coupled plasma optical emission spectroscopy. A comparison between the resultant measurements and the compositional limits specified in ASTM 308M-10 (Table 3-1) confirmed that the starting material was within specifications.

Table 3-1 Measured assay (weight %) of the aluminum 6061 utilized in comparison to established wrought compositional limits (ASTM 308M-10).

	Element								
	Al	Mg	Si	Fe	Cu	Cr	Ti	Mn	Zn
Measured	Bal.	0.90	0.52	0.17	0.20	0.08	0.01	0.01	0.00
Specified	Bal.	0.8-1.2	0.4-0.8	0.7*	0.15-0.4	0.04-0.35	0.15*	0.15*	0.25*

* Indicates maximum concentration allowable.

All starting billets were machined from the extruded bar stock of AA6061 to produce a rectangular geometry with a nominal length and width of 31.7mm and 12.7mm respectively. Each slug was annealed by heating at 415ºC for 3 hours in air followed by furnace cooling to room temperature to coarsen pre-existing precipitates into an incoherent state and thereby soften the alloy prior to rolling. Annealed specimens were then rolled at room temperature with a Ruesch Differential Rolling Mill (roller diameter 101.6mm, roller width 152.4mm) featuring two rollers with independently controlled rotational velocities. In all ASR trials, the top roller velocity was set to a higher value than that utilized for the bottom roller. No lubricant was applied to either the specimens or the rollers to maximize shear deformation during the rolling process. A minimum of three specimens were rolled for each condition investigated. In some instances, specimens were rolled in a unidirectional (UD) manner wherein the orientation of the bar was not altered between subsequent passes. However, in other scenarios, the specimen was rotated between subsequent passes. The three options considered were rotation by 180˚ about the normal axis (NA), rolling axis (RA), and transverse axis (TA) as shown in Figure 3-1.

To investigate the effect of starting thickness, specimens with initial thicknesses 3.2mm, 6.4mm,12.7mm, 19.1mm and 25.4mm were rolled through 4 passes to achieve a total thickness reduction of approximately 80%. TA rotation was applied between consecutive passes. The effect of roller velocity was investigated by setting the roller speeds (top: bottom) to 6:4.3 revolutions per minute (rpm), 12:8.5 rpm and 24:17 rpm to obtain a constant velocity ratio (VR) of 1.4. These specimens were rolled through 16 passes while again employing the TA rotation between consecutive passes to achieve an overall thickness reduction of approximately 80%. To establish the effects of the rolling pass step size, reductions of approximately 2.54mm, 1.27mm, 0.64mm and 0.32mm per pass were applied to specimens until a net reduction of 80% was realized in each instance. It should be noted that this rolling schedule employed equal thickness reductions in terms of number rather than percentage during each rolling pass. This thereby mandated the application of 2, 4, 8 and 16 passes respectively to achieve the same near net reduction targeted (80%). Finally, the effect of VR was investigated by setting the top roller velocity to 24 rpm while varying the velocity of the bottom roller to obtain VRs of 1, 1.2, 1.4, 1.6, 1.8, 2.0 and 2.2. In these trials, each sample was subjected to a TA rotation between consecutive passes in which a step reduction of 0.64 mm/pass was applied until a near total thickness reduction of 80% was achieved. A summary of the rolling parameters investigated is presented in Table 3-2.

Characterization of the rolled specimens included orientation imaging microscopy (OIM), hardness measurements and tensile testing. For the former, polished cross-sectional mounts of the starting billet and rolled products were prepared by first mounting sections

using a Struers CitoPress-5 automatic mounting press and then loading the mounts within a Struers Tegramin apparatus for polishing. The specimens were first ground using a 1200 grit silicon carbide disc and subsequently polished in stages using cloth pads and suspensions of 15, 3 and 1 μm diamond and finished with 0.05 μm colloidal silica suspension. Microstructures were then studied using a HKL EBSD (electron backscatter diffraction) system equipped with a Nordlys Oxford Instruments detector attached to a Hitachi S-4700 cold field emission scanning electron microscope (SEM) operated at 20 KV. A step size of 1 and 0.2 μm was used during EBSD analysis to index the base metal and rolled specimens. A standard noise reduction of all the maps was performed by first extrapolating wild spikes. This was followed by a moderate level of zero solution extrapolation. Hardness measurements were made on the rolled specimens using a LECO Vickers hardness testing machine operated with an applied load of 10g. Mean hardness were calculated from 5 measurements made on each sample evenly along the ND surfaces of three identically rolled specimens split evenly between the top and bottom variants in each instance. Rolled products were then machined into a geometry appropriate for tensile testing in accordance with ASTM standard B557M. Tensile specimens were tested with an Instron Satec model 5594 200HVL hydraulic load frame equipped with a low range (50kN) load cell, wedge grips and an Epsilon model 3542 extensometer that remained affixed to the specimen for the duration of the test. All reported tensile properties represent an average of three independent tests.

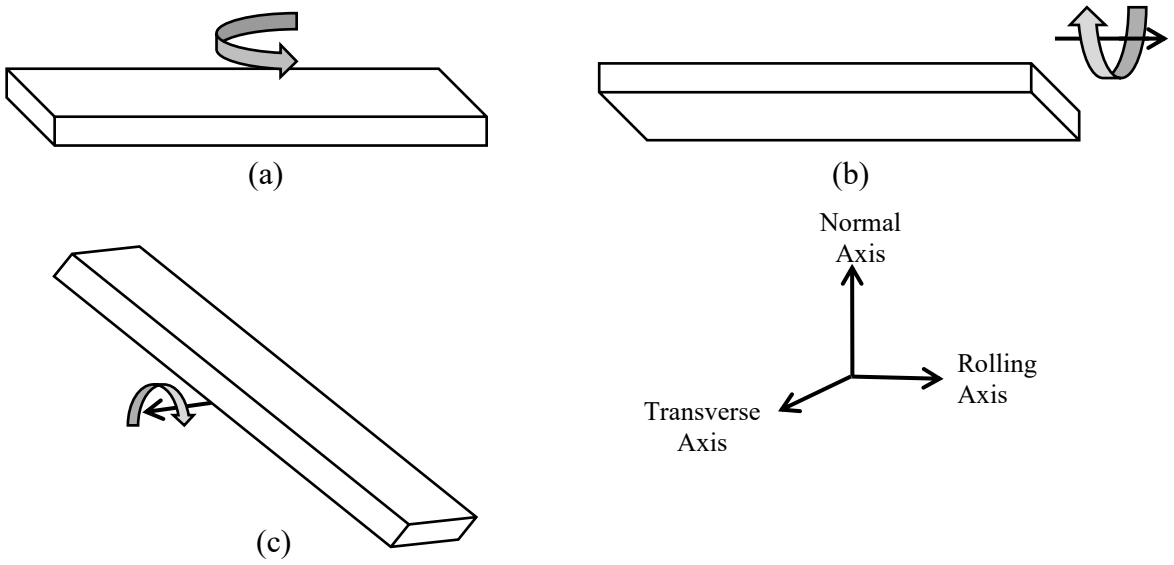

Figure 3-1 Schematics showing the different means of specimen rotation that were applied between passes. Rotation about the (a) normal axis (NA), (b) rolling axis (RA), and (c) transverse axis (TA). When there was no rotation between passes this was denoted as unidirectional (UD).

Table 3-2 A summary of all the rolling parameters investigated.

Rolling Parameters					
Roller Velocity (rpm)		**Starting Thickness (mm)**	**Rolling Orientation**	**Number of Passes**	**Velocity Ratio**
Top roller	**Bottom Roller**				
6	4.3	3.2	Normal Axis (NA)	2	1.0
12	8.5	6.4	Rolling Axis (RA)	4	1.2
24	17	12.7	Transverse Axis (TA)	8	1.4
		19.1	Unidirectional (UD	16	1.6
		25.4			1.8
					2.0
					2.2

3.3 RESULTS AND DISCUSSION

3.3.1 EFFECTS OF ROLLER VELOCITY

When assessing this parameter, the rollers were set to different velocities to achieve a constant velocity ratio of 1.4. As stated earlier, the starting billets were annealed at 415ºC for 3 hours resulting in a yield strength of 56 ±4MPa, 98 ±2MPa ultimate tensile strength and 29 ±2% elongation calculated from five measurements. Note that for each rolling scenario, the top roller was set to a higher velocity than the bottom roller. The tensile and hardness test results are presented in Figure 3-2. Measured values of the yield strength (YS) for the different roller velocities ranged between 199 to 211 MPa while ultimate tensile strengths ranged from 225 to 230 MPa. Obviously, roller velocity was not an influential factor for either attribute. Although averaged values for tensile ductility decreased slightly with increasing roller velocity the nature of the error bars implied that roller velocity was not influential on this attribute either. Similarly, there were no significant transitions in the hardness of rolled products as the roller velocities were increased (Figure 3-2c).

It has been demonstrated through experiments and finite element modelling that the shear stress imposed by a slow moving roller on a material rolled asymmetrically is greater than that of a faster moving roller [62]. The explanation for this behavior could not be ascertained without considering the position of the neutral point; that is where the average specimen velocity equals the velocity of the roller within the roll gap. It is important to note that the neutral point also corresponds to that wherein the maximum pressure is applied during rolling [60]. In symmetric rolling, the position of the neutral

points of both rollers coincide within the roll gap whereas in ASR, they occur at different positions.

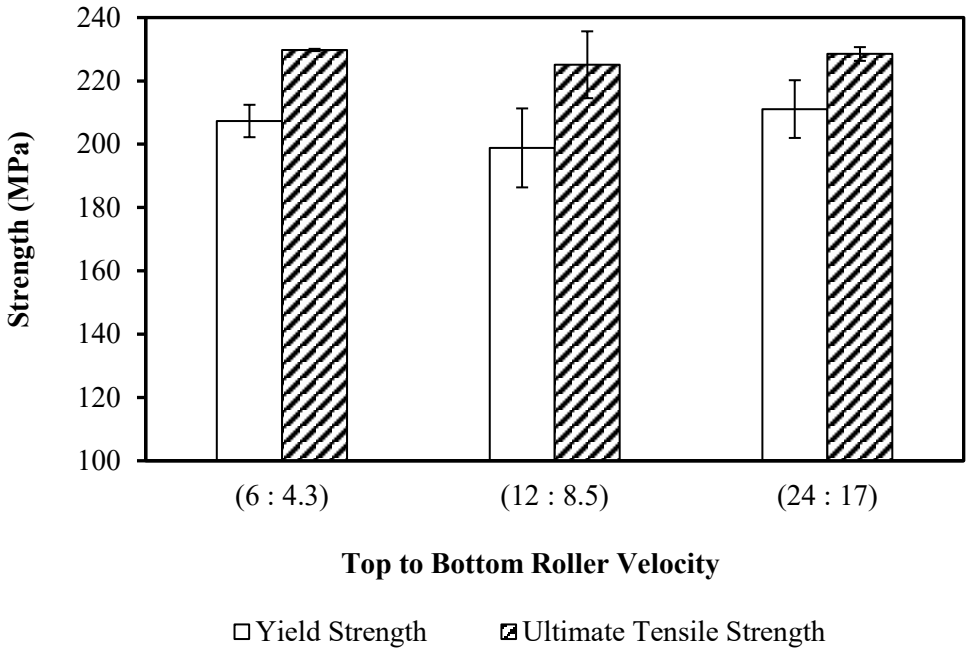

(a)

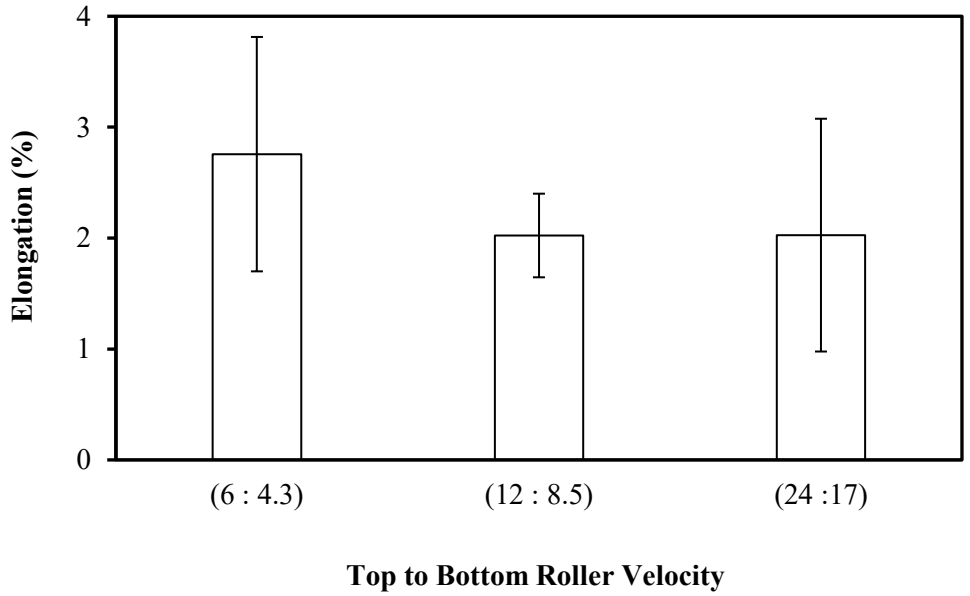

(b)

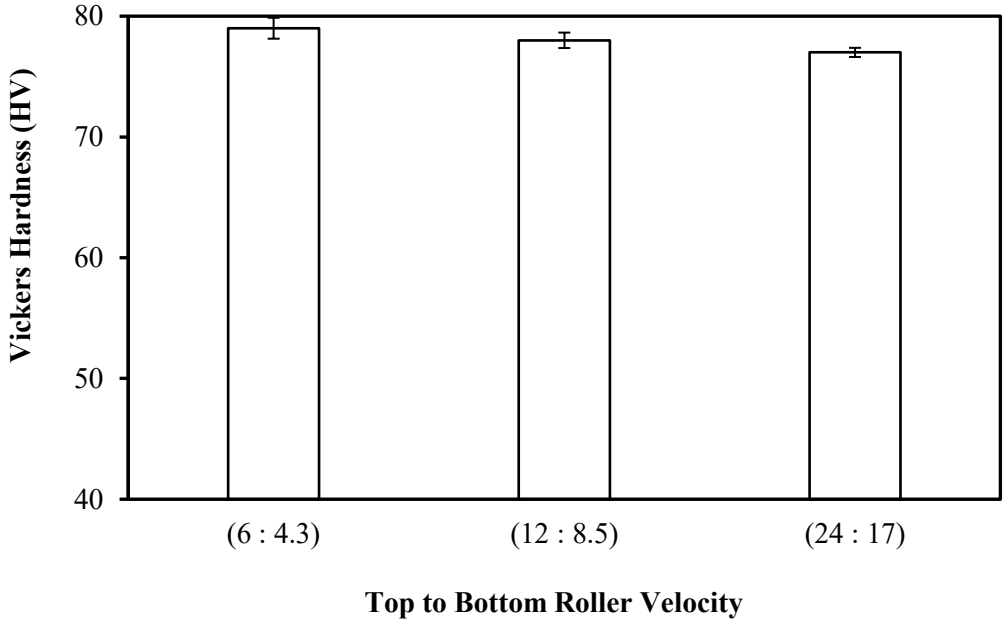

(c)

Figure 3-2 Comparison of the mechanical properties of AA6061 processed with different roller velocities (a) YS and tensile strength (b) elongation to failure and (c) hardness.

For this reason, the shear strain profile developed through the thickness of the rolled specimen is partially dictated by the positions of the neutral points [62]. Hence, it would at first seem reasonable to assume in this work that the shear stress imposed by the set of slower moving rollers would be higher than that of the faster moving ones. Apparently, this was not the case given that none of the mechanical attributes varied with roller velocity. The reason for this was rooted in the fact that the effect of the neutral points on the shear stress is particularly dependent on the velocity ratio [62][107]. Since the velocity ratio was kept constant the effective shear strain localized within the specimen as a consequence of the neutral points during ASR would have been nearly equal or identical.

This understanding is also supported by a mathematical equation derived for the shear strain (Υ) induced in a material during ASR using rollers of the same diameter but of different velocities as was the case in this work [108]:

$$\gamma = \frac{1}{h_i + h_f} R \cos^{-1}\left(1 - \frac{h_i - h_f}{2R}\right)\left(1 - \frac{v_2}{v_1}\right) \quad (13)$$

where R is the radius of the roller, v_1 and v_2 are the velocities of the faster and slower rollers, while h_i and h_f are the initial and final thicknesses of the rolled metal. From equation 1 it is notable that the shear strain is dependent on the velocity ratio. Hence, the strain hardening effect which would have been produced due to the asymmetry between the roller velocities for each set of rollers would have been effectively identical given that all materials were rolled in the same apparatus to the same net strain. For this reason, varying the roller velocities while maintaining a fixed velocity ratio failed to produce any significant changes in the mechanical properties of the rolled materials. This explanation is consistent with results on the effects of velocity ratio which are discussed later. It has also been reported that the rolling force and torque required to reduce the specimen thickness during ASR normally decreases with increasing velocity ratio [109]. Again, considering that the velocity ratio was kept constant during the rolling process, it is reasonable to conceive that the rolling force, or torque required to deform the alloy remained within the same regime for each set of roller velocities.

3.3.2 EFFECTS OF SPECIMEN STARTING THICKNESS

While investigating this process parameter, specimens with starting thicknesses 19.1mm and 25.4mm experienced extensive alligator cracking at their ends. For this reason, characterization of these products was discontinued. Tensile and hardness data for defect-free products are shown in Figure 3-3. These findings indicated that the YS and tensile strength of the rolled material decreased gradually with increasing starting thickness. The specimen rolled with a starting thickness of 3.2 mm recorded the highest YS ~ 248MPa which was 11% superior to that of the specimen rolled with a starting thickness of 6.4mm. Conversely, the lowest YS (212MPa) was recorded by the specimen rolled with the largest starting thickness (12.7mm). Similarly, the highest ultimate tensile strength (260MPa) was also recorded by the specimen rolled with the smallest starting thickness (3.2mm). This value surpassed that of the specimen rolled with a starting thickness of 12.7mm by approximately 13%. It can be inferred that the specimen with the smallest starting thickness (3.2mm) was probably subjected to the highest level of shear deformation. This may have resulted in extensive strain hardening which most likely accounted for the increased strength recorded. Plausibly, the specimen with the smaller starting thickness could have also experienced a higher degree of microstructural refinement compared to the specimens with a larger starting thickness.

The plot of elongation to fracture versus starting thickness (Figure 3-3b) did not reveal a statistically discernable trend for this attribute. The same was found for the hardness results (Figure 3-3c), as the measured values for the different starting thicknesses fell within a narrow range of 80 to 87 HV (Vickers hardness).

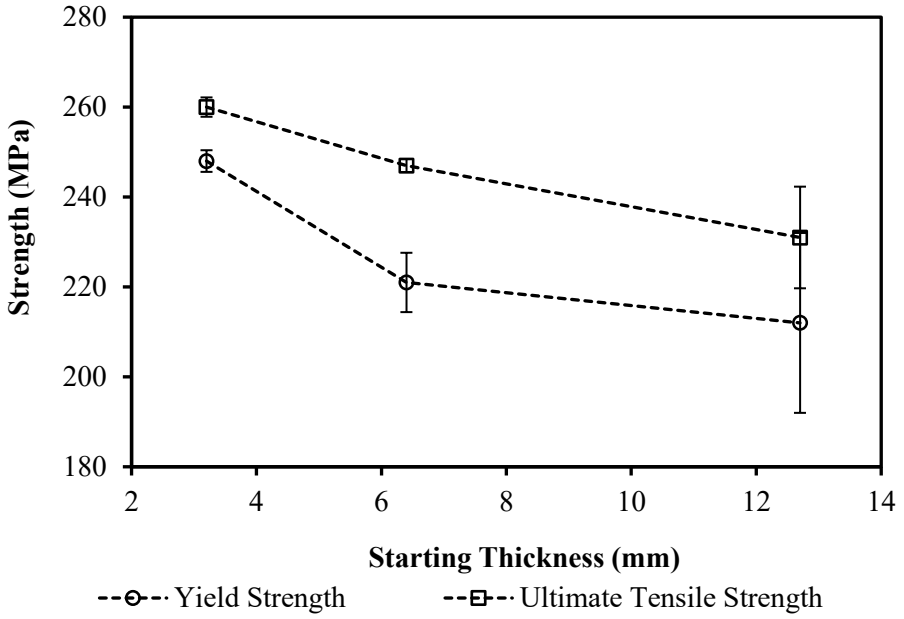
280
260
240
220
200
180
Strength (MPa)
2
4
6
8
10
12
14
Starting Thickness (mm)
Yield Strength
Ultimate Tensile Strength

(a)

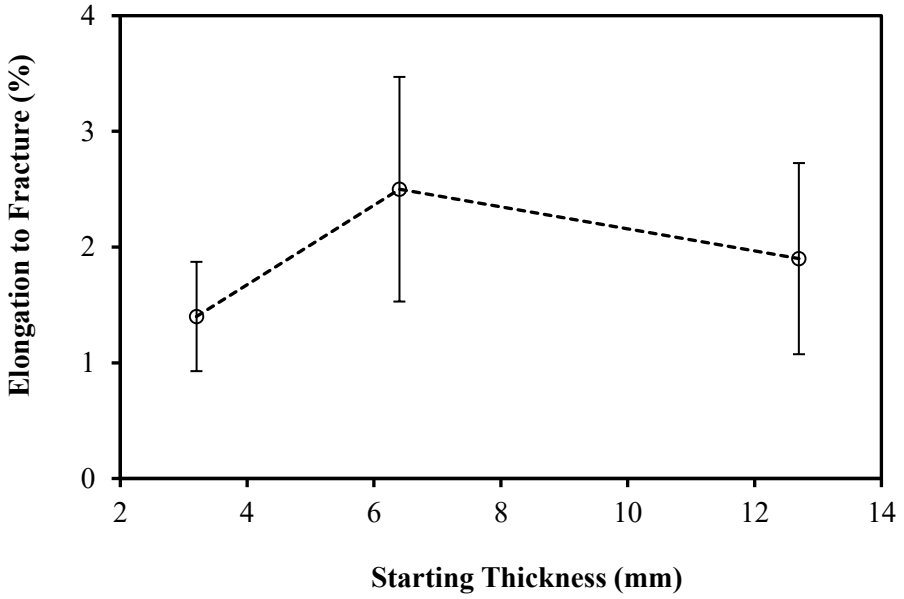
4
3
2
1
0
Elongation to Fracture (%)
2
4
6
8
10
12
14
Starting Thickness (mm)

(b)

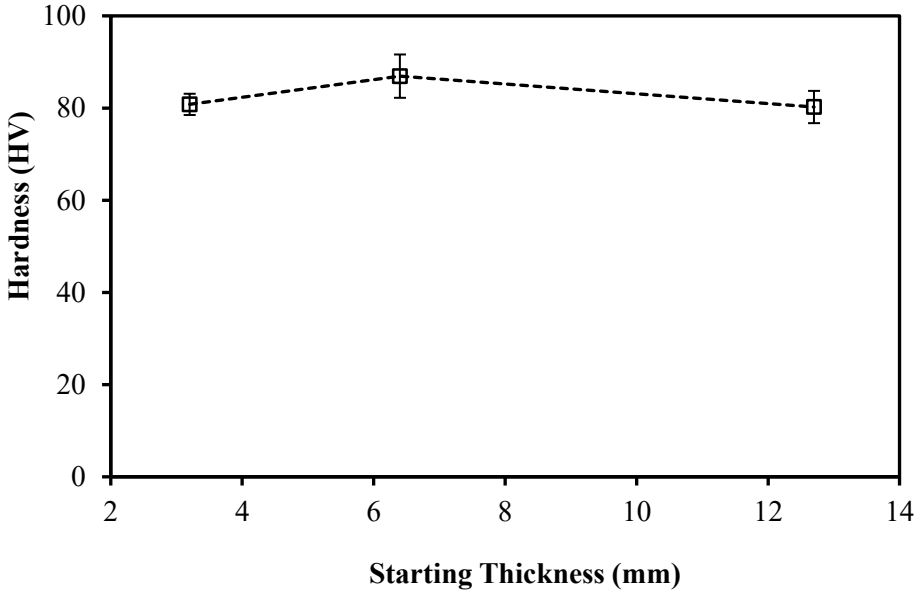

(c)

Figure 3-3 Effects of starting thickness on the mechanical properties of AA6061 processed via ASR. (a) YS and ultimate tensile strength, (b) elongation to failure, and (c) hardness.

3.3.3 EFFECTS OF ROLLING ORIENTATION

The effects of rolling orientation are shown in Table 3-3. Here, the lowest (233MPa) and highest (252MPa) average YS values were recorded by the UD and ND rolling directions respectively whereas intermediate values were measured in the cases of TD and RD. Statistically, there were no clear differences amongst the processes. Likewise, the average UTS values and hardnesses were also comparable and showed no remarkable relationships with the way the sample was rotated between passes. These findings were in agreement with Bobor et al whom investigated the effect of this variable on AA7075 and also concluded that these same mechanical properties were independent of the rolling orientation [105].

Table 3-3 Comparison of the tensile properties of specimens rolled through different rolling directions.

Rolling Direction	Hardness (HV)	Tensile Properties		
		Yield (MPa)	UTS (MPa)	Elongation (%)
UD	100±19	233±5	262±3	3±1.1
RD	89±6	240±4	267±5	3±0.5
TD	96±5	249±6	270±8	2±0.6
ND	94±5	252±17	276±0.2	3±0.5

3.3.4 EFFECTS OF NUMBER OF PASSES

To determine the effects of the number of ASR passes, specimens with a constant starting thickness of 6.35mm were rolled with a velocity ratio of 1.4 while employing TA rotation between consecutive passes to achieve an overall thickness reduction of approximately 80%. Plots showing hardness and tensile properties as functions of the number of passes utilized to achieve this reduction are shown in Figure 3-4. Here, hardness, YS, and UTS all declined as the number of passes was increased (i.e. as the incremental reductions (mm/pass) became progressively smaller). In all three mechanical attributes, the declines were most prolific when transitioning the process from 2, to 4, and then 8 passes. After this, the properties became nominally static such that those for the 8 pass and 16 pass specimens were statistically equivalent. The ductilities of all the different samples averaged around 2.7% and there was no obvious trend as a function of the number of

passes utilized. Utilizing true stress versus true strain data, the strain hardening exponent was also determined and plotted against the number of passes applied (Figure 3-4(d)).

To better understand the mechanical property results, EBSD analyses were completed on specimens rolled under the extreme boundaries of the range investigated for this particular processing parameter - 2 and 16 passes. EBSD was also applied to a sample of the alloy prior to rolling in the annealed condition for comparison purposes. It should be noted that the grain boundaries on the EBSD maps are displayed in black and white lines. The former indicate high angle grain boundaries (HAGBs) whereas the latter denote low angle boundaries (LAGBs).

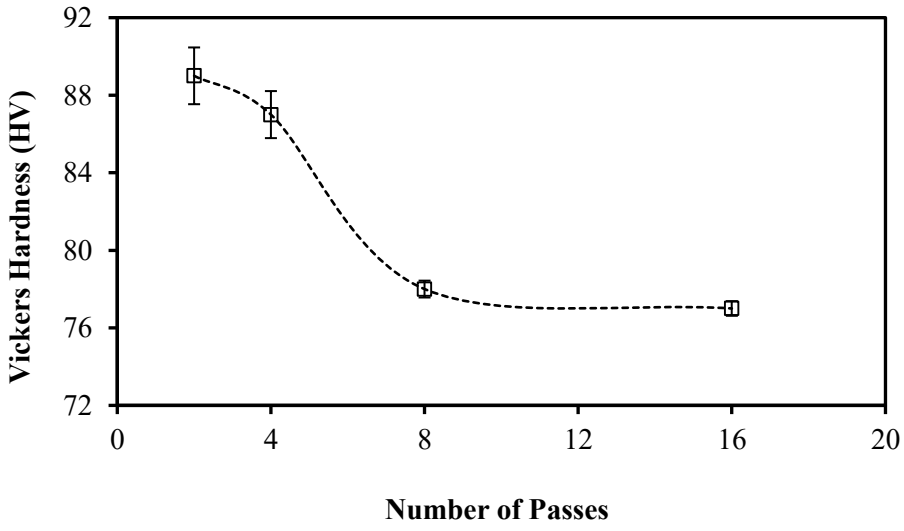

(a)

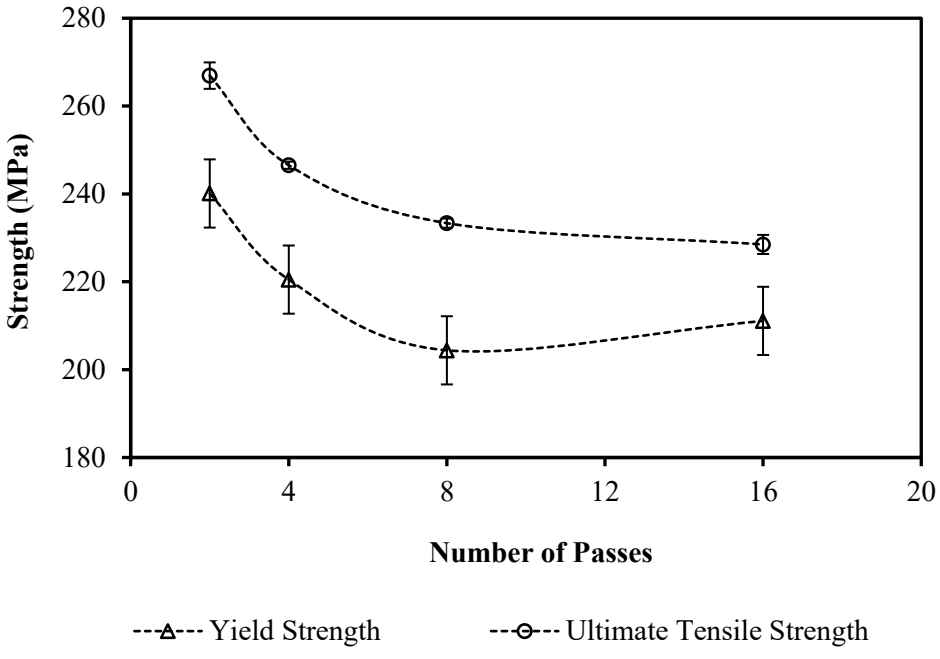
280
260
240
220
200
180
Strength (MPa)
0
4
8
12
16
20
Number of Passes
Yield Strength
Ultimate Tensile Strength

(b)

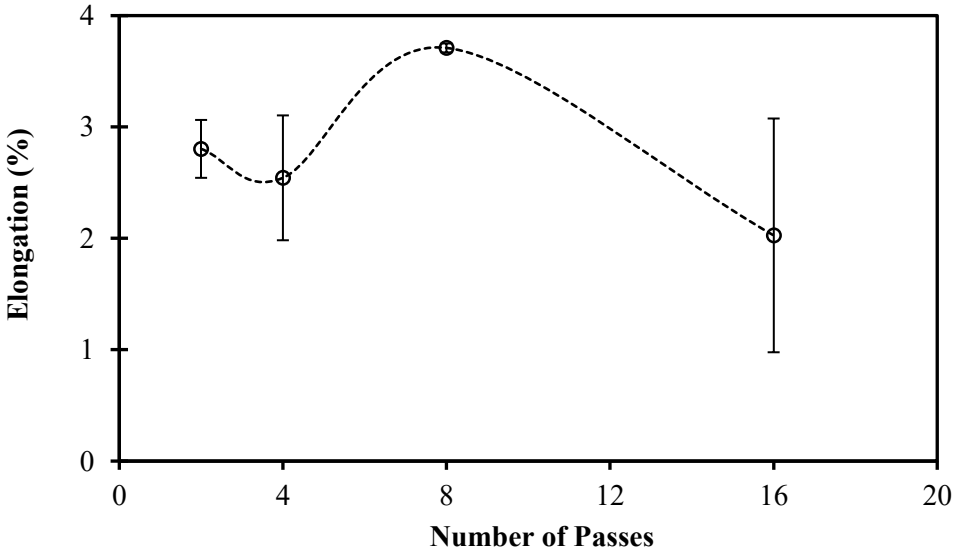
4
3
2
1
0
Elongation (%)
0
4
8
12
16
20
Number of Passes

(c)

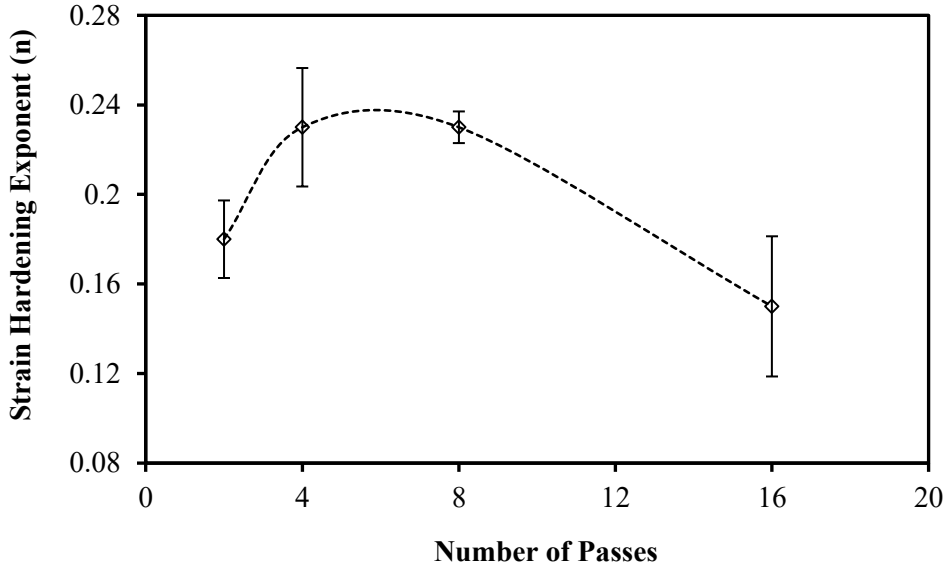

(d)

Figure 3-4 Effects of the number of passes utilized to achieve a fixed area reduction of 80% on (a) hardness, (b) YS/UTS, (c) elongation to failure, and (d) strain hardening exponent.

Undeformed AA6061-O consisted of grains ranging between 40 -120µm (Figure 3-5a). The microstructure was dominated by HAGBs as a proportionately lower amount of sub-grains was discernible. The texture of the starting billet was found to have a cube texture {001}<100> as shown in the pole figure in Figure 3-5. This type of texture is normally observed in annealed and recrystallized FCC metals and it is not considered favourable with regards to enhancing the formability of a sheet. For this reason, metal processing procedures such as asymmetric rolling are employed to produce shear textures that are nearly homogenous throughout the thickness of rolled sheets. Upon transitioning to analysis of the rolled samples, EBSD indexing became prodigiously difficult. This was

a result of the severe strains introduced by cold ASR. For this reason, maps of a size equivalent to that generated for the strain-free annealed material could not be produced; a satisfactory indexing rate could only be obtained at higher magnifications. Maps gathered from the specimens rolled through 2 and 16 passes are shown in Figure 3-6 and Figure 3-7 respectively. It was noted that both rolled specimens displayed a microstructure comprised of grains elongated parallel to the rolling direction as expected. Visual inspection of the EBSD maps also suggested that the microstructural homogeneity improved with a decrease in the number of passes. This observation was attributed to the higher level of shear stress with the greater thickness reduction (i.e. 2 passes). This notion was supported by equation 1, as the shear strain induced by ASR would increase as the difference between the starting and final thicknesses became progressively greater. It has been shown that ASR improves the microstructural homogeneity of AA6061 [110].

Qualitative assessment of EBSD maps implied that the specimen rolled through 2 passes contained a reduced concentration of LAGBs. This observation was then substantiated quantitatively by the mis-orientation data shown in Figure 3-8. These data indicated that the specimen rolled through 2 passes contained 58% LAGBs, whereas this increased to 80% in the 16 pass product. For the sample rolled through 2 passes, the pole figures indicated that a {111}<112> shear texture component was apparent (Figure 3-6). This type of texture found in the sample rolled through two passes would have contributed to higher strengths impacted to this specimen compared to the 16 pass rolled counterpart. The presence of a relatively large amount of HAGBs in highly deformed aluminum alloys have been reported by other researchers [107][111][112].

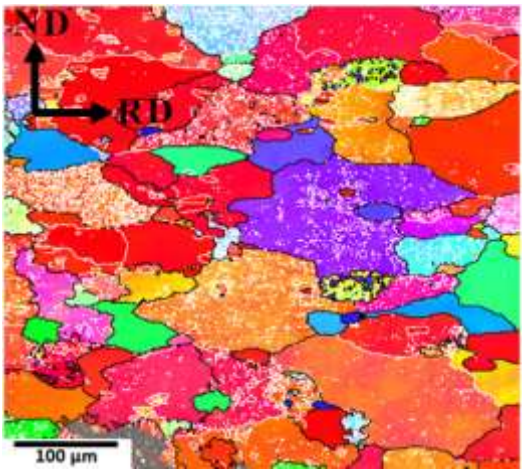

(a)

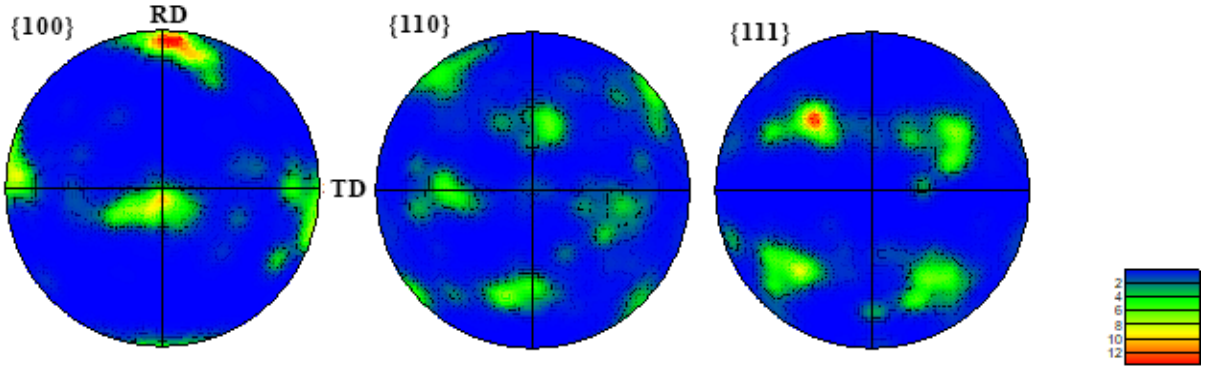

(b)

Figure 3-5 EBSD map acquired from the (a) base metal and (b) pole figures.

Per the EBSD map shown in (Figure 3-5a), the starting parent metal was almost completely devoid of sub-grains (i.e. LAGBs). ASR would have introduced a high density of dislocations into this material due to shear deformation. However, a certain level of energy would have also been required to rearrange these dislocations into sub-grains; in particular, those with a polygonal shape. Although the specimens were all rolled at ambient temperature, it was obvious that the specimen rolled through 2 passes had a partially polygonised substructure. Here, the sub-grains appeared cellular and were

larger in size compared to the specimen rolled through 16 passes. The pole figures presented in Figure 3-7 for the sample rolled through 16 passes revealed a Goss texture {110}<001>. Here, it is known that shear deformations comparable to those experienced in ASR can result in the formation of low and high angle grain boundaries through continuous dynamic recrystallization [113]. Hence, it was postulated that the exceptionally severe strain generated during 2 pass ASR was sufficient to bring about this phenomenon to thereby instill coarser, cellular sub-grains and a higher fraction of HAGBs in the finished product.

A recent study by Nakai et al has shown that the YS of AA6061 was influenced by sub-grains and that coarser sub-grains were more effective in promoting gains in YS [114]. The flow behavior of alloys is commonly described by the Holloman equation [115]:

$$\sigma = K\varepsilon^n \qquad (2)$$

where n is the strain hardening exponent, K is the strength coefficient, σ is the true stress and ε is the true strain. The value of n is indicative of the extent to which the material can deform prior to necking. Essentially, a high value of n indicates that the material can deform appreciably before plastic instability. In Figure 3-4d, the strain hardening exponent increased marginally from 0.18 at 2 passes to 0.23 where it remained constant through 4 and 8 passes before declining to 0.15 at 16 passes. In certain instances, aluminum alloys undergo dynamic recovery to produce sub-grains (LAGBs). It is known that this lowers the work hardening rate, and in turn, the strain hardening exponent [116]. Observation of EBSD data acquired from 2 pass and 16 pass specimens (Figure 3-6, Figure 3-7 and Figure 3-8) suggested that a greater extent of dynamic recovery had in fact prevailed in the latter specimen. Hence, the measured difference in the concentration

of LAGBs (Figure 3-8) for the 16 pass specimen was likely responsible for the lower strain hardening exponent.

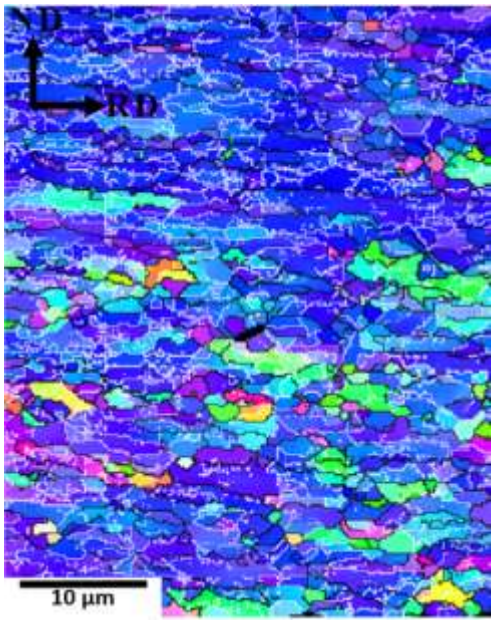

(a)

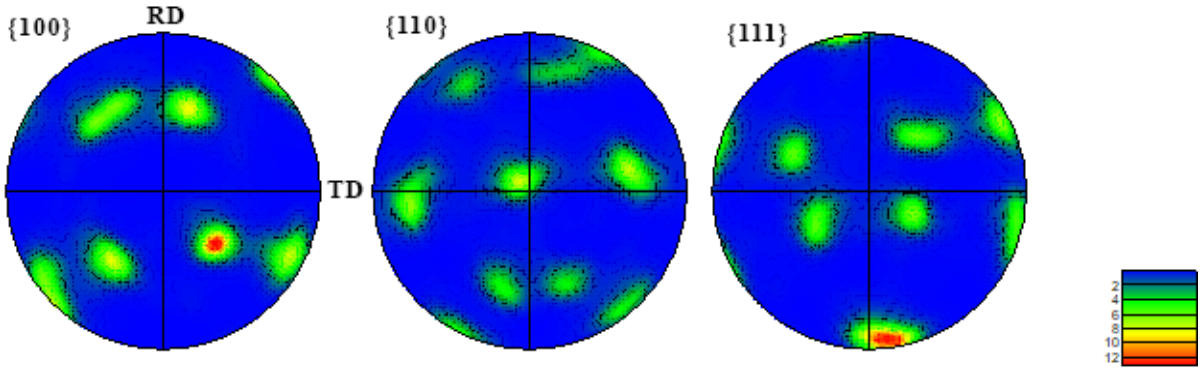

(b)

Figure 3-6 EBSD map acquired from ASR specimen rolled through (a) 2 passes and (b) pole figures.

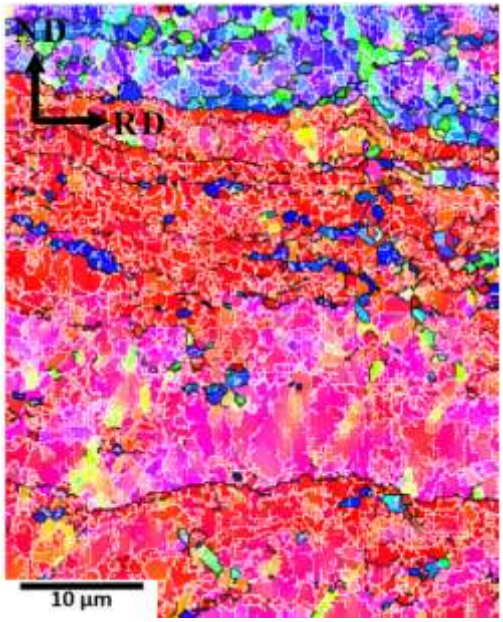

(a)

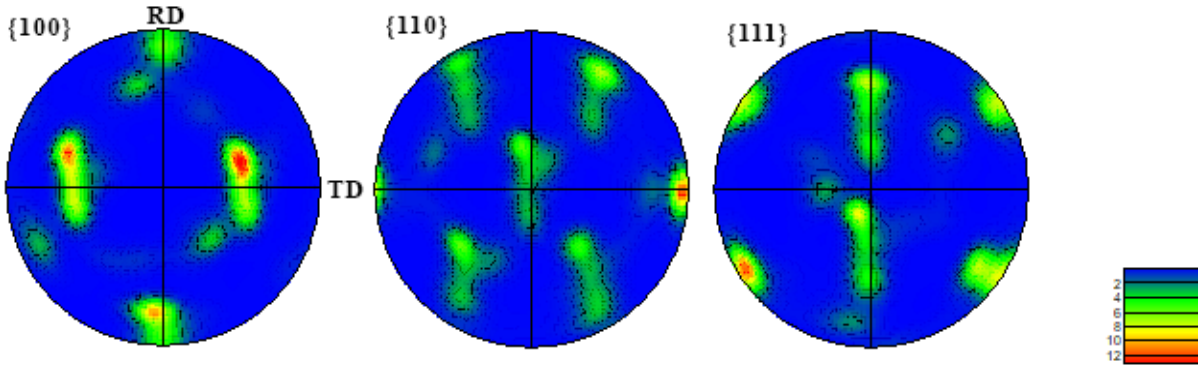

(b)

Figure 3-7 EBSD map acquired from ASR specimen rolled through (a) 16 passes and (b) pole figures.

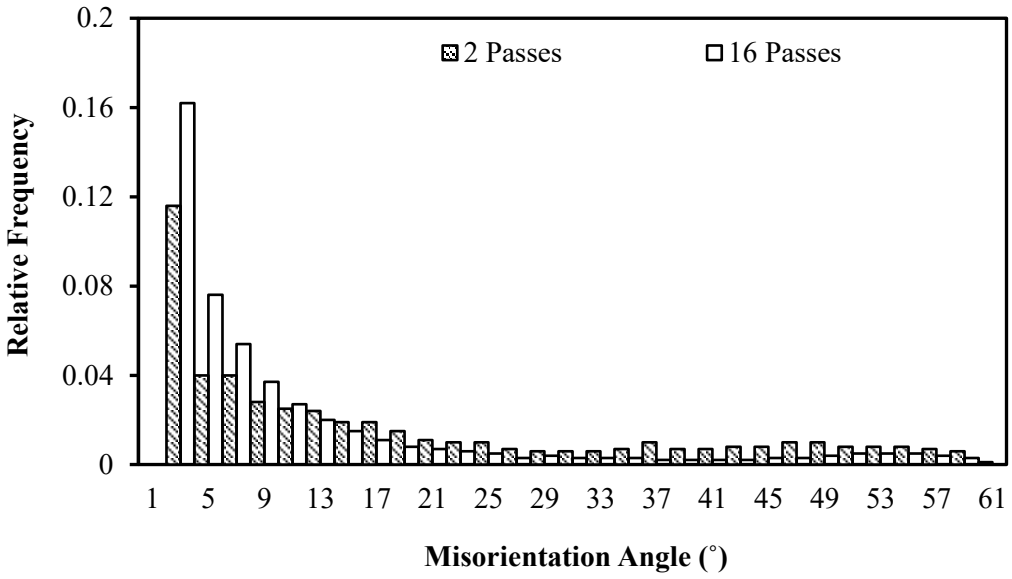

(a)

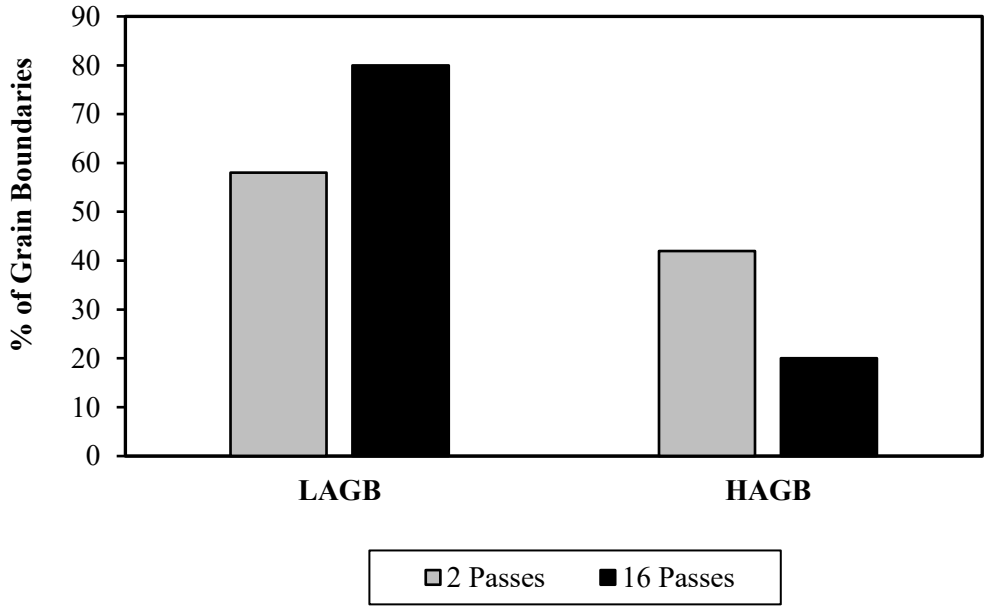

(b)

Figure 3-8 Quantitative assessments of the grain boundary mis-orientation angles in specimens that were rolled to 80% reduction via ASR in either 2 or 16 passes. (a) frequency distribution plot of mis-orientation angles and (b) nominal fractions of HAGBs and LAGBs.

3.3.5 EFFECTS OF VELOCITY RATIO

The final variable considered was velocity ratio (VR). In doing so, the top roller velocity was fixed at 24 rpm while that of the bottom roller was adjusted to obtain VR values of 1.0, 1.2, 1.4, 1.6, 1.8, 2.0 and 2.2. Accordingly, the symmetrically rolled specimen was that rolled with a VR of 1. It was observed that the YS exhibited a modest upward trend increasing from 224 MPa for symmetrical rolling up to a final value of 239 MPa when the most intense ASR was applied with a VR of 2.2 (Figure 3-9). UTS data followed a similar trend although the net transition was modestly larger (240MPa to 275MPa) and amounted to a gain of ~10% for the ASR process. Ductilities and strain hardening exponents failed to show discernable trends that correlated to VR. However, hardness data revealed a more succinct upward trend with increasing VR favoring the use of ASR. Despite this trend, it should be noted that the differences in hardness were marginal. Presumably, this observation may be attributable to the larger plastic strain induced in the material as the VR was increased.

EBSD was completed on specimens rolled with VR values at the extremities of the range considered (1.0 and 2.2) as shown in Figure 3-10 and Figure 3-11. The microstructure of the specimen processed with a VR of 1.0 was dominated by LAGBs. This was also observed in a study where pure aluminum was processed in a similar manner [66]. According to equation 1, the shear strain imposed on an asymmetrically rolled material is influenced by the VR starting at zero for symmetrical rolling and then increasing with a rising VR. The texture information collected from the sample rolled symmetrically

indicated that the texture induced here was a {110}<211> brass texture component (Figure 3-10).

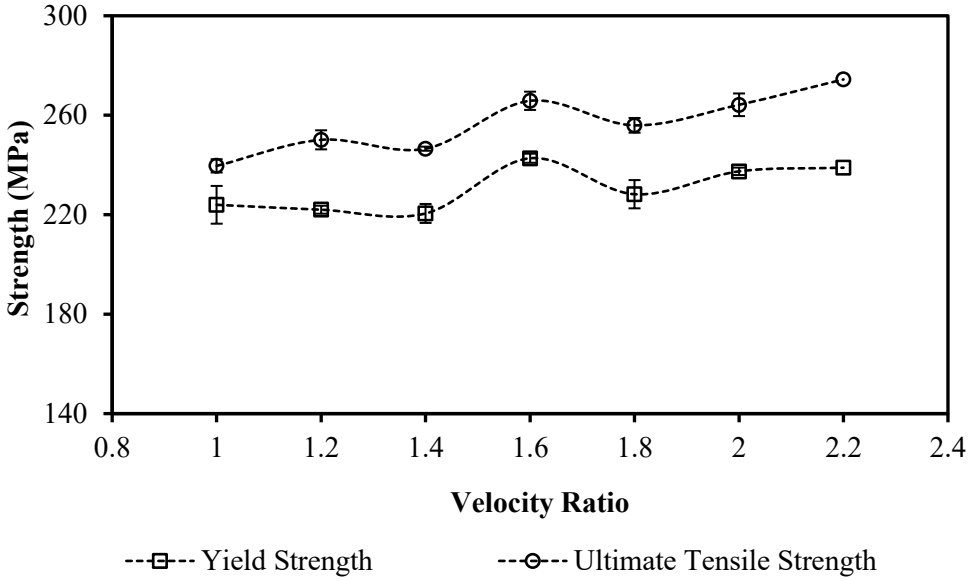

(a)

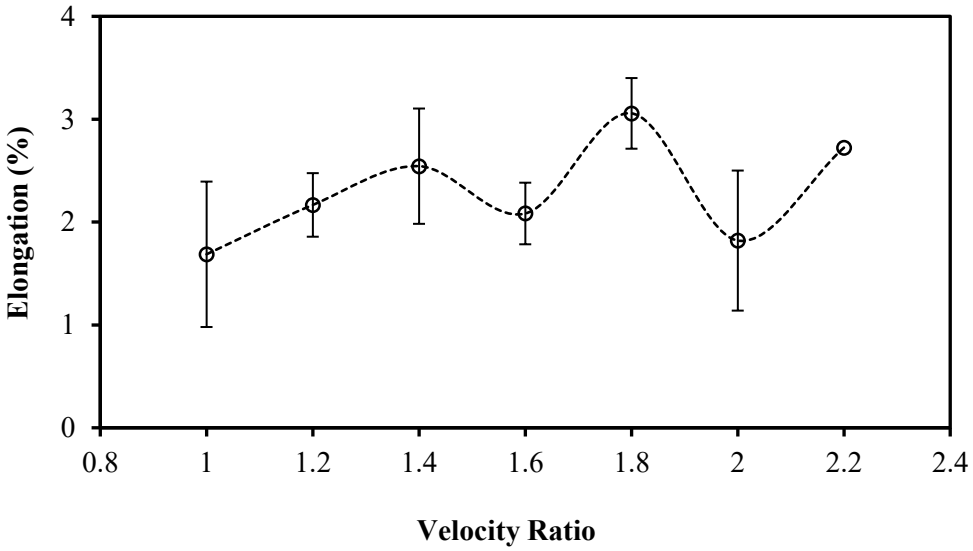

(b)

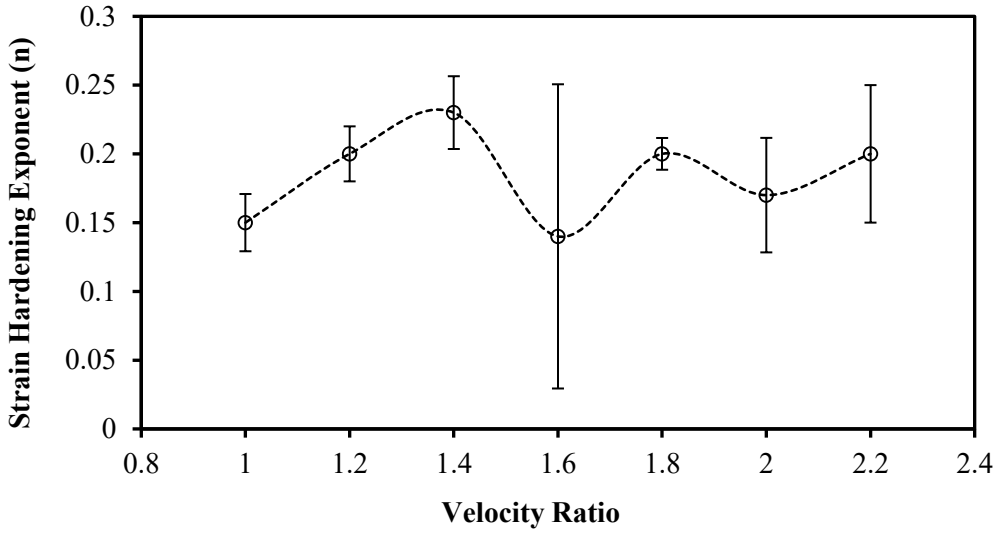

(c)

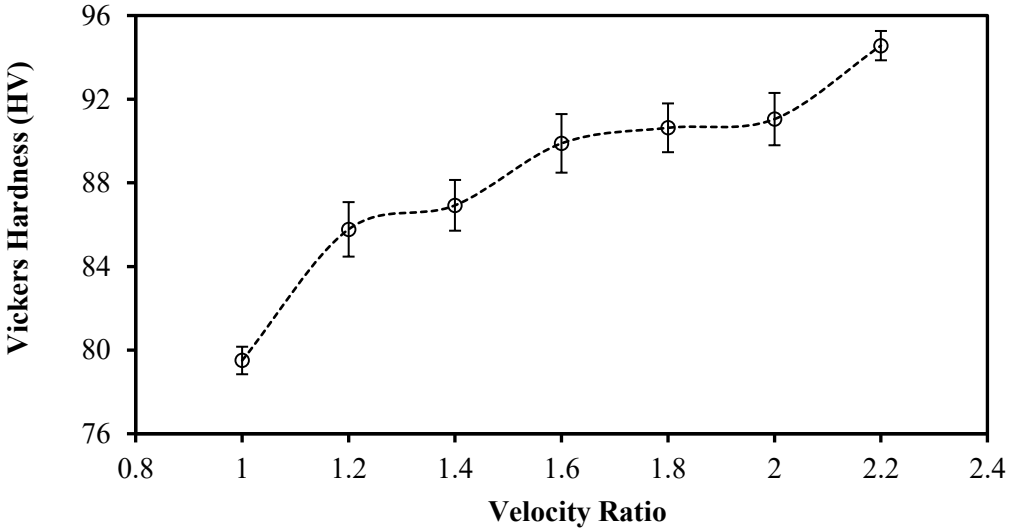

(d)

Figure 3-9 Comparison of the mechanical properties of AA6061 rolled with different velocity ratios (a) yield strength and tensile strength, (b) elongation to failure, (c) strain hardening exponent, and (d) hardness.

On the other hand, the sample rolled asymmetrically with a velocity ratio of 2.2 exhibited a texture similitude to a {111}<110> shear texture component Figure 3-11. In addition, the subgrain structure appeared coarser in the specimen rolled with a velocity ratio of 2.2 compared to its symmetrically rolled counterpart. As indicated earlier, the coarser subgrain structure offers a greater resistance to dislocation movement than recrystallized grains. The tensile properties also revealed that VRs below 1.6, may not have sufficiently invoked shear strains that would have produced yield strengths that surpassed the YS of the symmetrically rolled specimen. Hence, the higher gains in YS measured for the specimens rolled with VRs equal to and greater than 1.6. Notably, gains of about 7% and 12% were realized in yield and tensile strengths respectively for the asymmetrically deformed specimen with VR=2.2 compared to the symmetrically rolled one. Ultimately, ASR was beneficial in improving the mechanical properties compared to conventional symmetric rolling.

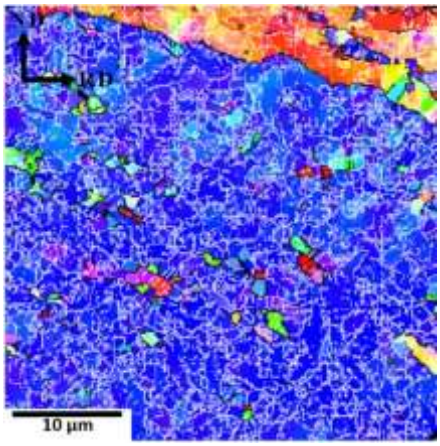

(a)

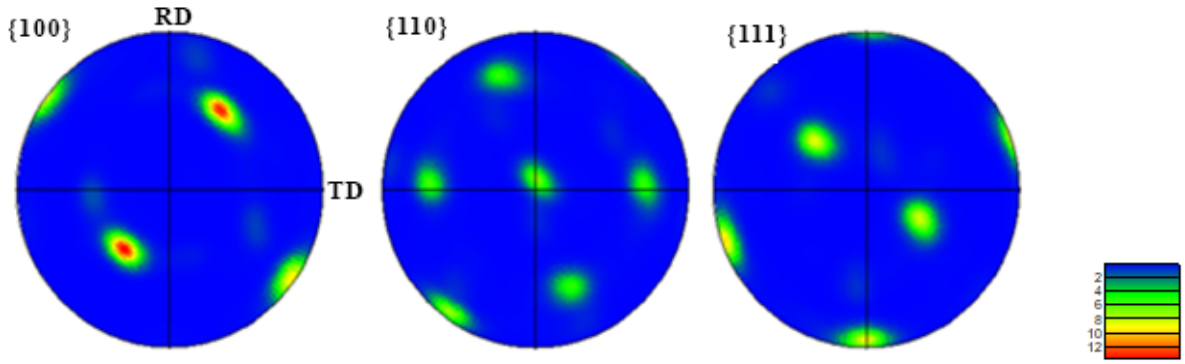

(b)

Figure 3-10 EBSD map acquired from sample rolled with a VR of (a) 1 (symmetric) and (b) pole figure.

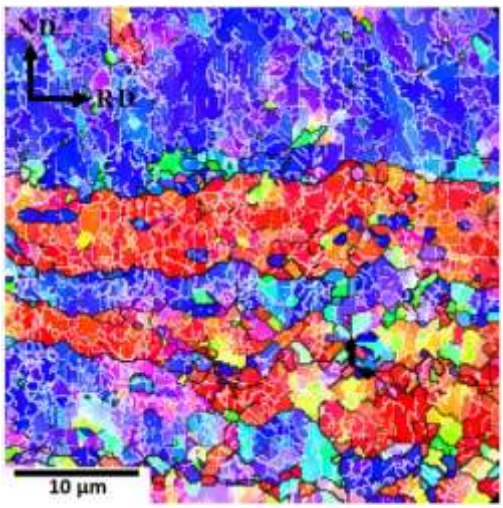

(a)

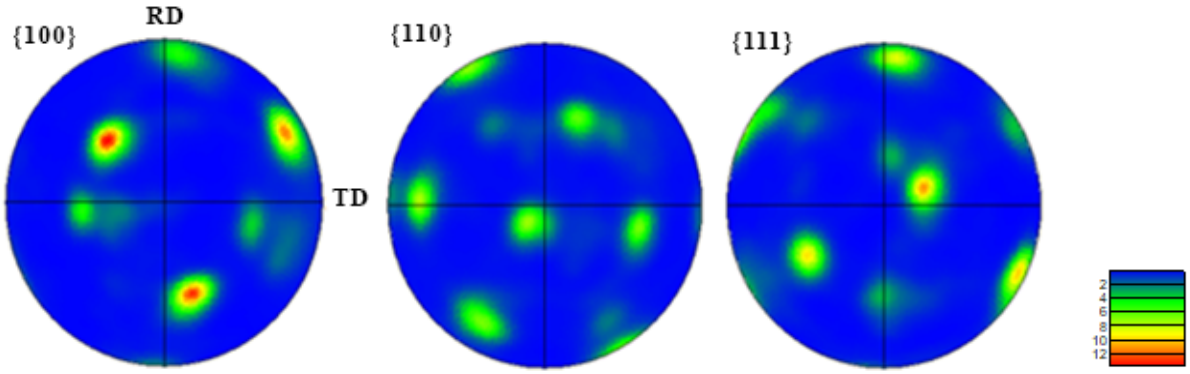

(b)

Figure 3-11 EBSD map acquired from sample rolled with a VR of (a) 2.2 (asymmetric) and (b) pole figures.

3.4 CONCLUSIONS

From the work completed in this study the following conclusions have been reached:

1. It was found that decreasing the starting thickness increased the tensile strength of AA6061 presumably due to higher shear strains induced in the material with the smaller initial thickness.
2. Changes to roller velocities and rolling direction did not impart any significant gains in the mechanical properties of AA6061, although increases in the velocity ratio and the number of passes during rolling yielded improvements.
3. ASR produced superior mechanical properties in AA6061 than symmetric rolling. The highest mechanical properties were exhibited by specimens rolled with the highest velocity ratio (2.2).
4. EBSD analyses revealed that the microstructure was more homogeneous in the specimen rolled through 2 passes compared to the 16 pass counterpart. This implied that homogeneity in the microstructure was attained more effectively by decreasing the number of passes during ASR.

Acknowledgements

The authors would like to graciously acknowledge the financial support provided by Boeing Research and Technology (research contract 11-6392), the Natural Sciences and Engineering Research Council of Canada (NSERC) via collaborative research and development grant #451466 and GKN Sinter Metals. Laboratory assistance provided by Mr.Randy Cooke, Mrs. Patricia Scallion, and Mr. Dean Grijm at Dalhousie University is gratefully acknowledged as well.

CHAPTER 4 PROCESSING OF A TERNARY AL-SC-ZR POWDER METALLURGY ALLOY VIA SPARK PLASMA SINTERING AND HOT ASYMMETRIC ROLLING

M.Y. AMAGADZIE[1], I.W. DONALDSON[3], AND D.P. BISHOP[2]

1 – Graduate Student, Dalhousie University, Halifax, Nova Scotia, Canada
2 – Professor, Materials Engineering, Dalhousie University, Halifax, Nova Scotia, Canada
3 – Director of R&D North America, GKN Sinter Metals LLC, Auburn Hills, Michigan, USA

Status: Published Book Chapter in "Spark Plasma Sintering of Materials: Advances in processing and applications". Springer. (2019). Pages 219 – 237.

Author Contribution: All experimental work was completed by Mark Y. Amegadzie with the exception of TEM work done by Abdul Khan at the University of Manitoba. The first draft of this paper was written by Mark Y. Amegadzie. Supervision was provided by D. Paul Bishop. Technical guidance and subsequent editing of the paper were performed by all the affiliate authors.

4.1 ABSTRACT

The addition of scandium as the primary alloying element to aluminum alloys has made them useful for aeronautical and automotive industrial applications due to their low inherent density and thermal stability. In the present work, a powder metallurgy approach premised on spark plasma sintering coupled with asymmetric rolling was considered as a means of processing an Al-Sc-Zr alloy. Increasing SPS temperatures were found to promote progressively greater extents of precipitate coarsening coupled with a reduction in strength yet an improvement in ductility. The application of asymmetric rolling

improved the properties of all as-sintered products significantly and was particularly beneficial at the lower range of hot rolling temperatures considered. TEM analyses revealed that rolling temperature had negligible effects on the coarsening behavior of pre-existing $Al_3(Sc,Zr)$ precipitates in the sintered product while EBSD studies implied that subgrain strengthening was the primary mechanism underpinning the superior tensile properties measured in the rolled products.

4.2 INTRODUCTION

Aluminum powder metallurgy (PM) is a net-shape metal forming technology in which metallic powders are converted into engineered products with tight dimensional tolerances. This manufacturing process offers advantages such as the capacity for high-volume production, ability to fabricate light weight products, favorable process economics, as well as the efficient use of energy and raw materials. The automotive industry has been particularly receptive to this process as it has been implemented in the fabrication of a growing list of structural parts for this sector dating back to 1992 [117]. Exemplary parts fabricated through aluminum PM have included shock absorber parts, piston rods, gears, oil pump rotors, cam-shaft bearing caps, and more recently, transmission components such as an award-winning planetary reaction carrier.

The core consolidation phases of the process are die compaction followed by liquid phase sintering. Combined, these steps aim to convert the raw powder into a coherent product that offers a high level of metallurgical integrity and a shape approaching that of the intended component design. However, the surface film present on aluminum-based

powder particles poses certain technological challenges in this context. Studied by many authors, this feature has been frequently characterized as a hydrated film of Al_2O_3 that contains adsorbed molecules of H_2O [118] and CO_2. The alumina component exhibits a high thermodynamic stability that cannot be eliminated by conventional tactics such as gaseous reduction with hydrogen or carbon monoxide gas. Consequently, attempts to remediate this challenge have emphasized alternate practices including chemical modification with magnesium [119], degassing studies [120], as well as hot pressing in a vacuum atmosphere [121].

More recently, the technology of spark plasma sintering (SPS) has emerged as a new means to overcome the surface film constraint [122][56]. This process typically applies a high amperage DC current and uni-axial pressure simultaneously to compact and sinter the powder in a single operation [123]. Unlike conventional sintering, the SPS process affords rapid heating rates and reduced sintering temperatures that suppress microstructural coarsening. It has been demonstrated that the surface oxides at inter-particle contact points can be mitigated by SPS [122]. However, a semi-continuous network of residual oxides still prevails in the sintered product.

A residual oxide network is undesirable as it can be detrimental to mechanical properties; in particular, tensile ductility and dynamic properties such as fatigue. As such, it was hypothesized that if severe shear deformation was applied to an SPS product that this could physically disrupt the remnants of this feature and, in turn, improve mechanical properties. One means of deformation in this manner is asymmetric rolling (ASR). In

this practice, the thickness of a bar is reduced by passing it through a pair of rollers with each run at a different rotational speed [64][66]. This is known to induce exceptionally high levels of shear stress within the material which could present an effective means to fracture and distribute residual oxides within the final product. As such, ASR was applied to SPS-consolidated preforms made from a prealloyed aluminum powder (Al-0.3Sc-0.2Zr in wt%) in this study in an effort to gather some preliminary data on this concept.

4.3 MATERIALS

The raw powder utilized in this study was manufactured via nitrogen gas atomization at Kymera International in Germany. The morphology of the powder was mainly spherical (Figure 4-1) and had a D_{50} of 75µm as measured through laser scattering (Figure 4-2). Inductively Coupled Plasma Spectroscopy was used to determine the chemical composition of the powder as shown in Table 4-1. This confirmed that the powder was in reasonable agreement with the nominal target of Al-0.3Sc-0.2Zr (weight %); a chemistry of Al-0.2Sc-0.05Zr in atomic %. Trace concentrations of iron, silicon, and magnesium were also detected.

Figure 4-1 SEM image of Al-0.3Sc-0.2Zr gas atomized powder.

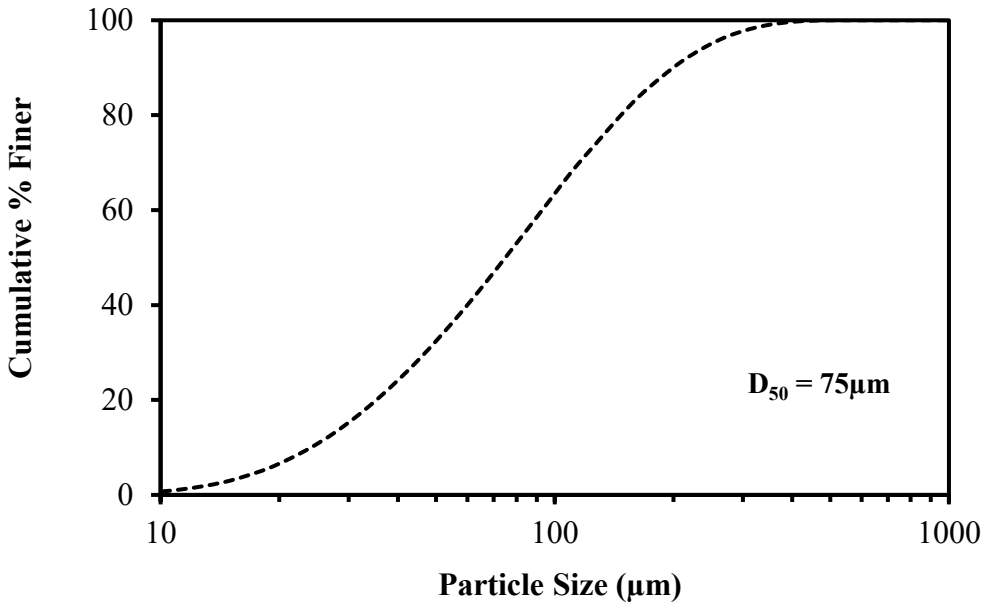

Figure 4-2 Particle size distribution of the Al-0.3Sc-0.2Zr powder.

Table 4-1 Measured assay (weight%) of the starting prealloyed powder.

	Composition (weight %)					
	Sc	**Zr**	**Fe**	**Si**	**Mg**	**Al**
Nominal Target	0.30	0.20	---	---	---	Bal.
Measured	0.33	0.17	0.08	0.02	0.01	Bal.

4.4 EXPERIMENTAL PROCEDURES

The as-received powder was spark plasma sintered in a SPS Model 10-3 unit manufactured by Thermal Technologies Inc. operated with pulsed DC current. Specimens were processed in a graphite tool set; at the start of each run, the die was lined with a new sheet of graphite foil. The thermal cycle involved heating the powder to the set temperature (500ºC, 550ºC or 600ºC) at 50K/min under a mechanical vacuum atmosphere and an applied pressure of 5MPa. Samples were then isothermally held at temperature for 120 seconds before pressure was ramped to 50MPa. Once the maximum pressure was reached, each sample was cooled to room temperature, de-pressurized, and removed from the furnace. The resultant product was a cylindrical puck 40mm in diameter and 7mm in height. All sintered specimens were ground slightly to remove any remnants of the graphite foil. Sintered densities were measured using Archimedes principle coupled with vacuum assisted infiltration in accordance with MPIF standard 42. Rectangular bars with dimensions 31.7 mm X 12.7 mm x 6.4 mm were machined from sintered pucks, pre-heated for 20 minutes, and then asymmetrically rolled in a Reusch rolling mill manufactured by International Rolling Mills, USA. Pre-heat temperatures of 200ºC, 300ºC, 400ºC and 500ºC were considered. Each specimen was subjected to two rolling

passes and was rotated by 180º about the rolling direction between passes. The net thickness reduction achieved after rolling was approximately 80%.

Tensile specimens were machined from the rolled bars and tested with an Instron Satec model 5594 200HVL hydraulic load frame equipped with a 50kN load cell, wedge grips and an Epislon model 3542 extensometer which remained affixed to the specimen through to fracture. Hardness measurements were made using a LECO Vickers Hardness Testing Machine operated with an applied load of 10kg. Average hardness readings were determined from a minimum of 5 measurements. Microstructural characterization included optical microscopy (OM), electron backscatter diffraction (EBSD) and transmission electron microscopy (TEM). For OM/EBSD work, cross sections of the material in question were mounted using a Struers CitoPress-5 automatic mounting press. Mounts were then loaded in a Struers Tegramin autopolisher, planed with a 1200 grit silicon carbide disc and subsequently polished in stages using cloth pads and diamond suspensions from 15, 3 and 1 μm, before finishing with 0.05 μm colloidal silica suspension. EBSD studies employed a Hitachi S-4700 Cold Field Emission Scanning Electron Microscope (SEM) equipped with a HKL system and Nordlys Oxford Instruments detector. Sections of samples for TEM analysis were first thinned to ~100 microns using a 400 grit sandpaper. This was followed by using a puncher to make 3mm disks prior to dimpling. Finally, the foils were electropolished using a Tenupol 3 Twin Jet Polisher in a solution comprising of 90% methyl alcohol and 10% perchloric acid at a temperature of -30ºC. TEM studies were completed with a FEI Talos F200X system operated at 200KV.

4.5 RESULTS AND DISCUSSION

4.5.1 METALLURGICAL ATTRIBUTES OF SPS PROCESSED SPECIMENS

The as-received powder was first processed via SPS at temperatures of 500ºC, 550ºC and 600ºC. Representative micrographs of the as-sintered microstructures are shown in Figure 4-3. At the lowest temperature the general quality of sinter was reasonable as inter-particle bonding had transpired and the level of residual porosity was moderate. Both traits improved with further increases in SPS temperature. The specimen sintered at the highest temperature considered appeared to be fully dense and the prior particle boundaries were less visible thereby implying a more acute level of inter-particle bonding. The visual trend in densification agreed with bulk density measurements (Figure 4-4). In this sense, the densities of all specimens were relatively high while those sintered at 550ºC and 600ºC were effectively fully dense.

EBSD was employed to better understand the evolution of the microstructure. Figure 4-5 shows EBSD maps of as-sintered specimens processed at the lowest and highest temperatures investigated. The black and white lines represent grain boundaries with mis-orientation angles >15º and <15º respectively. The former are referred to as high angle grain boundaries (HAGBs) while the latter as low angle grain boundaries (LAGBs) or subgrains. EBSD confirmed that both materials were largely comprised of equiaxed grains that spanned a comparable range of grain sizes. The average grain size in each case was found to be ~11µm. Interestingly, the use of progressively higher SPS temperatures did not appear to invoke any obvious coarsening of the grains. This was potentially attributable to the presence of the $Al_3(Sc,Zr)$ phase which effectively pins

grain boundaries [124]. This was consistent with optical images as no obvious differences in the extent of grain coarsening were observed. Quantitative analyses revealed that in both specimens an equivalent ratio of HAGB:LABG prevailed (Figure 4-6). Hence, the general nature of grain boundaries in the specimens were also unaffected by differences in SPS temperature.

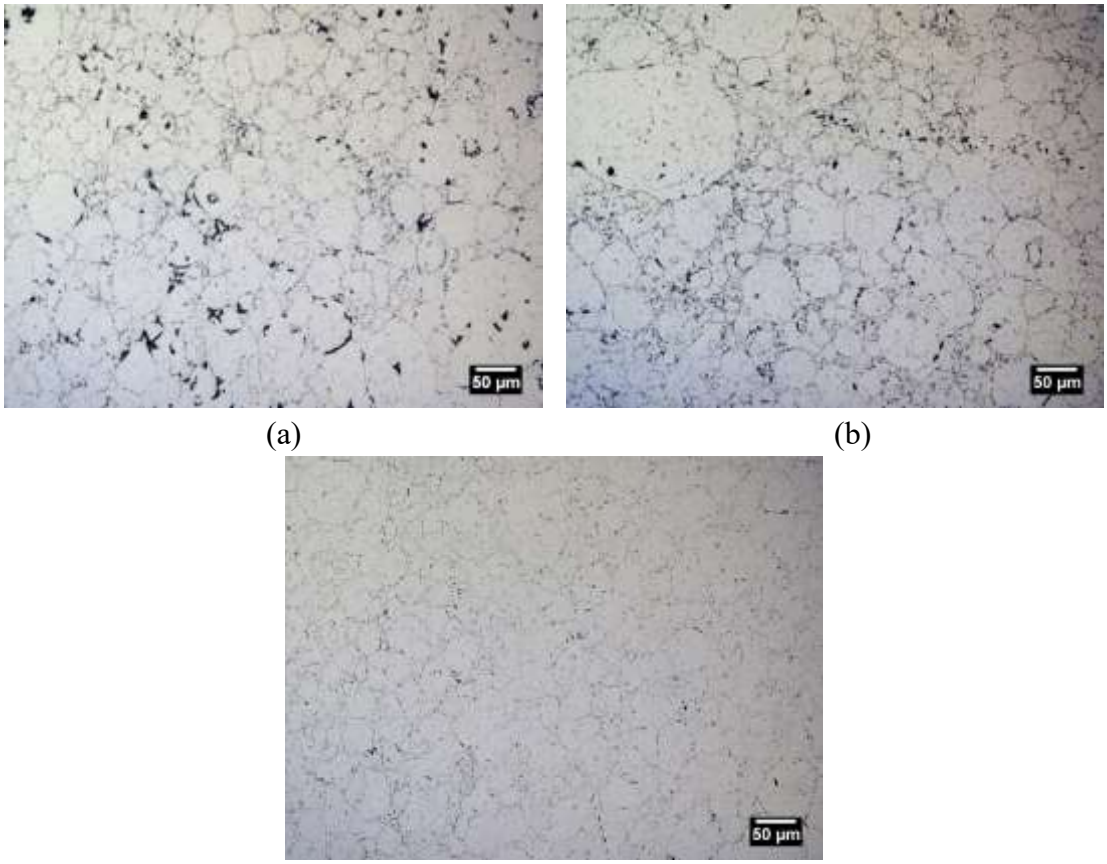

(a) (b)

(c)

Figure 4-3 Optical micrographs of specimens SPS processed at (a) 500˚C (b) 550˚C and (c) 600˚C.

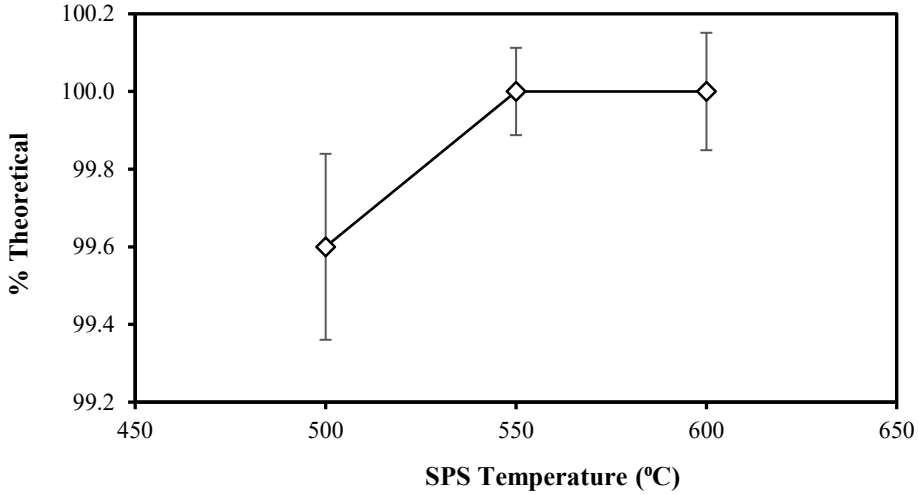

Figure 4-4 Final product density as a function of sintering temperature.

Next, tensile properties of the as-sintered products were assessed (Figure 4-7). Here it was noted that the yield strength decreased with increasing sintering temperature. This attribute declined by 16% as SPS temperature was raised from 500ºC to 550ºC. The loss then increased to 35% when a SPS processing temperature of 600ºC was employed. The ultimate tensile strengths declined in a comparable fashion although the extent of the transition was less acute. In contrast, the ductility improved with increasing SPS temperature from a starting value of ~1% to nearly 16% when sintered at 600°C. Akin to yield strength and UTS, the hardness data presented in Figure 8 also demonstrated a downward trend with increasing SPS temperature.

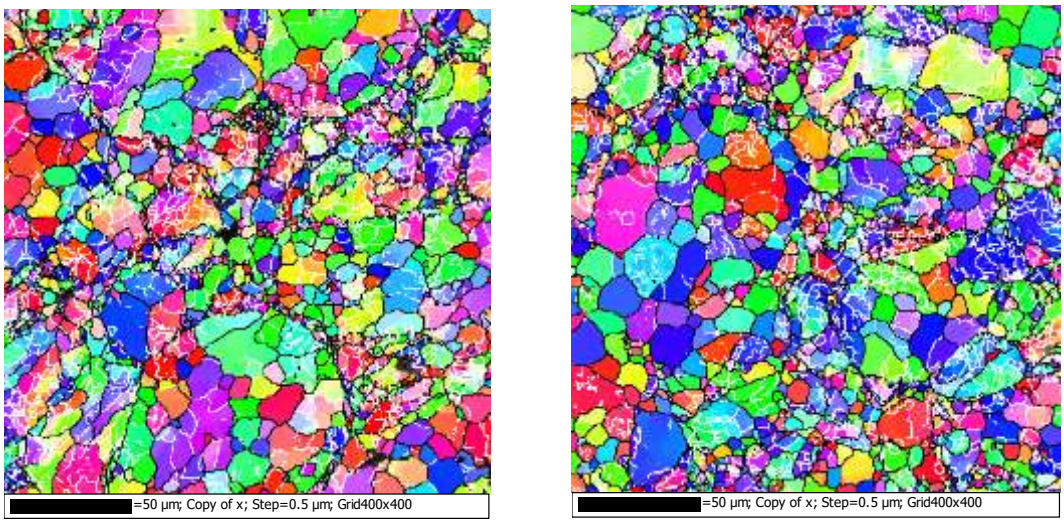

(a) (b)

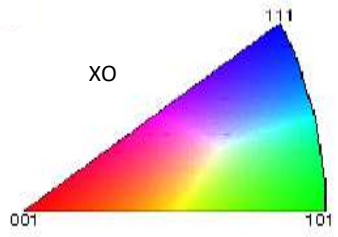

(c)

Figure 4-5 EBSD results for specimens SPS processed at (a) 500˚C and (b) 600˚C. (c) corresponding inverse pole figure indicating crystallographic directions with respect to the horizontal direction of the maps. Black lines indicate HAGBs; white lines LAGBs.

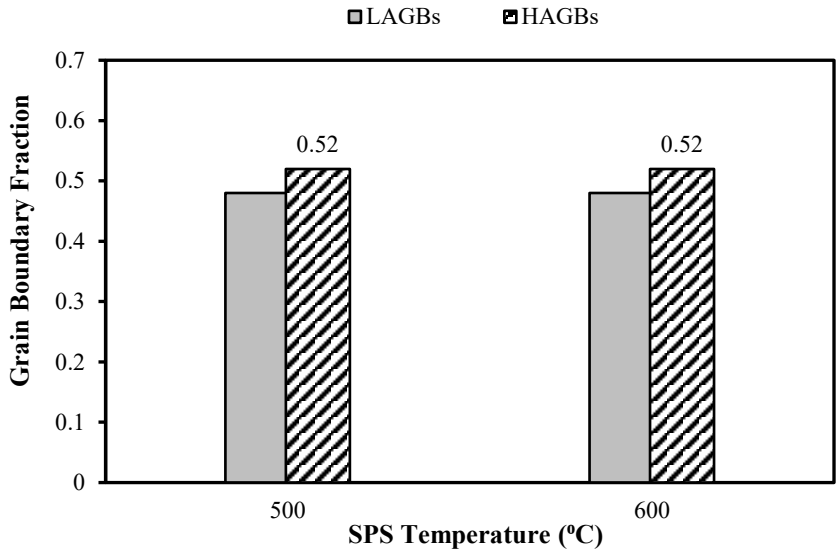

Figure 4-6 Fractions of LAGBs and HAGBs in samples SPS processed at 500˚C and 600˚C.

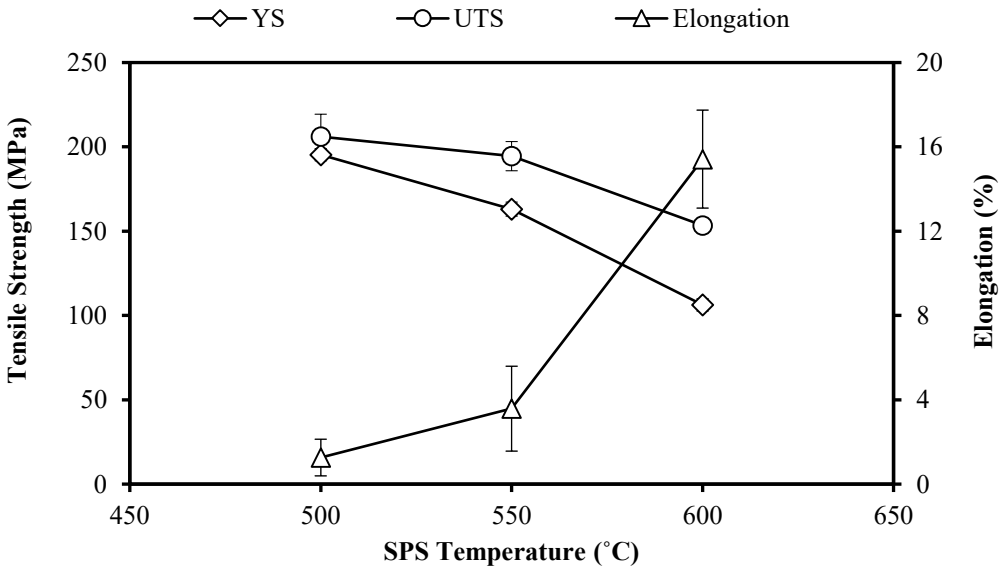

Figure 4-7 Tensile properties of SPS processed specimens consolidated at 500˚C, 550˚C and 600˚C.

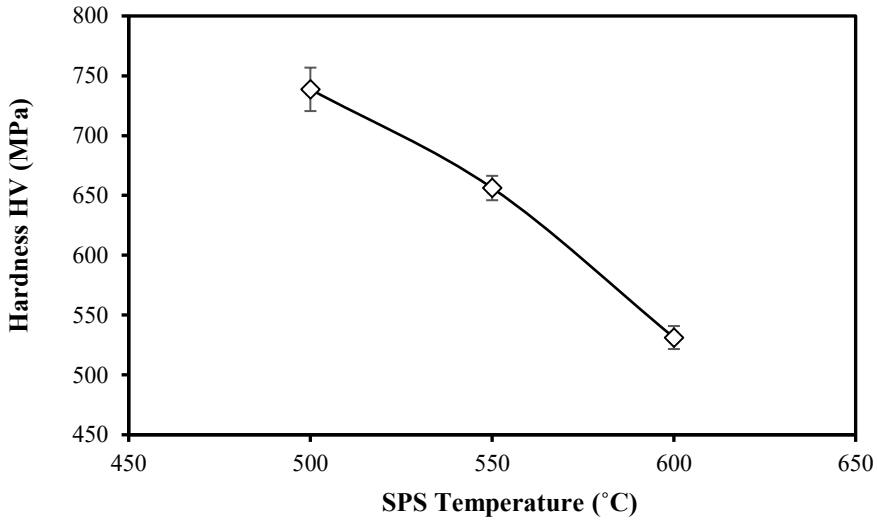

Figure 4-8 Comparison of the hardness of sintered preforms at temperatures of 500˚C, 550˚C and 600˚C.

Data in Figures 4-3 and 4-5 confirmed that fundamental changes to the underlying grain structure which could potentially explain the noted transitions in hardness and tensile properties had not occurred. Conversely, gradual improvements in sinter quality (Figure 4-3) and density (Figure 4-4) had transpired that should have been influential. Gains in these traits would certainly be expected to improve tensile ductility but not diminish yield strength. Hence, TEM studies were completed to assess the presence and potential evolution of secondary phases that existed within the materials.

Bright field images (Figure 4-9 (a) and (b)) confirmed that a rather abundant secondary phase with a spherical morphology was homogenously distributed within samples sintered at the lowest and highest temperatures investigated. The phase appeared to remain coherent with the α-aluminum matrix in both instances as evident by coffee bean contrast [125]. Dark field images (Figure 4-9 (c) and (d)) confirmed that particles of the secondary phase had a diameter of ~4 to 10 nm in the specimen sintered at 500ºC but had

grown to a size of ~20 to 35 nm when SPS was completed at 600ºC. Selected area diffraction patterns recorded near the <100> zone axis are shown in Figure 4-9 (e) and (f). Both patterns were comprised of bright reflection spots from the FCC α-aluminum matrix coupled with an identical array of super lattice reflections. The only noted difference was that the super lattice reflections were somewhat diffuse in the 500°C sample yet sharp and focused in the product consolidated at 600°C.

Collectively, TEM findings indicated that the secondary phase was most likely $L1_2$ precipitates of $Al_3(Sc,Zr)$ in both samples [126]. It is known that the $Al_3(Sc,Zr)$ phase can impart significant strengthening in Al-Sc-Zr alloy systems [126][127]. Furthermore, in precipitation hardened alloys, the size and distribution of the precipitates present typically underpins mechanical properties. In this sense, fine, coherent precipitates are generally synonymous with relatively high yield strength yet moderate tensile ductility. This situation then begins to reverse as the precipitates coarsen and concurrently, inter-particle spacing increases. TEM revealed that $Al_3(Sc,Zr)$ precipitates had clearly coarsened as the SPS temperature was increased from 500 to 600°C. Hence, the evolution of this phase was thereby viewed as the dominant contributor towards the noted transitions in tensile properties. It is also noteworthy that in a recent study coherent $Al_3(Sc,Zr)$ precipitates were found to hinder recrystallization [124]. It appeared that this beneficial effect had also transpired in the PM systems studied given that EBSD revealed a highly comparable grain structure devoid of excessive coarsening regardless of the sintering temperature employed.

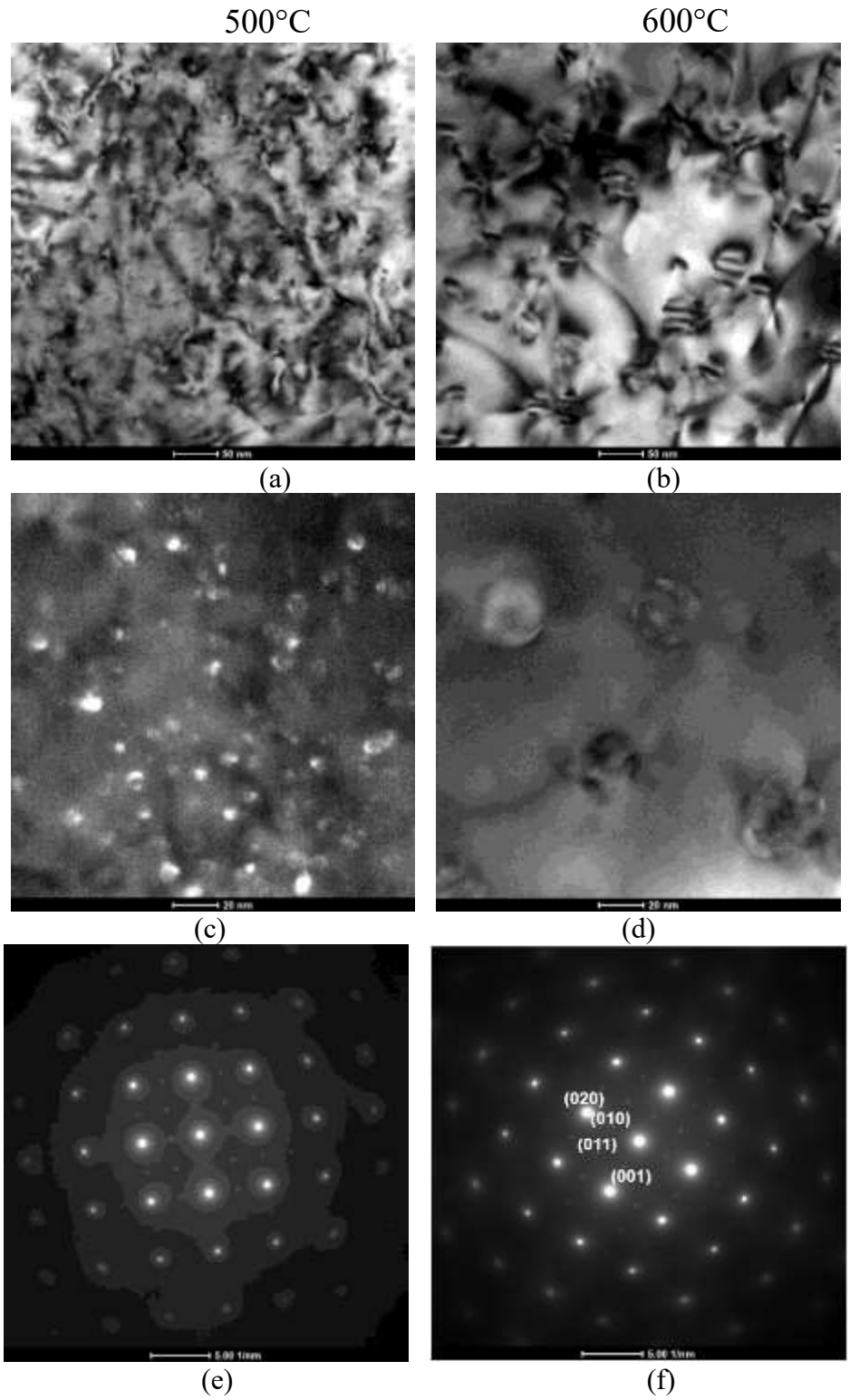

Figure 4-9 TEM results acquired from SPS specimens consolidated at 500ºC and 600ºC. Bright field images ((a) and (b)), dark field images ((c) and (d)), and selected area diffraction patterns recorded with the beam oriented closely parallel to the <100> zones axis ((e) and (f)).

In light of the measurable change in $Al_3(Sc,Zr)$ precipitate size and coherency, it would be expected that the yield strength of the material would decline as noted earlier. However, a transition in how such precipitates interact with dislocations was also anticipated - from precipitate shear to the Orowan bypass mechanism. The former is typically associated with a heightened yield strength and represent a scenario wherein dislocations slice through the small precipitates. Precipitate shearing is the dominant strengthening mechanism when precipitates are about 5nm or less [124]. Conversely, the latter is synonymous with an inferior yield strength but an enhanced capacity for strain hardening as dislocations cannot cut through the large precipitates but are forced to loop around them instead. Evidence of this phenomenon can be gleaned from stress-strain data as an increase in the strain hardening exponent (n). Data on this attribute are presented in Figure 4-10. This confirmed that a progressive and statistically relevant increase in the strain hardening exponent occurred with increasing SPS temperature.

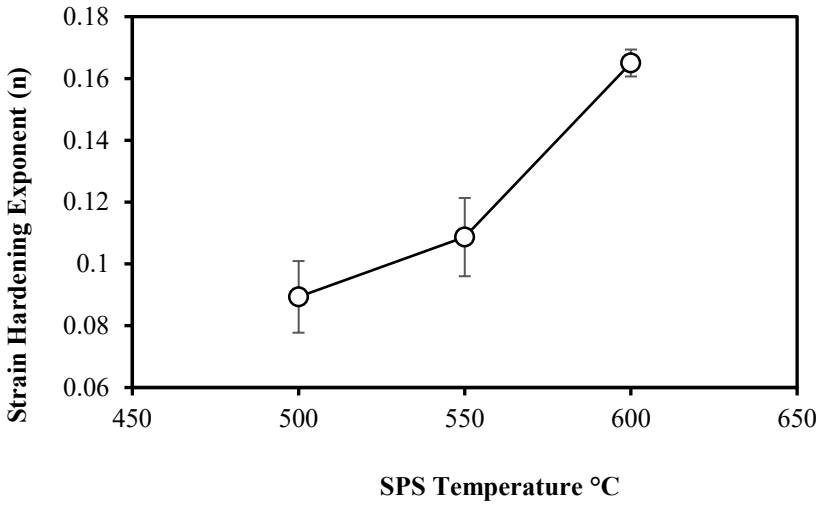

Figure 4-10 A plot of strain hardening exponent (*n*) measured for Al-0.3Sc-0.2Zr specimens consolidated at 500˚C, 550˚C and 600˚C.

4.5.2 EFFECTS OF HOT ASYMMETRIC ROLLING

After SPS, the sintered specimens were preheated to 200ºC, 300ºC, 400ºC and 500ºC in a furnace before ASR. The deformed microstructures are presented in the optical micrographs shown in Figure 4-11. In all instances, the starting equiaxed grain structure (Figures 4-3 and 4-5) was heavily deformed and now elongated in the rolling direction. All rolled products were seemingly at full density, including the preform initially sintered at 500°C which contained a measurable fraction of residual porosity (Figure 4-4). This observation indicated that the ASR process was effective at eliminating this microstructural defect from the SPS products.

Data on the hardness of the rolled products are shown in Figure 4-13. Generally, hardness decreased with increasing ASR temperature except for the specimen sintered at 550ºC wherein hardness largely remained static. Relative to their as-sintered counterparts (Figure 4-8), specimens subjected to ASR at 200ºC were found to incur the greatest gains in hardness. For example, in the material sintered at 600ºC, hardness increased from 531 to 684 HV because of ASR. Net improvements of 102HV and 68HV were noted for samples sintered at 500 and 550ºC respectively. When higher ASR temperatures were utilized the gains became less pronounced. Relative to their as-sintered counterparts, the hardness of the SPS 600ºC/ASR 500ºC sample was now only 88HV higher while that of the SPS 500ºC/ASR 500ºC sample was actually softer by 11HV.

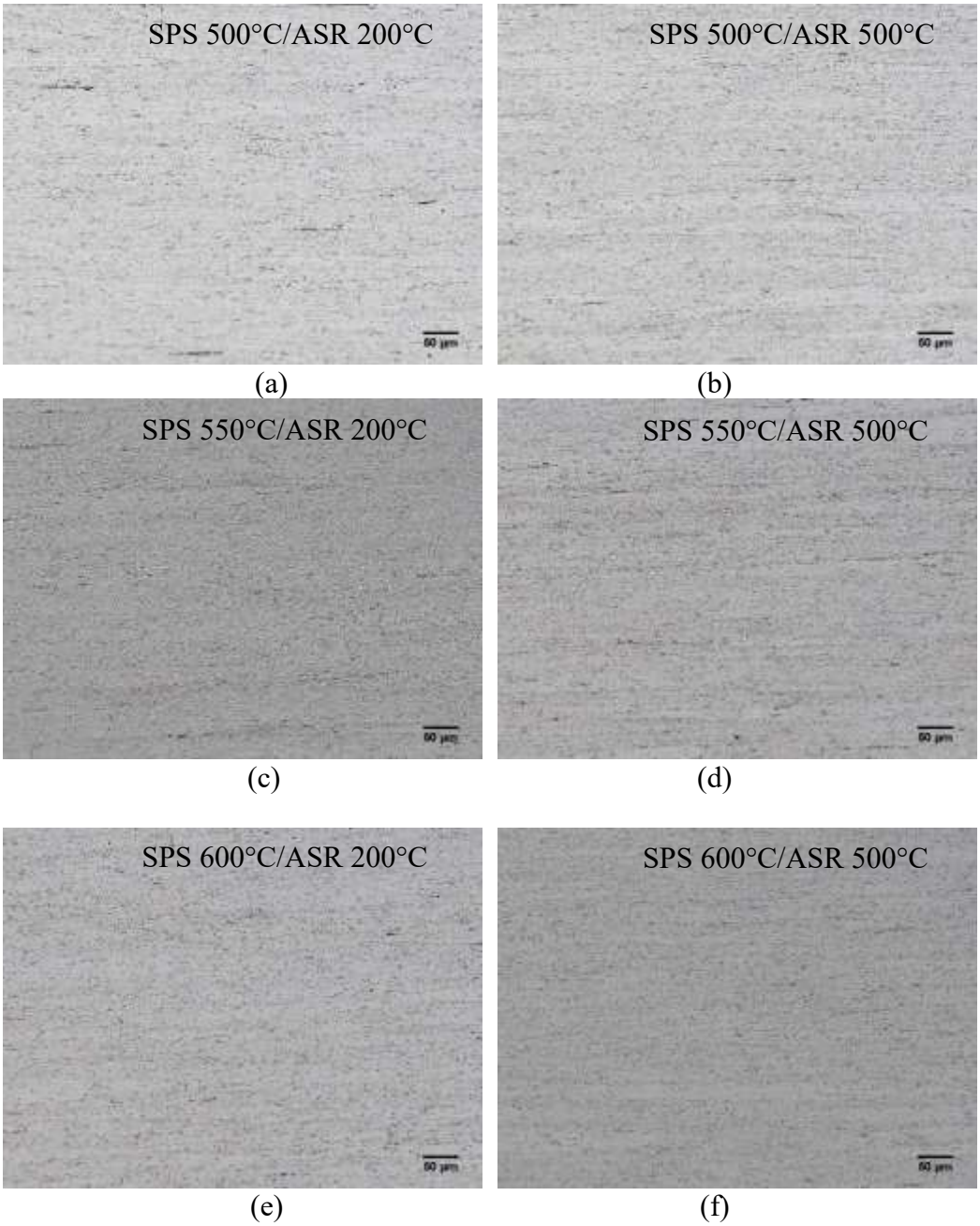

Figure 4-11 Optical micrographs of specimens processed through various combinations of SPS and ASR.

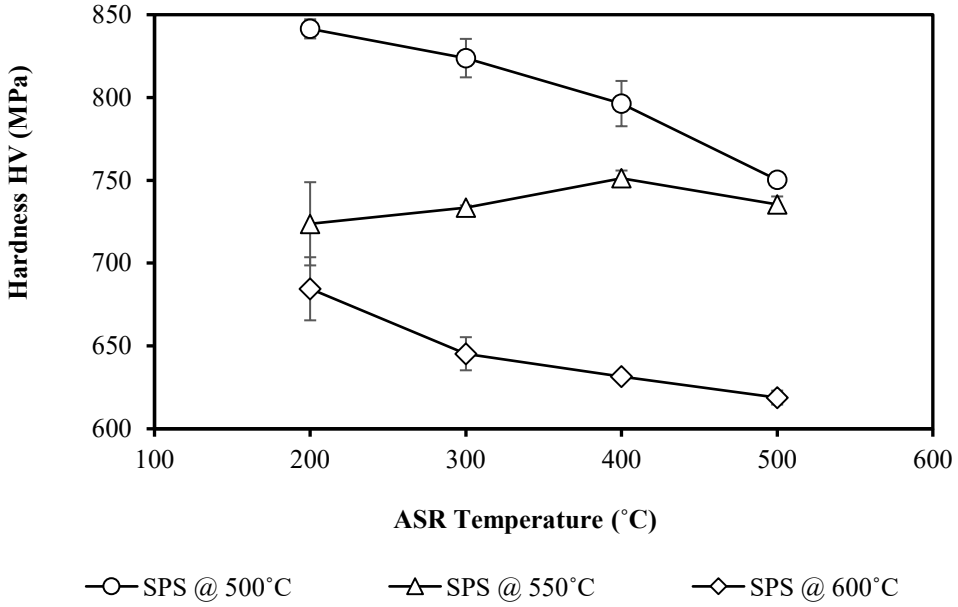

Figure 4-12 Comparison of the hardness of sintered preforms asymmetrically rolled at temperatures of 200˚C, 300˚C, 400˚C and 500˚C.

As shown in Figure 4-14 & Figure 4-15, the yield strength/UTS decreased subtly as the ASR temperature increased. Meanwhile, the percent elongation to failure increased considerably with increasing roll temperature except for the preform sintered at 600ºC which recorded ~4% ductility at 200ºC and then remained stagnant at 6% from 300ºC to 500ºC (Figure 4-16). The preform sintered/rolled at 500ºC /200ºC had out-performed the other preforms sintered at 550 and 600ºC and then rolled at 200ºC by exhibiting a nominal yield strength of 241MP compared to values of 216MPa and 178MPa respectively. These results implied that the preform sintered at 500ºC was more responsive to hot ASR than those sintered at 550ºC and 600ºC.

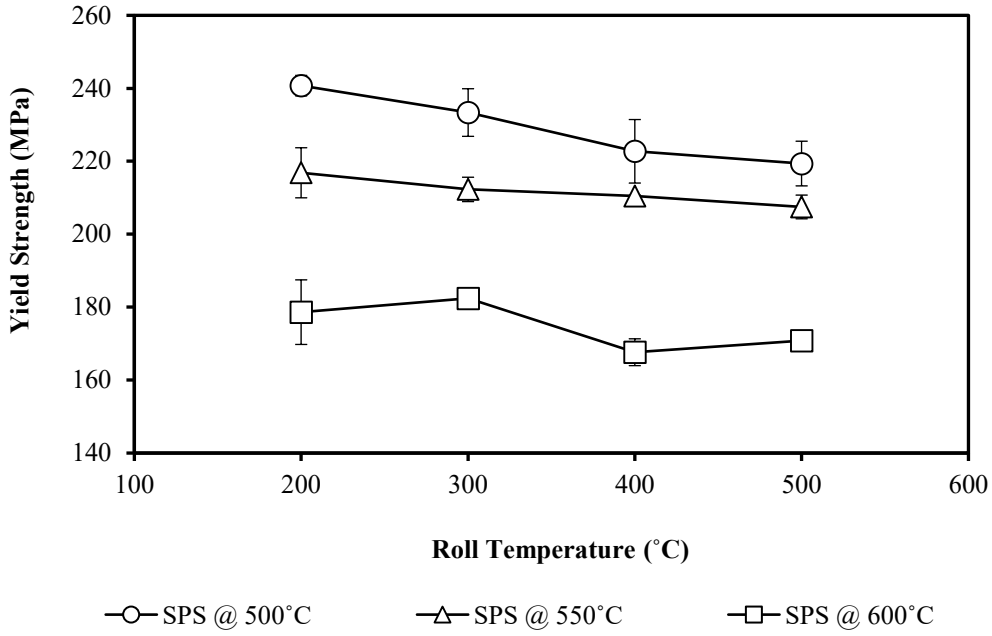

Figure 4-13 Comparison of the yield strengths of SPS processed specimens rolled at temperatures of 200˚C, 300˚C, 400˚C and 500˚C.

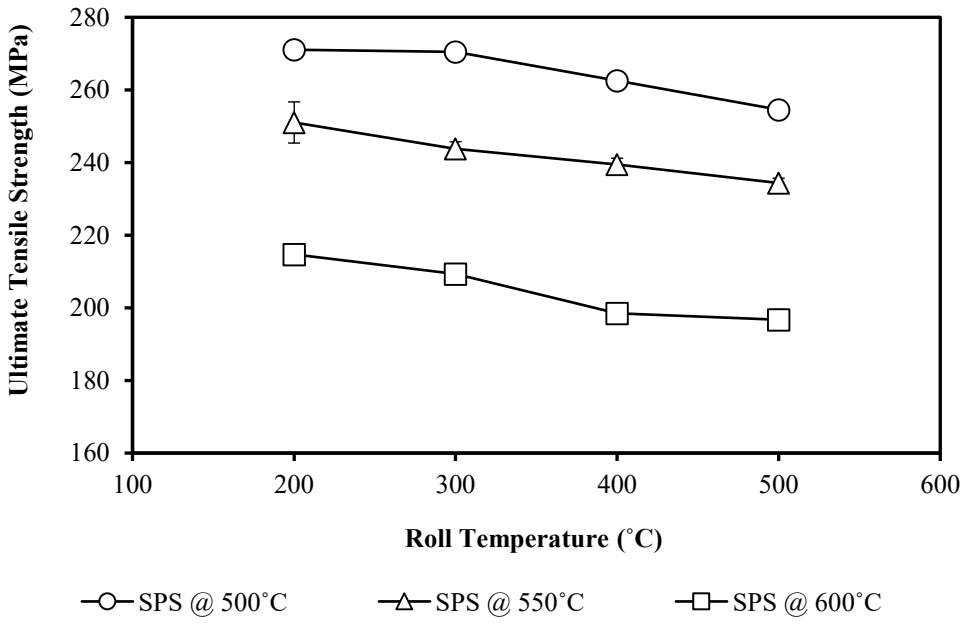

Figure 4-14 Comparison of the tensile strengths of SPS processed specimens at roll temperatures of 200˚C, 300˚C, 400˚C and 500˚C.

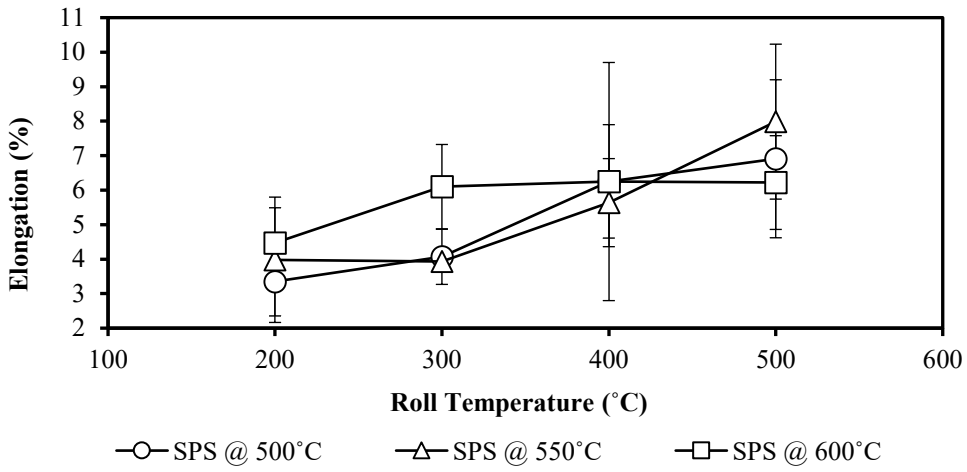

Figure 4-15 Comparison of the tensile properties of SPS processed specimens at roll temperatures of 200˚C, 300˚C, 400˚C and 500˚C.

In general, the as-sintered products exhibited lower tensile strengths and higher ductilities than their rolled counterparts. Interestingly, the yield strengths of all the sintered preforms rolled at 500ºC constituted the lowest yield strengths measured for the different rolling temperatures although comparatively, these values remained greater than the yield strengths of their as-sintered counterparts. In this sense, the yield strengths measured for the products sintered at 500ºC, 550ºC and 600ºC were 195MPa, 163MPa and 106MPa respectively. Once these same materials were rolled at 500ºC, these values then increased to 219MPa, 207MPa and 171MPa. The magnitude and trend of these values confirmed that the rolling process had significantly influenced the tensile strength of the sintered preforms.

One of the targets of this work was to identify SPS + ASR parameters that would produce a material with the best combination of yield strength and elongation. To investigate this, the elongation to failure was plotted against the yield strength (Figure 4-17). All

products originally sintered at 600ºC exhibited an inferior combination of tensile properties. On the contrary, those sintered at 500ºC offered the best balance of properties as shown by the encircled region in Figure 4-16.

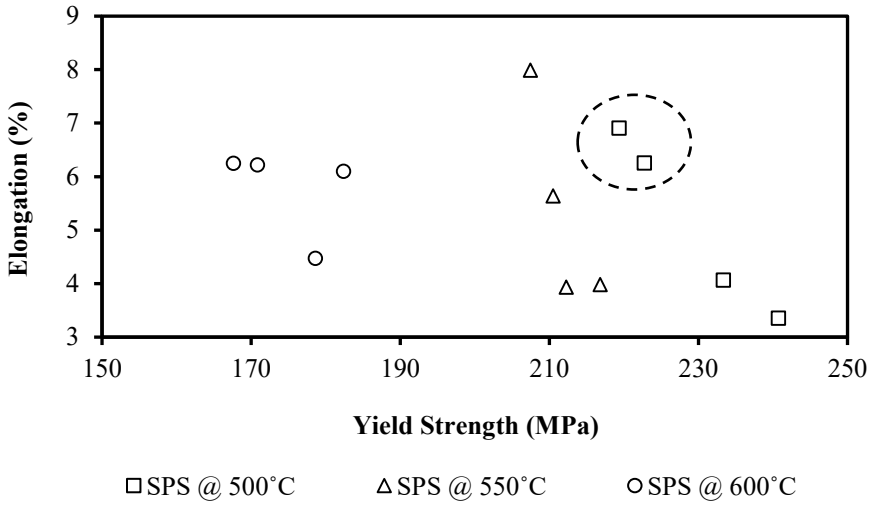

Figure 4-16 Comparison of the yield strengths for the SPS processed specimens rolled at different temperatures.

Analyses were then completed using EBSD and TEM techniques to examine microstructures of the rolled products in greater detail. Previous TEM analyses confirmed that the $Al_3(Sc,Zr)$ precipitates had coarsened from a nominal size of 5nm to 30nm as the SPS temperature was increased from 500 to 600ºC. Meanwhile, it is important to note that the highest ASR temperature did not exceed 500ºC; the lowest sintering temperature considered. Hence, it would be counterintuitive to expect the size of the precipitates to increase appreciably during hot ASR. This was corroborated by the TEM micrographs presented in Figure 4-18 for specimens sintered at 500ºC /rolled at 200ºC and 600ºC /rolled at 500ºC. These micrographs clearly substantiated that the $Al_3(Sc,Zr)$ precipitates had not coarsened during rolling.

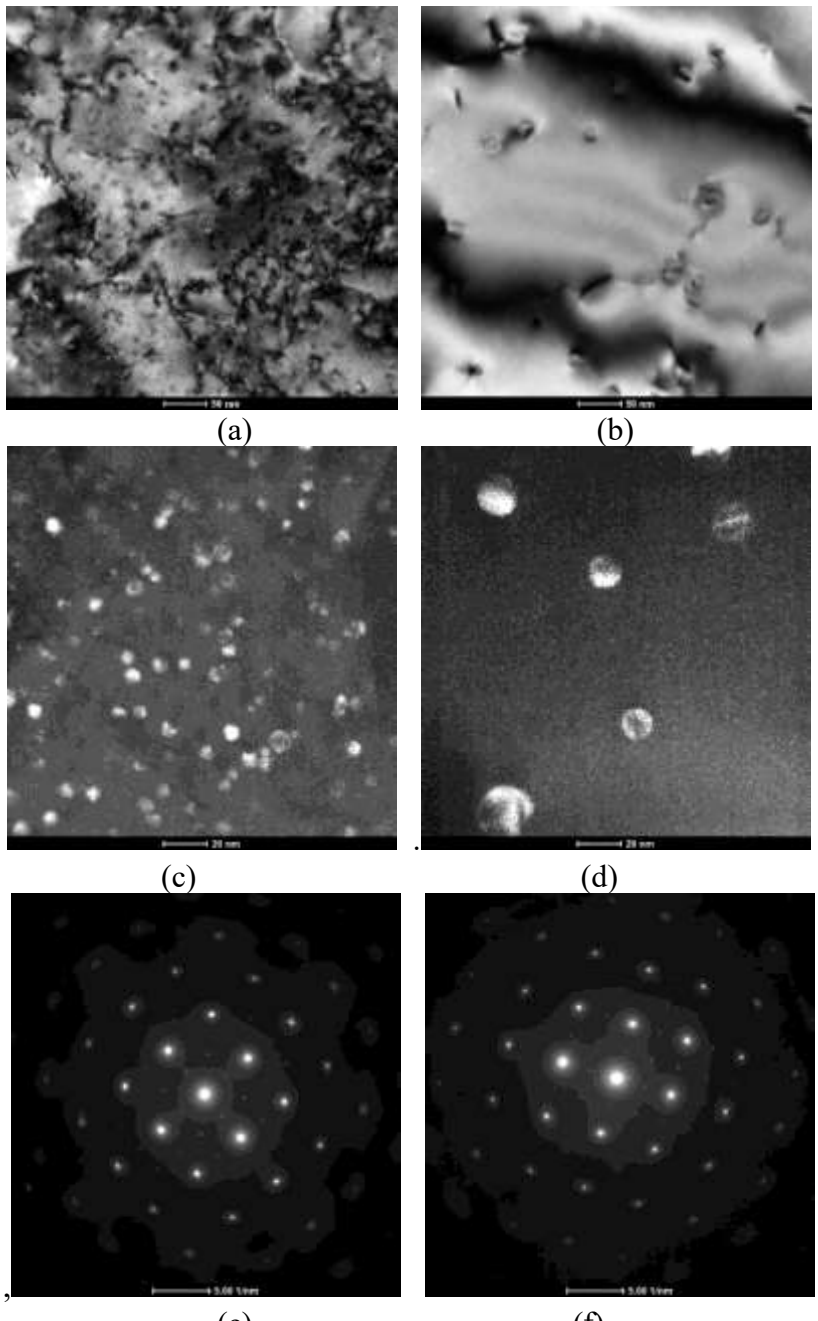

Figure 4-17 TEM results acquired from SPS specimens consolidated via SPS at 500ºC + ASR at 200ºC (a,c,e) and SPS at 600ºC + ASR at 500ºC (b,d,f). Bright field images ((a) and (b)), dark field images ((c) and (d)), and selected area diffraction patterns recorded with the beam oriented closely parallel to the <100> zones axis ((e) and (f)).

Examples of EBSD findings are given in Figure 4-19 and Figure 4-20. These images implied that dynamic recrystallization was operative and that this effect occurred to a greater extent in the specimen sintered/rolled at 600ºC/200ºC compared to its 500ºC/200ºC counterpart. As stated earlier, the coherent precipitates which prevailed in the 500ºC sintered preform should have pinned grain boundaries and in-turn stifled recrystallization. It is important to note that the preservation of a non-recrystallized structure would have also contributed to the measured gains in yield/tensile strengths.

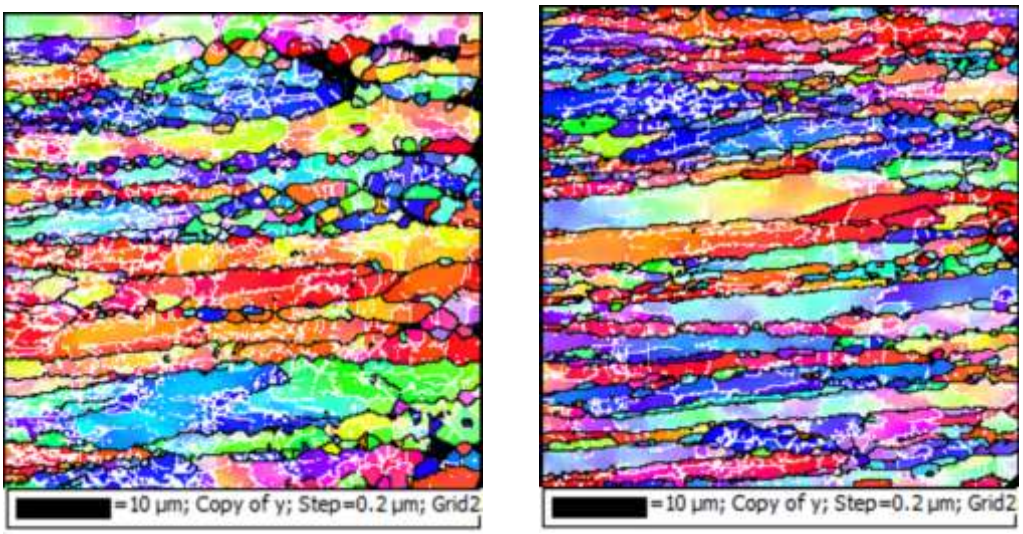

(a) (b)

Figure 4-18 EBSD maps of specimens sintered at 500ºC and subsequently hot rolled at (a) 200ºC (b) 500ºC. Black lines indicate HAGBs; white lines LAGBs.

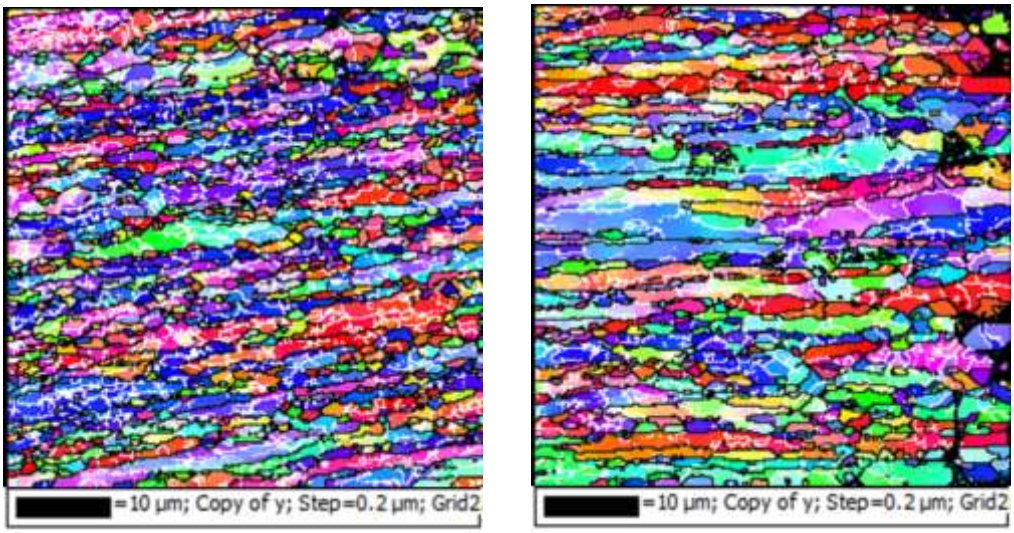

(a) (b)

Figure 4-19 EBSD maps of specimens sintered at 600ºC and subsequently hot rolled at (a) 200ºC (b) 500ºC. Black lines indicate HAGBs; white lines LAGBs.

To better understand the trends in tensile properties, a continued analysis of the EBSD data was done in conjunction with the TEM results. It can be recounted that the yield strength obtained for the specimen sintered/rolled at 500ºC/200ºC was ~26% higher than that of the specimen sintered/rolled at 600ºC/200ºC. Nevertheless, the yield strength decreased with increasing roll temperature in both instances. It has already been established in this study that the size $Al_3(Sc,Zr)$ precipitates was not affected by the hot ASR process, regardless of the temperature employed. This implied that the $Al_3(Sc,Zr)$ precipitates could not have been exclusively responsible for the trends in tensile properties; a more plausible feature of relevance were the LAGB concentrations. In this sense, in Figure 4-6 it was determined that the starting billets sintered at 500ºC and 600ºC were effectively identical in terms of their respective concentrations of LAGBs (48%) and HAGBs (52%). This situation was then changed appreciably after ASR as evident in Figure 4-20 which compares the fraction of LAGBs with the yield strengths of the rolled

products. Statistical analyses of the grain boundary misorientation angles showed that the specimen sintered at 500ºC/rolled at 200ºC contained the highest fraction of LAGB (62%) compared to only 39% for the specimen sintered at 600ºC/rolled at 200ºC. In addition, the fraction of LAGBs measured in the specimens SPS processed at 500ºC /rolled at 200ºC and 500ºC were higher than counterparts sintered at 600ºC/rolled at 200ºC and 500ºC. Furthermore, it can be recounted that the precipitate size was not influenced significantly by the rolling process, confirming that the precipitates were not primarily responsible for the trends in mechanical properties of the rolled products. Collectively, the fraction of LAGB decreased with increasing roll temperature and yield strength correlated well with the evolution of the fraction of LAGBs. This led to the conclusion that the key mechanism responsible for the increased strengths instilled through hot ASR was subgrain strengthening. This is consistent with the works of other researchers who have reported improved strengths in aluminum alloys due to this effect [128][31].

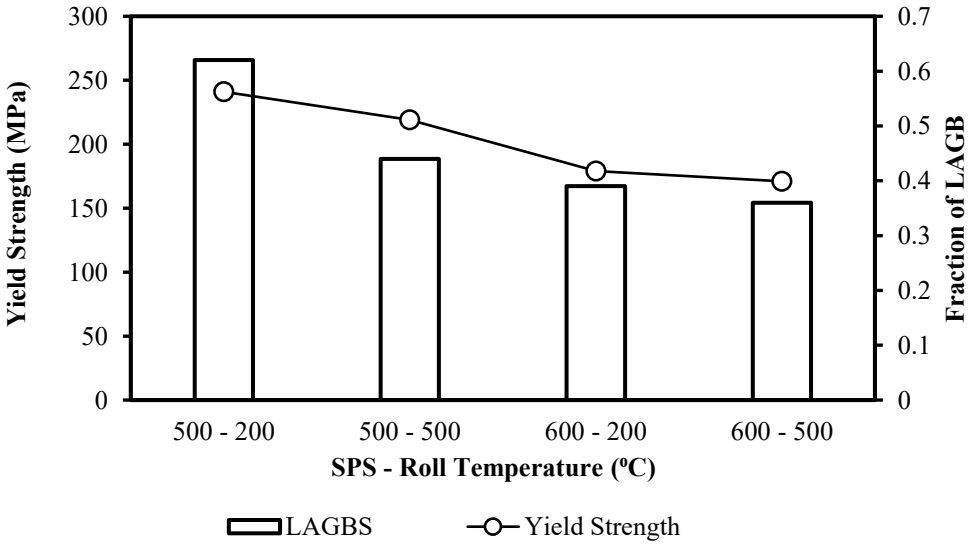

Figure 4-20 Trends in yield strength and the fraction of LAGBs for different SPS+ASR processes.

4.6 CONCLUSIONS

1. The Al-0.3Sc-0.2Zr powder was successfully consolidated through SPS.
2. Heating associated with the SPS process invoked the formation of $Al_3(Sc,Zr)$ precipitates. This phase coarsened appreciably as the SPS temperature increased from 500ºC to 600ºC and was the primary driving force behind observed trends in tensile properties.
3. SPS-consolidated billets of the Al-0.3Sc-0.2Zr alloy were responsive to hot ASR. All rolling schedules imparted full densification as well as higher mechanical properties compared to their as-sintered preforms.
4. The hot ASR process had no appreciable influence on the coarsening of $Al_3(Sc,Zr)$ precipitates that pre-existed in the sintered preforms.
5. Decreases in the rolling temperature yielded marginal improvements in the mechanical properties of the Al-0.3Sc-0.2Zr PM alloy.
6. Lower SPS and ASR temperatures promoted the formation of higher concentration of subgrains in the final product.
7. The specimen sintered at 500ºC and rolled at 200ºC exhibited the highest concentration of LAGBs and the most desirable combination of hardness and tensile properties.

Acknowledgements

The authors would like to graciously acknowledge the financial support provided by Boeing Research and Technology (research contract 11-6392), the Natural Sciences and Engineering Research Council of Canada (NSERC) via collaborative research and development grant #451466 and GKN Powder Metallurgy. TEM Assistance provided by Dr. Derek Oliver and Dr. William Caley at the Manitoba Institute for Materials

(University of Manitoba) is graciously acknowledged as is the laboratory assistance provided by Mr.Randy Cooke, Mrs. Patricia Scallion, and Mr. Dean Grijm at Dalhousie University.

CHAPTER 5 ISOTHERMAL FORGING OF A SPARK PLASMA SINTERED AL-0.3SC-0.2ZR POWDER METALLURGY ALLOY

M.Y. Amegadzie[1], A. Taylor[3], R. L. Hexemer[4], B.W. Williams[5], I.W. Donaldson[6] and D. Paul Bishop[2]

1 – Graduate Student, Dalhousie University, Halifax, Nova Scotia, Canada
2 – Professor, Materials Engineering, Dalhousie University, Halifax, Nova Scotia, Canada
3 - Vice President – Lightweight Technology, GKN Sinter Metals LLC, Auburn Hills, Michigan, USA
4 – Research Engineer, GKN Sinter Metals LLC, Conover, North Carolina, USA
5 – Research Scientist, CanmetMATERIALS, Natural Resources Canada, Hamilton, Ontario, Canada
6 – Director of R&D North America, GKN Sinter Metals LLC, Auburn Hills, Michigan, USA

Status: Published Journal Paper. International Journal of Powder Metallurgy. (2018) Volume 54, Issue 3. Pages 47-57.

Author Contributions: All experimental work was completed by Mark Y. Amegadzie. the first draft of this paper was written by Mark Y. Amegadzie. supervision was provided by D. Paul Bishop. The first draft of this paper was written by Mark Y. Amegadzie whereas the final manuscript was as a result of editing by all affiliate authors.

5.1 ABSTRACT

Aluminum alloys containing scandium as the primary alloying element continue to gain significant importance in the aeronautical and automotive industries due to their low intrinsic density and mechanical stability at elevated temperatures. The majority of work completed on these materials have emphasized wrought and cast product forms. However, powder metallurgy technologies represent an attractive alternative as the high cost of scandium can be offset by efficiencies in material consumption via net shape processing. In this work, a prealloyed powder of Al-0.3Sc-0.2Zr was spark plasma

sintered and then isothermally forged. Core processing variables emphasized the net strain and the applied strain rate utilized in forging. Both factors influenced the microstructure and tensile properties of the forged products. Forging to strains ≤ 0.8 under a relatively fast rate of 1 s^{-1} yielded forged products with the most desirable combination yield strength, UTS, and tensile ductility. All of these properties experienced some level of decline when large strains 1.6 and slow strain rates (0.01 s^{-1}) were applied.

5.2 INTRODUCTION

Aluminum powder metallurgy (PM) is a commercialized manufacturing technology currently utilized to fabricate a growing number of automotive components. Common examples include cam shaft bearing caps [129], transmission components, and heat sinks [130]. In all instances, these products are fabricated in high annual volumes by means of press-and-sinter PM. Here, the sequence of events typically includes blending of the starting raw powders, followed by die compaction, sintering, and then sizing to refine dimensional tolerances. This process is capable of producing geometrically complex parts in a manner that is both effective and efficient. However, it does have some inherent constraints. For instance, the raw powder blends cannot be fully prealloyed as this deteriorates die compressibility. Secondly, liquid phase sintering coupled with the presence of magnesium additions are mandatory when a dense, well sintered product is sought. Such factors impose clear limitations on the range of alloy chemistries that can be successfully processed and can lead to microstructural coarsening and/or problematic distortion in the sintered product.

In an effort to circumvent the aforementioned issues, numerous researchers are now investigating spark plasma sintering (SPS) [131] as an alternate means of consolidating aluminum powders. In this process, powder is loaded in a conductive tool set (typically graphite) that is then rapidly heated through the flow of high, pulsed DC current, while being uni-axially compacted at the same time. The entire process is conducted under vacuum or a protective gas atmosphere and essentially combines compaction and sintering in a single operation. Key advantages include the facts that cycle times are relatively brief (i.e. minutes versus hours for conventional liquid phase sintering), the powder can be fully prealloyed to any composition desired, magnesium additions are not required, microstructural coarsening is limited, and full density products are the norm. Powders successfully processed via SPS to date span a wide range of chemical formulations extending from pure aluminum [56][132] to fully prealloyed binary (i.e. Al-Sc) [133] and ternary (i.e. Al-Fe-Ni) [134] systems, and those that embody complex wrought alloy chemistries such as 7055 [135], 7075 [136], 2219 [137], and 2024 [138]. Although SPS maintains significant merit from a metallurgical standpoint, commercial application of this technology to directly fabricate parts with a complex, engineered shape remains highly challenging. As such, the majority of SPS products are simply shaped pucks, discs, etc. Post-SPS machining is one option through which the desired geometry could be introduced. However, such processes are expensive and invariably introduce high levels of material waste. A more promising option is upset forging whereby geometry is introduced via plastic flow in a nominally net shape manner. Such practices are also known to invoke concomitant gains in mechanical properties when forging sintered aluminum preforms [139][140]. The fabrication of aluminum

components via SPS + Forge processing thereby holds promise as a means to devise a net shaped product with an advantageous microstructure and mechanical properties. As a precursory step in this direction, SPS + hot upset forging studies were applied to an Al-Sc-Zr prealloyed powder. Products were then characterized to assess the final densities, microstructures, and tensile properties.

5.3 EXPERIMENTAL PROCEDURES

Sintering was completed in a SPS Model 10-3 unit manufactured by Thermal Technologies Inc. operated with pulsed DC current. Key parameters included a heating rate of 50K min^{-1}, sintering temperature of 500°C, isothermal hold time of 120s, uni-axial pressure of 50MPa, and a vacuum atmosphere. All specimens were processed in graphite tooling machined to produce cylindrical pucks with final dimensions of 40 mm diameter x 27 mm thick. Sintered specimens were then lightly machined to remove any remnants of graphite remaining after SPS and then hot upset forged under isothermal conditions using an Interlaken model SP225 hydraulic press with a rated capacity of 110 ton with a hydraulic accumulator system that allowed high punch velocities to be achieved. All samples were preheated in an oven at 500°C for 1 hour and then transferred to pre-heated platens, also at 500 °C, in press for upset forging. Boron nitride was used for lubrication purposes. Forging parameters of core interest were the forging strain and strain rate. In order to investigate the effect of forging strain, samples were forged to yield true strains of 0.4, 0.8 , and 1.6 while keeping the strain rate constant at 1 s^{-1}. A nonlinear displacement versus time function was used to obtain a constant strain-rate. For comparative purposes, a representative sample was also forged (0.8 strain) but with a

slower strain rate of 0.01 s^{-1}. Sintered densities were measured using Archimedes principle in tandem with vacuum assisted infiltration in accordance with MPIF standard 42. Tensile samples were then machined from the forged pucks and tested with an Instron Satec model 5594 200HVL hydraulic load frame equipped with a 50kN load cell, wedge grips and an Epsilon model 3542 extensometer that remained attached to the sample through to fracture. Microstructural characterization included optical microscopy, scanning electron microscopy (SEM), and electron backscatter diffraction (EBSD). The latter two means of assessment involved the use of a Hitachi model 4700 SEM coupled with a HKL EBSD system equipped with a Nordlys Oxford Instruments Detector for EBSD acquisition. A rather rigorous sample preparation approach was needed for this aspect of the research. This included hot mounting the specimens and grinding and polishing with a Struers Tergramin Automatic Polisher. Preliminary sample preparation included grinding with a 1200 silicon carbide disc followed by a step by step polishing procedure. This polishing sequence employed a 15μm, 3 μm, 1 μm diamond suspension and finally a 0.05 μm, all of which constituted a total polishing time of about 1.5 hours.

5.4 MATERIALS

The powder utilized in this study was produced through nitrogen gas atomization at Ecka Granules GmbH (Velden, Germany). This was a fully prealloyed material with a targeted ternary formulation of Al-0.3Sc-0.2Zr. As shown in Table 5-1, the final chemistry was in close agreement with the nominal values sought aside from some minor impurities as commonly encountered in aluminum. The morphology of the powder is shown in Figure 5-1 wherein a nominally spherical shape prevailed. The measured particle size

distribution for the powder as determined by laser light scattering (Malvern, Mastersizer model 3000) is shown in Figure 5-2.

Table 5-1 Chemical assay (weight %) of the starting prealloyed powder.

	Composition (weight %)					
	Sc	**Zr**	**Fe**	**Si**	**Mg**	**Al**
Nominal Target	0.30	0.20	---	---	---	Bal.
Measured	0.33	0.17	0.08	0.02	0.01	Bal.

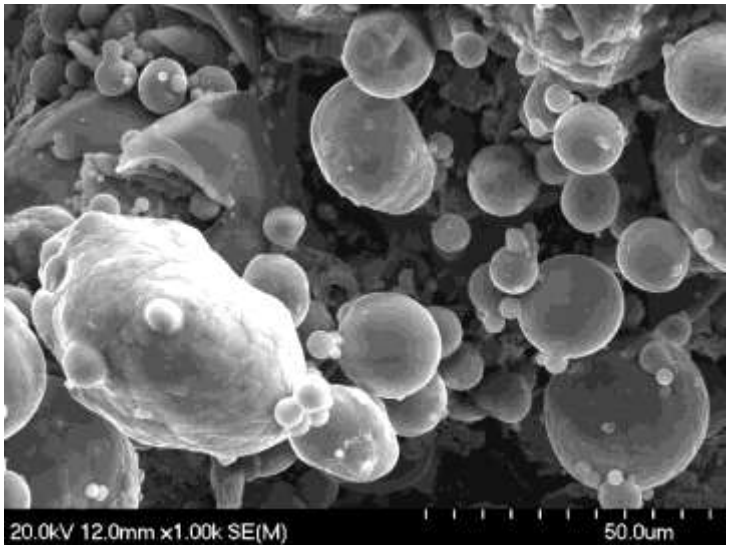

Figure 5-1 Image of the gas atomized Al-0.3Sc-0.2Zr powder.

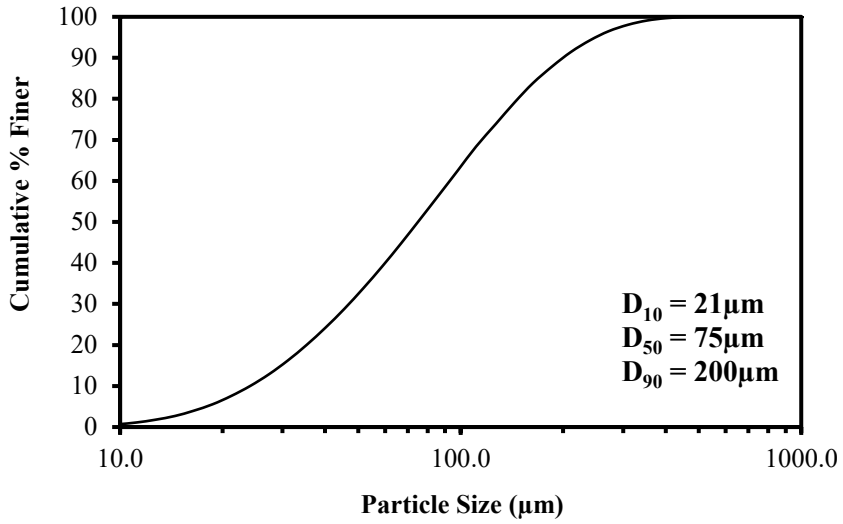

Figure 5-2 Particle size distribution of the Al-0.3Sc-0.2Zr powder.

5.5 RESULTS AND DISCUSSION

5.5.1 EFFECTS OF NET FORGING STRAIN

To assess the effects of net forging strain, sintered slugs were forged at 500°C to true strains of 0.4, 0.8 and 1.6 using a constant strain rate of $1s^{-1}$. Flow curves depicting typical true stress versus true strain data for these specimens are plotted in Figure 5-3. Each curve increased in a sharp linear manner at the onset of deformation until a stress value of ~45MPa was reached. This represented the region within which elastic deformation prevailed. Tight consistency amongst the specimens indicated that variations in the net amount of applied forging strain had no meaningful impact on this mode of deformation. Flow stress then transitioned into a non-linear behaviour indicating that plastic deformation now prevailed. Here, flow stress diminished subtly and then rose in a gradual manner. All curves followed a very similar path but it was

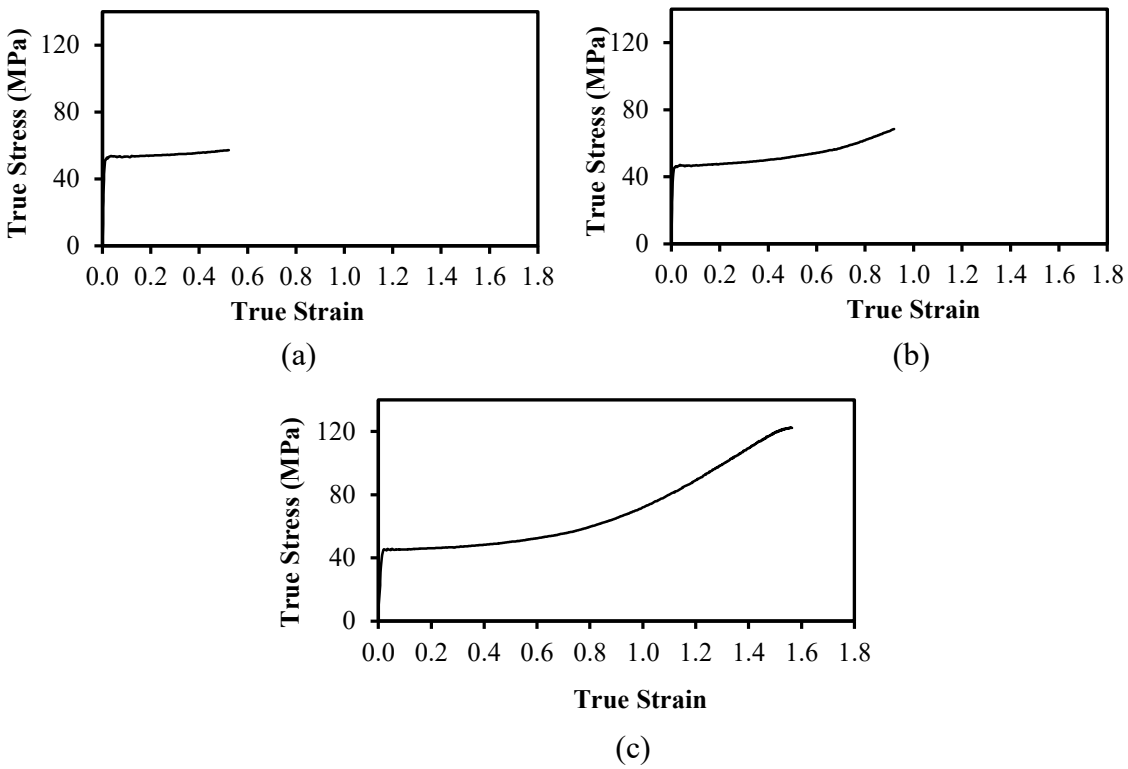

Figure 5-3 True stress versus true strain plots for samples forged to net true strains of (a) 0.4, (b) 0.8 and (c) 1.6 .

only in the sample forged to 1.6 strain that a peak flow stress was achieved followed by a small decline in stress with further strain near the end of the test. Generally, the compressive flow stress curves for PM aluminum alloys subjected to hot deformation has been found to decrease with increasing plastic strain upon transitioning from elastic to plastic behaviour [6]. This observation has been attributed to the probable occurrence of softening mechanisms that include dynamic recovery, dynamic recrystallization, and/or dynamic precipitation [141][142]. Although materials with high stacking fault energies such as pure aluminum alloys rarely experience dynamic recrystallization [143], this phenomenon has been observed during the hot deformation of chemically complex aluminum alloys [143][144]. This suggests that the determining factor for the occurrence

of dynamic recrystallization in aluminum alloys cannot be exclusively linked to its stacking fault energy. In a latter section, a more detailed analysis on the possible occurrence of dynamic recrystallization using EBSD is discussed. Nevertheless, strain softening of the forged samples appeared to have been eclipsed by another mechanism as evident by the progressive rise in the flow curves during plastic deformation. It was postulated that this was principally a result of increasing frictional forces between the platens. At high levels of strain, the diameter of the forged disc increases significantly leading to increased frictional forces applied on the cylinder. The magnitude of these forces would have become progressively larger as strain rose and concomitantly, the contact area between the sample and the platens increased thereby over-shadowing any underlying metallurgical transitions in the material.

Data on the densities of sintered and forged specimens as a function of the forging strain are shown in Figure 5-4 while the corresponding microstructures as viewed through optical microscopy are shown in Figure 5-5. After SPS alone, the product exhibited a final density of 99.1% of theoretical. This was consistent with microstructural observations (Figure 5-5 (a)) in that porosity was present at a low level. In most instances, porosity was present as an inter-particle feature. However, residual pores within the actual powder particles themselves were also observed on a sporadic basis. It was also noted that prior particle boundaries were readily observed through the microstructure suggestive that inter-particle bonds were of a moderate quality. A recent study by Cooke et al demonstrated that SPS temperatures upwards of 600°C [140] could largely eliminate residual porosity and improve the quality of sinter bonds. However,

such gains invoked non-recoverable coarsening of the $Al_3(Sc,Zr)$ precipitates and acute declines in critical mechanical traits such as tensile yield strength. As a core objective of this research was to produce a dense, yet strong, forged product, a relatively low SPS temperature of 500°C was maintained in anticipation that forging would remediate the porosity/bonding issues with minimized precipitate coarsening. This was found to be true for the case of residual porosity as all forged products were 100% dense (Figure 5-4). This indicated that all of the forging strains considered were equally effective in terms of post-SPS densification. The effective absence of residual porosity was also apparent in the optical micrographs of Figure 5-5. In addition, these images revealed that grains were now elongated perpendicular to the direction of applied forging load and that the extent of this effect became more pronounced as the amount of net strain increased.

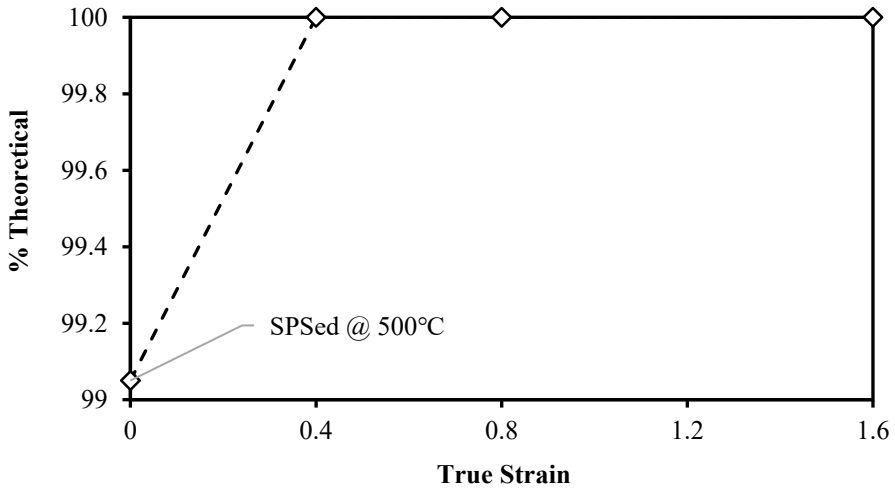

Figure 5-4 Final product density as a function of applied forging strain.

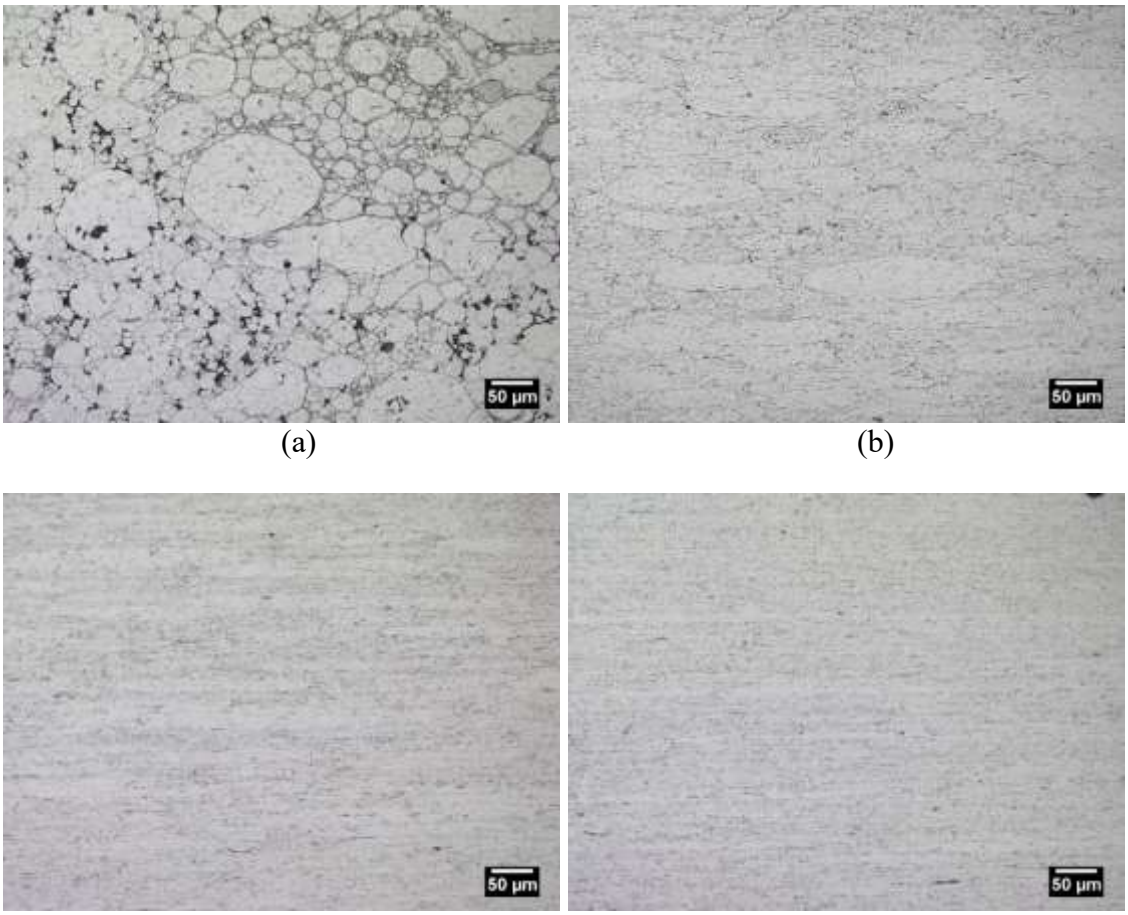

(a) (b)

(c) (d)

Figure 5-5 Microstructures of Al-0.3Sc-0.2Zr products. (a) as-SPS processed versus counterpart samples isothermally forged at 450°C to net true strains of (b) 0.4 (c) 0.8 and (d) 1.6.

Engineering stress-strain curves that illustrate the effects of forging strain on tensile properties are shown in Figure 5-6. In the absence of forging, the stress rose in a linear manner followed by fracture at a UTS of ~170MPa with an effective absence of plastic deformation. A yield strength could not be measured for the material using the standard offset method as the ductility was extremely low (<<1%). This behaviour was in stark contrast to that observed for forged products. Here, yield strengths and UTS values lied within the range 150-173MPa and 175-218MPa respectively while ductilities were all appreciable coming in at 12 to 24%. As such, all forged products offered significant

gains in tensile attributes, with the most prominent benefits realized in tensile ductility (i.e. forged samples were at least 40 times more ductile).

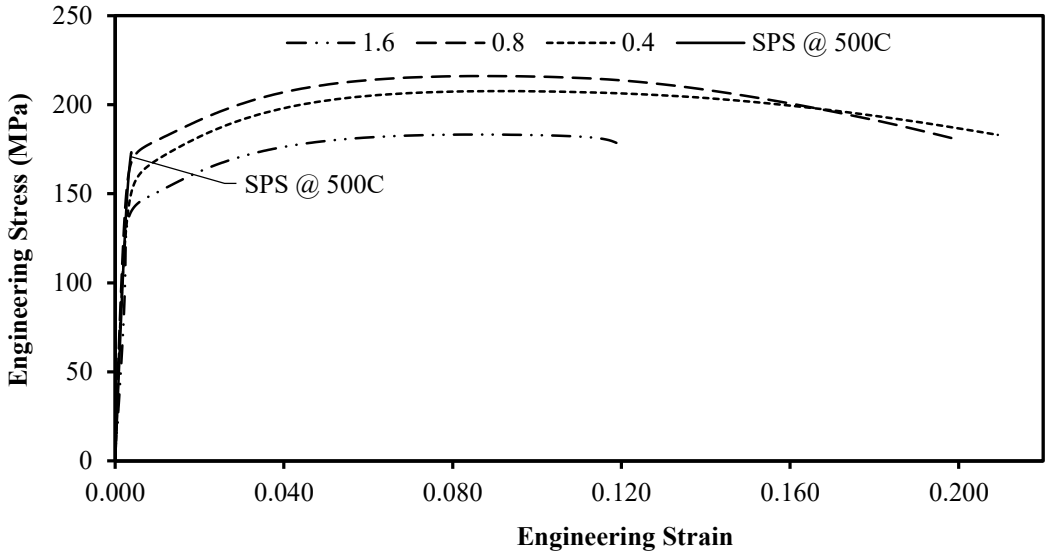

Figure 5-6 Typical engineering stress-strain curves acquired from samples in the as-SPSed condition and those processed through SPS + forging to net strains of 0.4, 0.8, 1.6.

The latter trait was highly evident in fracture surface images recorded from samples prepared with and without a post-SPS forging operation. Exemplary images of which are shown in Figure 5-7. In this sense, brittle fracture is typically synonymous with the presence of smooth facets and/or in the case of sintered materials, an obvious presence of prior particle boundaries. Both of these traits were evident in the image taken from the fracture surface of the unforged specimen. Conversely, heightened tensile ductility is invariably linked to micro-void coalescence which was the prominent feature in forged fractures. The general brittle/ductile nature of fracture was also macroscopically obvious in the broken test specimens as the brittle material had a flat profile wherein extensive necking was obvious in the test bars machined from forged slugs.

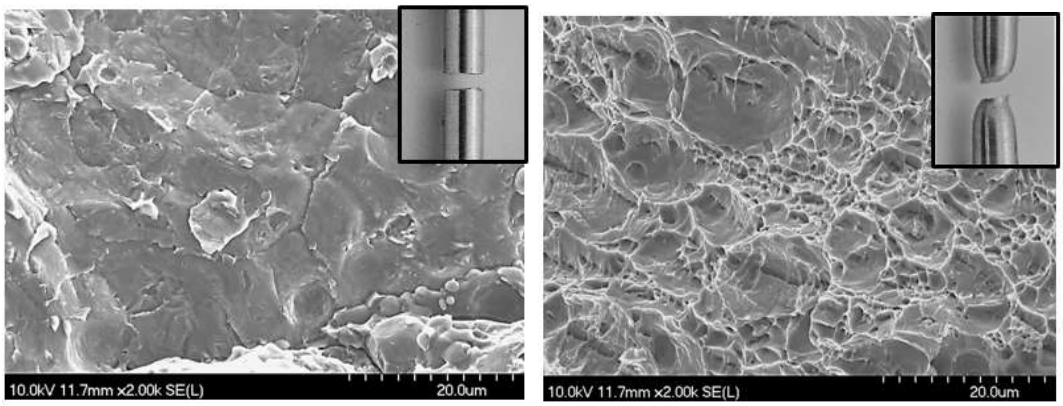

(a) (b)

Figure 5-7 Fracture surfaces observed in (a) SPS processed sample and (b) a SPS+forged sample (forging strain = 0.4). Inserts reveal the macroscopic nature of each fracture.

While all forging strains imparted tangible gains in tensile properties, the effect was most pronounced in materials forged to 0.4 and 0.8 strain. Interestingly, yield strength, UTS and tensile ductility were all reduced when forging was increased to 1.6. To investigate this observation in more detail, samples of each material were examined using EBSD. Resultant images are shown in Figure 5-8. It is important to note that the grain boundaries displayed on the EBSD maps appear as black and white lines. The black lines are ascribed to high angle grain boundaries (HAGBs) whereas white lines denote low angle boundaries (LAGBs). From literature, HAGBs are interfaces between crystals with boundary mis-orientations greater than 15˚ whilst LAGBs on the other hand are comprised of discrete arrays of dislocations with mis-orientations less than 15˚. The former are synonymous with recrystallized metals while the latter constitute noon-recrystallized “sub-grains”.

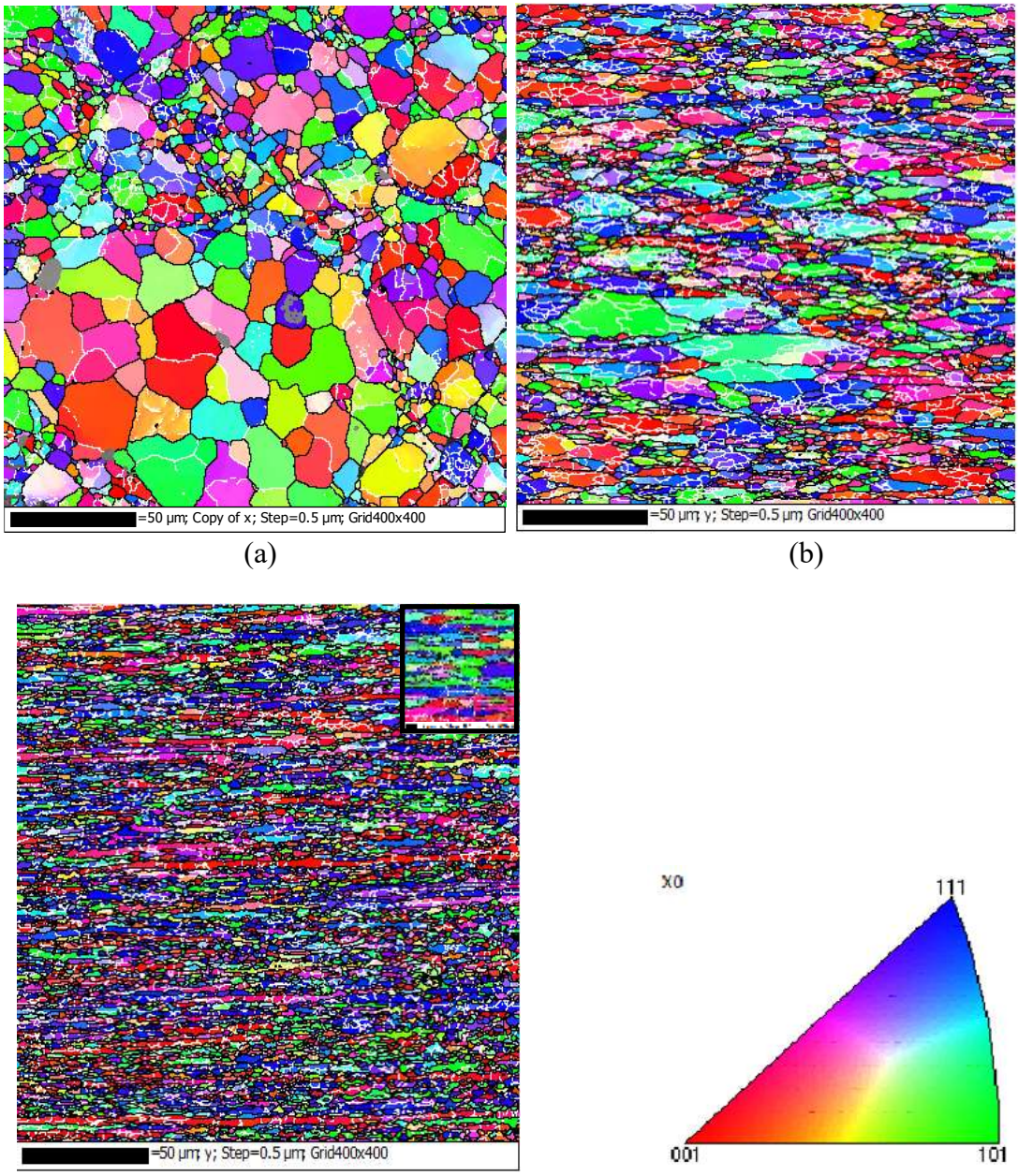

Figure 5-8 EBSD images acquired from (a) an SPS processed sample and those isothermally forged to (b) 0.4 and (c) 1.6 true strain - insert image shows grains at a magnification 5 times greater. The corresponding inverse pole figure is presented in (d).

Generally, the microstructure of the SPS processed sample was comprised of equi-axed grains ranging from 10 to 30 μm in size with some grains < 5 μm observed. HAGBs dominated the structure with a limited concentration of subgrains detected. Forged specimens were notably different in that the grains were now heavily elongated as a result of plastic deformation and exhibited a more refined grain size. The material forged to 0.4 strain was riddled with an abundance of sub-grains as evident in the micrographs and in statistical analyses of the grain boundary misorientation angles (Figure 5-9). That forged to 1.6 appeared to exhibit the smallest grain size of all the materials considered. However, it was also noted that HAGBs were now more prevalent. Fundamentally, the refined grain size in forged products would have been expected to offer an increased yield strength/UTS relative to the non-forged material without having an overtly negative impact on ductility. As this was not the case in tensile data (Figure 5-6) it was thereby inferred that other factors were at play. Some level of in-situ precipitate coarsening was one plausible factor given the elevated temperatures associated with forging and the extensive pre-heat periods required. Mechanistically, this transition would be expected to decrease yield strength and enhance ductility, yet the magnitudes of change were expected to be relatively low given the exceptional thermal stability inherent to $Al_3(Sc,Zr)$ precipitates. In this sense, the estimated point of elastic-to-plastic transition point was marginally lower in forged materials and thereby compliant with this concept. However, the 40-fold+ gain in ductility was far too excessive to be ascribed solely to precipitate coarsening. Hence, it was postulated that forging also instilled an intense disruption of the oxide networks that prevailed after SPS. This would have led to

metallic bonding throughout the material and the large increases in tensile ductility observed.

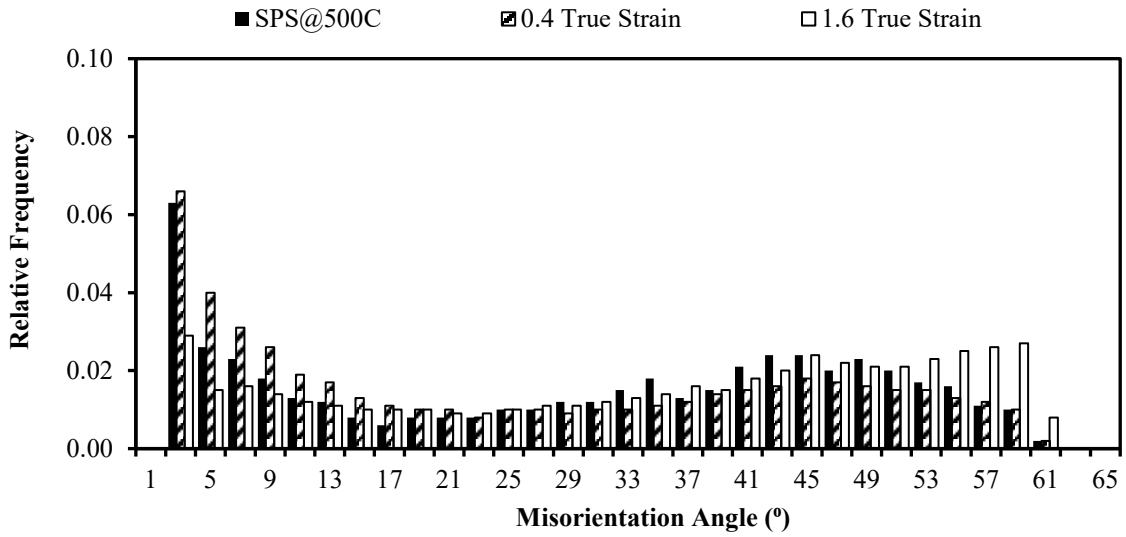

Figure 5-9 Statistical assessment of the grain boundary misorientation angles for the specimens presented in Figure 5-8.

As noted earlier, a transition in tensile properties occurred amongst the forged materials when strain was increased to 1.6. Here, yield strength, UTS, and ductility all declined relative to counterparts only forged to lesser strains of 0.4 and 0.8. It is postulated that this behaviour stemmed from the activation of dynamic recrystallization when samples were forged to the highest amount of strain considered. In recent years, EBSD has been used to investigate this phenomenon by quantifying the evolution of grain boundary angles during hot deformation of aluminum alloys [141][145]. In these works, comprehensive analyses on the evolution of grain boundary angles with forging strain were completed to verify the possibility of dynamic recrystallization. In this context, fractions of the misorientation angles between LAGBs (2-5° and 6-15°) and HAGBs (16-30° and >30°) were computed and plotted as functions of forging strain. As the forging

strain was increased, the fraction of LAGBs decreased whereas that of the HAGBs increased particularly for grains with misorientation angles >30° thereby indicating that the net forging strain was an important factor in the formation of new grains and the dynamic recrystallization thereof. Data illustrating the application of this same concept to forged samples of the Al-0.3Sc-0.2Zr alloy are shown in Figure 5-10. Here, it was observed that the fractions of LAGBs gradually declined while those with a misorientation angle >30° increased to a significant extent with rising forging strain. This thereby confirmed that dynamic recrystallization was indeed most pronounced in the sample forged to 1.6 true strain. Given that HAGBs represent a less potent strengthening feature than LAGBs, the notable declines in yield strength and UTS when forging to 1.6 strain were logical. However, the observation that ductility had also declined was somewhat counter-intuitive. It is known that adiabatic shear bands can be formed in aluminum alloys when subjected to high levels of plastic deformation and that these features can compromise tensile ductility [146]. Hence, it was rationalized that micro adiabatic shear bands had likely formed upon forging to the highest strain and that these were ultimately responsible for the decline in ductility.

5.5.2 EFFECTS OF STRAIN RATE

In this stage of research, SPS processed samples were forged to achieve a net strain of 0.8 but at differing strain rates of 0.01 and 1 s^{-1}. Flow curves acquired while forging slugs under these conditions are presented in Figure 5-11. Generally, the flow curves rose linearly before transitioning into plastic flow after which stress then diminished slightly before rising gradually again towards the end of the deformation. Such behaviour was consistent with that observed when studying the effects of net forging strain (Figure 5-3).

One striking difference was that the flow stresses were notably higher when utilizing the faster strain rate. In this sense, the precursory linear-elastic region of the curve for the specimen forged at a strain rate of $1s^{-1}$ extended to an appreciably higher stresses. Hence, the elastic to plastic transition stress was ~48MPa yet only 28MPa when forging was completed at $0.01s^{-1}$. This equated to a 42% reduction in flow stress that prevailed over the full range of strain considered so as to displace the entire flow stress curve for the faster rate well above that for the slowly forged counterpart. This was largely as expected since aluminum alloys are known to exhibit strain rate sensitivity, especially when deformation is completed at elevated temperatures.

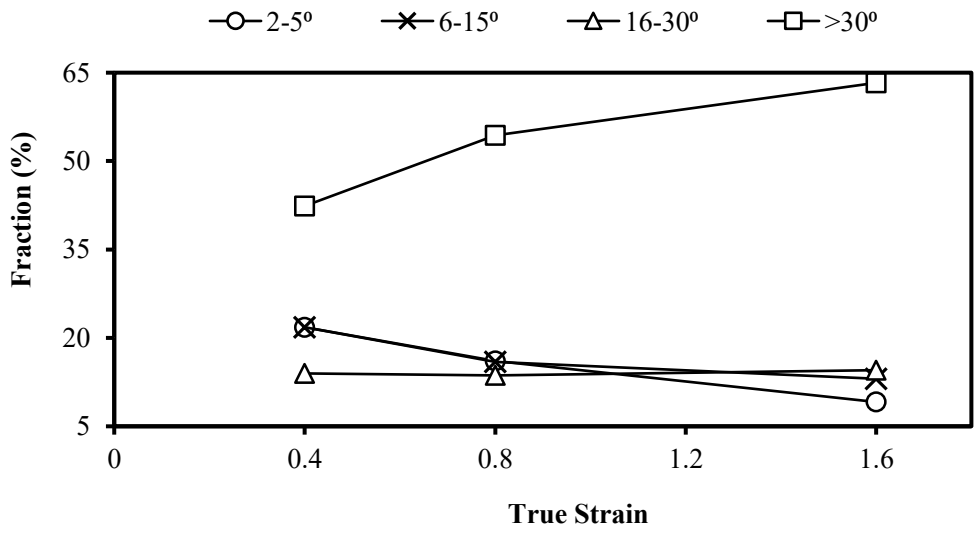

Figure 5-10 Effect of forging strain on the fractions of grain boundary misorientation angles present in forged samples of Al-0.3Sc-0.2Zr.

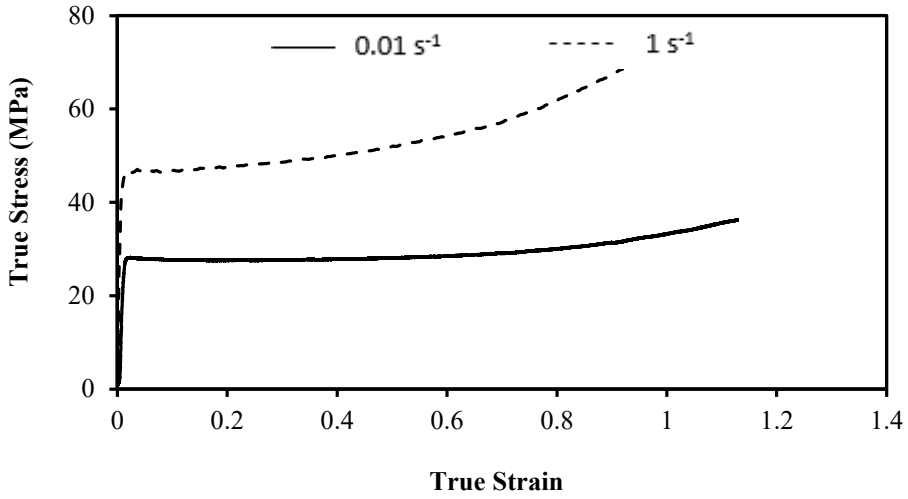

Figure 5-11 Flow stress curves acquired while forging sintered specimens at the two strain rates considered.

Tensile specimens were then machined from the forged slugs and tested. Exemplary engineering stress-strain curves are shown in Figure 5-12. It was noted that the yield strengths of the materials forged at 1 s^{-1} and 0.01s^{-1} were 173MPa and 147 MPa respectively. The UTS was also higher in the specimens forged at the faster rate while tensile ductility was reduced. The microstructures of each specimen were then studied in an attempt to ascertain the reasoning for the observed differences in tensile behaviour. This commenced with optical metallography as shown in Figure 5-13. From the micrographs, it was obvious that both strain rates were effective at eliminating porosity from the sintered preforms. This was substantiated through physical density measurements wherein it was confirmed that each material was essentially 100% dense. Hence, appreciable densification differences were absent and therefore not a factor of influence. The grains also appeared to be elongated transverse to the forging direction to a comparable extent in each case.

As optical metallography failed to reveal any obvious differences, EBSD analyses were completed (Figure 5-14 and Figure 5-15). Here, it was evident that the sample forged at 1 s^{-1} contained a higher concentration of subgrains. That forged with a strain rate of 0.01 s^{-1} seemed to exhibit nominally coarser grains and a higher concentration of HAGBs (Figure 5-15). Combined, these factors implied that the material forged at the slower rate had experienced a higher degree of dynamic recrystallization. The slowly forged specimen would have endured plastic deformation over a period of time two orders of magnitude longer than its rapidly forged counterpart. This would have exasperated the propensity for recrystallization consistent with EBSD findings. Given that ductility was not compromised at the slower strain rate it was also concluded that the formation of adiabatic shear bands had not occurred under these forging conditions.

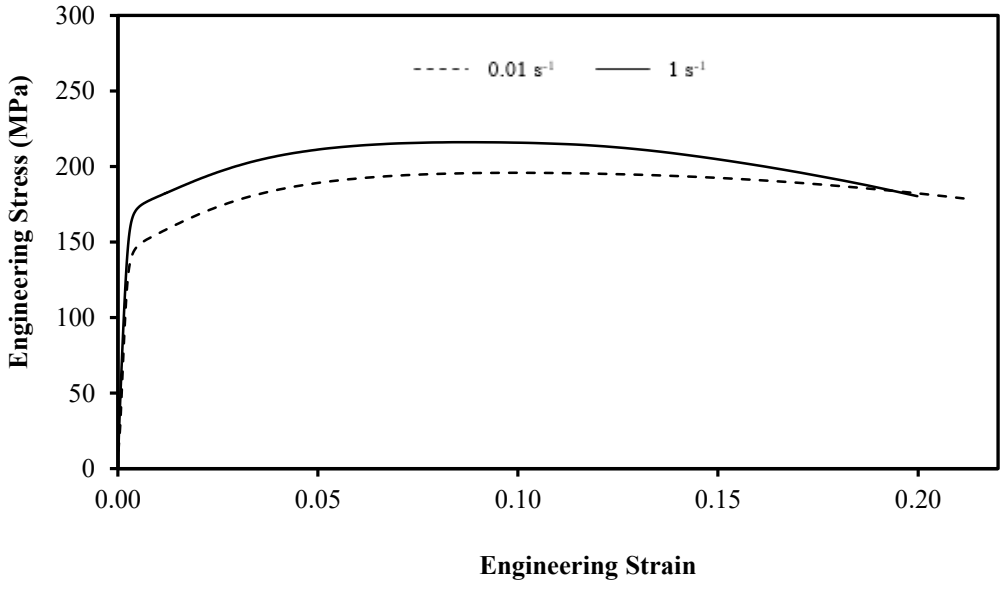

Figure 5-12 Tensile curves for samples machined from pucks forged at strain rates of 1 s^{-1} and 0.01 s^{-1}. Both materials forged to a net true strain of 0.8.

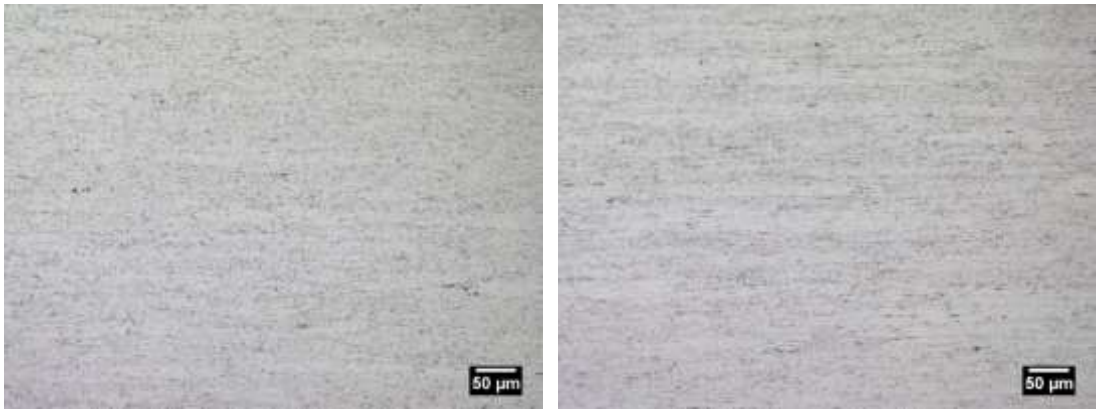

(a) (b)

Figure 5-13 Microstructures observed via optical metallography in samples forged at strain rates of (a) 0.01 s^{-1} and (b) 1 s^{-1}.

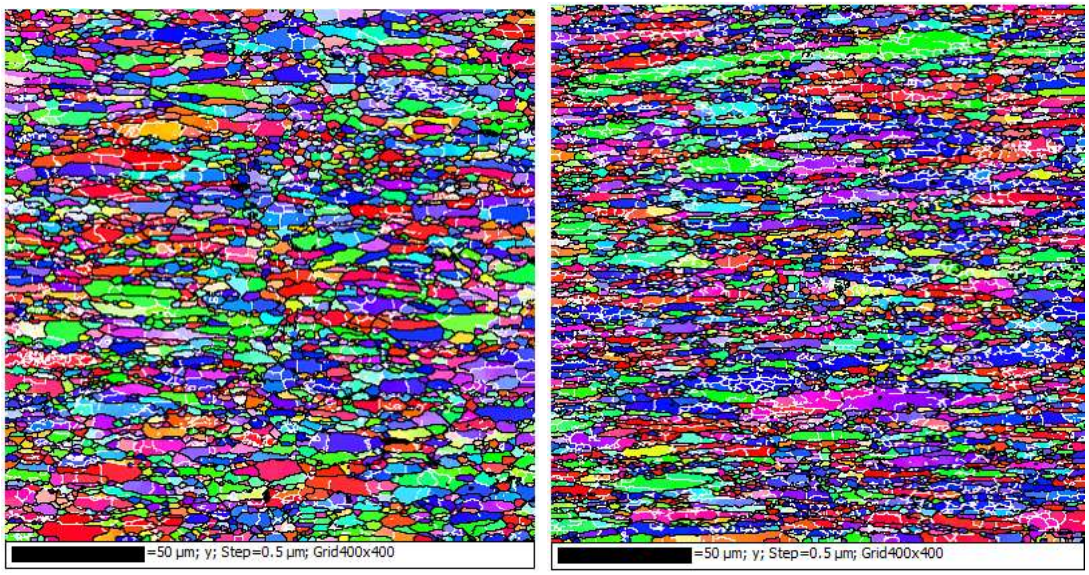

(a) (b)

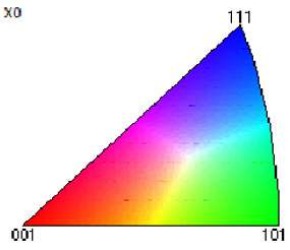

(c)

Figure 5-14 EBSD maps recorded from samples forged at (a) 0.01 s^{-1} and (b) 1 s^{-1} with the corresponding inverse pole figure provided in (c). Both samples forged to a net true strain of 0.8.

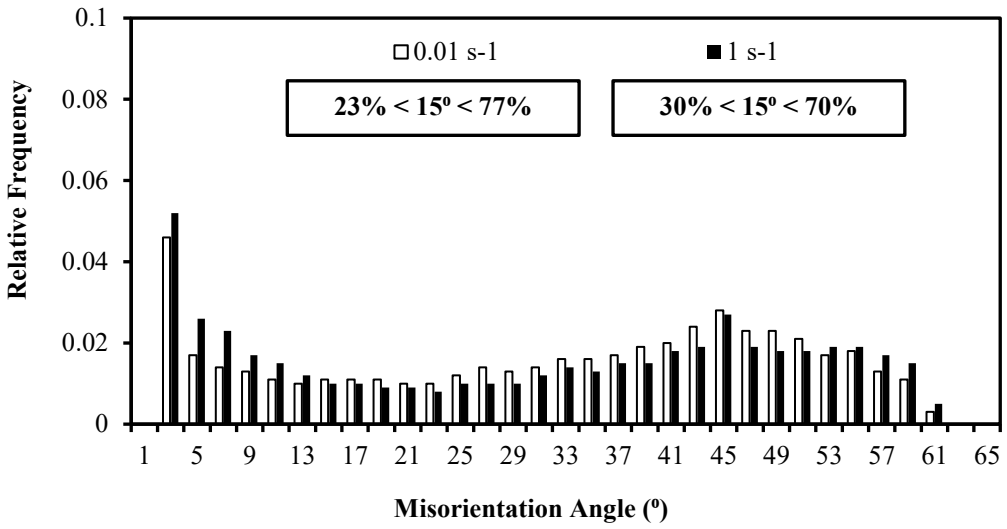

Figure 5-15 Statistical assessment of the grain boundary misorientation angles for the specimens presented in

Figure 5-14.

5.6 CONCLUSIONS

Through the research completed in this study, the following conclusions were reached:

1. All of the forging strains and strain rates considered were sufficient to impart full densification to the preforms of Al-0.3Sc-0.2Zr originally consolidated through SPS.
2. A minimum net forging strain of 0.4 was sufficient to produce significant enhancements in all tensile properties. Ductility experienced the most significant gains as >40x improvements were realized.
3. Excessive plastic strain (1.6) promoted dynamic recrystallization and the formation of adiabatic shear bands. Collectively, these features invoked declines in all tensile properties.
4. The strain rate applied in forging had no effect on densification but was found to influence the tensile properties of forged products. Slower rates enhanced dynamic

recrystallization which degraded yield strength and UTS while offering minor gains in tensile ductility.

5. Net forging strain and strain rate influenced the tensile properties of forged products. Both factors would need to be considered when a forged product with optimized mechanical properties is desired.

Acknowledgements

The authors would like to graciously acknowledge the financial support provided the Natural Sciences and Engineering Research Council of Canada (NSERC) via the collaborative research and development grant CRDPJ 486528. Laboratory assistance provided by colleagues at Dalhousie University (Randy Cooke, Dean Grijm) and Canmet Materials (Jonathan McKinley and Lucian Blaga) is gratefully appreciated as well.

CHAPTER 6 THERMAL-MECHANICAL WORKING OF SPARK PLASMA SINTERED PREFORMS FABRICATED FROM ALUMINUM 2219 POWDER

M.Y. Amegadzie[1], B. S. Amirkhiz[3], B.W. Williams[4], I.W. Donaldson[5], and D.P. Bishop[2]

1 – Graduate Student, Dalhousie University, Halifax, Nova Scotia, Canada
2 – Professor, Materials Engineering, Dalhousie University, Halifax, Nova Scotia, Canada
3 – Research Scientist, CanmetMATERIALS, Natural Resources Canada, Hamilton, Ontario, Canada
4 – Research Scientist, CanmetMATERIALS, Natural Resources Canada, Hamilton, Ontario, Canada
5 – Director of R&D North America, GKN Sinter Metals LLC, Auburn Hills, Michigan, USA

Status: Paper submitted to the journal "Materials Science and Engineering A".

Author Contribution: All experimental work was completed by Mark Y. Amegadzie. TEM work was performed by B. S. Amirkhiz at CanmetMATERIALS. The first draft of this paper was written by Mark Y. Amegadzie. Supervision was provided by D. Paul Bishop. Technical guidance and subsequent editing of the paper were performed by affiliate authors.

6.1 ABSTRACT

The effects of spark plasma sintering (SPS) coupled with hot upset forging of aluminum 2219 powder were studied. SPS was found to be an effective means of consolidating the powder as select specimens achieved full theoretical density. Although these as-sintered products also demonstrated a reasonable combination of tensile properties, they were greatly improved after forging. The most acute gains were observed in tensile ductility wherein 3x-4x improvements transpired. TEM analyses confirmed that forging manifested an appreciable disruption of the residual oxide networks present in the as-sintered product which was believed to be the primary driver of tensile property

enhancements. SPS+forge products were also responsive to T87 heat treatment. Typical T87 values for tensile yield strength, UTS and elongation to fracture were 350MPa, 465MPa, and 10% respectively. Interestingly, these values were attainable over a wide range of sintering and forging temperatures. TEM analyses confirmed that θ′ was the dominant precipitate present in the SPS+forge T87 products.

6.2 INTRODUCTION

Conventional powder metallurgy (PM) involves the production of parts from metal powders through a press and sinter process. The merits offered by this approach typically include near net shape fabrication, limited energy consumption, and economic benefits via high production rates. Over the years, ferrous PM components have maintained high levels of commercialized usage in the manufacture of automobile components. However, this sector is currently confronted with surging costs for petroleum products and federal mandates that stipulate progressively steeper reductions in greenhouse gas emissions from automobiles in the years ahead. While these circumstances are being addressed through several approaches, a common tactic that invariably benefits them all is vehicle mass reduction. Here, lightweight materials are under study as potential replacements for comparatively heavy conventional systems such as plain carbon steels. Options of interest include aluminum alloys [147], advanced high strength steels [148], magnesium alloys [149], and fiber reinforced composites [150] amongst others.

Aluminum alloys have enjoyed widespread success in this context given that these materials are readily available in large quantities, are economically feasible, offer

attractive mechanical/physical properties, and can be processed through a wide array of metal forming technologies including PM. Exemplary lightweight automotive components fabricated through aluminum PM include camshaft bearing caps, retainer rings, heat sinks [151], and critical components in automatic transmissions such as planetary reaction carriers [152]. To expand this scope of products, aluminum PM material development is essential and has been the research thrust in many instances. For example, studies have addressed the development of high strength Al-Zn-Mg PM systems [153], thermally conductive alloys [154], durable metal matrix composites [155], and PM counterparts to Al-Si casting alloys [156] as well as thermally stable systems such as 2618 [157]. Work on the latter is of particular interest since thermal stability is a common issue for many aluminum alloys while elevated temperatures are integral to numerous structural engine and transmission products that could be fabricated via PM. Accordingly, the research in this study seeks to build in this direction but with an emphasis on aluminum alloy 2219; an Al-Cu-based alloy designed for elevated temperature service yet primarily employed within the aerospace industry [158][159][160].

Previous studies have demonstrated that Al-Cu based alloys can be processed successfully via conventional press and sinter PM [157][161]. However, all these systems included small, yet controlled, additions of magnesium. This element is critical as it will disrupt the otherwise stable shell of alumina present on the exterior surfaces of the starting powder particles to a point where sintering is able to proceed [162]. Conversely, magnesium is deliberately avoided in 2219 as it compromises the desired formation of θ-

type ($CuAl_2$) phases within the microstructure. To ameliorate this constraint, a non-conventional approach to sintering was implemented. Commonly denoted as spark plasma sintering (SPS), it has been demonstrated that this technology can readily consolidate aluminum powders in the complete absence of magnesium [56]. However, remnants of the alumina shells still prevail within the post-SPS microstructure and likely have adverse effects on the finished product [136][55][163]. Hence, all SPS products were hot forged as this is known to disrupt this microstructural feature and maximize mechanical properties in conventionally sintered aluminum PM systems [76] [164]. The investigation of a SPS+forge processing scheme on aluminum 2219 powder was thereby pursued in this research, as it was viewed as a novel concept with commercial relevance.

6.3 MATERIALS

The base powder utilized in this study was a fully prealloyed powder (hereafter referred to as PA2219) manufactured by gas atomization at Ecka Granules GmbH (Velden, Germany). In doing so, wrought 2219 plate was melted and then atomized using high pressure nitrogen gas. The powder was then sieved to isolate particles within a size range of +45/-400 μm prior to SPS processing. The chemical composition of this cut of powder was quantified through Inductively Coupled Plasma Spectroscopy (ICPS). Results indicated that it conformed to the composition guidelines for wrought 2219 according to ASTM B209 (Table 6-1). It also had a spherical to rounded morphology as shown in Figure 6-1. The particle size distribution as measured using laser light scattering (Malvern, Mastersizer model 3000) is shown in Figure 6-2. The corresponding 90%, 50%, and 10% passing sizes were 258, 109, and 52μm respectively.

Table 6-1 Measured assay (weight%) of the +45/-400 µm PA2219 powder as compared with the specified compositional limits for wrought aluminum 2219 per ASTM B209.

	Composition (weight %)									
	Cu	Mn	V	Zr	Ti	Fe	Si	Mg	Zn	Al
Spec.	5.8 - 6.8	0.2 - 0.4	0.05-0.15	0.1 – 0.25	0.02 - 0.1	0.3*	0.2*	0.02*	0.1*	Bal.
PA2219	6.02	0.21	0.11	0.12	0.04	0.07	0.09	0.01	0.07	Bal.

* Indicates maximum permissible concentration.

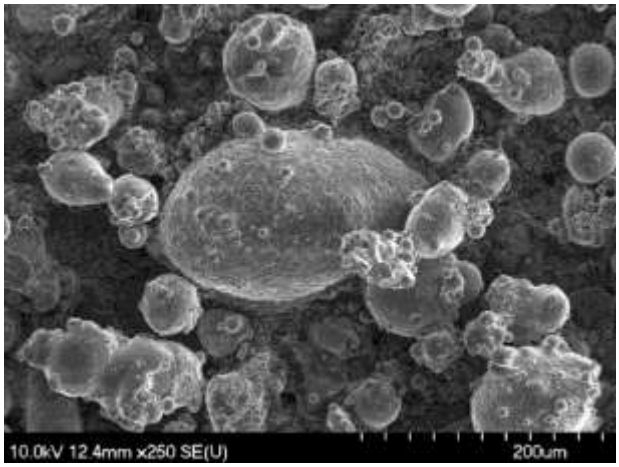

Figure 6-1 Image of the gas atomized PA2219 powder.

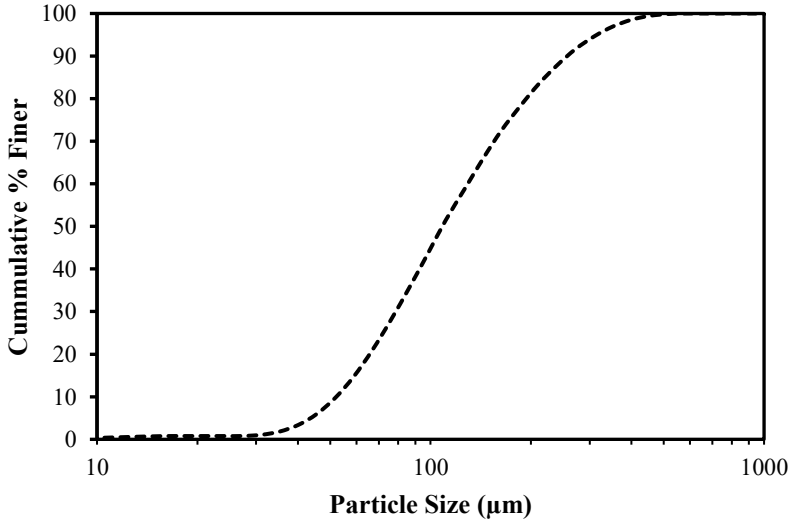

Figure 6-2 Particle size distribution of the PA2219 powder.

6.4 EXPERIMENTAL PROCEDURES

PA2219 was initially consolidated into 40mm diameter pucks via SPS using a Model 10-3 unit (Thermal Technologies Inc.) equipped with graphite tooling lined with graphite foil. All runs were completed under a mechanical vacuum atmosphere ($P = 10^{-2}$ torr) using pulsed DC current (on 36ms: off 8ms). The sintering cycle involved heating the powder at a rate of 50ºC/min to targeted sintering temperatures of 450ºC, 500ºC or 550ºC under a fixed pressure of 5MPa. The temperature was then held at the required value and the pressure ramped to 50MPa where it was held for 2 minutes prior to cooling to room temperature.

After sintering, select pucks were machined into cylindrical specimens (38 mm in diameter x 25 mm in height), sprayed with boron nitride, dried, and then preheated in a furnace for 1 hour to the temperature required for isothermal forging (200ºC, 300ºC, 400ºC, or 500ºC). Pre-heated specimens were then transferred to an Interlaken model SP225 hydraulic press equipped with flat platens that were also pre-heated to the forging temperature of interest and isothermally forged at a strain rate of 1 s^{-1} to a net true strain of 80%. In certain instances, samples were characterized in the T1 temper (as-sintered or sintered+forged conditions) while in others a T87 heat treatment was integrated into the production cycle. A T87 heat treatment was chosen since this heat treatment is known to increase the strength and hardness of AA2219. For the latter, sintered pucks were hot forged to 70% thickness reduction, solutionized in air at 535ºC for 1 hour, and quenched in water. Each was subsequently cold forged to achieve an additional 10% thickness reduction (net value of 80%) prior to artificial aging at 175ºC for 18 hours.

Round threaded-end tensile specimens were machined from the SPS/SPS+forged products to a geometry compliant with ASTM E8M. Each was then tested with an Instron Satec model 5594 200HVL hydraulic frame equipped with a 50kN load cell and an Epsilon model 3542 extensometer that remained attached to the sample through the point of fracture. In all instances, three replicate specimens were tested from which averaged tensile properties were deduced. Densities of the sintered preforms were determined using oil infiltration in combination with Archimedes principle per MPIF standard 42. The theoretical densities of the specimens were calculated using a standardized rule of mixtures.

Microstructural analyses were accomplished through a combination of light microscopy, scanning electron microscopy (SEM), electron backscatter diffraction (EBSD) and transmission electron microscopy (TEM). As needed, cross sections of specimens were mounted in epoxy using a Struers CitoPress-5 automatic mounting press. The mounted specimens were then ground with a 1200 grit silicon carbide disc and subsequently polished in a Struers Tegramin Autopolisher through a series of cloth pads and solutions (15, 3, 1 μm diamond suspensions and finally 0.05 μm colloidal silica). Optical microscopy was accomplished using a Zeiss Axiotech upright microscope equipped with a halogen light source. SEM and EBSD analyses employed a Hitachi S-4700 Cold Field Emission SEM equipped with a HKL system and Nordlys Oxford Instruments detector. Specimens for TEM examination were mechanically thinned to 3mm and then ion milled using a Gatan 691 PIPS. TEM analyses were completed with a Tecnai Osiris TEM equipped with X-FEG gun operated at 200 keV. This included the acquisition of

conventional bright and dark field images, scanning TEM (STEM) imaging using bright field and Z-contrast high angle annular dark field (HAADF) detectors, and elemental mapping by means of energy dispersive spectroscopy (EDS).

6.5 RESULTS AND DISCUSSION

6.5.1 SPARK PLASMA SINTERING RESPONSE OF PA2219

Research commenced with an evaluation of the effects of SPS temperature on the PA2219 powder. Representative microstructures of the products as observed through light microscopy are presented in Figure 6-3. Images revealed a high sinter quality as evident by the visible absence of interparticle boundaries. Also of interest was the fraction of retained porosity. This feature appeared as distinct spherical pores within the optical micrographs. The general trend observed was that the fraction of visible pores decreased with increasing SPS temperature. In this sense, the specimen sintered at the lowest temperature (450ºC) exhibited the highest concentration while those sintered at 500ºC and 550ºC were seemingly pore-free. This observation was consistent with density measurements (Figure 6-4). These data indicated that the 450ºC specimen was 98.8% dense compared to counterparts sintered at 500ºC and 550ºC which attained full (100%) density.

Next, tensile tests were completed to further assess the performance of the as-sintered preforms (Figure 6-5). Here trends in the data were relatively flat as there were no dramatic gains/losses in tensile properties noted as a function of SPS temperature. However, it did appear that there was a minor reduction in yield strength concomitant

with a minor improvement in UTS as sintering temperature increased. For instance, when the SPS temperature was increased from 450ºC to 550ºC, there was a net decline in yield strength of 15MPa while UTS rose by 7MPa. The ductilities were all similar and fell within a range of 6-8%.

As shown in Figure 6-6, SEM assessment indicated that the principal microstructural constituents resolvable within the sintered preforms were secondary phase particles distributed within the α-aluminum matrix. The particles were typically ~1-8μm in size, exhibited a rounded/irregular morphology, and were found to be enriched in aluminum and copper via EDS. This suggested that these were likely $CuAl_2$ (θ). The particles were relatively small and homogenously distributed at the lowest SPS temperature assessed. As sintering temperature increased, some became obviously coarser as a result of greater heat input. This may have contributed to the slight decline in yield strength with increasing temperature. Essentially, finely dispersed particles provide an effective barrier to the motion of dislocations unlike larger particles which invoke the Orowan bypass mechanism. The precipitate-shear dislocation interaction is typical of finer particles and synonymous to higher yield strength. It was also noticed that some transitioned into a plate/needle like morphology at a SPS temperature of 550ºC. At this temperature, it was likely that some of the $CuAl_2$ (θ) particles had dissolved into solid solution and then precipitated out as the product was subsequently cooled to room temperature.

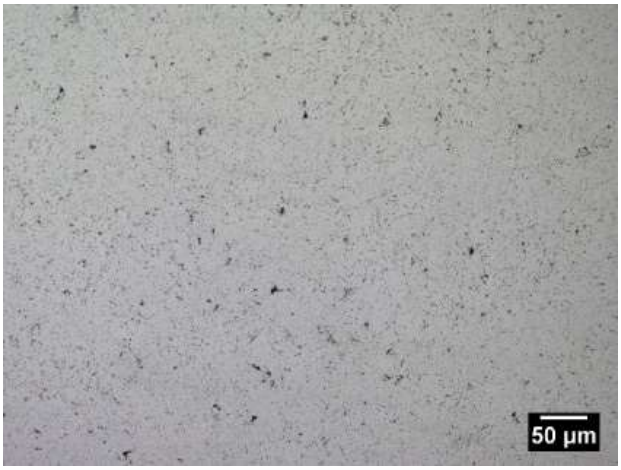

(a)

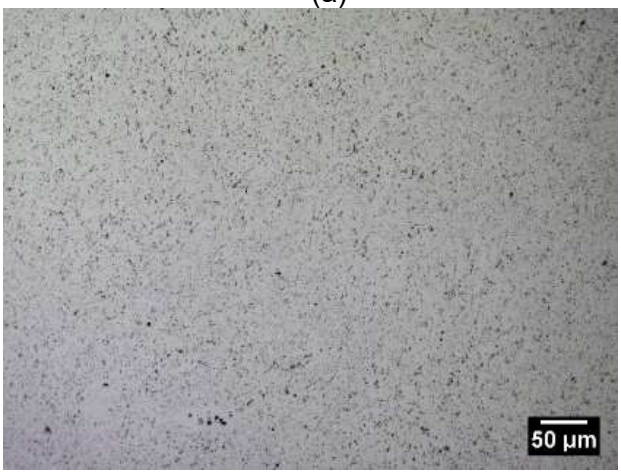

(b)

(c)

Figure 6-3 Micrographs of PA2219 SPSed at (a) 450ºC, (b) 500ºC and (c) 550ºC.

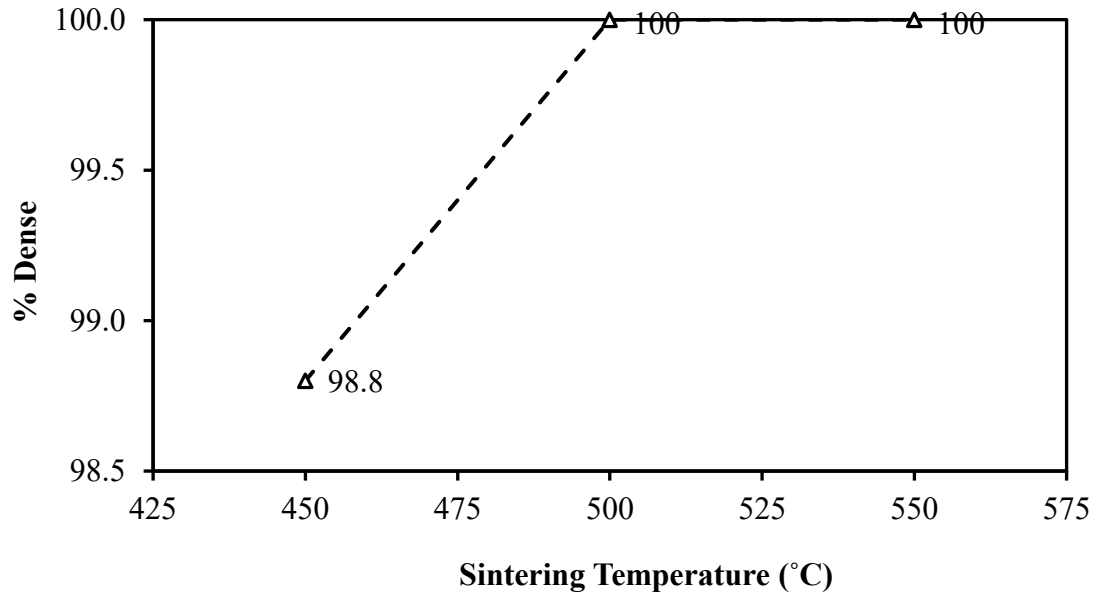

Figure 6-4 Effects of spark plasma sintering temperature on the final density of the consolidated product.

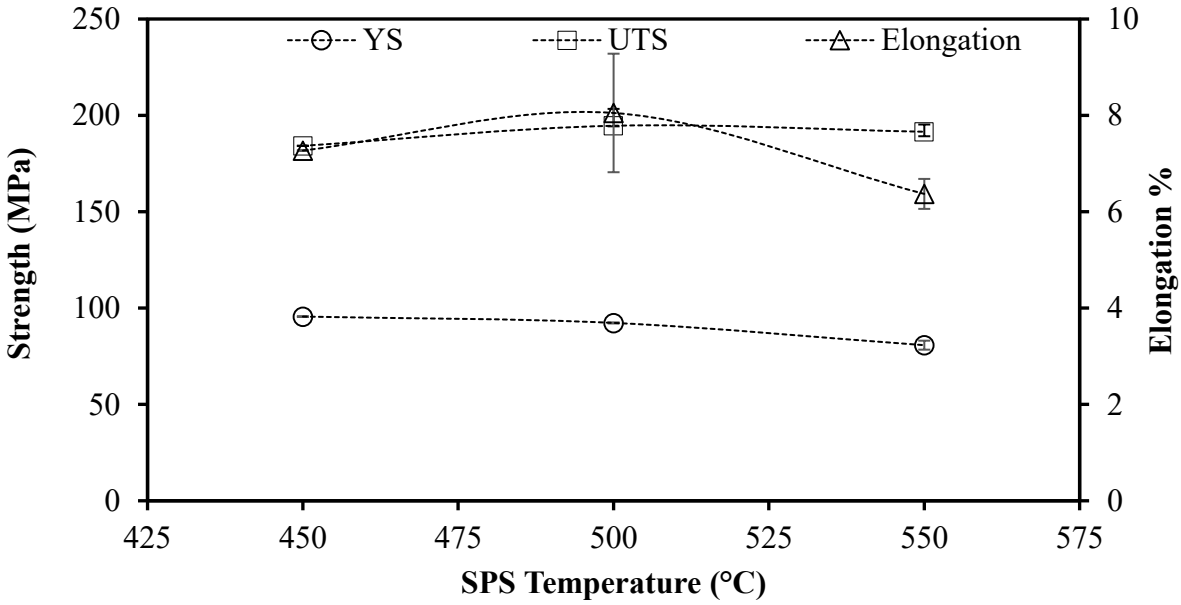

Figure 6-5 Tensile properties of SPS processed specimens of PA2219. All samples in the as-sintered (T1) condition.

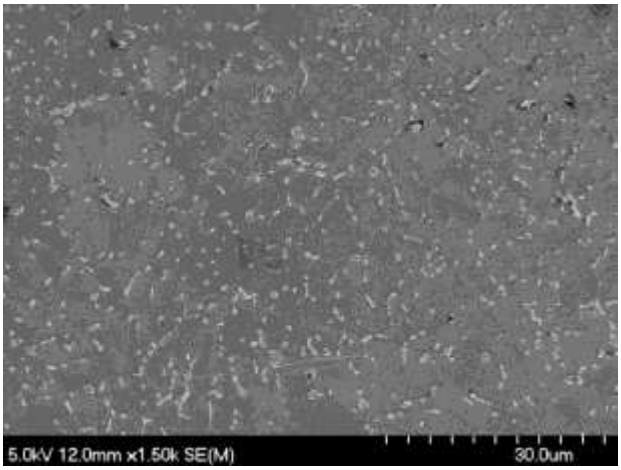

(a)

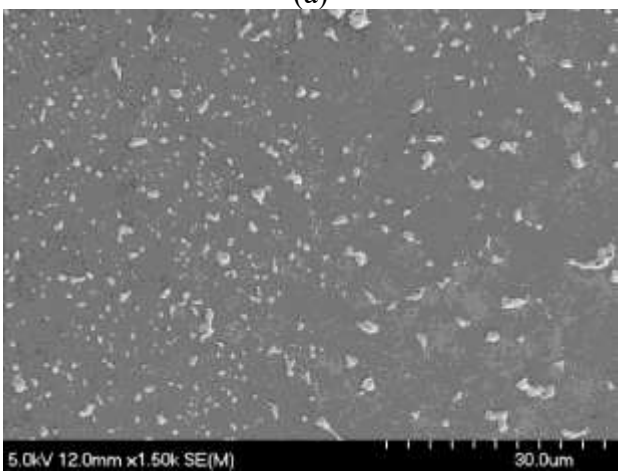

(b)

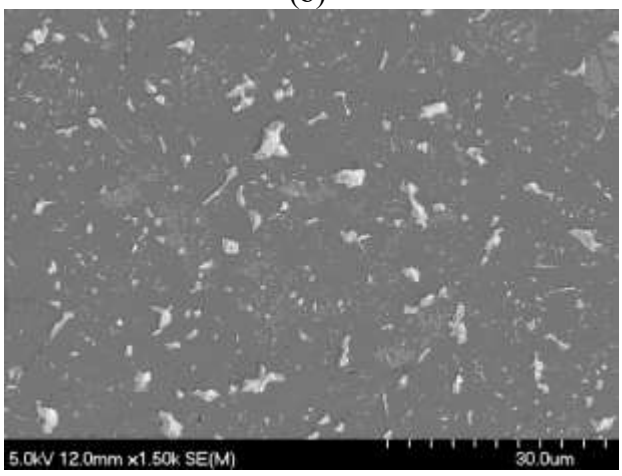

(c)

Figure 6-6 SEM images of samples consolidated at (a) 450ºC, (b) 500ºC and (c) 550ºC via SPS.

Another feature of considerable interest was the grain structure. Accordingly, electron backscatter diffraction (EBSD) analyses were employed to examine this attribute. It should be noted that the grain boundaries in the EBSD maps are displayed as white and black lines; these delineate grains with boundary angles <15º (low angle grain boundaries (LAGBs) or sub-grains) and >15º (high angle grain boundaries (HAGBs)) respectively. Direct inspection of EBSD maps (Figure 6-7) confirmed that the grains coarsened progressively as the sintering temperature increased. Consequently, this decreases the grain boundary area needed for impeding the motion of dislocations. This would have partly contributed to the slight downward trend in yield strength with increasing SPS temperature. Furthermore, the concentration of subgrains decreased with increasing SPS temperature falling from 28% to 23% to 10% in the 450ºC, 500ºC and 550ºC samples respectively. This indicated that some level of annealing had transpired in the preform to rid itself of LAGBs as the SPS temperature increased.

The final means of microstructural assessment involved TEM inspection. Exemplary data for the specimen SPS processed at 500ºC are shown in Figure 6-8 and Figure 6-9. Firstly, the general microstructure of the SPS preform is presented in a lower magnification bright field image (Figure 6-8). Here, the as-sintered microstructure was dominated mainly by $CuAl_2$ (θ) particles located near grain boundaries and within the grains themselves. Further examination of the sintered microstructure revealed a thin film at prior particle boundaries (Figure 6-9(a)). EDS mapping revealed that this thin layer was enriched in oxygen and existed as a continuous film.

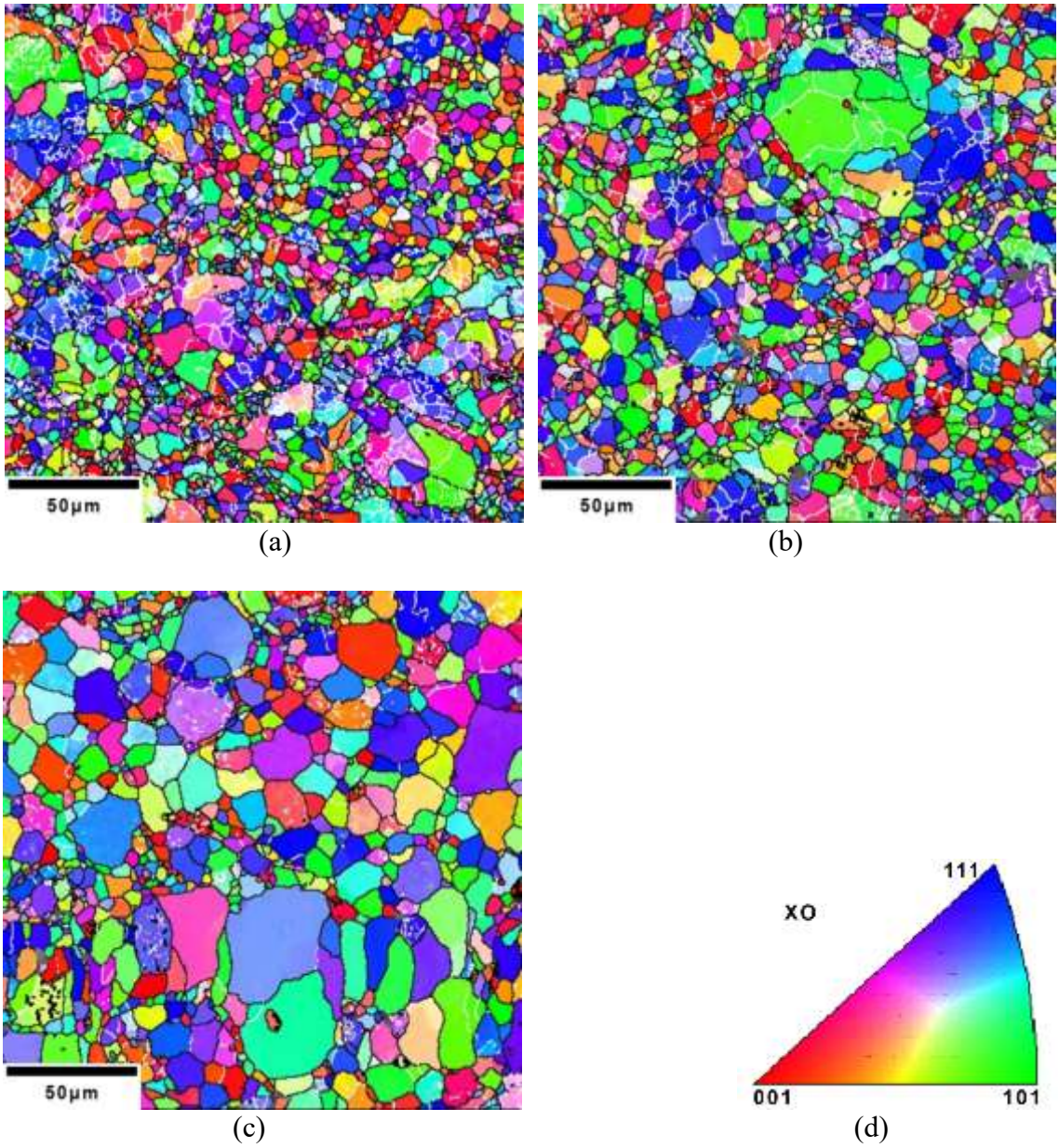

Figure 6-7 EBSD maps of specimens SPS processed at (a) 450ºC (b) 500ºC and (c) 550ºC. All samples were loaded vertically during SPS processing.

The PA2219 powder was produced through gas atomization. The gas itself was a mixture of nitrogen and oxygen in a 97:3 volume % ratio. Oxygen was an essential element as it passivated the surfaces of all powder particles to facilitate safe handling during SPS. Hence, the source of the oxide film observed via TEM would have been the passive layer deliberately engineered into the raw powder. The nominally continuous nature of this film indicated that the extent of its disruption during SPS was incomplete. Accordingly, an oxide network would have prevailed within all SPS products to the detriment of important mechanical properties such as tensile ductility (Figure 6-5).

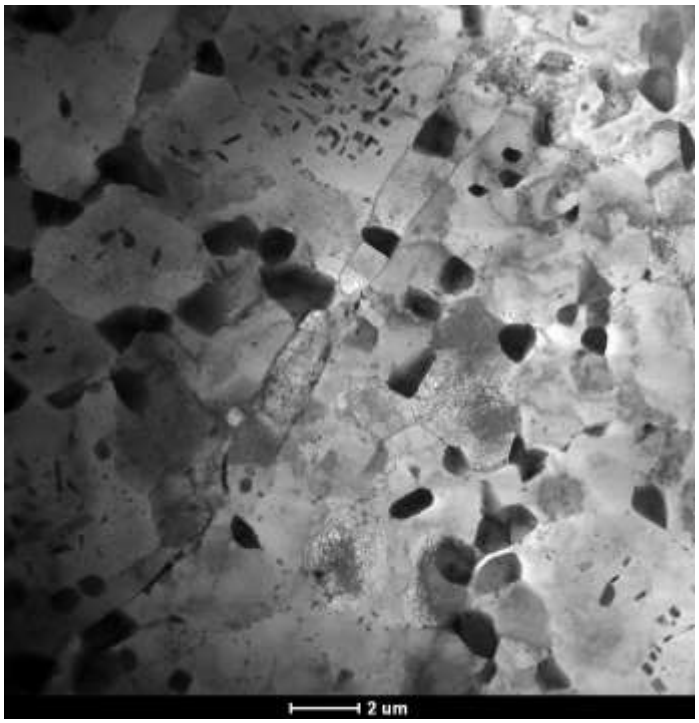

Figure 6-8 Bright field TEM micrograph revealing the general nature of θ-phase precipitates/dispersoids within a specimen of PA2219-T1 SPS processed at 500ºC.

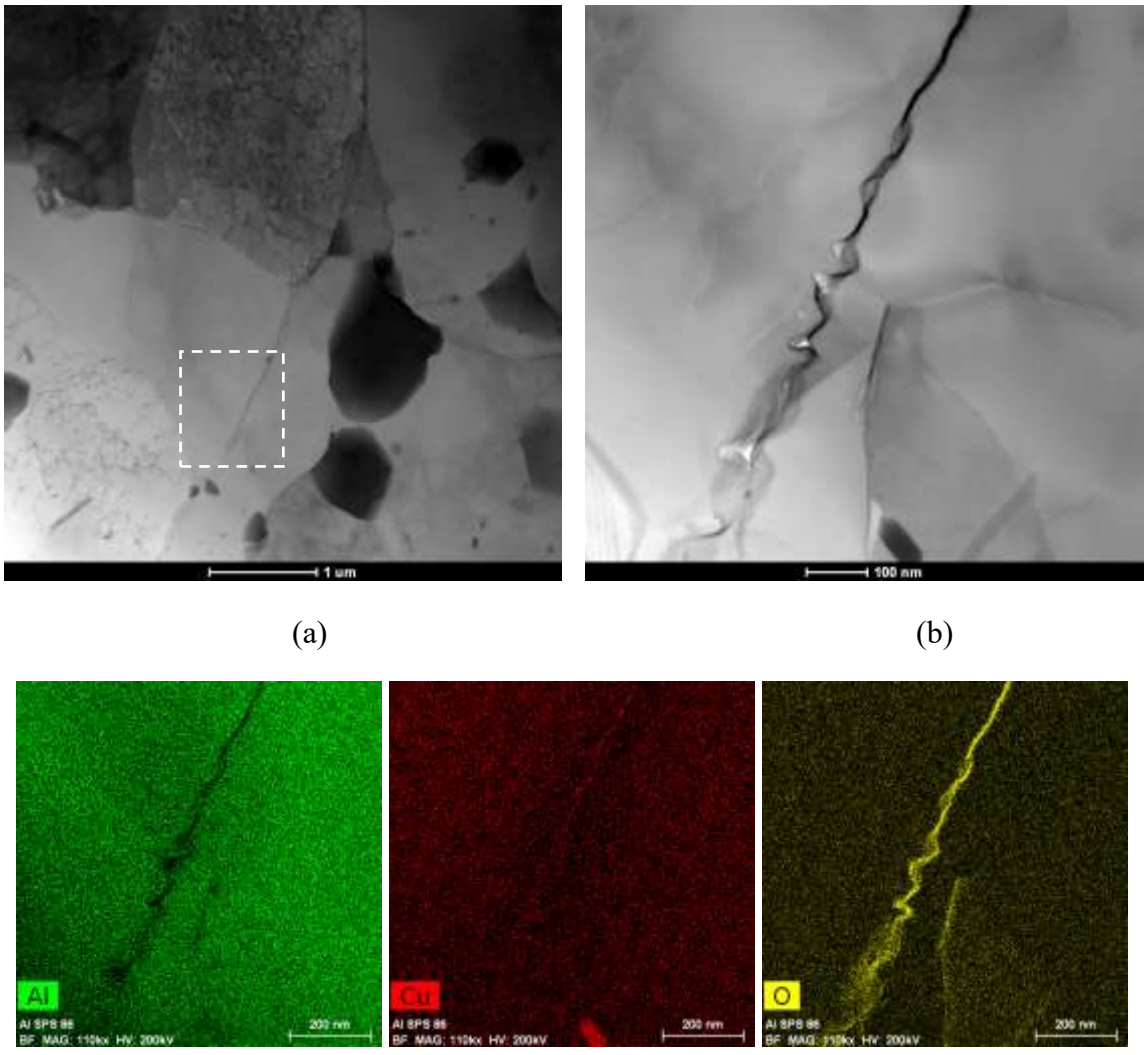

(a) (b)

(c) (d) (e)

Figure 6-9 TEM images of a prior particle boundary present in a specimen of PA2219-T1 SPS processed at 500ºC. (a) BF image, (b) BF image of inset region defined in (a), and ESD elemental maps for (c) Aluminum, (d) Copper, and (e) Oxygen.

6.5.2 FORGEABILITY OF SPS PRODUCTS

SPS specimens were hot forged at various temperatures in the next phase of research. Traditionally, thermo-mechanical testing system, such as a Gleeble is used to obtain true stress-strain response of materials at elevated temperatures. In the current work, the load and displacement data from the compressive flow behaviour during forging runs on the 110 ton (225 kip) hydraulic press were utilized to produce true stress-true strain plots. A constant strain rate of 1 s^{-1} was achieved by adjusting the displacement versus time response of the main hydraulic cylinder on the press. Curves acquired from specimens processed at each SPS temperature of interest and then forged at 500ºC are shown in Figure 6-10. Typically, the flow curve increased linearly to a stress of ~53 MPa before fluctuating downward and then transitioning into a prolonged period of nominally steady state plastic flow. The initial decline in the plastic region is attributable to the engagement of softening mechanisms such as dynamic recovery, dynamic recrystallization and/or dynamic precipitation [141][142]. Conversely, the concomitant rise in flow stress near the end of the cycle stemmed from an accumulation of friction between the sample and the platens. Evidently, the minor differences in density (Figure 6-4) and microstructure (Figure 6-6) did not have a meaningful impact on forging response. The flow curves acquired when specimens SPS processed at 500ºC were forged at 200ºC to 500ºC were also plotted (Figure 6-11). Essentially, the elastic to plastic transition occurred at a progressively higher stress as the forging temperature decreased (Figure 6-10(b)). This was expected as the material became softer with increasing forge temperature. The net difference amount to a 5x decline in the required forging pressure as temperature increased from 200 to 500°C.

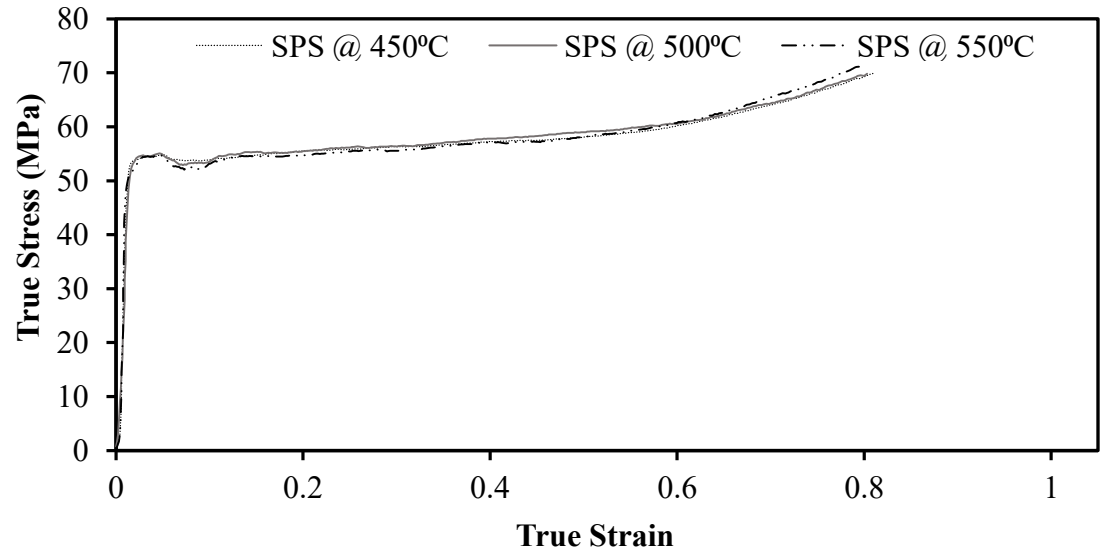

Figure 6-10 Compressive flow curves acquired when forging preforms were originally sintered at different temperatures.

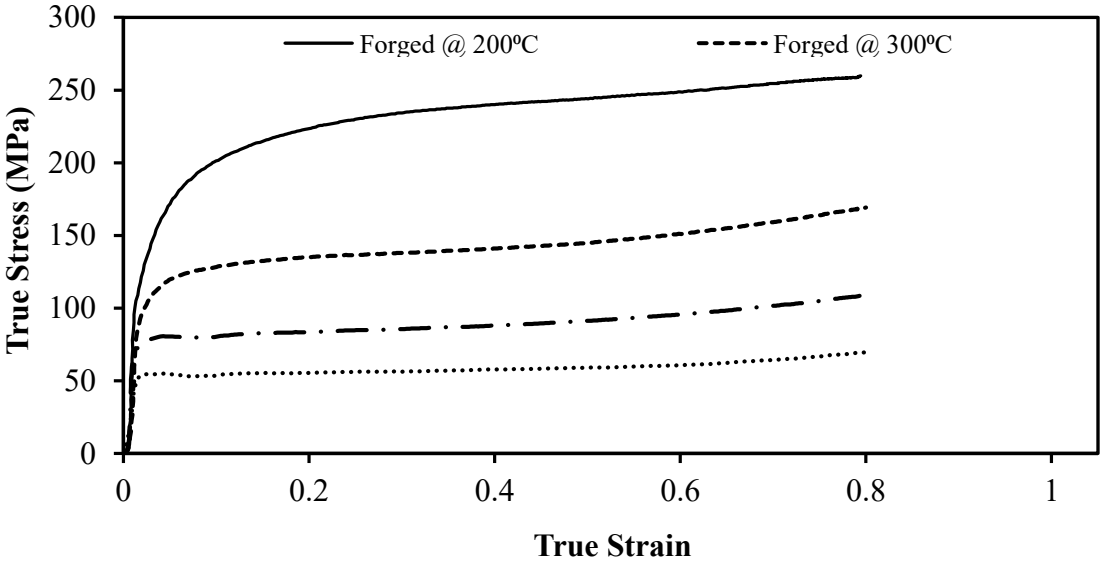

Figure 6-11 Compressive flow curves acquired when sintered preforms were forged at different temperatures. All samples consolidated via SPS at 500ºC.

6.5.3 METALLURGICAL ASSESSMENT OF FORGED SPECIMENS

SEM images of specimens SPS processed at 500ºC and forged at 200ºC to 500ºC are shown in Figure 6-12. These illustrate the general trend observed in that residual porosity was seemingly absent from all specimens. This included those originally sintered at 450ºC wherein its obvious presence was noted in the as-sintered preform (Figure 6-4). This confirmed that forging provided an effective means of eliminating residual porosity in the SPS products.

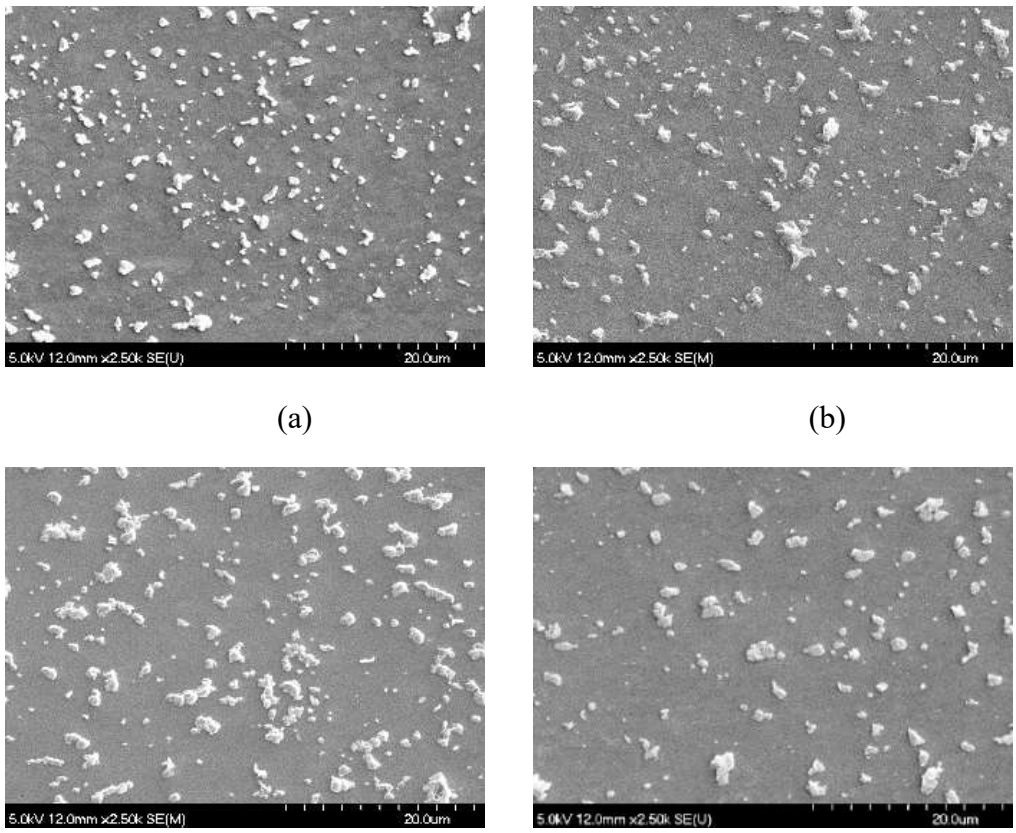

Figure 6-12 SEM images of specimens SPS processed at 500ºC and forged at (a) 200ºC (b) 300ºC (c) 400ºC and (d) 500ºC. All specimens in the T1 temper.

Tensile data for SPS+forge samples are given in Table 6-2. All specimens, regardless of forging temperature, exhibited tensile properties that were significantly improved relative to their non-forged counterparts (Figure 6-5). For example, the yield strength and UTS were nearly doubled as a result of forging. Gains were even more acute for elongation to fracture wherein 3-4x improvements were noted. Such improvements in tensile properties, particularly in ductility, were viewed to be rather remarkable from a PM standpoint. More specifically, obvious transitions were noted when considering data for samples SPS processed at 500ºC and then forged at different temperatures. Here, the yield strength decreased measurably as forging temperature increased from 200 to 400ºC culminating in a net loss of 99MPa (47%). The trend then reversed rather sharply under the highest forging temperature of 500ºC as improvements in yield strength and UTS transpired. It is postulated that the behaviour came as a result of changes to the underlying structure of θ-type precipitates. In this sense, when forging at temperatures of 200 to 400°C, any pre-existing θ-type precipitates would have over-aged in-situ as the billet was held at the temperature of interest.

Table 6-2 Tensile properties of PA2219 in the as SPS+forged condition (T1).

SPS Temperature (ºC)	**Forge Temperature** (ºC)	**Yield Strength** (MPa)	**UTS** (MPa)	**Elongation** (%)
450	500	142 ± 1	304 ± 3	23 ± 2.2
500	500	138 ± 1	302 ± 1	24 ± 1.0
550	500	127 ± 3	291 ± 2	24 ± 2.8
500	200	212 ± 1	261 ± 2	16 ± 1.1
500	300	148 ± 1	211 ± 2	23 ± 2.0
500	400	113 ± 5	226 ± 4	24 ± 0.4
500	500	138 ± 1	302 ± 1	24 ± 1.0

The rate of this effect would have increased with rising temperature such that the precipitates present in the 400°C forging would have coarsened the most to prompt the greatest net decline in T1 yield strength; and concomitantly, a rise in ductility. This is consistent with the fact that the recommended annealing temperature for wrought 2219 is 415°C. Upon shifting the forging temperature to 500°C precipitates would no longer tend to coarsen, but instead, tend to dissociate. The respective copper atoms would thereby diffuse into solid solution at the forging temperature. The dissolved copper would have then precipitated out of solution (a) upon cooling and (b) when held at ambient temperature prior to tensile testing in accordance with the meta-stable sequence of θ-type events [12]. The resultant precipitates would have been relatively fine in size and more homogenously distributed within the final microstructure to instill the observed gains in yield strength and UTS.

Select specimens were then subjected to a T87 heat treatment. Data on the tensile properties for these are presented in Table 6-3. Properties were quite comparable amongst the samples tested. Here, yield strengths and UTS values were all on the order of 354 and 466MPa respectively while elongations ranged from 9 to 13% with a possible preference towards the use of a higher SPS temperature. As expected, the T87 heat treatment resulted in significant strength improvement over their as-sintered and SPS + forge T1 counterparts and represented the highest strength products produced to this point. It appeared that the parameters implemented for SPS and forging had minimal impact as all T87 samples exhibited comparable properties.

Table 6-3 Mechanical properties of SPS+forged products subjected to T87 heat treatment.

SPS Temperature (ºC)	**Forge Temperature** (ºC)	**Yield Strength** (MPa)	**UTS** (MPa)	**Elongation** (%)
450	500	357 ± 2	465 ± 3	9 ± 0.4
500	200	354 ± 1	467 ± 2	9 ± 0.9
500	500	352 ± 6	466 ± 4	10 ± 2.4
550	500	354 ± 1	466 ± 1	13 ± 1.1

To understand the T87 samples in more detail, microstructural studies via electron microscopy were completed. Figure 6-12 shows the microstructures of specimens SPS processed at 500ºC/forged (T87) at 200ºC and 500ºC as observed through SEM. Comparatively, there was an acute reduction in the amount of coarsened $CuAl_2$ (θ) phase present relative to that observed in the as-sintered (Figure 6-6) and sintered+forged (Figure 6-12) microstructures. The inclusion of a proper solutionization stage (535ºC for 1 hour followed by a water quench) was clearly responsible for the observed reduction. The fact that some remnant θ particles (~2-5μm in size) persevered was not surprising as the alloy maintained a total copper concentration of 6.02 weight % (Table 6-1); a value that was in excess of the maximum amount dissolvable in aluminum (5.65 weight%). EBSD was then performed to study the evolution of the grain structure in the T1 and T87 conditions. This began by examining a T1 specimen SPS processed at 500ºC/forged at 500ºC (Figure 6-14). Data revealed the presence of grains that were oriented transverse to the direction of the applied forging load. A statistical assessment of the misorientation grain boundary angles revealed that the respective amounts of HAGBs and subgrains were 62% and 38% (Figure 6-14 (c)). It should be recalled that in the specimen sintered

at 500ºC, only ~23% of the grain boundaries were subgrains. This increase indicated that dynamic recovery had most likely occurred during the forging process.

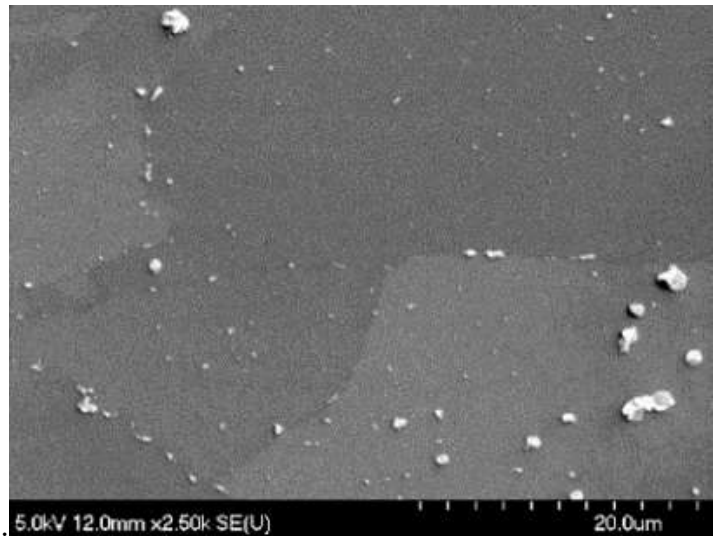

(a)

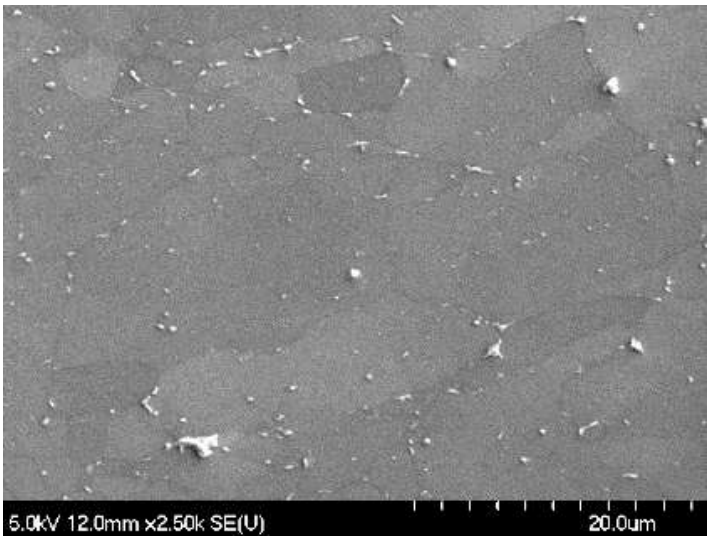

(b)

Figure 6-13 SEM images of SPS+forge-T87 materials. Specimens were SPS processed at 500ºC and then forged at (a) 200ºC and (b) 500ºC prior to final heat treatment into the T87 state.

In T87 specimens SPS processed at 500ºC/forged at 200ºC and 500ºC, the grains were again elongated perpendicular to the direction of applied forging load (Figure 6-15). However, the average grain size was now much larger in the T87 products with this effect becoming more pronounced at the higher forging temperature. In addition, smaller grains were observed associated with subgrains and grain boundaries of the larger grains in the specimen SPS processed at 500ºC/forged at 500ºC (T87). It is unclear why this was the case since several reasons can be attributed to abnormal grain growth which primarily results in the bimodal distribution of grains in aluminum alloys. Meanwhile, it can be speculated that discontinuous dynamic recrystallization could have been activated which resulted in grain coarsening at grain boundaries during ageing. Similarly, continuous dynamic recrystallization could also have been activated through the same partial phenomenon and later transitioned into static recrystallization. It should be noted that incomplete continuous dynamic recrystallization has been reported in AA2219 hot compressed at temperatures above 200ºC [165]. The probable occurrence of these processes could be linked to the coexistence of smaller grains in direct contact with low angle grain boundaries and boundaries in the specimen forged at the higher temperature.

In addition, grains in the specimens forged in the T87 temper were ~14 times larger than those observed in the T1 specimen (Figure 6-14). Not surprisingly, grain growth was accompanied with an acute reduction in the concentration of subgrains in T87 specimens (Figure 6-15). This was substantiated by the statistical misorientation data in Figure 6-16. Collectively, both T87 specimens exhibited relatively low concentrations (7%, 16%) of low angle grain boundaries as compared the T1 counterpart (38%).

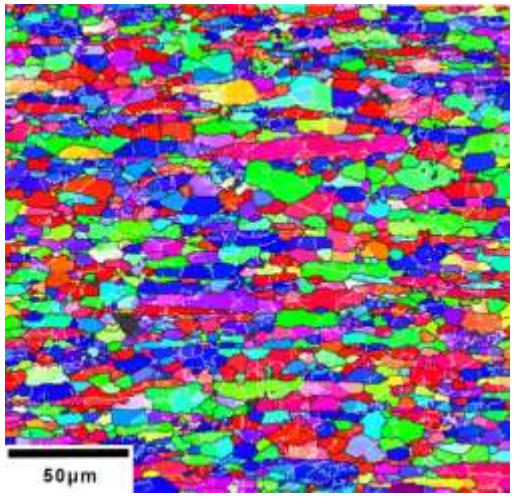

(a)

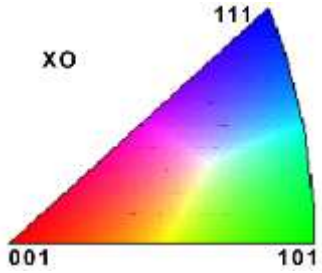

(b)

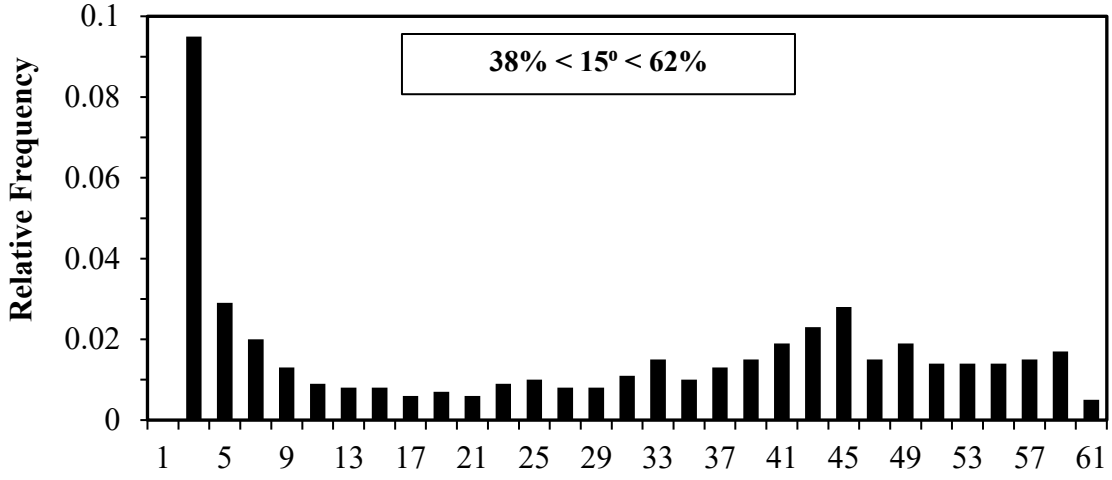

(c)

Figure 6-14 EBSD analysis of the specimen SPS processed at 500ºC and then forged at 500ºC (T1 condition). (a) grain misorientation map, (b) inverse pole figure, and (c) statistical assessment of the grain boundary misorientation angles. Forging load was applied in a vertical direction.

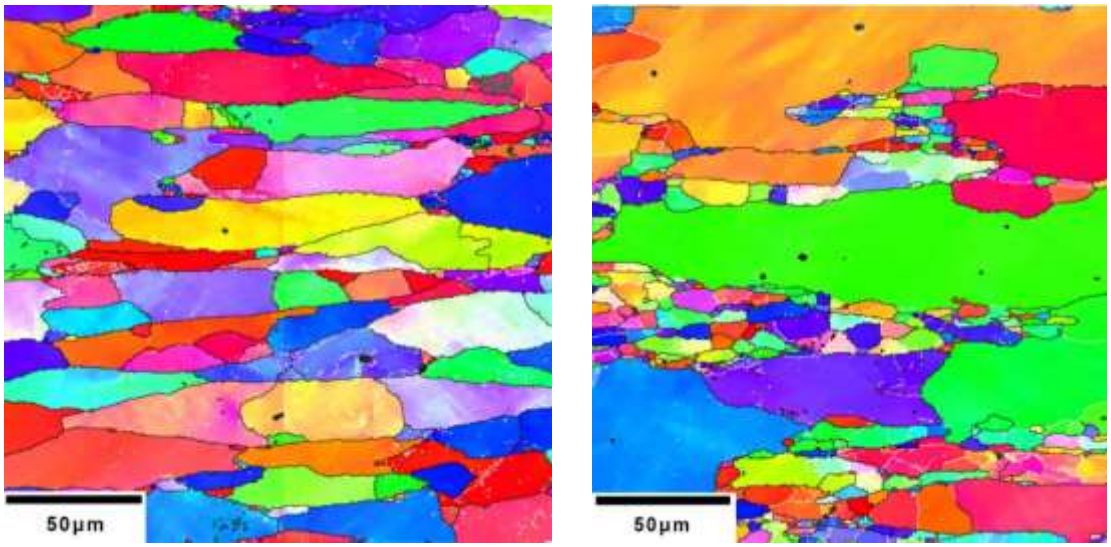

(a) (b)

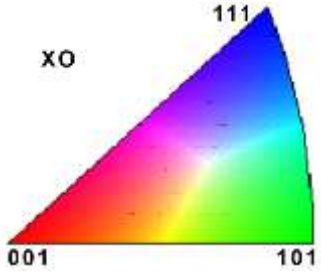

(c)

Figure 6-15 Grain misorientation maps of SPS+forged T87 specimens. Samples were SPS processed at 500ºC and then forged at (a) 200ºC or (b) 500ºC prior to heat treatment. The corresponding inverse pole figure is provided in (c). Forging load was applied in a vertical direction.

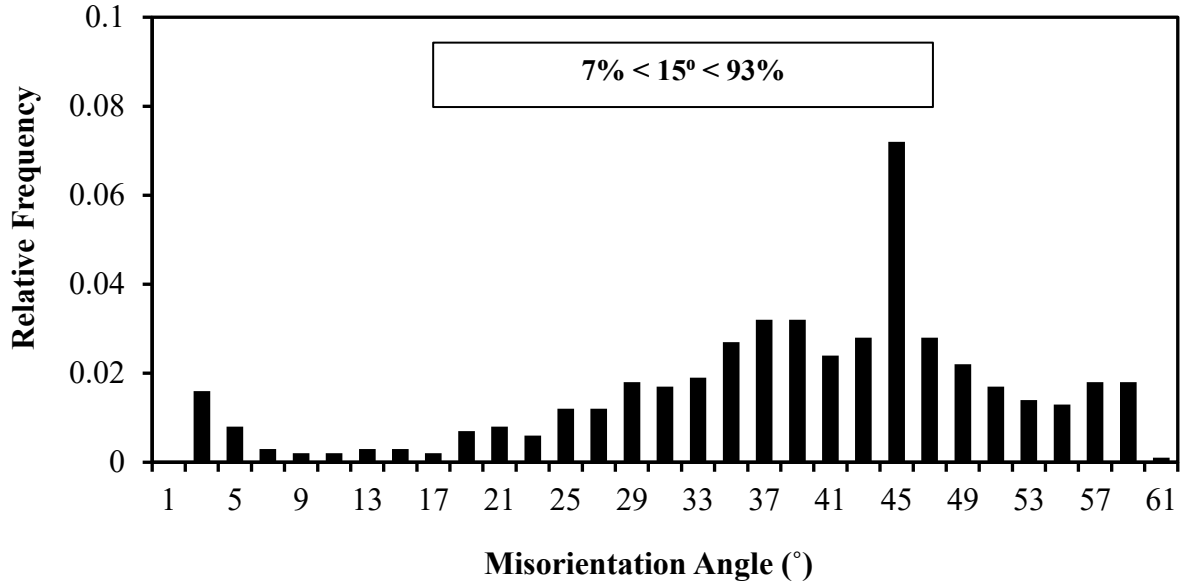

(a)

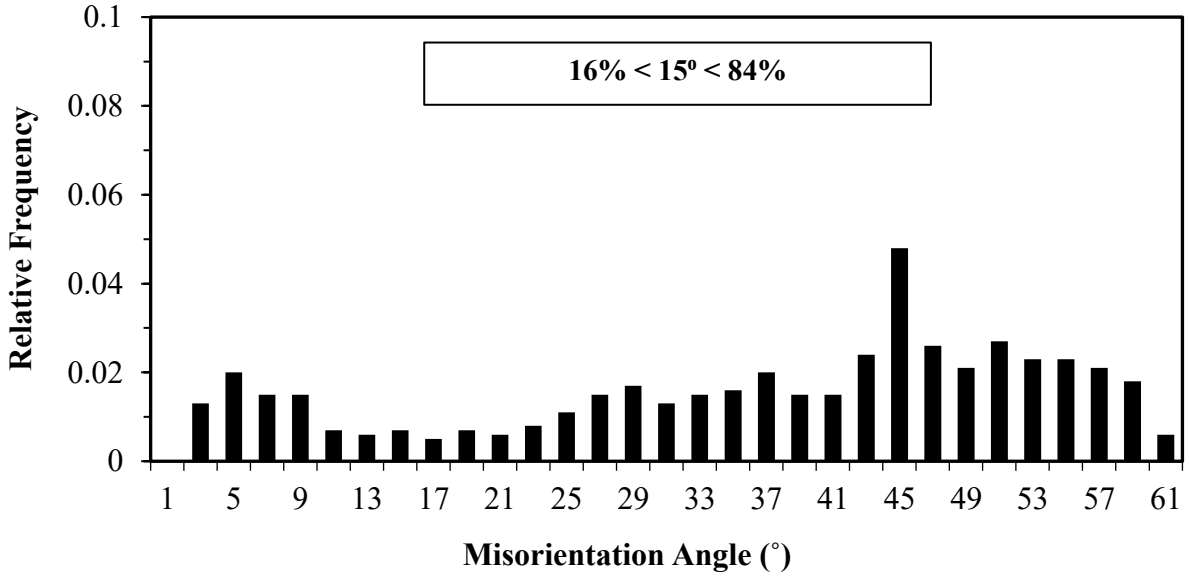

(b)

Figure 6-16 Statistical assessment of the grain boundary misorientation angles of the specimens SPS processed at 500ºC and then forged at (a) 200ºC and (b) 500ºC prior to heat treatment.

TEM analyses of the precipitates within a forged sample subjected to T87 heat treatment (SPS processed at 500ºC and forged at 500ºC) are shown in Figure 6-17 and Figure 6-18. All grains were found to contain plate-like precipitates that were obviously aligned with select habit planes. As shown in Figure 6-17, the precipitates were typically ~250nm in diameter and 15nm in thickness. Somewhat larger particles were also observed yet these were localized to grain boundaries. In order to get a sense of the difference between these intergranular and intragranular phases, a HAADF imaging mode was applied (Figure 6-17(b)) as this provides Z-contrast. In this image secondary phases localized on the grain boundaries were significantly brighter than those within the grains. This indicated that the former were enriched in elements with a higher atomic number other than Cu. Zirconium was the only element detected in the alloy (Table 6-1) that fulfilled this concept. Accordingly, these particles were likely enriched in this element.

Additional bright field images of the precipitates as viewed along [001] and [011] zones axes are shown in Figure 6-18 together with the corresponding selected area diffraction patterns (SADPs). In the [001] orientation (Figure 6-18(a),(b)), the precipitates were viewed in an edge-on manner and lied parallel to the {001} family of planes. The pattern of superlattice reflections within the corresponding SADP was highly consistent with those observed for θ' type precipitates by other researchers [166][167]. Similar observations were noted when the sample normal was oriented closely parallel to the [011] zone axis (Figure 6-18(c), (d)). Here again, the superlattice reflections were consistent with the presence of θ' type precipitates substantiating that this was indeed the

dominant precipitate within the forged T87 product, and as such, the principal strengthening mechanism.

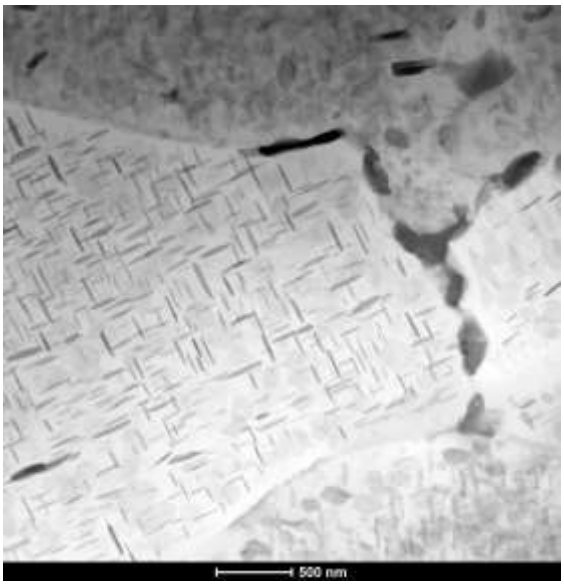

(a)

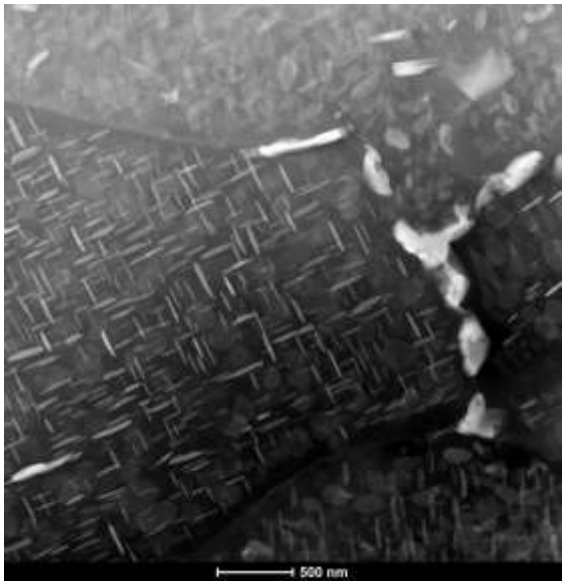

(b)

Figure 6-17 Precipitates observed in SPS+forged+T87. (a) Bright field and (b) corresponding HAADF micrographs. Sample was SPS processed at 500°C and then forged at 500°C prior to T87 heat treatment.

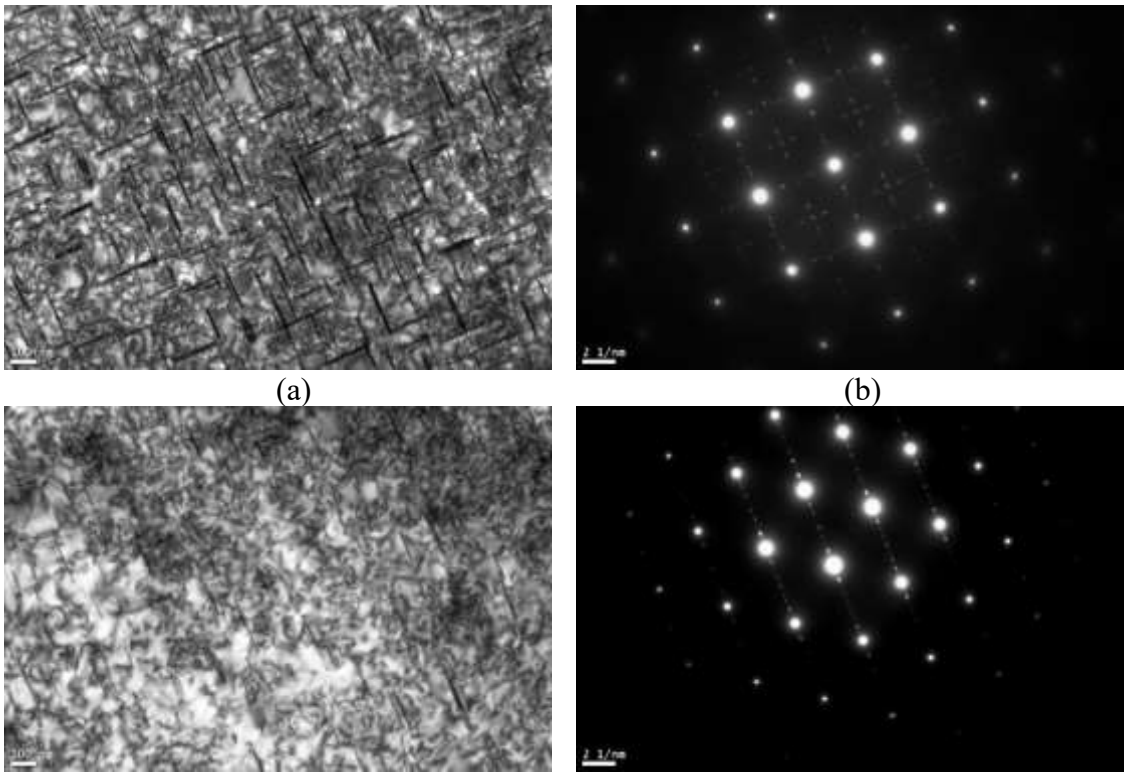

Figure 6-18 TEM analysis of the precipitates present in SPS+forged+T87. (a) Bright field TEM micrograph and (b) corresponding [001] diffraction pattern. (c) Bright field TEM micrograph and (d) corresponding [011] diffraction pattern. Sample was SPS processed at 500°C and then forged at 500°C prior to T87 heat treatment.

Further examination of the microstructure emphasized an assessment of prior particle boundaries. An example of this feature within a forged T87 product is shown in Figure 6-19 along with the accompanying EDS map for oxygen. These findings confirmed that the prior particle boundaries were now quite distorted as compared to those present in the starting billet (Figure 6-9). This was clearly a consequence of plastic deformation that transpired during forging. The principal benefit of which is illustrated in the EDS map for oxygen (Figure 6-19(b)). Here it was noted that the oxide films were no longer smooth and continuous. Instead, they were quite fragmented such that direct metal-to-metal bonding was now a prominent attribute. This implied that the prior particle boundaries (which were predominantly oxide-to-oxide contacts in the as-sintered

material) now included significant regions of proper metallic bonding. It is believed that this was the principal mechanism responsible for the significant rise in tensile properties noted between T1 samples in the as-sintered state (Figure 6-5) versus those that were processed through an SPS + forge sequence (Table 6-2). These benefits then prevailed through the incorporation of a T87 treatment as yield strength and UTS increased substantially, whilst the material maintained a significant level of ductility.

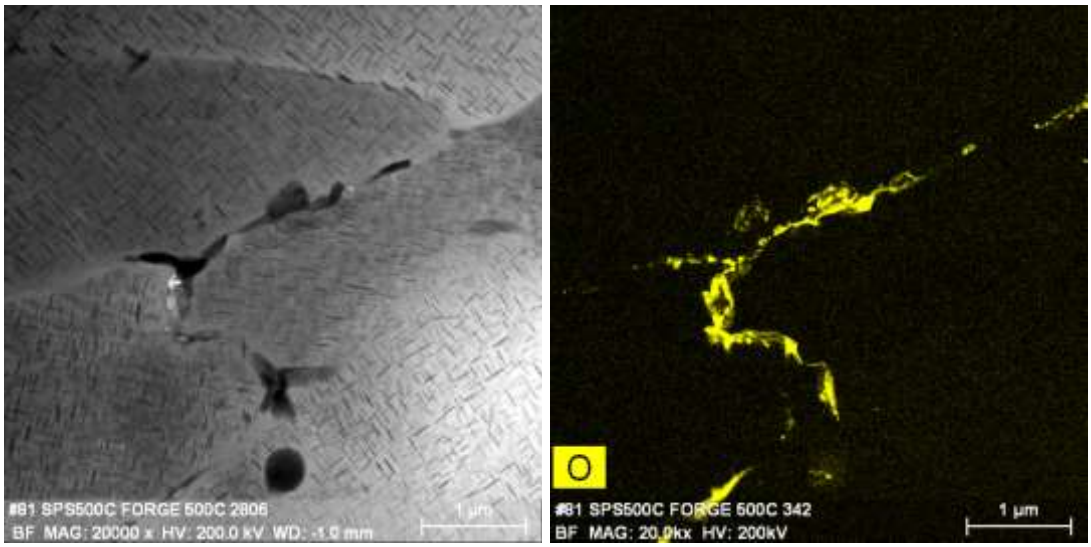

(a) (b)

Figure 6-19 TEM analysis of a prior particle boundary present in a specimen of PA2219-T87. (a) BF image and (b) elemental map for oxygen. Sample was SPS processed at 500°C and then forged at 500°C prior to T87 heat treatment.

6.6 CONCLUSIONS

1. PA2219 powder was highly responsive to SPS processing as sintered products demonstrated near full density and a reasonable combination of strength and ductility.

2. Hot upset forging was an effective means of disrupting the residual oxide networks and the small fraction of residual pores that were present in sintered billets of PA2219. These changes were synonymous with marked increases in tensile yield strength, UTS, and most dramatically, elongation to fracture implying they underpinned these enhancements.
3. Sintered billets of PA2219 were responsive to hot forging under a wide range of temperatures.
4. Significant gains in tensile yield strength and UTS were universally instilled in the SPS+forge products despite wide adjustments to the sintering and forging temperatures.
5. TEM analyses confirmed that sinter+forge T87 products contained an abundance of θ' precipitates which were viewed as the dominant strengthening mechanism.

Acknowledgements

The authors would like to acknowledge the Natural Sciences and Engineering Research Council of Canada (NSERC) for financial support via the Collaborative Research & Development grant CRDPJ 486528 - 15. Dr. Bernhard Mais (Kymera International) is acknowledged for the provision of the powdered metals employed. Laboratory assistance provided by colleagues at Dalhousie University (Randy Cooke, Dean Grijm, Greg Sweet, Angus MacPherson, Peter Jones and Mark Macdonald) and CanmetMATERIALS (Jonathan McKinley, Lucian Blaga) is gratefully appreciated as well.

CHAPTER 7 CONCLUSION

The over-arching objective of this research was to develop SPS-ASR/forging sequences for processing two prealloyed PM aluminum powders of interest. One was a ternary Al-0.3Sc-0.2Zr system whereas the other was chemically equivalent to the wrought aluminum alloy 2219 (Al-6.3Cu-0.3Mn-0.2Zr-0.1V-0.1Ti). These PM alloys were selected in consultation with our industrial partners, GKN Powder Metallurgy and Boeing, and were thereby identified as systems of commercial and practical relevance to industrial operations. Each alloy was initially produced as a powder form through gas atomization and classification. Powders were then consolidated through spark plasma sintering and subsequently processed using one or more forms of thermal-mechanical work.

7.1 ASYMMETRIC ROLLING (ASR) OF WROUGHT 6061

Prior to commencing research on PM systems, a sense of the response of aluminum alloys to ASR was determined by studying the effects of fundamental attributes such as roller velocity, starting thickness of specimen, rolling direction, number of passes and velocity ratio using wrought AA6061 as a precursory material. The roller velocities were varied in magnitude to achieve the same velocity ratio. The result of this assessment revealed that the different roller velocities did not have any significant effect on the mechanical properties. This was because the effective shear strain localized within the rolled specimen was effectively equal for all combinations of roller velocities considering that they were all set to achieve the same velocity ratio. It was also determined that the specimen with the smallest starting thickness would have experienced the highest level

shear deformation and in turn the highest level of strain hardening. This resulted in gains in the mechanical properties of specimens processed with smaller starting thicknesses. The rolling directions were altered by processing through designated rolling paths referred to as transverse direction, reverse direction, normal direction and unidirectional. Here, no significant changes in mechanical properties were realized irrespective of which rolling direction was employed during ASR. EBSD analyses were utilized to complement the data on the effects of number of passes and velocity ratio. The parent metal (AA6061-O) as evaluated through EBSD revealed it was essentially devoid of subgrains and exhibited a cube texture {001}<100>. When ASR was performed using 2, 4, 8 and 16 passes, it was found that the most effective method of obtaining the best mechanical properties was using the least number of passes. The yield strength of the specimen processed with 2 passes was 240 MPa compared to 211 MPa for the 16 pass specimen. The difference in tensile properties was partly accounted for by {111}<112> shear texture developed within the specimen rolled with 2 passes and {110}<001> Goss texture in the specimen processed through 16 passes. EBSD studies also revealed that the specimen rolled through 2 passes exhibited a reduced concentration of low angle grain boundaries compared to that rolled through 16 passes. Finally, ASR produced superior mechanical properties in wrought AA6061 than symmetric rolling. Indeed, the ASR process (VR=2.2) induced a texture resembling the {111}<110> shear texture whereas a {110}<211> brass texture was generated within the symmetrically rolled (VR=1) counterpart. It was concluded that the best ASR schedule comprised a velocity ratio of 2.2, rotating the sample in the reverse direction during subsequent passes, and using the least number of passes to achieve the net strain targeted. These findings provided

valuable insight on ASR technology that were then leveraged in the next stage of research that involved the Al-Sc-Zr ternary powder system.

7.2 SPS AND HOT ASR/UPSET FORGING OF AL-0.3SC-0.2ZR

Preliminary experiments on SPS of the ternary (Al-0.3Sc-0.2Zr) system confirmed that it exhibited a favourable response to this manner of processing. Evidence in support of this came in a variety of forms. For one, several of the SPS temperatures investigated (550˚C and 600˚C) were found to yield full density products. EBSD analyses confirmed that these as-sintered materials were devoid of microstructural texture, maintained a relatively small grain size, and contained an equal balance of HAGBs and LAGBs. TEM assessments indicated that the principal strengthening phase was $L1_2$ precipitates of Al_3(Sc,Zr) and that these had coarsened from a nominal size of ~4-10nm to ~20-35nm when the SPS temperature was increased. As a result of these microstructural traits, the sintered products exhibited reasonable tensile properties (yield strength ~195 MPa max.) and hardness (740 MPa max) although these were found to decline with rising SPS temperature. These losses were accompanied by a surge in tensile ductility which improved from <1% to peak value of ~15%. The coarsening of the Al_3(Sc,Zr) precipitates was thereby viewed as the dominant contributor towards the noted transitions in the assessed mechanical properties.

With an understanding of how the ternary system responded to SPS established, this line of research was then extended to assess the effects of post-SPS ASR and hot forging in two parallel streams of study. In ASR experiments, sintered billets were pre-heated to

various temperatures and then rolled under conditions derived in the precursory ASR study dedicated to wrought 6061. Examination of the rolled products via light microscopy revealed that the specimens were seemingly devoid of residual porosity. This even included those initially sintered at 500ºC which exhibited the highest concentration of pores (~1%) amongst its sintered counterparts. Tensile and hardness tests were then performed on the rolled products. Significant gains were realized in the specimens, and particularly so, in those initially sintered at the lower temperature of 500ºC. In this sense, the preform sintered/rolled at 500ºC /200ºC exhibited a nominal yield strength of 241MPa that represented a gain of nearly 24% relative to the as-sintered counterpart. Similar improvements were noted when using higher rolling temperatures, but optimal increases were consistently realized when the lowest rolling temperature was implemented. Interestingly, TEM studies confirmed that the precipitate size was unaffected by the rolling temperature, hence modifications to $Al_3(Sc,Zr)$ phase did not contribute to the decline in tensile strength during ASR. Rather, the trends were attributable to sub-structure strengthening as determined through EBSD. As such, the microstructure of the specimens which exhibited higher tensile strengths were characterized with a higher concentration of subgrains.

When the effects of forging on the ternary system were assessed, specimens were hot upset forged to achieve a net strain of either 0.4, 0.8, or 1.6 using a strain rate of 1 s^{-1}. Upon inspection of the resultant flow curves it was observed that all were overlapping such that the net strain had minimal effect. In each instance stress initially rose in a linear-elastic manner to a peak flow stress of ~45 MPa before transitioning into the non-

linear plastic region. This implied that the various forging strains applied had not affected the mode of deformation. During plastic flow, stress rose subtly at first with increasing strain, but then in a more obvious manner towards the end of the tests. This was attributed to friction between the sample and platens which masked the observation of any softening mechanisms that may have been active. However, through EBSD, it was demonstrated that dynamic recrystallization had transpired to a greater extent in the specimen forged to the highest net strain. This was evident in tensile property measurements as those achieved when forging to a net strain of 1.6 were inferior to counterpart specimens forged to lesser values of 0.4 and 0.8. It was also postulated that the decline could have been caused partly by the formation adiabactic shear bands. In these studies, the tensile strengths obtained due to forging were within the range of 150-173MPa for YS, 175-218 for UTS and 12-24% for ductility.

While investigating the effects of strain rate, the flow behavior again exhibited a linear elastic region which transitioned into a non-linear plastic response. The peak flow stresses recorded were 48 MPa and 28 MPa for strain rates of $1s^{-1}$ and $0.01s^{-1}$ respectively. Such behaviour indicated that the Al-0.3Sc-0.2Zr PM alloy was strain rate sensitive. In terms of strength, the specimen forged with the higher strain rate had a yield strength of 173 MPa compared with 147 MPa recorded for the specimen forged with the lower strain rate. Regardless of what strain rate was applied, both were effective in eliminating residual porosity from the sintered preforms. This was corroborated with density measurements. EBSD analyses revealed that the material forged with a slower strain rate was more susceptible to dynamic recrystallization as the fraction of HAGBs

was greater compared to its more expediently forged counterpart. This occurred since the material forged slowly had spent a longer time at the elevated forging temperature. It should be noted that the benefit of using a higher strain rate is not only limited to the merits of enhanced mechanical properties but also to cost savings that can be realized through short production times.

A summary of the optimal properties derived from sintering plus subsequent processing via ASR and upset forging is shown in Table 7-1. Out of the SPS temperatures investigated, the specimen sintered at 600ºC exhibited inferior tensile strength but superior ductility. However, the specimen spark plasma sintered at 500ºC was more responsive to hot working than its sintered counterparts 550ºC and 600ºC. The optimum SPS+ASR combination corresponded with SPS at 500ºC + ASR at 500ºC. The best combination of SPS+forge was also automatically adjudged SPS at 500ºC + forge at 500ºC considering that the sinter-forge operations were only performed at 500ºC. However, the ideal strain and strain rate for forging were 0.8 and 1 s^{-1} respectively. The yield and tensile strengths for the SPS+ASR duo was higher by ~21 and 15% respectively relative to the SPS+forge counterpart (Table 7-1). Conversely, the ductility of the SPS+forge specimen was almost 2.6 times higher than that of the SPS+ASR counterpart. This observation is attributable to longer preheat times utilized prior to forging that would have promoted extensive microstructural coarsening in the forged products.

Table 7-1 Summary of the properties measured for Al-0.3Sc-0.2Zr when processed through SPS with and without thermal mechanical working.

SPS Temperature (ºC)	**ASR Temperature** (ºC)	**Forge**			**Density (%)**	**Hardness (MPa)**	**Yield Strength** (MPa)	**UTS** (MPa)	**Elongation** (%)
		Temp. (ºC)	**Strain**	**Strain Rate** (s^{-1})					
500	N/A	N/A			99.6	739	195	206	1
550	N/A	N/A			100	656	163	195	4
600	N/A	N/A			100	531	106	153	15
500	500	N/A			N/A	750	219	255	7
500	N/A	500	0.8	1	100	N/A	173	218	18

7.3 SPS AND HOT UPSET FORGING OF PA2219

In the final stage of research, the effects of SPS and SPS+upset forge processing on PA2219 powder were investigated. SPS studies began by consolidating the powder into cylindrical pucks at temperatures of 450ºC to 550ºC. After preliminary microstructural examination, it was revealed that the specimen sintered at 450ºC was the only product that contained an obvious level of porosity. Physical density measurements substantiated this finding as the specimens sintered at 500ºC and 550ºC attained full densification compared to 98.8% theoretical density obtained for the specimen sintered at 450ºC. Further microstructural examination via SEM and TEM revealed the presence of second phase particles identified as (θ) $CuAl_2$. These existed as relatively coarse (~5 to 10μm) intergranular particles and as precipitates of a smaller size yet broad size range within the aluminum grains. EBSD analyses added to the microstructural understanding as it revealed a progressive increase in grain size accompanied by a depletion of subgrains

with increasing SPS temperature. On the other hand, the tensile strengths and elongations to fracture were relatively comparable regardless of SPS temperature implemented.

Sintered pucks of PA2219 were then upset forged with analyses completed on products in the T1 and T87 tempers. Initially, compressive true stress-true strain plots derived during the forging process itself were studied. Interestingly, the nature of deformation appeared to have been unaffected by the sintering temperature as each specimen exhibited an effectively identical flow curve when forged under the same combination of temperature and strain rate. Conversely, forging temperature was very influential. Here, the flow stress coinciding with the elastic-plastic transition decreased significantly as forging temperature increased. Such behaviour was as expected and is explained by increased thermal softening with rising forge temperature. Through EBSD analyses, it was shown that the fraction of subgrains in the microstructure after forging increased significantly. It was therefore concluded that the main softening mechanism that transpired during the deformation process was dynamic recovery.

The forged microstructures in both tempers were completely devoid of residual pores initially present in the sintered microstructures. Further observation via SEM unveiled the presence of intergranular particles of $CuAl_2$ that persisted within both samples as well. However, these were less abundant and much finer in the T87 tempered product owing to the incorporation of a proper solutionization treatment. TEM assessments confirmed that this manner of heat treatment also imparted a more favourable distribution (sub-micron, uniformly distributed) of $CuAl_2$ precipitates within the aluminum grains of the T87

product. TEM also confirmed that the continuous oxide layer present in the SPS preform was heavily disrupted as a result of upset forging.

On the tensile properties of specimens forged in the T1 condition, the yield strength and UTS decreased slightly with increasing SPS temperature. Also, the elongations were enhanced significantly; most notably in specimens forged at 500ºC as total elongation to fracture was 24%. When forged and heat treated to the T87 condition, the tensile strengths obtained were almost identical irrespective of the forging temperature utilized. Now, the yield strengths hovered around 354 MPa whereas the UTS values were all ~466 MPa. Both values represented dramatic gains over the T1 counterparts.

A comparison of the tensile properties for wrought 2219 and those measured for PA2219 specimens processed through SPS-forge-heat treat sequences are shown in Table 7-2. In the T1 temper, the most advantageous samples were achieved when sintered/forged at 500ºC/500ºC. All tensile properties of this material were significantly higher than those typical of annealed 2219-O. Here, the yield strength was nearly 2x higher without any negative impact on ductility as this property was also superior (~33% higher). These same trends did not persevere after T87 heat treatment. Now, the wrought material exhibited a statistically higher yield strength (10%) and moderately improved UTS (2%). However, it was found to maintain a ductility that was 30% lower than the PM counterpart.

Table 7-2 Comparison of the tensile properties for wrought AA2219 (typical) versus those measured in SPS+forged PA2219 products.

SPS/Forge (ºC)	Material-Temper	Yield Strength (MPa)	UTS (MPa)	Elongation (%)
N/A	AA2219-O	76	172	18
N/A	AA2219-T87	393	476	10
500/500	PA2219-Forged (T1)	138	291	24
550/500	PA2219-Forged (T87)	354	466	13

7.4 FUTURE WORK

The research covered in this thesis provides a comprehensive basis for the understanding of the thermomechanical response of Al-0.3Sc-0.2Zr and PA2219 aluminum PM alloys to SPS and hot ASR/upset forging. However, due to limited time, the author could not have possibly covered all variants of mechanical tests and microstructural studies available in materials science and engineering research. Accordingly, the author has formulated suggestions for future work that would provide complementary information and probably even lead to improvement of the mechanical properties and a better understanding of the thermomechanical response of the PM alloys studied. One pertains to dynamic mechanical testing. For industrial applications, the fatigue behaviour of materials is of significant value and importance particularly where most products are subjected to cyclic loading in service. It will therefore be imperative to determine the fatigue properties of the PM alloys studied after SPS and ASR/upset forging in order to better understand their commercial feasibility.

Secondly, it was postulated in this work that during forging at higher strains and strain rates, there is the propensity to form adiabactic shear bands. This attribute in fact was considered to have partly contributed to lowering the tensile properties of the ternary Al-0.3Sc-0.2Zr alloy at higher strains. It is important to note that the mode of deformation employed after SPS confines the thermal energy within the specimen particularly in the forging scenario where the platens were preheated. It is however undisputable to reason that the conditions set by this process could favour the formation of adiabactic shear bands. Hence, the need to investigate the evolution of adiabatic shear bands during forging in these PM alloy systems.

Research findings have also shown that the percent cold work adopted during T87 heat treatment of AA2219 is critical to producing the maximum strength in the material. A study has shown that applying a 7 % cold work holds prospect to imparting higher strengths during T87 heat treatment of AA2219 [168]. It is therefore suggested that some variations of cold work from 5 to 15% prior to ageing should be explored to ascertain their effects on strength of the PM systems investigated using the same SPS + ASR/upset forging sequences investigated.

Finally, one of the interesting areas of microstructural analysis is texture. The formability as well as properties of most materials have been linked to the evolution of texture in them. For this reason, it would be useful to complete additional studies on the evolution of texture during SPS and subsequent processing through upset forging and ASR of the PM alloys investigated. This information would go further to help understand the

differences that arise in the performance of PM aluminum alloys in comparison to their wrought counterparts.

Also, the raw data from spark plasma sintering could be studied to determine the time frame within which densification and microstructural coarsening occur within the respective PM alloy systems. This will enhance the understanding of the densification mechanisms that transpire during spark plasma sintering of the powder metallurgy systems.

REFERENCES

[1] A. Salak, *Ferrous powder metallurgy*. Cambridge International Science Publishing, 1997.

[2] R. M. German, *Powder metallurgy & particulate materials processing*. Princeton, New Jersey: Metal Powder Industry, 2005.

[3] R. Orrù, R. Licheri, A. M. Locci, A. Cincotti, and G. Cao, "Consolidation/synthesis of materials by electric current activated/assisted sintering," *Mater. Sci. Eng. R Reports*, vol. 63, no. 4–6, pp. 127–287, Apr. 2009.

[4] X. Phung, J. Groza, E. A. Stach, L. N. Williams, and S. B. Ritchey, "Surface characterization of metal nanoparticles," *Mater. Sci. Eng. A*, vol. 359, no. 1–2, pp. 261–268, Apr. 2003.

[5] R. W. Cooke, G. Steedman, I. W. Donaldson, and D. P. Bishop, "Preliminary studies on the development of hot forged Al PM technology," *Proc. 2013 Int. Conf. Powder Metall. Part. Mater.*, pp. 3108–3119, 2013.

[6] W. G. E. Mosher *et al.*, "On hot deformation of aluminium – silicon powder metallurgy alloys," *Powder Metall.*, vol. 54, no. 3, pp. 366--375, 2011.

[7] R. E. D. Mann, R. L. Hexemer, I. W. Donaldson, and D. P. Bishop, "Hot deformation of an Al-Cu-Mg PM alloy," *Mater. Sci. Eng. A*, vol. 528, pp. 5476–5483, 2011.

[8] A. M. Kawałek, H. S. Dyja, Ł. Sołtysiak, S. J. Mróz, and P. Szota, "Analysis of the asymmetric plate rolling process," *Mater. Sci. Forum*, vol. 706–709, pp. 1438–1443, May 2012.

[9] Y. H. Ji and J. J. Park, "Development of severe plastic deformation by various asymmetric rolling processes," *Mater. Sci. Eng. A*, vol. 499, no. 1–2, pp. 14–17, May 2009.

[10] Y. M. Hwang and G. Y. Tzou, "Analysis of asymmetrical hot strip rolling by the slab method," *J. Mater. Eng. Perform.*, vol. 4, no. 3, pp. 265–274, May 1995.

[11] J. E. Hatch, *Aluminum: Properties and physical metallurgy*. ASM International, 1984.

[12] W. F. Smith, *Structure and Properties of Engineering Alloys*, 2 edition. New York: McGraw-Hill Science/Engineering/Math, 1993.

[13] R. N. Wilson and P. G. Partridge, “The nucleation and growth of S’ precipitates in an aluminium-2.5% copper-1.2% magnesium alloy,” *Acta Metall.*, vol. 13, no. 12, pp. 1321–1327, May 1965.

[14] J. L. Murray, “The aluminum-copper system,” *Int. Met. Rev.*, vol. 30, no. 1, pp. 211–234, 1985.

[15] J. G. Kaufman, *Introduction to aluminum alloys and tempers*. ASM International, 2000.

[16] V. A. Narasayya, P. Rambabu, M. K. Mohan, R. Mitra, and N. E. Prasad, “Tensile deformation and fracture behaviour of an aerospace aluminium alloy AA2219 in different ageing conditions,” *Procedia Mater. Sci.*, vol. 6, pp. 322–330, 2014.

[17] K. J. Abhay, P. R. Narayanan, and K. Sreekumar, “Liquation cracking of Al-6.3 Cu alloy propellant storage tank – A case study,” *Eng. Fail. Anal.*, vol. 16, pp. 1587–1596, 2009.

[18] L. A. Willey, “U.S. Patent: 3,619,181,” 1971.

[19] J. Røyset and N. Ryum, “Scandium in aluminium alloys,” *Int. Mater. Rev.*, vol. 50, no. 1, pp. 19–44, 2005.

[20] K. E. Knipling, R. A. Karnesky, C. P. Lee, D. C. Dunand, and D. N. Seidman, “Precipitation evolution in Al-0.1Sc, Al-0.1Zr and Al-0.1Sc-0.1Zr (at.%) alloys during isochronal aging,” *Acta Mater.*, vol. 58, no. 15, pp. 5184–5195, 2010.

[21] E. M. Savitsky, V. F. Terehova, I. V. Burov, and O. P. Naumkin, “Study of rare earth crystals and alloys,” in *Proceedings of the fourth conference on rare earth research*, L. Eyring, Ed. 1964, pp. 409–420.

[22] H. Okamoto, “Al-Sc (Aluminum-Scandium),” *J. Phase Equilibria*, vol. 12, no. 5, pp. 612–613, 1991.

[23] G. Cacciamani *et al.*, “Thermodynamic measurements and assessment of the Al-Sc system,” *Intermetallics*, vol. 7, no. 1, pp. 101–108, 1999.

[24] J. Røyset and N. Ryum, “Kinetics and mechanisms of precipitation in an Al-0.2wt.% Sc alloy,” *Mater. Sci. Eng. A*, vol. 396, no. 1–2, pp. 409–422, 2005.

[25] M. E. Drits, E. J. Kadaner, T. V Dobatkina, and N. I. Turkina, “Scandium aluminum interactions in the aluminum-rich side of the Al-Sc system,” *Russ. Metall.*, vol. 4, pp. 152–154, 1973.

[26] V. I. Kononenko and S. V Golubev, “Phase diagrams of binary systems of aluminum with La, Ce, Pr, Nd, Sm, Eu, Yb, Sc, and Y,” *Russ. Metall.*, vol. 2, pp. 193–195, 1990.

[27] J. L. Murray, “The Al-Sc (aluminum-scandium) system,” *J. Phase Equilibria*, vol. 19, no. 4, pp. 380–384, 1998.

[28] E. A. Marquis and D. N. Seidman, “Nanoscale structural evolution of Al3Sc precipitates in Al(Sc) alloys,” *Acta Mater.*, vol. 49, no. 11, pp. 1909–1919, 2001.

[29] M. J. Jones and F. J. Humphreys, “Interaction of recrystallization and precipitation: The effect of Al3Sc on the recrystallization behaviour of deformed aluminium,” *Acta Mater.*, vol. 51, pp. 2149–2159, 2003.

[30] W. Lefebvre, F. Danoix, H. Hallem, B. Forbord, A. Bostel, and K. Marthinsen, “Precipitation kinetic of Al3(Sc,Zr) dispersoids in aluminium,” *J. Alloys Compd.*, vol. 470, no. 1–2, pp. 107–110, 2009.

[31] V. Radmilovic, A. Tolley, Z. Lee, and U. Dahmen, “Core-shell structures and precipitation kinetics of Al3 (Sc, Zr) Li2 intermetallic phase in Al-rich alloy,” *Metal. - J. Metall.*, vol. 12, no. 4, pp. 309–314, 2006.

[32] E. Clouet, L. Lae, T. Epicier, W. Lefebvre, M. Nastar, and A. Deschamps, “Complex precipitation pathways in multicomponent alloys,” *Nat. Mater.*, vol. 5, pp. 482–488, 2006.

[33] V. I. Yelagin, V. V. Zakharov, S. G. Pavlenko, and T. D. Rostova, “Influence of zirconium additions on ageing of Al-Sc alloys,” *Phys. Met. Metallogr.*, vol. 60, no. 1, pp. 88–92, 1985.

[34] V. V. Zakharov, “Stability of the solid solution of scandium in aluminum,” *Met. Sci. Heat Treat.*, vol. 39, pp. 61–66, 1997.

[35] E. A. Marquis, D. N. Seidman, and D. C. Dunand, “Effect of Mg addition on the creep and yield behavior of an Al-Sc alloy,” *Acta Mater.*, vol. 51, pp. 4751–4760, 2003.

[36] J. J. Dunkley, “Producing metal powders,” *Met. Mater.*, vol. 6, no. 6, pp. 361–364, 1990.

[37] A. Lawley, *Atomization: The production of metal powders*. Metal Powder Industries Federation, 2003.

[38] K. Bauckhage, O. Andersen, S. Hansmann, W. Reich, and P. Schreckenberg, “Production of fine powders by ultrasonic standing wave atomization,” *Powder Technol.*, vol. 86, no. 1, pp. 77–86, 1996.

[39] R. Anderson, “Powder metallurgy at Pratt & Whitney,” *Int. J. powder Metall.*, vol. 26, no. 2, pp. 171–178, May 1990.

[40] W. J. Boettinger, “Microstructural variations in rapidly solidified alloys,” *Mater. Sci. Eng.*, vol. 98, pp. 13–130, 1998.

[41] L. Ackermann, I. Guillemin, R. Lalauze, and C. Pijolat, *Study of water desorption during degassing of aluminium powders*, High Stren. 1985.

[42] Y. Champion and J. Bigot, “Synthesis and structural analysis of aluminum nanocrystalline powders,” *Nanostructured Mater.*, vol. 10, no. 7, pp. 1097–1110, 1998.

[43] M. Yamasaki and Y. Kawamura, “Effect of vacuum degassing on surface characteristics of rapidly solidified Al-based alloy powders,” *Mater. Trans.*, vol. 45, no. 4, pp. 1335–1338, 2004.

[44] A. I. Litvintsev and L. A. Arbuzova, “Kinetics of degassing of aluminum powders,” *Sov. Powder Metall. Met. Ceram.*, vol. 6, no. 1, pp. 1–10, 1967.

[45] J. L. Estrada, J. Duszczyk, and B. M. Korevaar, “Heating sequence and hydrogen evolution in alloyed aluminium powders,” *J. Mater. Sci.*, vol. 26, pp. 1631–1634, 1991.

[46] G. Sweet, “Advanced sintering techniques of aluminum: spark plasma sintering,” Apr. 2014.

[47] O. Guillon, B. Gonzalez-Julian, Jesus Dargatz, T. Kesse, G. Schierning, J. Räthel, and M. Herrmann, “Field-assisted sintering technology/spark plasma sintering: mechanisms, materials, and technology developments,” *Adv. Eng. Mater.*, pp. 830–849, 2014.

[48] D. M. Hulbert *et al.*, “The absence of plasma in ‘spark plasma sintering,’” *J. Appl. Phys.*, vol. 104, no. 3, p. 33305, Apr. 2008.

[49] S. Nouari, “Spark Plasma Sintering of Al6061 and Al2124 Alloys,” *Adv. Mater. Res.*, vol. 284–286, pp. 1656–1660, Apr. 2011.

[50] G. Xie, “Spark plasma sintering: A useful technique to develop large-sized bulk metallic glasses,” *J. Powder Metall. Min.*, vol. 02, no. 02, Apr. 2013.

[51] E. A. Olevsky and L. Froyen, “Impact of thermal diffusion on densification during SPS,” *J. Am. Ceram. Soc.*, vol. 92, pp. S122–S132, Apr. 2009.

[52] E. A. Olevsky, S. Kandukuri, and L. Froyen, “Consolidation enhancement in spark-plasma sintering: Impact of high heating rates,” *J. Appl. Phys.*, vol. 102, no. 11, p. 114913, Apr. 2007.

[53] Z. A. Munir, U. Anselmi-Tamburini, and M. Ohyanagi, “The effect of electric field and pressure on the synthesis and consolidation of materials: A review of the spark plasma sintering method,” *J. Mater. Sci.*, vol. 41, no. 3, pp. 763–777, 2006.

[54] R. M. German, *Sinterng Theory and Practice*. New York: Wiley Interscience, 1996.

[55] G. Xie *et al.*, “Effect of Mg on the sintering of Al-Mg alloy powders by pulse electric-current sintering process,” *Mater. Trans.*, vol. 45, no. 3, pp. 904–909, 2004.

[56] G. A. Sweet, M. Brochu, R. L. Hexemer Jr., I. W. Donaldson, and D. P. Bishop, “Microstructure and mechanical properties of air atomized aluminum powder consolidated via spark plasma sintering,” *Mater. Sci. Eng. A*, vol. 608, pp. 273–282, Apr. 2014.

[57] X. Song, X. Liu, and J. Zhang, “Neck formation and self-adjusting mechanism of neck growth of conducting powders in spark plasma sintering,” *J. Am. Ceram. Soc.*, vol. 89, no. 2, pp. 494–500, Apr. 2006.

[58] G. Xie *et al.*, “Behavior of oxide film at interface between particles of Al-Mg alloy powder compacts prepared by pulse electric current sintering,” *Japan J. Appl. Phys.*, vol. 42, pp. 4725–4728, 2003.

[59] A. V Vydrin and E. E. Chvanova, “Force required in significantly asymmetric sheet rolling,” *Steel Transl.*, vol. 40, no. 1, pp. 65–67, May 2010.

[60] G. Dieter, *Mechanical metallurgy*, 3 edition. New York: McGraw-Hill Science/Engineering/Math, 1986.

[61] H. Yu *et al.*, “Asymmetric cryorolling for fabrication of nanostructural aluminum sheets,” *Sci. Rep.*, vol. 2, May 2012.

[62] R. Roumina and C. W. Sinclair, “Deformation geometry and through-thickness strain gradients in asymmetric rolling,” *Metall. Mater. Trans. A*, vol. 39, no. 10, pp. 2495–2503, May 2008.

[63] S.-H. Kim, J.-H. Ryu, K.-H. Kim, and D. N. Lee, “The evolution of shear deformation texture and grain refinement in asymmetrically rolled aluminum sheets,” *J. Soc. Mater. Sci. Japan*, vol. 51, no. 3Appendix, pp. 20–25, 2002.

[64] F. J. P. Simões, R. J. A. de Sousa, J. J. A. Grácio, F. Barlat, and J. W. Yoon, “Effect of asymmetrical rolling and annealing the mechanical response of an 1050-o sheet,” *Int. J. Mater. Form.*, vol. 2, no. 1, pp. 891–894, May 2009.

[65] J. Jiang, Y. Ding, F. Zuo, and A. Shan, “Mechanical properties and microstructures of ultrafine-grained pure aluminum by asymmetric rolling,” *Scr. Mater.*, vol. 60, no. 10, pp. 905–908, May 2009.

[66] F. ZUO, J. JIANG, A. SHAN, J. FANG, and X. ZHANG, “Shear deformation and grain refinement in pure Al by asymmetric rolling,” *Trans. Nonferrous Met. Soc. China*, vol. 18, no. 4, pp. 774–777, May 2008.

[67] A. Kawałek, “The theoretical and experimental analysis of the effect of asymmetrical rolling on the value of unit pressure,” *J. Mater. Process. Technol.*, vol. 157–158, pp. 531–535, May 2004.

[68] G. Y. Kalutskii, K. A. Gogaev, V. S. Voropaev, and V. V Nepomnyashchii, “Asymmetric rolling of metal powders and granules,” *Powder Metall. Met. Ceram.*, vol. 46, no. 3–4, pp. 197–201, May 2007.

[69] C. H. Lee, J. P. Park, and Y. H. Moon, “Differential speed rolling to reduce warping in bimetallic slab,” *Adv. Mech. Eng.*, vol. 6, no. 0, p. 375162, May 2015.

[70] W. F. Hosford and R. M. Caddell, *Metal forming, mechanics and metallurgy*, 4th ed. Cambridge University Press, 2014.

[71] H. Yu *et al.*, “Fabrication of ultra-thin nanostructured bimetallic foils by accumulative roll bonding and asymmetric rolling,” *Sci. Rep.*, vol. 3, May 2013.

[72] “ASM Handbook: Powder metal technologies and applications,” vol. Volume 7, 1998.

[73] G. E. Dieter, H. A. Kuhn, and L. S. Semiatin, Eds., *Handbook of workability and process design*. ASM International, 2003.

[74] “Forming and forging,” *ASM Int.*, vol. Volume 14, 1998.

[75] M. P. Groover, *Fundamentals of modern manufacturing: Materials, processes and systems*, 3rd ed. John Wiley & Sons, Inc., 2007.

[76] M. Y. Amegadzie, A. Taylor, R. L. Hexemer, I. W. Donaldson, B. W. Williams, and D. P. Bishop, “Isothermal forging of a spark plasma sintered Al-0.3sc-0.2zr powder metallurgy alloy,” *Int. J. Powder Metall.*, vol. 54, no. 3, pp. 47–57, 2018.

[77] H. Zhang, L. Li, D. Yuan, and D. Peng, “Hot deformation behavior of the new Al-Mg-Si-Cu aluminum alloy during compression at elevated temperatures,” *Mater. Charact.*, vol. 58, pp. 168–173, 2007.

[78] D. feng LI *et al.*, “Dynamic recrystallization behavior of 7085 aluminum alloy during hot deformation,” *Trans. Nonferrous Met. Soc. China (English Ed.*, vol. 26, pp. 1491–1497, 2016.

[79] D. feng LI *et al.*, “Dynamic recrystallization behavior of 7085 aluminum alloy during hot deformation,” *Trans. Nonferrous Met. Soc. China (English Ed.*, vol. 26, pp. 1491–1497, 2016.

[80] S. Gourdet and F. Montheillet, “An experimental study of the recrystallization mechanism during hot deformation of aluminium,” *Mater. Sci. Eng. A*, vol. 283, pp. 274–288, 2000.

[81] N. Ravichandran and Y. V. R. K. Prasad, “Dynamic recrystallization during hot deformation of aluminum: A study using processing maps,” *Metall. Trans. A*, vol. 22A, pp. 2339–2348, 1991.

[82] X. H. Fan, M. Li, D. Y. Li, Y. C. Shao, S. R. Zhang, and Y. H. Peng, “Dynamic recrystallisation and dynamic precipitation in AA6061 aluminium alloy during hot deformation,” *Mater. Sci. Technol.*, vol. 30, no. 11, pp. 1263–1272, 2014.

[83] F. L. Jiang, H. Zhang, S. C. Weng, and D. F. Fu, “Characterization of dynamic microstructural evolution of AA7150 aluminum alloy at high strain rate during hot deformation,” *Trans. Nonferrous Met. Soc. China (English Ed.*, vol. 26, pp. 51–62, 2016.

[84] F. J. Humphreys and M. Hatherly, *Recrystallization and related annealing phenomena*, 2nd ed. Elsevier, 2004.

[85] M. E. Kassner and S. R. Barrabes, “New developments in geometric dynamic recrystallization,” *Mater. Sci. Eng. A*, vol. 410–411, pp. 152–155, 2005.

[86] M. R. Rokni, A. Zarei-Hanzaki, A. A. Roostaei, and H. R. Abedi, “An investigation into the hot deformation characteristics of 7075 aluminum alloy,” *Mater. Des.*, vol. 32, pp. 2339–2344, 2011.

[87] N. P. Guraoĵ, A. O. Adesola, J. A. Odeshi, and G. A. Szpunar, “On the evolution of heterogeneous microstructure and microtexture in impacted aluminum–lithium alloy,” *J. Alloys Compd.*, vol. 578, pp. 183–187, 2013.

[88] S. Kikuchi and S. Nishikawa, “Diffraction of cathode rays by calcite,” *Nature*, vol. 122, no. 3080. p. 726, 1928.

[89] J. A. Venables and C. J. Harland, “Electron back-scattering patterns—A new technique for obtaining crystallographic information in the scanning electron microscope,” *Philos. Mag.*, vol. 27, no. 5, pp. 1193–1200, 1973.

[90] J. A. Venables and R. Bin-Jaya, “Accurate microcrystallography using electron back-scattering patterns,” *Philos. Mag.*, vol. 35, no. 5, pp. 1317–1332, 1977.

[91] V. Randle, *Microtexture determination and its applications*, 2nd ed. Maney, 2003.

[92] A. J. Schwartz, M. Kumar, B. L. Adams, and D. P. Field, Eds., *Electron backscatter diffraction in materials science*, 2nd ed. Springer, 2000.

[93] O. Engler and V. Randle, *Introduction to texture analysis: Macrotexture, microtexture and orientation mapping*, Second. CRC Press, Taylor and Francis Group, 2010.

[94] S. Suwas and R. K. Ray, *Crystallographic texture of materials*. Springer, 2014.

[95] G.-C. Wang and T.-M. Lu, *RHEED transmission mode and pole figures: Thin film and nanostructure texture analysis*. 2014.

[96] R. D. Doherty, “Recrystallization and texture,” *Prog. Mater. Sci.*, vol. 42, no. 1–4, pp. 39–58, 1997.

[97] H. Jin and D. J. Lloyd, “Effect of a duplex grain size on the tensile ductility of an ultra-fine grained Al–Mg alloy, AA5754, produced by asymmetric rolling and annealing,” *Scr. Mater.*, vol. 50, no. 10, pp. 1319–1323, Sep. 2004.

[98] Q. Cui and K. Ohori, “Grain refinement of high purity aluminium by asymmetric rolling,” *Mater. Sci. Technol.*, vol. 16, no. 10, pp. 1095–1101, 2012.

[99] S. Suwas, S. Biswas, and D. I. Kim, “Analysis of microstructure and texture evolution in pure magnesium during symmetric and asymmetric rolling,” *Acta Mater.*, vol. 57, no. 17, pp. 5061–5077, 2009.

[100] Y. Ding, J. Jiang, and A. Shan, “Microstructures and mechanical properties of commercial purity iron processed by asymmetric rolling,” *Mater. Sci. Eng. A*, vol. 509, no. 1–2, pp. 76–80, May 2009.

[101] J. Lee and D. N. Lee, “Texture control and grain refinement of AA1050 Al alloy sheets by asymmetric rolling,” *Int. J. Mech. Sci.*, vol. 50, pp. 869–887, 2008.

[102] G. Angella, D. Dellasega, S. Farè, and M. Vedani, “A comparison between asymmetric rolling and accumulative roll bonding as means to refine the grain structure of an Al-Mg-Si alloy,” *Metall. Sci. Technol.*, vol. 28, pp. 22–26, 2010.

[103] R. Valiev, “Nanostructuring of metals by severe plastic deformation for advanced properties,” *Nat. Mater.*, vol. 3, no. 8, pp. 511–516, 2004.

[104] H. Jin and D. J. Lloyd, “Evolution of texture in AA6111 aluminum alloy after asymmetric rolling with various velocity ratios between top and bottom rolls,” *Mater. Sci. Eng. A*, vol. 465, no. 1–2, pp. 267–273, Sep. 2007.

[105] K. Bobor, Z. Heged\Hus, J. Gubicza, I. Barkai, P. Pepper, and G. Krállics, “Microstructure and mechanical properties of Al 7075 alloy processed by differential speed rolling,” *Mech. Eng.*, vol. 56, no. 2, pp. 111–115, May 2012.

[106] H. Jin and D. J. Lloyd, “The reduction of planar anisotropy by texture modification through asymmetric rolling and annealing in AA5754,” *Mater. Sci. Eng. A*, vol. 399, no. 1–2, pp. 358–367, Sep. 2005.

[107] C. Ma, L. Hou, J. Zhang, and L. Zhuang, “Influence of thickness reduction per pass on strain, microstructures and mechanical properties of 7050 Al alloy sheet processed by asymmetric rolling,” *Mater. Sci. Eng. A*, vol. 650, pp. 454–468, 2016.

[108] S.-B. Kang, B.-K. Min, H.-W. Kim, D. S. Wilkinson, and J. Kang, “Effect of asymmetric rolling on the texture and mechanical properties of AA6111-aluminum sheet,” *Metall. Mater. Trans. A*, vol. 36, no. 11, pp. 3141–3149, Aug. 2005.

[109] S. A. A. A. Mousavi, S. M. Ebrahimi, and R. Madoliat, “Three dimensional numerical analyses of asymmetric rolling,” *J. Mater. Process. Technol.*, vol. 187–188, pp. 725–729, 2007.

[110] M. Wronski, K. Wierzbanowski, S. Wronski, B. Bacroix, and P. Lipinski, “Experimental and finite element analysis of asymmetric rolling of 6061 aluminum alloy using two-scale elasto-plastic constitutive relation,” *Arch. Metall. Mater.*, vol. 62, no. 4, pp. 1991–1999, 2017.

[111] W. J. Kim, Y. K. Sa, H. K. Kim, and U. S. Yoon, “Plastic forming of the equal-channel angular pressing processed 6061 aluminum alloy,” *Mater. Sci. Eng. A*, vol. 487, no. 1–2, pp. 360–368, 2008.

[112] P. Li, K. M. Xue, X. X. Wang, and C. H. Qian, “Refinement and consolidation of pure Al particles by equal channel angular pressing and torsion,” *Trans. Nonferrous Met. Soc. China (English Ed.*, vol. 24, no. 5, pp. 1289–1294, 2014.

[113] R. Kaibyshev, T. Sakai, H. Miura, J. J. Jonas, and A. Belyakov, “Dynamic and post-dynamic recrystallization under hot, cold and severe plastic deformation conditions,” *Prog. Mater. Sci.*, vol. 60, pp. 130–207, 2013.

[114] M. Nakai and G. Itoh, “The effect of microstructure on mechanical properties of forged 6061 aluminum alloy,” *Mater. Trans.*, vol. 55, no. 1, pp. 114–119, 2014.

[115] J. H. Holloman, “Tensile deformation,” *Trans. Metall. Soc. AIME*, vol. 162, pp. 268–290, 1945.

[116] G. E. Totten and D. S. MacKenzie, *Handbook of aluminum: Vol. 1: Physical metallurgy and processes*. CRC Press, 2003.

[117] J. M. Capus, *Metal powders: A global survey of production, applications and markets*, 4th ed. Elsevier, 2005.

[118] M. Yamasaki and Y. Kawamura, “Changes in the surface characteristics of gas-atomized pure aluminum powder during vacuum degassing,” *Mater. Trans.*, vol. 47, no. 8, pp. 1902–1905, Mar. 2006.

[119] K. Kondoh, A. Kimura, and R. Watanabe, “Effect of Mg on Sintering Phenomenon of Aluminum Alloy Powder,” *J. Japan Soc. Powder Powder Metall.*, vol. 47, no. 1, pp. 36–41, Mar. 2000.

[120] S. D. Kirchoff, J. Y. Adkins, W. M. Griffith, and I. A. Martorell, “Effective method for degassing evaluation of aluminum PM alloys,” *Rapidly Solidified Powder Alum. Alloy.*, Mar. 1986.

[121] W. E. Quist and R. E. Lewis, “The need for rapidly solidified powder metallurgy aluminum alloys for aerospace applications,” *ASTM STP 890*, pp. 7–38, 1986.

[122] G. Xie *et al.*, “Effect of interface behavior between particles on properties of pure Al powder compacts by spark plasma sintering,” *Mater. Trans.*, vol. 42, no. 9, pp. 1846–1849, Mar. 2001.

[123] S. X. Song, Z. Wang, and G. P. Shi, “Heating mechanism of spark plasma sintering,” *Ceram. Int.*, vol. 39, no. 2, pp. 1393–1396, 2013.

[124] Z. Jia, J. Røyset, J. K. Solberg, and Q. Liu, “Formation of precipitates and recrystallization resistance in Al–Sc–Zr alloys,” *Trans. Nonferrous Met. Soc. China*, vol. 22, no. 8, pp. 1866–1871, Feb. 2012.

[125] C. B. Fuller, J. L. Murray, and D. N. Seidman, “Temporal evolution of the nanostructure of Al(Sc,Zr) alloys: Part I – Chemical compositions of Al3(Sc1−xZrx) precipitates,” *Acta Mater.*, vol. 53, no. 20, pp. 5401–5413, Mar. 2005.

[126] M. Vlach *et al.*, “Precipitation in cold-rolled Al–Sc–Zr and Al–Mn–Sc–Zr alloys prepared by powder metallurgy,” *Mater. Charact.*, vol. 86, pp. 59–68, Mar. 2013.

[127] T. D. Rostova, V. G. Davydov, V. I. Yelagin, and V. V Zakharov, “Effect of scandium on recrystallization of aluminum and its alloys,” *Materials Science Forum*. pp. 793–798, 29-Mar-2000.

[128] V. V. Zakharov, “Effect of scandium on the structure and properties of aluminum alloys,” *Met. Sci. Heat Treat.*, vol. 45, no. 7–8, pp. 246–253, 2003.

[129] T. B. Gurganus, “Aluminum powder applications,” *Adv. Mater. Process.*, pp. 57–59, 1995.

[130] “‘FocusPM News | Metal Powder Industries Federation.’ [Online]. Available: https://www.mpif.org/News/FocusPM/2016/061616-PM-Design-Excellence-Awards-Announced.asp.”

[131] M. Omori, “Sintering, consolidation, reaction and crystal growth by the spark plasma system (SPS),” *Mater. Sci. Eng. A*, vol. 287, no. 2, pp. 183–188, Apr. 2000.

[132] G. Xie, O. Ohashi, M. Song, K. Furuya, and T. Noda, “Behavior of oxide film at the interface between particles in sintered Al powders by pulse electric-current sintering,” *Metall. Mater. Trans. A*, vol. 34, no. 3, pp. 699–703, Apr. 2003.

[133] R. W. Cooke, N. P. Kraus, and D. P. Bishop, “Spark plasma sintering of aluminum powders prealloyed with scandium additions,” *Mater. Sci. Eng. A*, vol. 657, pp. 71–81, 2016.

[134] G. A. Sweet, R. L. Hexemer, I. W. Donaldson, and D. P. Bishop, “Effects of transition metal additions on the spark plasma sintering response of aluminum powders,” *PM2Tec 2014*, vol. 10, pp. 13–24, 2014.

[135] N. P. Kraus *et al.*, “Consolidation of aerospace grade aluminum 7055 powder through SPS-forge processing,” *Can. Metall. Quartelry*, vol. 56, pp. 137–147, 2017.

[136] A. S. Chua, M. Brochu, D. P. Bishop, A. S. Chua, M. Brochu, and D. P. Bishop, "Spark plasma sintering of prealloyed aluminium powders," *Powder Metall.*, vol. 58, no. 1, pp. 51–60, 2015.

[137] J. McNeil, R. L. Hexemer, I. W. Donaldson, and D. P. Bishop, "Consolidation of aerospace grade 2219 powder via spark plasma sintering," *PM2Tec 2016*, 2016.

[138] R. Zheng, Y. Sun, K. Ameyama, and C. Ma, "Optimizing the strength and ductility of spark plasma sintered Al 2024 alloy by conventional thermo-mechanical treatment," *Mater. Sci. Eng. A*, vol. 590, pp. 147–152, 2014.

[139] A. D. P. Ladelpha, M. P. Mosher, W. F. Caley, G. J. Kipouros, and D. P. Bishop, "On the simulation of wrought AA4032 via P / M processing," *Mater. Sci. Eng. A*, vol. 479, pp. 1–9, 2008.

[140] R. W. Cooke, G. A. Sweet, I. W. Donaldson, and D. P. Bishop, "Processing of an Al-Sc-Zr alloy via spark plasma sintering and hot forging," *Eur. PM Conf. Proc.*, 2016.

[141] Y. Deng, Z. Yin, and J. Huang, "Hot deformation behavior and microstructural evolution of homogenized 7050 aluminum alloy during compression at elevated temperature," *Mater. Sci. Eng. A*, vol. 528, no. 3, pp. 1780–1786, 2011.

[142] X. Huang, H. Zhang, Y. Han, W. Wu, and J. Chen, "Hot deformation behavior of 2026 aluminum alloy during compression at elevated temperature," vol. 527, no. 3, pp. 485–490, 2010.

[143] H. J. McQueen, S. Spigarelli, M. E. Kassner, and E. Evangelista, *Hot deformation and processing of aluminum Alloys*. CRC Press, 2017.

[144] L. Zhen, H. Hu, X. Wang, B. Zhang, and W. Shao, "Distribution characterization of boundary misorientation angle of 7050 aluminum alloy after high-temperature compression," vol. 9, pp. 754–761, 2008.

[145] C. Shi, J. Lai, and X. Chen, "Microstructural evolution and dynamic softening mechanisms of Al-Zn-Mg-Cu alloy during hot compressive deformation," pp. 244–264, 2014.

[146] B. Wang, R. Ma, J. Zhou, Z. Li, S. Zhao, and X. Huang, "Adiabatic shear localization in ultra fi ne grained 6061 aluminum alloy," *Mater. Sci. Eng. A*, vol. 675, pp. 221–227, 2016.

[147] J. Hirsch, "Recent development in aluminum for automotive applications," *Trans. Nonferrous Met. Soc. China*, vol. 24, pp. 1995–2002, 2014.

[148] J.-H. Schmitt and T. Lung, “New developments of advanced high-strength steels for automotive applications,” *Comptes Rendus Phys.*, vol. 19, pp. 641–656, 2018.

[149] M. K. Kulekci, “Magnesium and its alloys applications in automotive industry,” *Int. J. Adv. Manuf. Technol.*, vol. 39, no. 9–10, pp. 851–865, 2008.

[150] J. Holbery and D. Houston, “Natural-fiber-reinforced polymer composites in automotive applications,” *J. Miner. Met. Mater. Soc.*, vol. 58, no. 11, pp. 80–86, 2006.

[151] J. Capus, “US manufacturers at forefront at 2016 PM design competition,” *Met. Powder Rep.*, vol. 71, no. 5, pp. 318–320, 2016.

[152] D. Magid, “Achieving excellence in design: it takes an industry,” *Int. J. Powder Metall.*, vol. 54, no. 3, pp. 7–13, 2018.

[153] N. P. Kraus, R. L. Hexemer, I. W. Donaldson, and D. P. Bishop, “Consolidation of aerospace grade aluminum 7055 powder via sinter forge processing,” *Int. J. Powder Metall.*, vol. 52, no. 4, pp. 9–18, 2016.

[154] L. J. B. Smith, S. F. Corbin, R. L. Hexemer, I. W. Donaldson, and D. P. Bishop, “Development and processing of novel aluminum powder metallurgy materials for heat sink applications,” *Metall. Mater. Trans. A*, vol. 45, no. 2, pp. 980–989, 2013.

[155] G. A. Sweet, I. W. Donaldson, R. L. Hexemer, A. Taylor, and D. P. Bishop, “Powder metallurgical processing of a 2xxx series aluminum powder metallurgy alloy reinforced with AlN particulate additions,” *Mater. Sci. Eng. A*, vol. 755, pp. 10–17, 2019.

[156] W. G. Mosher, G. J. Kipouros, W. F. Caley, I. W. Donaldson, and D. P. Bishop, “On the Enhancement of a Hypoeutectic Al-Si PM Alloy,” *Can. Metall. Quartelry*, vol. 51, no. 1, pp. 39–47, 2012.

[157] R. W. Cooke, R. L. Hexemer, I. W. Donaldson, and D. P. Bishop, “Press-and-sinter processing of a PM counterpart to wrought aluminum 2618,” *J. Mater. Process.*, pp. 72–79, 2016.

[158] M. R. Rafi, F. Ahmad, N. Ikram, R. Ahmad, and A. Salam, “Development and strengthening of 2219 aluminium alloy by mechanical working and heat treatment,” *J. Appl. Sci.*, vol. 11, no. 10, pp. 1857–1861, 2011.

[159] V. Malarvizhi, S Balasubramanian, “Effect of welding processes on AA2219 aluminium alloy joint properties,” *Trans. Nonferrous Met. Soc. China*, vol. 21, no. 5, pp. 962–973, 2011.

[160] K. Surekha, B. S. Murty, and K. Prasad Rao, “Effect of processing parameters on the corrosion behaviour of friction stir processed AA 2219 aluminum alloy,” *Solid State Sci.*, vol. 11, pp. 907–917, 2009.

[161] R. W. Cooke, R. L. Hexemer, I. W. Donaldson, and D. P. Bishop, “Powder metallurgy processing of Al-Cu-Mg alloy with low Cu/Mg ratio,” *Inst. Mater. Miner. Min.*, vol. 55, no. 11, pp. 29–35, 2012.

[162] R. N. Lumley, T. B. Sercombe, and B. B. Schaffer, “Surface oxide and the role of magnesium during the sintering of aluminum,” *Metall. Mater. Trans. A*, vol. 30A, pp. 457–463, 1999.

[163] G. Xie, O. Ohashi, N. Yamaguchi, M. Song, K. Furuya, and T. Noda, “TEM observation of interfaces between particles in Al-Mg alloy powder compacts prepared by pulse electric current sintering,” *Mater. Trans.*, vol. 43, no. 9, pp. 2177–2180, 2002.

[164] G. A. Sweet *et al.*, “Microstructural evolution of a forged 2xxx series aluminum powder metallurgy alloy,” *Mater. Charact.*, vol. 151, pp. 342–350, 2019.

[165] L. Liu, Y. Wu, and H. Gong, “Effects of deformation parameters on microstructural evolution of 2219 aluminum alloy during intermediate thermo-mechanical treatment process,” *Materials (Basel).*, vol. 11, no. 9, 2018.

[166] J. Kang, Z. C. Feng, G. S. Frankel, I. W. Huang, G. Q. Wang, and A. P. Wu, “Friction stir welding of Al alloy 2219-T8: Part I-Evolution of precipitates and formation of abnormal Al2Cu agglomerates,” *Metall. Mater. Trans. A Phys. Metall. Mater. Sci.*, vol. 47, no. 9, pp. 4553–4565, 2016.

[167] H. Wang, Y. Yi, and S. Huang, “Influence of pre-deformation and subsequent ageing on the hardening behavior and microstructure of 2219 aluminum alloy forgings,” *J. Alloys Compd.*, vol. 685, pp. 941–948, 2016.

[168] R. K. Gupta, R. Panda, A. K. Mukhopadhyay, V. A. Kumar, P. Sankaravelayutham, and K. M. George, “Study of aluminum alloy AA2219 after heat treatment,” *Met. Sci. Heat Treat.*, vol. 57, no. 5–6, pp. 350–353, 2015.

APPENDIX A: SPARK PLASMA SINTERING THERMAL CYCLES

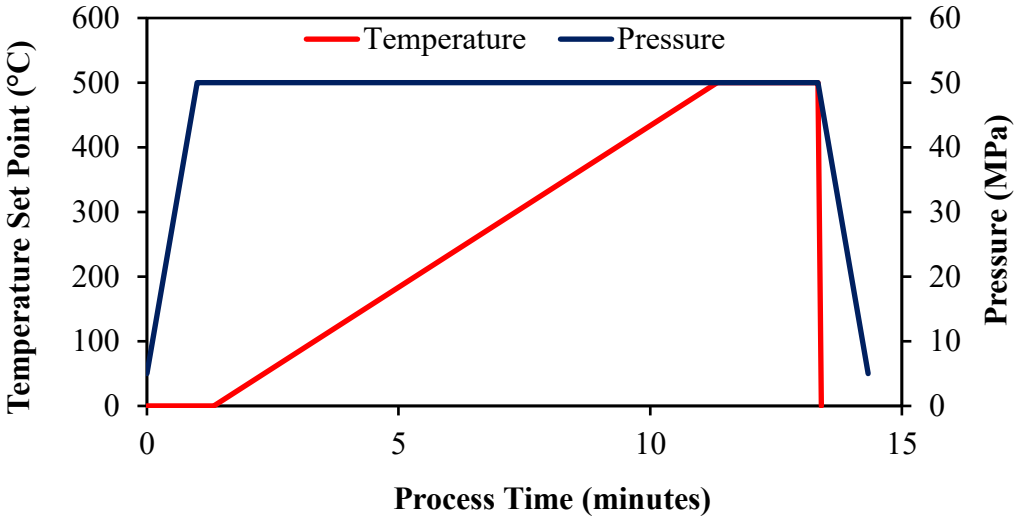

Figure A - 1 **Type I**: Maximum pressure of 50MPa is applied prior to any increase in temperature. This thermal cycle was utilized in chapter 5.

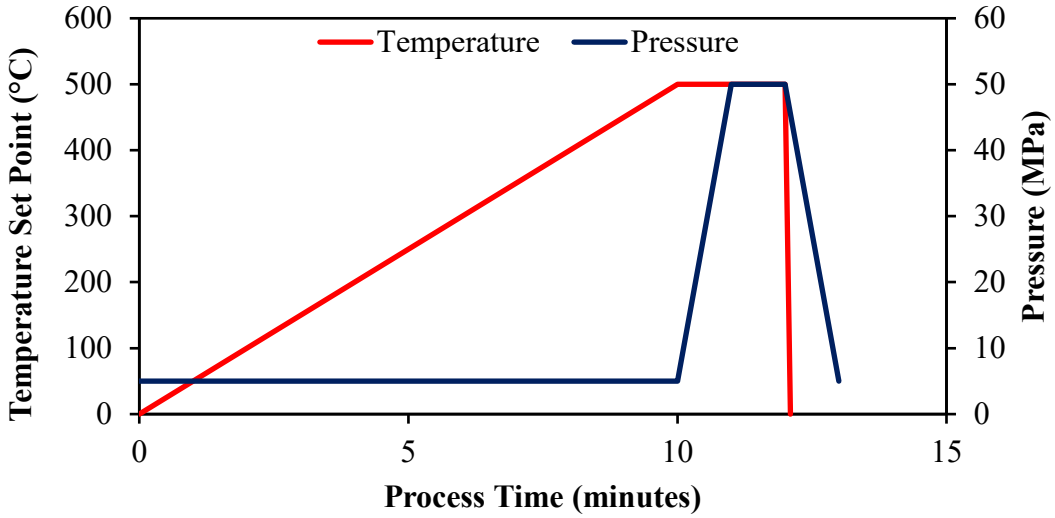

Figure A - 2 **Type II**: Maximum temperature is reached and held for 2 minutes before pressure is increased from a preload of 5MPa to 50MPa. This thermal cycle was utilized in chapters 4 and 6.

*** Laptop containing original raw data for spark plasma sintered specimens was stolen in laboratory. However, the schematic diagrams above depict the thermal cycles employed during spark plasma sintering (SPS) of all specimens.

APPENDIX B: COPYRIGHT RELEASE

Springer Nature Release (Chapter 4)

This Agreement between Dalhousie University -- Mark Amegadzie ("You") and Springer Nature ("Springer Nature") consists of your license details and the terms and conditions provided by Springer Nature and Copyright Clearance Center.

License Number	4715530712082
License date	Nov 24, 2019
Licensed Content Publisher	Springer Nature
Licensed Content Publication	Springer eBook
Licensed Content Title	Processing of a Ternary Al-Sc-Zr Powder Metallurgy Alloy via Spark Plasma Sintering and Hot Asymmetric Rolling
Licensed Content Author	M. Y. Amegadzie, I. W. Donaldson, D. P. Bishop
Licensed Content Date	Jan 1, 2019
Type of Use	Thesis/Dissertation
Requestor type	academic/university or research institute
Format	print and electronic
Portion	full article/chapter
Will you be translating?	no
Circulation/distribution	50000 or greater

Author of this Springer Nature content	yes
Title	Processing of a Ternary Al-Sc-Zr Powder Metallurgy Alloy via Spark Plasma Sintering and Hot Asymmetric Rolling
Institution name	Dalhousie University
Expected presentation date	Dec 2019
Requestor Location	Dalhousie University C360-5269 Morris Street Department of Mechanical Engineering Halifax, NS B3H 4R2 Canada Attn: Dalhousie University
Total	0.00 USD

Terms and Conditions

Springer Nature Customer Service Centre GmbH
Terms and Conditions

This agreement sets out the terms and conditions of the licence (the **Licence**) between you and **Springer Nature Customer Service Centre GmbH** (the **Licensor**). By clicking 'accept' and completing the transaction for the material (**Licensed Material**), you also confirm your acceptance of these terms and conditions.

1. Grant of License

1. 1. The Licensor grants you a personal, non-exclusive, non-transferable, world-wide licence to reproduce the Licensed Material for the purpose specified in your order only. Licences are granted for the specific use requested in the order and for no other use, subject to the conditions below.

1. 2. The Licensor warrants that it has, to the best of its knowledge, the rights to license reuse of the Licensed Material. However, you should ensure that the material you are requesting is original to the Licensor and does not carry the copyright of another entity (as credited in the published version).

1. 3. If the credit line on any part of the material you have requested indicates that it was reprinted or adapted with permission from another source, then you should also seek permission from that source to reuse the material.

2. Scope of Licence

2. 1. You may only use the Licensed Content in the manner and to the extent permitted by these Ts&Cs and any applicable laws.

2. 2. A separate licence may be required for any additional use of the Licensed Material, e.g. where a licence has been purchased for print only use, separate permission must be obtained for electronic re-use. Similarly, a licence is only valid in the language selected and does not apply for editions in other languages unless additional translation rights have been granted separately in the licence. Any content owned by third parties are expressly excluded from the licence.

2. 3. Similarly, rights for additional components such as custom editions and derivatives require additional permission and may be subject to an additional fee. Please apply to Journalpermissions@springernature.com/bookpermissions@springernature.com for these rights.

2. 4. Where permission has been granted **free of charge** for material in print, permission may also be granted for any electronic version of that work, provided that the material is incidental to your work as a whole and that the electronic version is essentially equivalent to, or substitutes for, the print version.

2. 5. An alternative scope of licence may apply to signatories of the STM Permissions Guidelines, as amended from time to time.

3. Duration of Licence

3. 1. A licence for is valid from the date of purchase ('Licence Date') at the end of the relevant period in the below table:

Scope of Licence	Duration of Licence
Post on a website	12 months
Presentations	12 months
Books and journals	Lifetime of the edition in the language purchased

4. Acknowledgement

4. 1. The Licensor's permission must be acknowledged next to the Licenced Material in print. In electronic form, this acknowledgement must be visible at the same time as the figures/tables/illustrations or abstract, and must be hyperlinked to the journal/book's homepage. Our required acknowledgement format is in the Appendix below.

5. Restrictions on use

5. 1. Use of the Licensed Material may be permitted for incidental promotional use and minor editing privileges e.g. minor adaptations of single figures, changes of format, colour and/or style where the adaptation is credited as set out in Appendix 1 below. Any other changes including but not limited to, cropping, adapting, omitting material that affect the meaning, intention or moral rights of the author are strictly prohibited.

5. 2. You must not use any Licensed Material as part of any design or trademark.

5. 3. Licensed Material may be used in Open Access Publications (OAP) before publication by Springer Nature, but any Licensed Material must be removed from OAP sites prior to final publication.

6. Ownership of Rights

6. 1. Licensed Material remains the property of either Licensor or the relevant third party and any rights not explicitly granted herein are expressly reserved.

7. Warranty

IN NO EVENT SHALL LICENSOR BE LIABLE TO YOU OR ANY OTHER PARTY OR ANY OTHER PERSON OR FOR ANY SPECIAL, CONSEQUENTIAL, INCIDENTAL OR INDIRECT DAMAGES, HOWEVER CAUSED, ARISING OUT OF OR IN CONNECTION WITH THE DOWNLOADING, VIEWING OR USE OF THE MATERIALS REGARDLESS OF THE FORM OF ACTION, WHETHER FOR BREACH OF CONTRACT, BREACH OF WARRANTY, TORT, NEGLIGENCE, INFRINGEMENT OR OTHERWISE (INCLUDING, WITHOUT LIMITATION, DAMAGES BASED ON LOSS OF PROFITS, DATA, FILES, USE, BUSINESS OPPORTUNITY OR CLAIMS OF THIRD PARTIES), AND
WHETHER OR NOT THE PARTY HAS BEEN ADVISED OF THE POSSIBILITY OF SUCH DAMAGES. THIS LIMITATION SHALL APPLY NOTWITHSTANDING ANY FAILURE OF ESSENTIAL PURPOSE OF ANY LIMITED REMEDY PROVIDED HEREIN.

8. Limitations

8. 1. ***BOOKS ONLY:*** Where **'reuse in a dissertation/thesis'** has been selected the following terms apply: Print rights of the final author's accepted manuscript (for clarity, NOT the published version) for up to 100 copies, electronic rights for use only on a personal website or institutional repository as defined by the Sherpa guideline (www.sherpa.ac.uk/romeo/).

9. Termination and Cancellation

9. 1. Licences will expire after the period shown in Clause 3 (above).

9. 2. Licensee reserves the right to terminate the Licence in the event that payment is not received in full or if there has been a breach of this agreement by you.

APMI Release (Chapter 5)

October 4, 2019

International Journal of Powder Metallurgy
APMI International
105 College Road East
Princeton, New Jersey
08540-6692
USA

I am preparing my PhD thesis for submission to the Faculty of Graduate Studies at Dalhousie University, Halifax, Nova Scotia, Canada. I am seeking your permission to include a manuscript version of the following paper(s) as a chapter in the thesis:

ISOTHERMAL FORGING OF A SPARK PLASMA SINTERED Al-0.3SC-0.2ZR POWDER METALLURGY ALLOY, M. Y. Amegadzie, B.W. Williams, A. Taylor, R. L. Hexemer, I. W. Donaldson and D. P. Bishop, International Journal of Powder Metallurgy, Vol. 54, No. 3, 47-57, 2018.

Canadian graduate theses are reproduced by the Library and Archives of Canada (formerly National Library of Canada) through a non-exclusive, world-wide license to reproduce, loan, distribute, or sell theses. I am also seeking your permission for the material described above to be reproduced and distributed by the LAC(NLC). Further details about the LAC(NLC) thesis program are available on the LAC(NLC) website (www.nlc-bnc.ca).

Full publication details and a copy of this permission letter will be included in the thesis.

Yours sincerely,

Mark Yao Amegadzie

Permission is granted for:

a) the inclusion of the material described above in your thesis.

b) for the material described above to be included in the copy of your thesis that is sent to the Library and Archives of Canada (formerly National Library of Canada) for reproduction and distribution.

Name:	James P. Adams	Title:	Executive Director/CEO
Signature:	[redacted]	Date:	October 04, 2019